

Aspects of Waste Heat Recovery and Utilisation (WHR&U) in Pebble Bed Modular Reactor (PBMR) Technology

by
Franck Mulumba Senda

*Thesis presented as partial fulfilment of the requirements for the degree of
Master of Science in Mechanical Engineering at the
University of Stellenbosch*



Supervisor: Mr Robert Thomas Dobson

March 2012

Declaration

By submitting this thesis electronically, I declare that the entirety of the work contained therein is my own, original work, that I am the owner of the copyright thereof (unless to extend explicitly otherwise stated) and that I have not previously in its entirety or part submitted it for obtaining my qualification.

Signature.....

FM Senda

Date.....

Copyright © 2012 Stellenbosch University
All rights reserved.

Summary

The focus of this project was on the potential application of waste heat recovery and utilisation (WHR&U) systems in pebble bed modular reactor (PBMR) technology. The background theory provided in the literature survey showed that WHR&U systems have attracted the attention of many researchers over the past two decades, as using waste heat improves the system overall efficiency, notwithstanding the cost of extra plant. PBMR waste heat streams were identified and investigated based on the amount of heat rejected to the environment.

WHR&U systems require specially designed heat recovery equipment, and as such the used and/or spent PBMR fuel tanks were considered by the way of example. An appropriately scaled system was designed, built and tested, to demonstrate the functioning of such a cooling system. Two separate and independent cooling lines, using natural circulation flow in a particular form of heat pipes called thermosyphon loops were used to ensure that the fuel tank is cooled when the power conversion unit has to be switched off for maintenance, or if it fails.

A theoretical model that simulates the heat transfer process in the as-designed WHR&U system was developed. It is a one-dimensional flow model assuming quasi-static and incompressible liquid and vapour flow. An experimental investigation of the WHR&U system was performed in order to validate the theoretical model results. The experimental results were then used to modify the theoretical heat transfer coefficients so that they simulate the experiments more accurately.

Three energy conversion devices, the dual-function absorption cycle (DFAC), the organic Rankine cycle (ORC) and the Stirling engine (SE), were identified as suitable for transforming the recovered heat into a useful form, depending on the source temperatures from 60 °C to 800 °C. This project focuses on a free-piston SE with emphasis on the thermo-dynamic performance of a SE heat exchanger. It was found that a heat exchanger with a copper woven wire mesh configuration has a relatively large gas-to-metal and metal-to-liquid heat transfer area. Tube-in-shell heat exchanger configurations were tested, with the working fluid flowing in ten copper inner pipes, while a coolant flows through the shell tube.

A lumped parameter model was used to describe the thermo-fluid dynamic behaviour of the SE heat exchanger. In order to validate the theoretical results, a uni-directional flow experimental investigation was performed. The theoretical model was adjusted so that it simulated the SE heat exchanger. It was found that after this correction the theoretical model accurately predicts the experiment. Finally, a dynamic analysis of the SE heat exchanger experimental set-up was undertaken to show that, although vibrating, the heat exchanger set-up assembly was indeed acceptable from a vibrational and fatigue point of view.

Opsomming

Die hoofmerk met hierdie projek was die moontlike aanwending van afvalhitteherwinning-en-benutting-(WHR&U-) stelsels in modulêre-gruisbedreaktor-(PBMR-) tegnologie. Agtergrondteorie in die literatuurondersoek toon dat WHR&U-stelsels al menige navorsers se belangstelling geprikkel het, hetsy vanweë die moontlike ekonomiese voordele wat dit inhou óf vir besoedelingsvoorkoming, bo-en-behalwe die koste van bykomende toerusting. Die PBMR-afvalhittestrome is ondersoek en bepaal op grond van die hoeveelheid hitte wat dit na die omgewing vrystel.

Om in die prosesbehoefte van WHR&U-stelsels te voorsien, moet goed ontwerpte, doelgemaakte hitteherwinningstoerusting in 'n verkoelings- en/of verhittingsproses gebruik word, dus is die PBMR as voorbeeld gebruik vir die konsep. 'n Toepaslik geskaleerde WHR&U-stelsel is dus ontwerp, gebou en getoets om die geldigheid van die stelselontwerp te toon. Twee onafhanklike verkoelingslyne, wat van natuurlike konveksie gebruik maak, in die vorm van hitte-pype of termoheuwel lusse, was gebruik om te verseker dat verkoeling verskaf word wanneer die hoof lus breek of instandhouding nodig hê.

'n Teoretiese model is ontwikkel wat die hitteoordragproses in die ontwerpte WHR&U-stelsel simuleer. Dié model was 'n eendimensionele vloeimodel wat kwasi-stasiese en onsaamedrukbare vloeistof- en dampvloei in die WHR&U-stelsel-lusse veronderstel. 'n Eksperimentele ondersoek is op die WHR&U-stelsel uitgevoer ten einde die teoretiese model se resultate te bevestig. Die eksperimentele resultate was dus geneem om die teoretiese hitteoordragkoëffisiënte aan te pas sodat dit die eksperimente kon simuleer.

Drie energieomsettingstoestelle, naamlik die dubbel funksie absorpsie siklus (DFAC), die organiese Rankine siklus (ORC) en die Stirling enjin (SE), is as geskikte toestelle uitgewys om die herwonne hitte op grond van brontemperature tussen 60 °C en 800 °C in 'n bruikbare vorm om te sit. Hierdie tesis het op vryesuier-SE's gekonsentreer, met klem op die hittedruiler. Meer bepaald is die termodinamiese werkverrigting van 'n SE-hittedruiler ondersoek. Daar is bevind dat 'n hittedruiler met 'n geweefde koperdraadmaas-samestelling oor 'n betreklik groot gas-tot-metaal- en metaal-tot-vloeistof-oordragoppervlakte beskik. Die verhitter en verkoeler is in 'n buis-in-mantel-vorm ontwerp, met die werksvloeistof wat deur tien koperbinne-pype vloei en 'n koelmiddel deur die mantelbuis.

'n Saamgevoegde-parameter-model is gebruik om die termodinamiese gedrag van die SE-hittedruiler te beskryf. Ten einde die teoretiese resultate te bevestig, is 'n eenrigtingvloei-proefondersoek uitgevoer. Die teoretiese model is aangepas sodat dit die SE-hittedruiler kon simuleer. Ná die nodige verstellings is daar bevind dat die teoretiese model die proefneming akkuraat voorspel. Laastens was 'n dinamiese ontleding van die SE-hittedruiler ook onderneem om te toon dat, hoewel dit vibreer, die hittedruiler proef samestel inderdaad veilig is.

Acknowledgements

I would like to gratefully acknowledge the following:

The almighty God, thank you Holy Father for your grace, may your name be glorified you were and will always be there for me. “Do you not know? Have you not heard? The LORD is the everlasting God, the Creator of the ends of the earth. He will not grow tired or weary, and his understanding no one can fathom. He gives strength to the weary and increases the power of the weak (Isaiah 40:28-29)”.

Mr Dobson, thank you for your consistent patience, scientific guidance and moral support throughout this project. Your knowledge and engineering approach has built a portion of library in me, that I will never be able to price.

My father, Joseph M Senda, thank you for your support, and the perseverance you taught me. These were very helpful in the completion of this project.

My wife, Arlette K Senda, thank you for your prayers, love, support and understanding throughout the time of my study.

My Children, Joseph M Senda, Aaron S Senda and Israel N Senda, thank you for your understanding during the hard times.

All my brothers, sisters and friends, thank you for all the great times we have been through together and your contribution throughout my study.

Apostle Christophe Odia and Aaron Thimothee Tshimaga, thank you for your spiritual support.

Mr Cobus Zietzman, Ferdi Zietzman, Anton van der Berg and all the employees of the Department of Mechanical Engineering workshop, thank you for the manufacturing all my experimental apparatus and offering technical support.

Dr Allyson Kreuiter, thank you for assisting me with the English language during the writing of this thesis.

NECSA, thank you for the financial support.

Dedication

To my family

“Surely you will summon nations you do not know, and nations that do not know you will hasten to you, because of the Lord your God, the Holy One of Israel, for he has endowed you with splendour of knowledge.”

Isaiah 55:5

Contents

Declaration	i
Summary	ii
Opsomming	iii
Acknowledgements	iv
Dedication	v
Contents	vi
List of figures	xii
List of tables	xv
Nomenclature	xvi
Abbreviations	xx
1 Introduction	1-1
1.1 Thesis focus areas	1-2
1.2 Objectives.....	1-3
1.3 Thesis layout	1-3
2 Literature survey	2-1
2.1 Description of a pebble bed modular reactor.....	2-2
2.2 Waste heat streams of a pebble bed modular reactor.....	2-2
2.2.1 The helium working fluid Brayton cycle	2-3
2.2.2 The reactor cavity cooling system	2-4
2.2.3 The core conditioning system	2-6
2.2.4 The core barrel conditioning system.....	2-6
2.2.5 Used and/or spent fuel tanks	2-7
2.3 Waste heat recovery and utilisation systems.....	2-8
2.4 Energy conversion devices	2-10
2.4.1 A dual-function absorption cycle.....	2-10
2.4.2 Organic Rankine cycle	2-12
2.4.3 Stirling cycle	2-13
2.4.4 Stirling engines	2-13
3 Waste heat recovery and utilisation systems for PBMR used fuel tanks	3-1

3.1	Application of a WHR&U system in the PBMR technology	3-1
3.2	The PBMR used fuel tank cooling design considerations	3-3
3.2.1	Defence-in-depth	3-3
3.2.2	Hazard mitigation	3-3
3.3	Geometrical design modelling.....	3-4
3.3.1	Cooling jacket	3-4
3.3.2	Heat transport design.....	3-5
3.3.3	Heat transfer process component design.....	3-6
3.3.3.1	Natural convection air-cooled condenser	3-6
3.3.3.2	Heat exchanger.....	3-9
3.3.4	Expansion tank	3-10
3.4	Mathematical modelling	3-10
3.4.1	Simplifying assumptions	3-10
3.4.2	Conservation equations	3-11
3.4.3	Heat transfer equations	3-12
3.4.3.1	Heat removed from the fuel tank by the cooling jacket	3-12
3.4.3.2	Heat removed from the loop by the air-cooled condenser	3-13
3.4.3.3	Heat removed from the loop by the heat exchanger	3-14
3.4.3.4	Energy transported by the working fluid transport.....	3-14
3.4.4	Integration of conservation equations.....	3-14
4	Use of Stirling engine for utilisation waste heat from a PBMR fuel tank	4-1
4.1	Free-piston Stirling engine	4-1
4.2	Free-piston Stirling engine components	4-1
4.2.1	Reciprocating elements	4-2
4.2.2	Heat exchangers.....	4-2
4.2.3	Flow friction effects in a Stirling engine heat exchanger	4-2
4.2.4	Oscillating flow in free piston Stirling engine heat exchanger.....	4-3
4.3	Stirling engine heat exchanger geometrical design.....	4-4
4.3.1	Heater and cooler design.....	4-5
4.3.2	Heat exchanger fin modelling	4-5
4.3.3	Regenerator design	4-9

4.4	Lumped parameter modelling of a Stirling engine heat exchanger	4-9
4.4.1	Energy losses through the Stirling engine heat exchanger	4-10
4.4.1.1	Energy loss due to flow friction effects	4-10
4.4.1.2	Energy loss due to working fluid leakage effects.....	4-11
4.4.1.3	Energy loss due to internal conduction.....	4-11
4.4.1.4	Energy loss due to radiation and convection.....	4-11
4.4.1.5	Energy loss due to external conduction.....	4-11
4.4.1.6	Energy loss due to the shuttle effect.....	4-12
4.4.2	The Schmidt assumptions	4-12
4.4.3	Nodal analysis.....	4-13
5	Waste heat recovery experimental and theoretical results.....	5-1
5.1	Experimental setup	5-1
5.1.1	Fuel tank	5-3
5.1.2	Cooling Jacket	5-3
5.1.3	Air-cooled condenser.....	5-3
5.1.4	Heat exchanger.....	5-4
5.2	Experimental testing procedure	5-4
5.3	Experimental and theoretical results.....	5-5
5.3.1	Sensitivity analysis of the WHR&U system theoretical model.....	5-5
5.3.2	Results	5-8
6	Stirling engine heat exchanger experimental and theoretical results.....	6-1
6.1	Experimental setup	6-1
6.1.1	Heat exchanger.....	6-2
6.1.2	Reciprocator.....	6-3
6.2	Heat exchanger testing experimental procedure.....	6-4
6.3	Heat exchanger theoretical model adjustment	6-5
6.4	Heat exchanger experimental and theoretical results	6-8
7	Dynamic analysis of the heat exchanger assembly	7-1
7.1	Introduction.....	7-1
7.1.1	Modal analysis	7-1
7.1.2	Analytical modal analysis of a mechanical system.....	7-1

7.2	Main sources of excitation in vibrations and their calculation.....	7-2
7.2.1	The shafts and couplings.....	7-2
7.2.2	The bearings.....	7-3
7.2.3	The electrical motor.....	7-3
7.2.4	The heat exchanger.....	7-3
7.3	Dynamic behaviour of the heat exchanger assembly.....	7-4
8	Discussion, conclusions and recommendations.....	8-1
8.1	The PBMR waste heat streams.....	8-1
8.2	Energy conversion devices.....	8-1
8.3	The validity of utilising the waste heat from the fuel tank.....	8-2
8.4	PBMR used and/or spent fuel tank WHR&U system theoretical model.....	8-3
8.5	Lumped parameter modelling of a Stirling engine heat exchanger.....	8-3
9	References.....	9-1
Appendix A Waste heat recovery systems thermal efficiencies computations algorithms.....		
A.1	Dual-function absorption cycle thermal efficiency.....	A-1
A.2	Organic Rankine cycle.....	A-3
A.3	Stirling engine thermal efficiency.....	A-3
Appendix B Integration of conservation equations and heat transfer dimensionless parameters.....		
B.1	Integration of conservation equations.....	B-1
B.2	Heat transfer dimensionless parameter.....	B-2
B.2.1	Convection, boiling, evaporative and Froude number.....	B-2
B.2.2	Friction factor.....	B-3
B.2.3	Nusselt Number.....	B-3
Appendix C Sample calculations.....		
C.1	Properties of fluid.....	C-1
C.1.1	Properties of air.....	C-1
C.1.2	Properties of water.....	C-1
C.2	Waste heat recovery.....	C-2
C.2.1	Theoretical calculations on the air-cooled condenser line.....	C-2

C.2.1.1 Air-cooled condenser heat transfer resistance	C-4
C.2.1.2 Temperatures at the next time step	C-5
C.2.1.3 Mass flow rate	C-6
C.2.1.4 Pressures at each time step.....	C-6
C.2.2 Calculation referring to the use of experimental data measured.....	C-7
C.2.3 Theoretical sample calculations on the heat exchanger line.....	C-7
C.2.3.1 Temperatures at the next time step	C-9
C.2.3.2 Mass flow rate	C-9
C.2.3.3 Pressure at each time step	C-10
C.2.4 Calculation referring to the use of experimental data measured.....	C-10
C.3 Stirling engine heat exchanger	C-11
C.3.1 The theoretical model	C-12
C.3.1.1 Number of holes in the mesh	C-12
C.3.1.2 Heat transfer area of the mesh	C-12
C.3.1.3 Cross-section area of the mesh holes	C-12
C.3.1.4 Volume of the metal	C-13
C.3.1.5 Void volume of the exchanger.....	C-13
C.3.1.6 Porosity.....	C-13
C.3.1.7 Number of fins	C-13
C.3.1.8 Mesh correction and compression factor.....	C-13
C.3.1.9 Laminating thickness.....	C-14
C.3.1.10 Hole hydraulic diameter	C-14
C.3.1.11 Specific surface area.....	C-14
C.3.2 Calculation of the new values of volume, temperature and pressure	C-14
C.3.3 The energy balance	C-15
C.3.4 Pressure drop.....	C-16
C.3.5 Mass flow density.....	C-16
C.3.6 Finned heat transfer coefficient	C-16
C.3.7 Unfinned heat transfer coefficient.....	C-17
C.3.8 Theoretical thermal resistance.....	C-17
C.3.9 Experimental thermal resistance	C-17

C.3.10 Correction of the thermal resistance.....	C-17
Appendix D Reciprocator dynamic and design calculations.....	D-1
D.1 Parameters of stroke and diameter of the piston.....	D-1
D.2 The reciprocator cylinder strength	D-1
D.3 The reciprocator closure strength.....	D-2
D.4 Piston Strength.....	D-3
D.4.1 Crank mechanism	D-3
D.4.2 Inertia	D-3
D.4.3 The components stiffness	D-5
D.4.4 The flywheel	D-5
D.4.5 Matrix characteristic of the dynamic behaviour of the SE heat exchanger experimental set-up	D-5
Appendix E Error Analysis.....	E-1
E.1 Systematic errors	E-1
E.2 Random errors	E-1
E.3 Absolute and relative errors	E-1
Appendix F Calibration of experimental measuring instruments.....	F-1
F.1 Calibration of thermocouples.....	F-1
F.2 Calibration of Endress and Hauser pressure sensor	F-2
F.3 Festo MS6-SFE flow sensor calibration	F-3

List of figures

Figure 2.1: Layout of a PBMR recuperative Brayton cycle	2-4
Figure 2.2: Decay heat after emergency shut down	2-5
Figure 2.3: The core conditioning system diagram process (Zibi and Koronchinsky, 2006)...	2-6
Figure 2.4: The Core barrel conditioning system (Slabber, 2006).....	2-7
Figure 2.5: Waste heat recovery and utilisation system schematic diagram.....	2-8
Figure 2.6: Thermal efficiency as a function of heat source temperature	2-10
Figure 2.7: Dual function absorption cycle	2-11
Figure 2.8: Organic Rankine cycle	2-13
Figure 3.1: A two-phase flow waste heat recovery and utilisation system	3-1
Figure 3.2: Cooling jacket details, a) section, b) cooling jacket, and c) fuel tank	3-4
Figure 3.3: Air-cooled condenser finned section.....	3-7
Figure 3.4: Manifold a) geometry, b) in and out cross-section.....	3-8
Figure 3.5: Heat exchanger configuration.....	3-9
Figure 3.6: Discretisation scheme for the waste heat recovery and utilisation system	3-11
Figure 3.7: Conservation equations control volumes, a) Mass, b) Momentum, c) Energy....	3-12
Figure 3.8: Heat removed from the fuel tank by the cooling jacket	3-12
Figure 3.9: Heat removed through an air-cooled condenser	3-13
Figure 3.10: Heat removed through heat exchanger	3-14
Figure 4.1: Diagram of a free piston Stirling engine.....	4-1
Figure 4.2: Wire mesh in a pipe; (a) loose and soldered sides representations, (b), Inner and outer pipe fins dimensions, (c) mesh dimensions.....	4-6
Figure 4.3: Heat exchanger thermal resistances	4-8
Figure 4.4: A free piston Stirling engine	4-10
Figure 4.5: Engine control volume	4-13
Figure 4.6: A Stirling engine mathematical model control volume layout.....	4-15
Figure 5.1: Schematic diagram of the experimental set-up	5-1
Figure 5.2: Waste heat recovery and utilisation system experimental set-up (without the air collector)	5-2
Figure 5.3: Heat exchanger and air-cooled condenser: (a) total thermal resistance, (b) heat transfer rate per degree unit.....	5-8
Figure 5.4: Single to two-phase mode: (a) air-cooled condenser temperatures,(b) fuel tank wall and cooling jacket temperatures.	5-8
Figure 5.5: Single to two-phase mode for air-cooled condenser line: (a) mass flow rate, (b) energy balance	5-10
Figure 5.6: Single to two-phase mode heat exchanger line: (a) heat exchanger temperatures, (b) fuel tank wall and cooling jacket temperatures.....	5-11

Figure 5.7: Single to two-phase mode for heat exchanger line: (a) mass flow rate, (b) energy balance 5-11

Figure 5.8: Heat pipe mode with loop filled with 75% of working fluid: (a) air-cooled condenser temperatures, (b) fuel tank wall and cooling jacket temperatures 5-13

Figure 5.9: Heat pipe mode with loop filled with 75% of working fluid air-cooled condenser line: (a) mass flow rate, (b) energy balance..... 5-13

Figure 5.10: Heat pipe operating mode heat exchanger line: (a)heat exchanger temperatures, (b) heat exchanger inlet and outlet temperatures,(c) cooling water inlet and outlet temperatures, (d) fuel tank wall and cooling jacket temperatures, (e) mass flow rate, (f) power balance5-14

Figure 6.1: regenerative heat exchanger experimental set-up 6-1

Figure 6.2: Schematic diagram of regenerative heat exchanger experimental set-up..... 6-2

Figure 6.3: Heater and cooler details 6-3

Figure 6.4: Reciprocator view assembly 6-4

Figure 6.5: Fin efficiency as a function of the fin length..... 6-7

Figure 6.6: The predicted and experimental heat exchanger temperatures, from start-up to steady state: (a) hot and cold water experimental and predicted, (b) air experimental and predicted, (c) hot and cold water experimental and prediction adjusted, (d) air experimental and prediction adjusted 6-8

Figure 6.7: The average heat transfer coefficient as a function of the Reynolds number: (a) as measured and predicted,(b) as measured, but prediction adjusted 6-9

Figure 6.8: The pressure drop as a function of the Reynolds number: (a) as measured and predicted, (b) as measured, but prediction adjusted..... 6-10

Figure 6.9: Dimensionless factors as measured and predicted: (a) friction factors, (b) colburn factors 6-10

Figure 6.10: The heat exchanger temperatures, as measured in an oscillating flow, from start-up to steady state :(a) frequency of 10 Hz, (b) frequency of 5 Hz 6-11

Figure 6.11: Steady state heat exchanger temperatures, as measured and predicted in an oscillating flow, a) frequency of 10Hz, b) frequency of 5 Hz..... 6-12

Figure 6.12: Steady state heat exchanger temperatures, as measured and predicted in an oscillating flow for half a second: (a) frequency of 15 Hz, (b) frequency of 7.5 Hz 6-12

Figure 6.13: Regenerator calculated temperature as a function of position: (a) oscillating flow, (b) unidirectional flow..... 6-13

Figure 6.14: Calculated, a) mass flow rate, b) pressure drop across the heat exchangers, c) pressure in the working spaces, d) overall heat transfer coefficient in the heat exchangers 6-14

Figure 6.15: Calculated, a) P-V diagram, b) Energy balance 6-14

Figure 7.1: Dynamic model of experimental set-up of heat exchanger 7-4

Figure B.1: Air-cooled condenser control volume B-2

Figure C.1: Geometric dimensions of the WHR&US experimental set-up C-2

Figure C.2: Stirling engine heat exchanger geometrical dimensions	C-11
Figure D.1: Closure stress analysis	D-3
Figure F.1: Pressure transducer calibration	F-3
Figure F.2: Flow sensor calibration	F-3

List of tables

Table 6.1: The corrected values of the porosity, volume and number of screens.....	6-7
Table 7.1: Frequency of excitation in vibration of shaft and coupling.....	7-2
Table 7.2: Frequency of excitation in vibration of bearings	7-3
Table 7.3: Frequency of excitation of the electrical motor	7-3
Table 7.4: Frequency of excitation in vibration of the heat exchanger	7-4
Table 7.5: Summary of kinetic and potential energy for each component of the heat exchanger experimental set-up.....	7-5
Table A.1: Summary of calculation for different characteristic points of the DFAC.....	A-1
Table C.1: Air cooled condenser layout geometrical dimensions and thermo-physical properties.....	C-3
Table C.2: WHR&US experimental setup grids dimensions.....	C-3
Table C.3: The time step interval, the initial values of the temperatures and mass flow rate .	C-3
Table C.4: The air collector dimensions, air velocity and heating element characteristics	C-5
Table C.5: The time step interval, the initial values of the temperatures and mass flow rate .	C-7
Table C.6: Heat exchanger layout geometrical dimensions and thermo-physical properties .	C-7
Table C.7: Geometrical data used in the Stirling engine heat exchanger theoretical model	C-11
Table D.1: The parameter of stroke and diameter of the piston	D-1
Table D.2: Maximum axial and hoop stress	D-1
Table D.3: The closure deflection, moment, stress and safety factor.....	D-2
Table D.4: Matrix mass constant summary.....	D-4
Table D.5: Reciprocator dynamic characteristics.....	D-4
Table D.6: Heat exchanger experimental set-up components stiffness	D-5
Table E.1: Air-cooled condenser line relative errors.....	E-2
Table E.2: Heat exchanger line relative errors.....	E-3
Table E.3: Stirling heat exchanger relative errors.....	E-3
Table F.1: K-type thermocouples calibration	F-1
Table F.2(a): T-type thermocouple calibration	F-1
Table F.2(b): T-type thermocouple calibration	F-2
Table F.3: T-type thermocouple calibration	F-2

Nomenclature

a	Fin width, m
A	Cross-sectional area, m^2
A_z	Heat transfer area, m^2
b	Fin length, m
B_o	Boiling number
C	Compression corrective factor
c	Specific heat, $kJ/kg K$
C_f	Coefficient of friction, compression factor
C_o	Convective number
d	Diameter, m
E	Young modulus, N/m^2 , enhancement factor
e	Specific total energy, $kJ/kg K$
Fr	Froude number
f	Friction factor coefficient
F	Form factor
G	Mass flux, kg/m^2s
g	Acceleration of gravity, m/s^2
Gr	Grashof number, $Gr = (g\beta\Delta T/(\mu/\rho)^2)L^3$
h	Heat transfer coefficient, $W/m^2 K$
h	Specific enthalpy, $kJ/kg K$
h_{fg}	Latent heat of vaporisation, kJ/kg
K	Minor loss coefficient
k	Thermal conductivity, $W/m K$
L	Length, m
m	Working fluid mass, kg
M	Mesh number (holes per 25.4 mm), mass, kg
M	Molecular weight, kg/mol
<i>Mesh</i>	Number of holes per 25.4 mm
\dot{m}	Mass flow rate, kg/s
n	Number
n_{fin}	Number of fins
Nu	Nusselt number, $Nu = hd/k$
P	Pressure, Pa
p	Perimeter, m
Pr	Prandtl number, $Pr = \mu c_p/k$
\dot{Q}	Thermal power, W
R	Specific gas constant, $J/kg K$
R	Thermal resistance, K/W
Ra	Rayleigh number, $Ra = GrPr$
Re	Reynolds number, $Re = \rho d_h \dot{x}/\mu$

S	Suppression factor
S_L	Longitudinal pitch, m
S_T	Transversal pitch, m
s	Safety factor
Sd	Pitch-diameter
St	Stanton number, $St = Nu / RePr$
T	Temperature °C or K; period, s
U	Heat transfer coefficient, $W/m^2 K$
u	Specific internal energy, $kJ/kg K$
V	Volume, m^3 , voltage, V
v	Velocity, m/s
X_{tt}	Martinelli parameter
x	Thermodynamic quality, mass fraction, displacement, m
\dot{x}	Velocity, m/s
z	Distance, m , No dimensional parameter
W	Wall thickness, m
w	Wetted area, m^2

Greek letters

α	Phase advance of the expansion space volume with respect to the compression space
α	Void fraction
β	Thermal expansion coefficient, K^{-1}
γ	Specific heat ratio, c_p/c_v
ε	Emissivity, Volume void fraction, fin volume void fraction, porosity
\emptyset	Phase advance of the displacer with respect to the piston
θ	Angle, °
δ	Phase advance of the compression space volume with respect to the piston
μ	Dynamic viscosity, Ns/m^2
ν	Kinematic viscosity, m^2/s
ν_p	Poisson's ratio
ρ	Density, kg/m^3
$\bar{\rho}$	Homogeneous density, kg/m^3
σ	Stress, N/m^2 , Stefan- Boltzmann constant, W/m^2K^4
λ	Radial clearance of piston in cylinder, m
J	Colburn factor
τ	Shear stress, N/m^2
ϕ^2	Two-phase multiplier
ψ	Prandtl number function
ω	Rotational speed, rad/s

Superscripts

<i>nd</i>	Second
<i>rd</i>	Third
<i>st</i>	First
<i>t</i>	Time step t
<i>dt</i>	Change of time

Subscripts

<i>a</i>	Air, ambient
<i>acc</i>	Air-cooled condenser
<i>ac</i>	Air collector
<i>atm</i>	Atmospheric
<i>bs</i>	Bubble suppression
<i>c</i>	Characteristic
<i>cb</i>	Convective boiling
<i>cj</i>	Cooling jacket
<i>co</i>	Condenser
<i>conv</i>	Convection
<i>cu</i>	Copper
<i>cw</i>	Cooling water
<i>d</i>	Diameter
<i>df</i>	Drag friction
<i>ds</i>	Dead space
<i>e</i>	Experimental, expansion
<i>elek</i>	Electrical
<i>eq</i>	Equivalent
<i>ev</i>	Evaporator
<i>f</i>	Fluid, factor
<i>fin</i>	Fin
<i>frict</i>	Friction
<i>ft</i>	Fuel tank
<i>g</i>	Gas
<i>h</i>	Homogenous, hot, hydraulic, heater
<i>he</i>	Heat exchanger
<i>hs</i>	Heat source
<i>i</i>	i^{th} Control volume or element
<i>in</i>	In
<i>ip</i>	Inner pipe
<i>j</i>	j^{th} Control volume or element
<i>k</i>	k^{th} Control volume

<i>lam</i>	Laminate
<i>L</i>	Length, longitudinal
<i>l</i>	Liquid,
<i>ln</i>	Logarithmic
<i>loss</i>	Loss
<i>m</i>	Mean, metal
<i>M</i>	Mesh
<i>max</i>	Maximum
<i>mon</i>	Manifold
<i>nb</i>	Nucleate boiling
<i>op</i>	Outer pipe
<i>out</i>	Out
<i>p</i>	Pipe, constant pressure
<i>pool</i>	Pool boiling
<i>r</i>	Regenerator
<i>ref</i>	Reference
<i>sat</i>	Saturation
<i>scr</i>	Screen
<i>sf</i>	Skin friction
<i>sh</i>	Shell
<i>sup</i>	Supply
<i>t</i>	Tank, theoretical
<i>T</i>	Transversal
<i>th</i>	Thermal
<i>tot</i>	Total
<i>TP</i>	Two phase
<i>unfin</i>	Without fins
<i>v</i>	Constant volume
<i>w</i>	Wall
<i>wa</i>	Water
<i>we</i>	Wetted
<i>wi</i>	Wire
<i>wf</i>	Working fluid
<i>wp</i>	Pipe wall
<i>ws</i>	Working space
<i>wy</i>	Wire in y direction
<i>wz</i>	Wire in z direction
<i>z</i>	Distance, z-direction

Abbreviations

<i>ACC</i>	Air-cooled condenser
<i>AHWR</i>	Advanced Heavy Water Reactor
<i>AVR</i>	Arbeitsgemeinschaft VersuchReaktor
<i>CBCS</i>	Core Barrel Conditioning System
<i>CCGT</i>	Closed cycle gas turbine
<i>CCS</i>	Core Conditioning System
<i>CFD</i>	Computational fluid dynamics
<i>DFAC</i>	Dual function absorption cycle
<i>DST</i>	Department of Science and Technology
<i>ESKOM</i>	Electricity Supply Commission
<i>FHSS</i>	Fuel handling and storage system
<i>GTHR</i>	Gas turbine helium reactor
<i>HTR</i>	High temperature reactor
<i>ID</i>	Inner diameter
<i>Ntu</i>	Number of transfer units
<i>OD</i>	Outer diameter
<i>ORC</i>	Organic Rankine cycle
<i>PBMR</i>	Pebble bed modular reactor
<i>RCCS</i>	Reactor cavity cooling system
<i>SE</i>	Stirling engine
<i>RPV</i>	Reactor pressure vessel
<i>THTR</i>	Thorium high temperature reactor
<i>US</i>	United States
<i>WHR</i>	Waste heat recovery
<i>WHRS</i>	Waste heat recovery system
<i>WHR&U</i>	Waste heat recovery and utilisation system

1 Introduction

Since the dawn of the Industrial Age, the accelerating pace of industrialization has seen a rapid and exponential decrease in the availability of natural energy sources. While certain lobby groups have warned of an energy crisis since the mid-twentieth century, the scale of the crisis has gained prominence in the consciousness of the moguls of industry in the last decade or so. Hence, since the beginning of the twenty-first century, energy conservation has become a major feature of interest in most industrialised countries. The economics of saving energy versus wasting it has driven industrial activists to pay more attention to energy conservation. This awareness started in the mid-1970s, when the oil producing countries used the oil price as a weapon against countries that supported Israel. The continuing rise in the price of oil and other finite energy sources, coupled with the evidence of the contribution of man to global warming, have, in the years since the signing of the Kyoto Protocol on Climate Change, sparked innovation aimed at energy conservation. Alternative energy sources include technologies such as hydroelectric, wave, solar energy, and nuclear power.

The implementation of energy conservation requires that all the possibilities of counteracting any potential loss of energy must be considered. This includes reducing heat losses from furnaces, thermal insulation, repair of steam leaks in power plants, and all other practices that may be implemented rapidly and, preferably at low cost. Once this is achieved, further strategies have to be developed to stabilise short-term energy conservation in systems by implementing permanent solutions. Permanent energy conservation solutions are more expensive, but result in energy benefits over many years. These permanent solutions are referred to as waste heat recovery systems (WHRs) (Reay, 1979).

Waste heat recovery systems have been used for many decades, particularly in power generation and energy intensive industries (Reiter, 1983). They conserve energy by storing and reusing available waste heat. They transfer energy from sources of waste heat to energy conversion systems, by using various types of heat recovery equipment. They reduce energy consumption which results in significant cost savings (Reiter, 1983; US Department of Energy, 2005). WHRSs form an important part of the methods developed to increase the efficiency of various energy saving systems. It is for this reason that, from 1959, energy conservation research has focussed on WHRSs. Examples of WHRSs in the automotive industry include, *inter alia*, Lotun's work on small-scale WHRSs for automotive application using steam technology and BMW's research on utilising steam technology to recover waste heat from the exhaust gas of their automobiles (Snyman et al., 2008).

Waste heat recovery systems are totally dependent on the temperature of the waste heat stream. A waste heat stream is a source of thermal energy generated by means of mechanical, electrical or any other form of industrial process, including chemical reactions, fuel combustion, furnace heat, and nuclear radiation decay, for which no useful application has been found. Unless utilised, the waste heat is dumped into the environment without being utilised for economically beneficial purposes. The attractive aspect of waste heat is the value

of the estimated cost saving, if losses are reduced. However, not all waste heat can be fully recovered. A significant amount of heat may be recovered by using specially designed heat recovery equipment, depending on the temperature of the heat source and the nature of the working fluid used in the system. WHRS equipment should be able to process waste heat at any temperature from chilled cooling water to the high-temperature waste heat of a nuclear reactor (Fujima et al., 2000). Usually high-temperature waste heat leads to more efficient energy recovery and cost effectiveness. Typical examples of WHRSs are preheating of fuel-air mixtures, space heating, and pre-heated boiler feed water or process water.

For high-temperature energy recovery, a cascade of waste heat recovery equipment may be used to ensure that the maximum amount of heat is recovered. An important application of waste heat equipment is in the use of high-temperature waste heat for air preheating or low-temperature waste heat for process feed water heating or steam generation.

1.1 Thesis focus areas

This thesis focuses on heat transfer and heat conversion by means of passive cooling processes using heat pipes and heat exchangers to construct waste heat recovery and utilisation (WHR&U) systems for a PBMR fuel tank. The main aim is to develop conceptual, design and modelling theories to construct a WHR&U system that will convert the recovered thermal energy into a useful form of energy, such as electricity, by means of an energy conversion system. The WHR&U system design and modelling theory developed in this project should comply with the nuclear safety requirements. Therefore, a back-up air-cooled condenser system was designed to prevent a failure of the cooling process in case of non-functioning of the energy conversion system. In this thesis, the energy conversion system is simulated using the heat exchanger cooling water.

Nuclear reactors generate very large amounts of energy using a small quantity of nuclear fuel (Slabber, 2006). They also produce high-temperature waste heat resulting from heat decay from the reactor facilities, which is normally vented to the environment. Depending on the temperature of the heat source, three possible energy conversion systems have been identified for the PBMR waste heat:

- an organic Rankine cycle (ORC) (250-350 °C),
- a dual function absorption cycle (DFAC) (≈ 100 °C),
- a Stirling engine cycle (probably > 450 °C).

This thesis has focused on the use of a free piston SE. Having no crank system, this particular engine is extremely reliable and hence suitable for nuclear or space exploration purposes. The design of a complete free piston SE is a very long process, and is not the focus of this project. However as an efficient SE depends on the SE heat exchanger performance, this project also concerned itself with fundamental work towards the so-called third-order lumped parameter modelling of a SE heat exchanger. To this end, and for the purpose of testing the hypothesis of this thesis, a SE heat exchanger was designed, constructed and tested in such a way as to

evaluate and predict the actual engine performances. Furthermore, to test SE heat exchanger, a reciprocator operating with a three-phase, asynchronous electric motor and a crankshaft was designed and built. Finally, a preliminary dynamic analysis was developed to predict the stability of the SE heat exchanger experimental set-up assembly with respect to fatigue and indefinite life.

The cooling process has been identified as a way of recovering and re-using waste heat for a PBMR power plant. Because of the complexity of a complete WHR&U system for a spent/used fuel tank, only specific aspects of the system were considered. These included:

- A proof of concept by building and testing a PBMR fuel tank WHR&U system scale model
- A free-piston SE design, but with specific emphasis on the heat exchanger

For each of these aspects, the theoretical modelling was considered and experiments were conducted to validate the theory.

1.2 Objectives

The objectives of this project are the following:

1. Identify the waste heat streams from a PBMR reactor that can be potentially harvested for utilisation in a power conversion process.
2. Analyse a suitable energy conversion system to use for the utilisation of the waste heat and, specifically, an ORC, a DFAC and/or a SE.
3. Demonstrate the validity of utilizing the waste heat from a fuel tank by building and testing a WHR&U system scale model. Here, the following must be considered:
 - a) Heat transport using natural circulation and two-phase flow in a thermosyphon closed loop.
 - b) Heat transfer using heat exchangers and a temperature/pressure control device.
 - c) An air-cooled backup system in case of a stoppage of the utilisation system.
4. Establish a theoretical model of the designed WHR&U system scale model, the results of which will be compared with experimental results.
5. Develop a lumped parameter model of a SE heat exchanger.
6. Evaluated the design of a SE heat exchanger suitable for such an engine by experimental and theoretical analysis.

1.3 Thesis layout

First, a literature study was conducted to identify the PBMR waste heat streams. This is presented in section 2. The WHRSs, as well as the analysis of a suitable energy conversion system; such as an ORC, a DFAC and a SE are also described.

Section 3 discusses the application of a WHR&U system in PBMR technology. The geometrical design algorithm of a PBMR used fuel tank WHR&U system heat pipes

thermosyphon loop, as well as the mathematical modelling theory used to simulate the loop heat transfer behaviour, is developed.

Section 4 describes the theory used to design a SE heat exchanger. The third-order lumped parameter modelling of a SE and a SE heat exchanger is also described.

Section 5 and section 6 describe the experimental apparatus, the experimental procedure and data handling of the PBMR used fuel tank WHR&U system scale model and the SE heat exchanger, respectively. A comparison of theoretical and experimental results allowing the validation of the PBMR used fuel tank waste heat recovery process and the SE heat exchangers theories developed in sections 3 and 4 respectively are also presented in section 5 and 6 respectively.

Section 7 describes the dynamic analysis of the heat exchanger experimental assembly. The prediction of the assembly stability, from a fatigue point of view, using modal analysis, is also discussed in this Section.

Section 8 presents conclusions to the project, as related to the original objectives and offers recommendations on future work.

2 Literature survey

South Africa has generated electricity for commercial use since 1881 (Eskom Heritage, 2009). This power was originally generated to support a growing mining industry. The discovery of South Africa's mineral wealth drove the process of expanding power generation from supplying mining towns to urban and national electrification. Since then, electricity has been an important life factor without which any person in South Africa would not be able to live. This has been demonstrated by the power shortages of the last three years (2006-2009) which not only affected personal lives, but also resulted in significant financial losses in business and industry (Ruppersberg, 2008). Therefore, such shortages are not acceptable and more power stations need to be built.

Given that coal is a major resource in South Africa, 88% of power stations use it to produce heat, which heats water to steam and thereby generate electricity. Because it uses coal, South Africa is known, world-wide, as one of the highest emitters per capita of greenhouse gases such as CO₂, SO₂ and NO_x. However, the country is committed to reducing these emissions and is a signatory to the United Nation's Framework Convention on Climate Change and the Kyoto Protocol (DST, 2007). South Africa is thus committed to reducing coal power generation from 88% to 78% by 2012 and to 70% by 2025. The power supply crisis has therefore accelerated the need to diversify South Africa's energy mix and its move to alternative energy sources such as natural gas, various forms of renewable energy, as well as nuclear power generation (Eskom's Climate Change Commitment, [S.a.]).

South Africa is also blessed with large deposits of uranium, which is a by-product of the gold mining industry. Many of the so-called 'mine dumps' in the gold mining areas of the country are being recycled to recover both gold and uranium. The South African government and ESKOM are looking towards increasing reliance on nuclear power generation as a means to ensure energy security. This will diversify the country's current energy supply and reduce its greenhouse gas emissions (South Africa.info, 2004). Nuclear power plants require advanced technologies, resulting in less air pollution and effective lower energy costs (Adak et al., 2006). This will reduce South Africa's dependence on coal and result in lower harmful emissions of sulphur, carbon and carbon dioxide. Nuclear fuels can easily be stored because the amount of nuclear fuel required for heat generation is much smaller than of fossil fuels (Slabber, 2008).

ESKOM is planning to increase its actual capacity of 42 GW by 4% per year, to 82 GW by 2015, of which 20 GW will be produced from nuclear power plants (South Africa.info, 2004). The increase in the number of nuclear power plants has led South Africa to research high temperature gas reactor technologies such as the pebble bed modular reactor (PBMR). The South African government has provided full support to the project since 2004 (Mayson, 2005). A demonstration plant of a PBMR was planned, but cost considerations and the potential for failure scuppered the project. This development does however not nullify the research that was undertaken for this project, as the work done can be applied to other waste energy sources, and high temperature reactor technology.

2.1 Description of a pebble bed modular reactor

A pebble bed modular reactor (PBMR) is a gas cooled reactor that was designed in Germany in the 1950s. It works well on paper, but despite many attempts, no one has yet succeeded in constructing a demonstration plant for commercial use. Some years ago, the South African government embarked on a project to attempt to produce a PBMR for commercial application, using technology that was developed during the years of the Apartheid era.

A PBMR is a helium-cooled graphite-moderated high-temperature reactor that makes use of a continuous fuelling system using spherical fuel elements with similar geometry to those used in the HTR10 of China, the AVR, and the THTR of Germany (Fuls et al., 2005). Fuel elements take the form of uranium dioxide kernels coated in silicon carbide and pyrolytic carbon. The resultant fuel pebble has a 60 mm diameter and the reactor is cooled by helium. The design greatly reduces the risk of any reactor core meltdown. The risk is in fact reduced to zero because the design automatically shuts down when there is a failure of the systems (Fuls et al., 2005).

The PBMR pressure vessel is 27 m high, with a 6.2 m internal diameter. It contains an annular fuel core located between the central and outer graphite reflectors. The reactor outer reflector and passive heat transfer medium are formed by a line of one meter thick graphite bricks. The graphite moderator slows and keeps the neutrons at the speed required for nuclear fission. The heat generated within the reactor pressure vessel (RPV) due to the interaction process of neutron fission is removed by helium coolant. It is transferred to energy conversion devices, which convert energy first from thermal to mechanical and then from mechanical to electrical power. The helium coolant enters the reactor at 500 °C and leaves at 900 °C to drive a turbine that produces mechanical power according to a closed Brayton cycle. The turbine is then mechanically linked to the gas compressor on one side and a generator through a speed-reducer gearbox on the other side producing 165 MWe (Dudley et al., 2006).

2.2 Waste heat streams of a pebble bed modular reactor

As mentioned in section 2.1, in a PBMR the helium coolant leaves the RPV at 900 °C and returns at 500 °C. During this process, the helium coolant passes through a number of thermal and mechanical devices constituting the reactor power plant. The difference between the overall temperature of the helium coolant entering and the temperature of the working fluid when leaving a specific device, will define the amount of heat that is rejected from the device to the environment. Some of the thermal and mechanical devices of a PBMR from which significant amounts of heat flows to the environment are the following:

- the Helium working fluid Brayton cycle,
- the decay heat and the reactor cavity cooling system RCCS,
- the core conditioning system (CCS) and the core barrel conditioning system (CBCS),
- the used and spent fuel tanks

2.2.1 The helium working fluid Brayton cycle

The helium working fluid Brayton cycle is a closed-cycle gas turbine (CCGT). The CCGT makes a PBMR possibly the best near-term power conversion method for maximizing the economic potential of heat generated from the reactor (Schleicher et al., 2001). It was first used over sixty years ago, with the commissioning of the fossil-fired pioneer plant in 1939 in Switzerland. Prior to 1978, only seven fossil-fired CCGTs using air, argon and helium, were built in Germany and Switzerland. The primary heat exchanger transfers heat to the working gas from its combustion product, with an estimated thermal efficiency of 30%. In 1970, the US and Germany were interested in the application of a helium CCGT for high-temperature gas cooled reactors, which became effective in the 1990's. Eventually, using highly effective plate fins recuperators and magnetic bearings, a net thermal efficiency of nearly 50% was achieved (Schleicher et al., 2001). Due to the PBMR's high temperature and system pressure, its thermal efficiency, defined in terms of the RPV input and output temperatures, is approximately 40% (The PBMR, [S.a]).

The CCGT does not transfer its heat to a secondary (steam) cycle; the heat is directly used to power the turbine of the generator system (see figure 2.1). This system comprises of two turbo-compressors used to maintain the required system pressure. For better efficiency, a recuperator transfers heat from the gas flowing into the low-pressure compressor to the gas flowing into the reactor unit. Helium coolant is compressed in two stages to maintain the required operating system pressure. Starting just after the pre-cooler, helium at a relatively low-pressure and a temperature of about 30 °C is compressed by a low-pressure compressor to an intermediate system pressure at a temperature of about 130 °C, after which it is cooled to a temperature of about 26 °C in an inter-cooler. A high-pressure compressor then compresses the helium to the required system pressure. To achieve the high net thermal efficiency of the PBMR power plant, the two compression stages require a cooling of the working helium to about 26 °C (Dardour et al., 2006).

Hot helium leaving the power turbine at a temperature of about 670 °C exchanges heat in the recuperator, with the cooler downstream helium leaving a high-pressure compressor at about 100 °C, before it re-enters the reactor unit. The heated helium with a mass flow rate of about 193.4 kg/sec leaves the recuperator at approximately 130 °C and flows to the pre-cooler where it cools to about 30 °C before it enters the low-pressure compressor (Dudley et al., 2006). The recuperator is thus one of the key components in CCGT, ensuring a high net thermal efficiency of the reactor. It must have a high heat transfer coefficient and small size to comply with the working requirements (Slabber, 2006). A compact plate recuperator that may achieve 96% effectiveness will be used in the PBMR plant (Schleicher et al., 2001). Therefore, heat at approximately 130 °C is removed from the CCGT through the inter-cooler and pre-cooler cooling water, respectively. Hence the pre-cooler and inter-cooler are the PBMR helium working fluid Brayton cycle potential sources of waste heat.

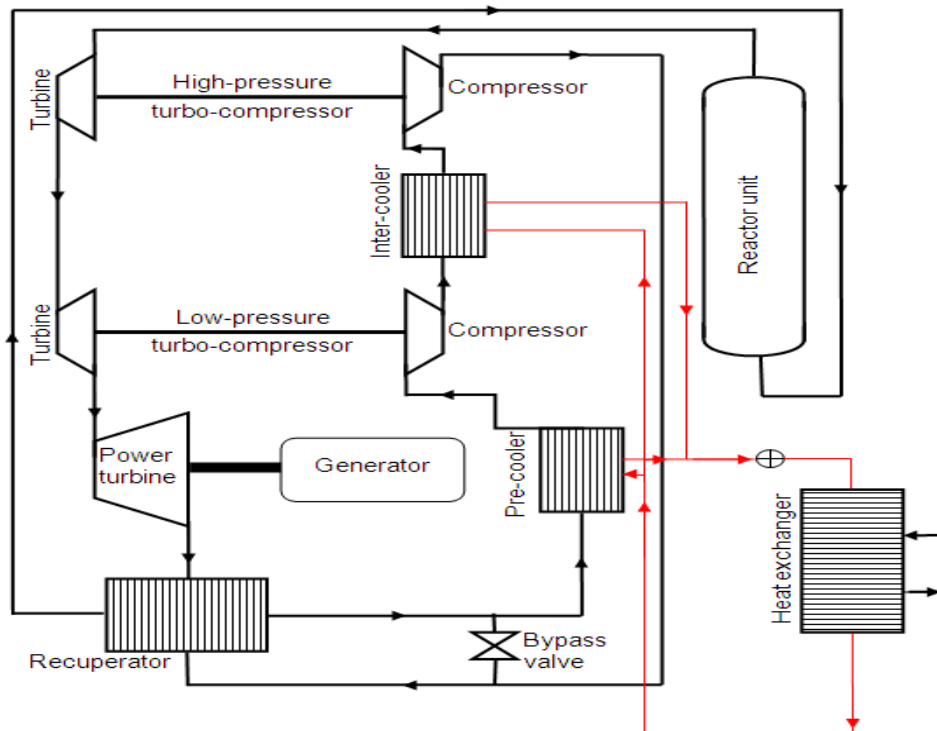


Figure 2.1: Layout of a PBMR recuperative Brayton cycle

After the reactor unit, the hot high-pressure helium is expanded in a high-pressure turbine, after which it is further expanded in a low-pressure turbine. The high-pressure turbine drives the high-pressure compressor while the low-pressure turbine drives the low-pressure compressor. After the low-pressure turbine, the helium is further expanded in the power turbine to produce electricity through a generator. The hot helium from the power turbine is cooled in the recuperator, after which it is further cooled in the pre-cooler to restart the process again. This completes the cycle.

2.2.2 The reactor cavity cooling system

Since a PBMR power plant operates at high temperature, decay or residual heat must be removed by an entirely passive system. This system is called the reactor cavity cooling system (RCCS). An entirely passive system means that no mechanical moving parts such as pumps or active controls are used. This system must thus make use of natural circulation using thermosyphon-type closed-loop heat pipes.

Decay heat is the heat generated within the reactor core as a result of the radioactive decay of the reactor fuel. Residual heat is the heat that remains in the nuclear fuel without being removed by the helium coolant flowing through the reactor core. The amount of residual or parasitic heat that needs to be removed from the RCCS is the waste heat of the reactor core that is transferred from the reactor vessel to the cavity around the vessel.

The following functions and basic requirements of a RCCS are given by Slabber (2006):

- The parasitic or residual heat as well as all waste heat must be removed during normal operation in order to maintain the RPV outside temperature not more than 400 °C.
- A limit design temperature of not more than 65 °C must be maintained for the concrete surfaces of the reactor cavity.
- After shut-down, the after-heat must be removed to maintain the RPV surface temperature at less than 400 °C.
- All decay heat and residual heat transferred to the reactor cavity during a pressurised or depressurised loss of the forced helium coolant should be removed.
- Under normal operating conditions, the RCCS must remove and reject to the environment approximately 1890 kW of heat and approximately 3580 kW during a depressurised loss of forced coolant.

The pressurised loss of forced coolant is a situation where there is no helium leakage from the primary cooling loop, but where the helium flow has stopped. The reactor will shut-down immediately and the decay heat, termed the after-heat, will start heating up the reactor. During this process the pressure in the helium loop will rapidly decrease to 6.8 MPa, and the reactor pressure vessel wall temperature will increase to approximately 474 °C (Slabber, 2006).

The depressurised loss of forced cooling is a situation where no helium is flowing through the reactor and that the helium inventory has been vented to the atmosphere because of a leakage in the primary loop. The pressure in the reactor is thus at the atmospheric pressure. During this process the wall temperature will increase to approximately 527 °C (Slabber, 2006).

Figure 2.2 shows the decay heat of a reactor from ten seconds after an emergency shut-down. The heat drops asymptotically from the nominal output power of approximately 400 MW to around 16 MW. After the initial asymptotically drop in the reactor output power, the generated heat drops exponentially to around 1.5 MW after 300 hours. The heat load in the RCCS after an emergency shut-down depends on the temperature difference between the reactor core and the RCCS. As shown in figure 2.2, Slabber (2008) found that this heat load may be determined by the only heat source of the reactor, which is the decay heat.

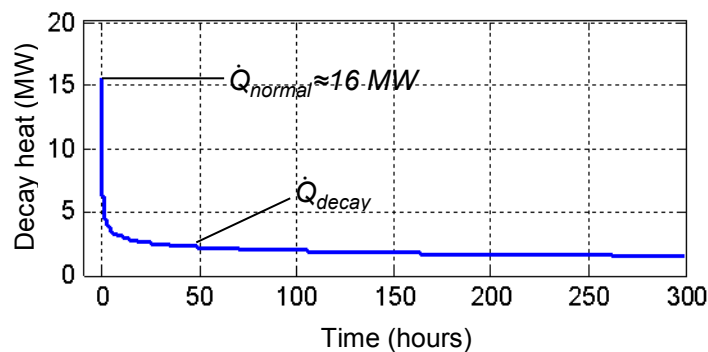


Figure 2.2: Decay heat after emergency shut down

The decay heat may be used to simulate the heat load on the RCCS during an emergency shut down. Slabber (2008) proposed that the decay heat may be given as

$$\dot{Q}_{decay} = 0.0622 \dot{Q}_{normal} t^{0.2} \quad (2.2.1)$$

where, t is the time and \dot{Q}_{normal} is the decay heat of 10 seconds after shut-down, in MW.

2.2.3 The core conditioning system

The core conditioning system (CCS) is another cooling system that is fitted into the reactor cavity to remove the core decay heat from the reactor when the Brayton cycle is not operational or when the motored turbo-generator set is not functional. It must remove 4.35 MW decay heat for the following conditions (Slabber, 2006):

- when the motored turbo-generator set is unable to remove decay heat at approximately a temperature of 387 °C, the CCS acts as a back-up to the motored turbo-generator set decay heat removal function,
- during main power system commissioning, the CCS circulates heated nitrogen for the primary loop initial clean-up system. This clean-up system removes moisture from the core graphite structures,
- during maintenance, the CCS provides a cooling flow to the reactor fuel removal chute in order to cool the fuel spheres that enter the core unloading devices.

Figure 2.3 shows a diagram of the CCS. The hot core outlet gas is extracted from the core outlet pipe and transported to the inlet of the CCS water-cooled heat exchanger. Heat is extracted from the system through the use of the CCS water cooler. The cooled helium leaving the CCS heat exchanger is then directed back to the core inlet pipe via the CCS blower. The blower controls the required mass flow rate through the system.

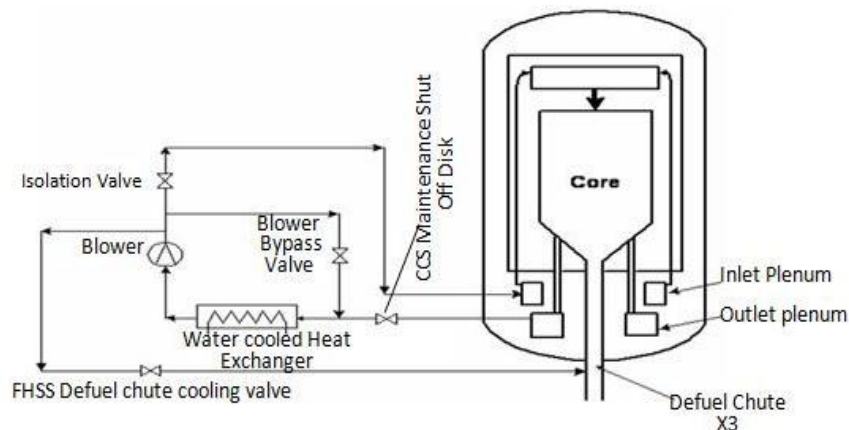


Figure 2.3: The core conditioning system diagram process (Zibi and Koronchinsky, 2006)

2.2.4 The core barrel conditioning system

The core barrel conditioning system (CBCS) is the third cooling system that is also fitted into the reactor cavity to control the core barrel temperature and removes up to 1.5 MW during all anticipated normal operating conditions. Hot helium is collected in the upper volume of the

RPV and directed to the CBCS, which is situated in the bottom volume of the power conversion unit citadel area. Within the CBCS vessel, helium is directed through a water-cooled heat exchanger where heat is removed from the system. Helium then flows through a centrifugal blower into the bottom volume of the RPV (see figure 2.4). Helium is distributed equally into the gap between the core barrel and the RPV. The helium flows up in the annulus between the RPV and the core barrel (Slabber, 2006).

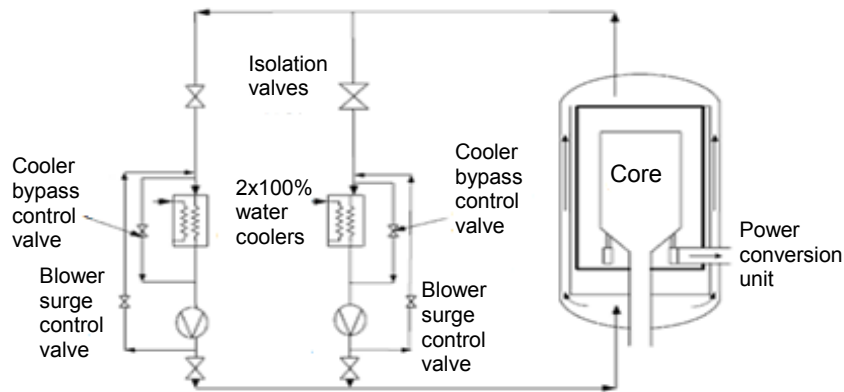


Figure 2.4: The Core barrel conditioning system (Slabber, 2006)

2.2.5 Used and/or spent fuel tanks

In a PBMR, the fuel pebbles re-cycle through the reactor several times in its lifetime until they are partially *burned* and/or optimally *used-up*. Partially burnt fuel may be removed for recycling while spent fuel will be removed from the reactor. The highly radioactive fuel removed will be stored in storage tanks. The PBMR has 12 storage tanks, capable of storing a total of more than six million spheres. (Fuls and Mathews, 2006)

A storage tank is a large cylindrical pressure vessel with a total height of 18 m and inner diameter of 3.1 m. The tank is made of carbon sealed steel, with a wall thickness of approximately 16 mm, capable of sustaining one MPa internal pressure. Inside the tank are a number of cooling tubes running from the bottom to the top. The fuel spheres are stored in an inert gas environment at atmospheric pressure. Each spent fuel sphere releases an amount of heat caused by the radioactive decay of unstable fission products inside the sphere. The amount of heat greatly depends upon the time that has elapsed from the moment the nuclear fission reaction has stopped. The decay heat is transferred from sphere to sphere to the tank surface area, and then by convection to the air on the outside. No heat is actively removed from inside the tank (Fuls et al., 2005).

Nuclear reactor spent fuel is initially thermally hot as well as highly radioactive. It is too dangerous for humans to directly handle spent fuel. It is exceedingly important to shield people and the environment in which they are living from radioactivity (Andrews, 2006). Radioactive products fall into three categories: un-reacted fuel, usually uranium; fission products; and activation products, most notably plutonium. Fission products are by far the

most radioactive; they take much longer to decay and so have the shortest half-life. Unreacted uranium and plutonium have vastly longer half-lives, but are correspondingly less radioactive. Radioactive products within the spent fuel will eventually continue to decay and, while decaying, radiation is emitted and simultaneously waste heat is released (Andrews, 2006).

Fuls and Mathews (2006) carried out a passive cooling analysis, which required the temperature of the fuel within the tank to be maintained below 400 °C. From the results, four crucial heat load scenarios describing the spent and used fuel tanks as potential energy savers were identified:

- A tank filled with spent fuel will have a thermal power of 140 kW and represents the highest heat load for closed-loop active cooling.
- A tank filled with used fuel will have a thermal power of approximately 640 kW and represents the highest heat load for open-loop active cooling.
- A tank filled to 5% capacity with spent fuel will have a thermal power of approximately 23 kW and represents the very lowest heat load for closed-loop active cooling, which may present problems during passive cooling.
- A tank filled to 25% capacity with used fuel will have a thermal power of approximately 220 kW and is the stage when the maximum fuel temperatures exist in the tank during loading, due to the high decay heat density relative to the small heat exposed heat transfer areas of the tank.

2.3 Waste heat recovery and utilisation systems

Once identified, waste heat may be upgraded again in a process where, not only it is recovered, but also reused. This process is referred to as WHR&U. As shown in figure 2.5, a WHR&U system requires waste recovery equipment to recover heat from the streams and transform it into a useful form for utilisation. This is done using energy conversion devices. Over the past two decades, much research, with satisfactory results has been directed at achieving this. Research carried out by others that shows how WHR&U systems can be applied, and the benefits thereof, follows.

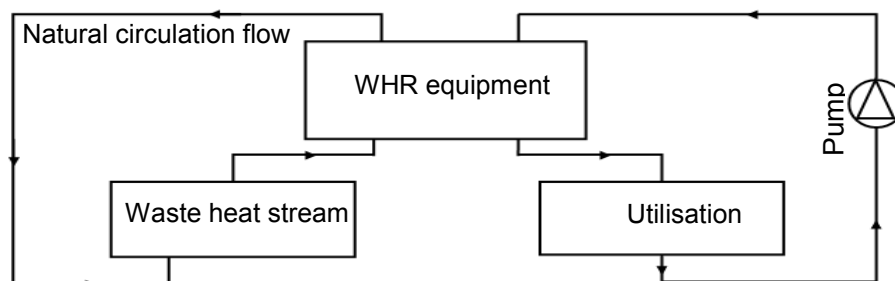


Figure 2.5: Waste heat recovery and utilisation system schematic diagram

Reay (1979) found that not only is heat recovery economical, but that it also reduces pollution. Energy may be recovered in many ways using WHR components, such as heat exchangers.

WHR components exchange heat between the waste heat stream loop and the utilisation loop working fluids, respectively. Using waste heat improves the energy yield and extends the life of the equipment used. This, including a wide variety of super-efficient heat recovery systems for all types of waste heat generated from various fuels and different industrial sources. Examples of industrial heat sources are: heavy fuel fired, gas fired, and gas turbine exhausts heat and/or process heat from a nuclear reactor. They may be consumed at different places in various forms like steam, hot water, chilling and refrigeration. WHR equipment, such as boilers, are used to convert waste heat into steam. They may be provided with economisers to improve their thermal output and efficiency (Waste heat recovery system [S.a.]).

Ferland (2007) developed some interesting ideas and technologies concerning industrial waste heat recovery. He mentioned the following technologies as the main key functions in order to reach the goal of the waste heat recovery process: sensible pre-heating, heating cooling, condensing economisers, thermal compression and power generation. Juchymenko (2007) proposed that it is more efficient to use an organic Rankine cycle to reutilise any waste heat at a temperature ≥ 95 °C in a process that generates electricity.

According to the US Department of Energy (2005) a large amount of heat supplied in most fuel-fired equipments is wasted as exhaust or flue gases. Combustion products removed from furnaces still hold considerable thermal energy. In this way, energy losses decrease the thermal efficiency of the system. It follows that in order to increase thermal efficiency of a system WHR&U should be used. Before a WHR&U system can be applied, however, heat losses must first be minimised. The US Department of Energy (2005) developed the most commonly used methods to recover and utilise waste heat that are totally dependent on the temperature of the heat source. These include processes such as pre-heating of the combustion products, load pre-heating, water heating and steam generation.

Fujima et al. (2000) proposed a zero waste heat release nuclear cogeneration system using carbon dioxide as a working fluid for the reactor and a heat recovery system in the secondary loop of a high-temperature gas reactor. They used a chemical process and heat pump to recover all heat rejected from the secondary loops of the reactor as hot and cold water. Hence, waste heat contained in water is not released into the environment as in conventional nuclear reactors.

From the above it may be seen that, the nature of WHR&U system equipment depends upon the nature and the temperature of the heat source (Reay, 1979). It consists of a number of heat transfer process devices, including the following: heat exchangers, waste heat vapour generators, heat pipe heat exchangers, and prime movers as sources of waste heat, waste incineration with heat recovery, heat pumps and solar heat recovery devices. These may be combined together in a system to meet the required needs of re-utilising waste heat for a particular source. This is done by first identifying the type of WHR&U system equipment and thereafter, the principal applications to use such as; gas-to-gas, gas-to-liquid systems, and liquid-to-liquid heat recovery equipment.

2.4 Energy conversion devices

In most of the waste heat streams of a PBMR, heat is wasted as a result of heat transfer transport mechanisms such as:

- Convection between the radioactive product flowing within the system and the internal component area,
- conduction through the component wall thickness and then later,
- convection and/or radiation between the external component area and its surroundings.

It follows that the energy efficiency of a PBMR power plant may be increased by using an energy conversion device in a WHR&U system to capture and reutilise much of the waste energy. The efficiency of a WHR&U system is directly dependent on the temperature range of the heat source. For some specific temperature ranges, the following energy conversion systems have been identified as appropriate for a PBMR WHR&U system (see figure 2.6):

- $60\text{ }^{\circ}\text{C} \leq T \leq 100\text{ }^{\circ}\text{C}$: a dual function absorption cycle (DFAC).
- $100\text{ }^{\circ}\text{C} \leq T \leq 350\text{ }^{\circ}\text{C}$: an organic Rankine cycle (ORC).
- $350\text{ }^{\circ}\text{C} \leq T \leq 800\text{ }^{\circ}\text{C}$: Stirling cycle (SC).

Figure 2.6 shows the simulation results of the thermal efficiency for the three identified energy conversion systems in terms of different temperatures of waste heat sources. The various energy conversion systems are now discussed below.

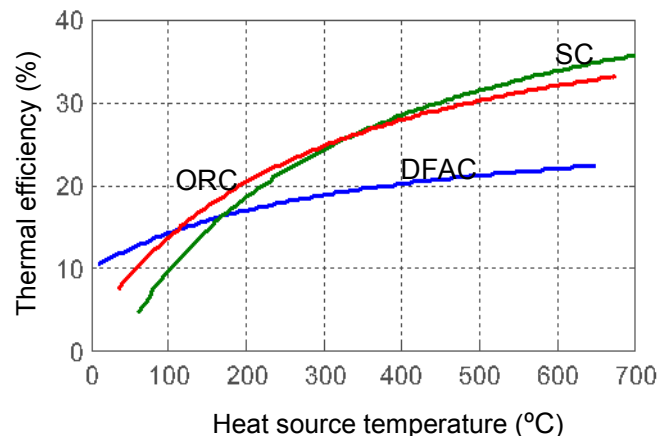


Figure 2.6: Thermal efficiency as a function of heat source temperature

2.4.1 A dual-function absorption cycle

Low-temperature is also a widely found heat source that may be upgraded for use. In the US, many refineries are used to provide heat processes and electricity. The heat converted into electricity is about 9.5% of the amount of the heat input in the refinery. Most of that heat is injected into the environment at temperatures too low to be useful (Pellegrino et al., 2007). In

addition to refining, there are many other industrial low-temperature waste heat streams such as in the chemical and forestry industries. Other energy sources such as solar, geothermal power plants and gas turbines have also been identified as low-temperature heat sources (Pellegrino et al., 2007).

Traditionally, waste heat was used for heat integration. Heat integration transfers low-temperature heat to even lower-temperature requirements. The demand for low-level temperature heat is still relatively limited and much of the waste heat is presently unused. Not long ago, waste heat powered-refrigeration was re-utilised in refineries to recover volatile products from waste heat sources, to remove bottlenecks in the process units and to improve separation efficiency (Erickson et al., 1998). However, the quantity of low-level waste heat available is well in excess of what would be required to meet all prospective refinery refrigeration needs. Options that generate power from waste heat can therefore be considered.

When presenting a dual function cycle with power production as the primary function, Goswami et al. (1999) found that, in many applications, refrigeration is produced more often than power. It takes not only power to produce refrigeration, but also refrigeration equipment. More waste heat is available than is required to provide all possible refrigeration needs. Also, refrigeration needs may sometimes be seasonal. Therefore, power generation can be considered as an additional benefit. It is particularly advantageous to have the technology that provides refrigeration as well as power, or a dual-function cycle (see figure 2.7). The refrigeration and power generated from waste heat can meet internal needs, and excess power can be exported. The dual-function aspect ensures that the waste heat is fully utilised year-round, always converting it to some useful product. This ensures that the capital equipment is consistently utilized.

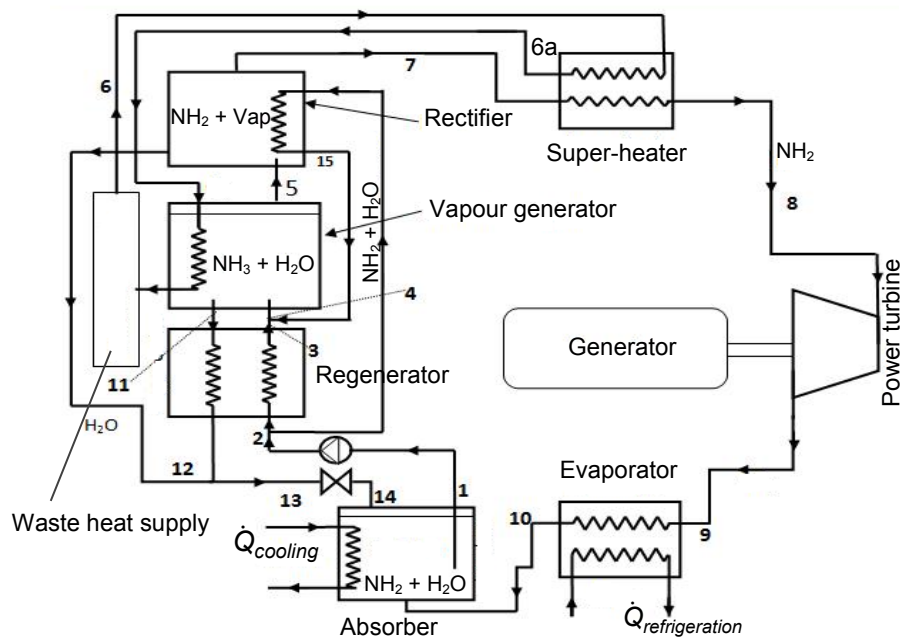


Figure 2.7: Dual function absorption cycle

A dual-function ammonia water system will be developed to convert the low-temperature waste heat source from a PBMR to useful power and/or refrigeration in interchangeable amounts, depending on the need. It will convert heat in the range 60-100 °C into power and refrigeration. A schematic flow diagram of the dual-function absorption cycle that will convert heat from the PBMR low waste heat stream into power is shown in Figure 2.7. It consists of a waste heat supply, absorber, regenerator, vapour generator, rectifier, super-heater, power turbine plus an electric generator, and an evaporator. The counter-current heat and mass transfer processes used in this cycle facilitate efficient heat extraction from sources with large temperature gradients. A closed-loop, single-phase flow with a transfer working fluid may be used to transfer heat from the waste heat supply to the cycle. With this system, low-temperature waste heat from several sources of the PBMR can be collected into a centralised absorption cycle.

In the power mode, the ammonia vapour drives the turbine and the resulting low-pressure ammonia vapour flows into the absorber, where it is absorbed in the strongly absorbent solution from the generator. The resulting weak (low absorption capacity) absorbent is pumped to the regenerator and then to the vapour generator. In the refrigeration mode, the high-pressure ammonia vapour flows to a condenser. The condensate is reduced and evaporated in an evaporator to produce refrigeration. The low-pressure vapour from the evaporator flows to the absorber to complete the cycle.

2.4.2 Organic Rankine cycle

The ORC is also known as the Clausius Rankine cycle. It makes use of an organic working fluid instead of water or steam. Lately, it has become a popular energy production cycle because it makes possible the use of low-temperature waste heat, typically in the range of 100-200 °C (Hettiarachchi et al., 2006). As is evident in figure 2.8, an ORC is also referred to as a binary cycle, because the secondary working fluid from the waste heat supply never comes in contact with the turbine-generator units. In the binary cycle, the organic or primary working fluid is pumped through a regenerator. The regenerator allows the preheating of the working fluid by de-superheating the expanded vapour. The preheated working fluid is then evaporated, superheated and expanded in a turbine, which drives a generator to convert work into electricity. This decreases the temperature and the pressure of the superheated vapour. The de-superheated vapour leaving the power turbine enters the regenerator where it exchanges heat with the condensed working fluid discharge from the working fluid cycle pump. The saturated vapour leaving the regenerator enters the condenser where it is cooled at constant pressure to become a saturated liquid. This liquid then re-enters the pump and the cycle repeats.

Most of the research findings in the literature include ways of maximising the efficiency of the thermodynamic cycle for optimum waste heat recovery (Wei et al., 2007). Since the primary and secondary working fluid travel through an entirely closed system, binary power plants have virtually no emissions into the atmosphere. The primary working fluid plays a significant

role in the use of the ORC process, which is determined by the application and the waste heat level (Borsukiewicz and Nowak, 2007). In many WHRS using the ORC, n-pentanes are used as working fluids because of their better performance compared to other working fluids (Hettiarachchi et al., 2006).

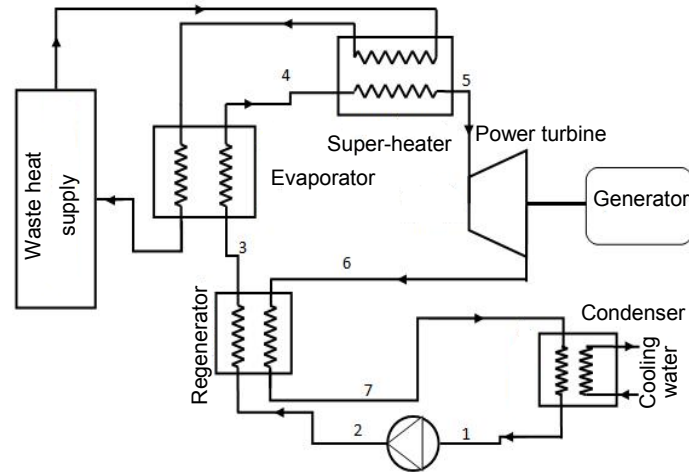


Figure 2.8: Organic Rankine cycle

2.4.3 Stirling cycle

For temperatures in the range 200-800 °C, the SEs cycle is a possible alternative to utilise waste heat, since, in contrast to an internal combustion engine, Stirling devices are able to run on any heat source (Snyman et al., 2008). Any form of heat, from chemical reactions to solar energy, may be used to run a Stirling device. The Stirling cycle lends itself naturally to consideration as an energy conversion system in the waste heat utilisation process for a PBMR waste heat streams at an average temperature of ≥ 200 °C.

Stirling cycles work on a very simple principle. A gas, enclosed in a working space, expands when heated, but contracts when cooled. The Stirling devices work according to a process in which a working gas is cyclically heated and cooled in working spaces. They use the pressure gradient between the working spaces to drive reciprocating elements. The Stirling cycle defines four types of devices, which may be used in the design of a Stirling machine: a refrigerating machine, heat pump, pressure generator and prime mover (Walker, 1980). Among the four types of Stirling devices this project focuses on SEs with emphasis on the heat exchanger.

2.4.4 Stirling engines

Stirling engines belong to a large family of heat engines. They convert heat into mechanical power, or vice versa. They operate on a closed regenerative thermodynamic cycle, with cyclic compression and expansion of the working gas. The gas flow is controlled by volume changes. All heat engines of the SE type do not deposit all their waste heat into the

environment as an important amount of it is conserved from one cycle and use it again in the next cycle, using a regenerative process within a heat exchanger, known as a regenerator. SEs are external combustion engines, since the heat is supplied to the engine from an external source of the engine. It is for this reason that they may be designed to run on any forms of heat source, and they do not produce pollution at all (Kolin, 1991).

The path of the working fluid between the hot and the cold sides prescribes a specific mechanical configuration of a SE. The prescription makes the design of the SE quite complicated because of the existence of hundreds of mechanical arrangements in a mechanical configuration of a SE. Mechanical configuration of SEs are generally divided into three groups, known as Alpha, Beta, and Gamma engines. The Alpha engines have two reciprocating elements in separate cylinders, which are connected in series to a hot cylinder, a regenerator, and a cold cylinder. In the Beta engines, the working fluid is displaced from one engine working space to another by a reciprocating element known as a displacer. A displacer resembles a large piston, except it is very light compare to a piston. In the Beta engine the displacer and the piston are in the same cylinder. The Gamma engine has a displacer and a power piston similar to the Beta machine, but in different cylinders (Walker, 1980)

3 Waste heat recovery and utilisation systems for PBMR used fuel tanks

Waste heat recovery and utilisation systems require especially and well-designed heat recovery equipment used in a heat transfer process such as cooling and/or heating. The use of heat recovery equipment in any waste heat environment should meet the needs of energy conservation for the heat source (Faridi, 2011). Following the literature study, and with the aid of Dobson (2008), an appropriate cooling process was researched and is now proposed. The proposed system will be applied to demonstrate its validity of utilising waste heat from the PBMR fuel tanks. This was done by building and testing a scale model that simulates the heat recovery and utilisation process of the fuel tank waste heat. The WHR&U system of a PBMR used fuel tank is described and discussed. First the design criteria options, followed by a PBMR fuel tank waste heat recovery design are presented, and then a mathematical model for a PBMR fuel tank WHR&U system will be developed.

3.1 Application of a WHR&U system in the PBMR technology

Figure 3.1 shows a schematic diagram of the two-phase flow WHR&U system that will be considered. It shows how waste heat will be recovered, transported and transferred from fuel tanks to where it will be reutilised in a process that will produce electricity through an appropriate energy conversion system. The following will be considered:

- a cooling jacket,
- heat transport, using natural circulation two-phase flow in a thermosyphon loop,
- temperature and pressure control, using a thermostatically controlled valve,
- heat transfer, using a heat exchanger and/or natural convection air-cooled condenser,
- an expansion tank,
- an energy conversion device.

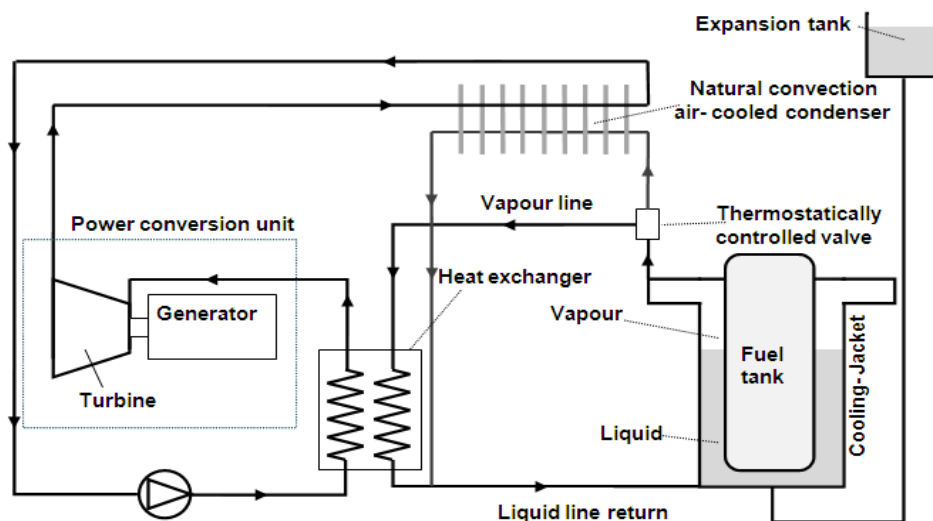


Figure 3.1: A two-phase flow waste heat recovery and utilisation system

Waste heat from a fuel tank will be recovered by submerging the tank into a cylindrical container filled with water. The spent fuel will transfer its decay heat through the tank wall to the water surrounding the tank in the cooling jacket. Steam is produced in the space above the cooling jacket water level. The fuel temperature in the tank is then reduced to a temperature slightly exceeding the cooling jacket operating temperature dictated by the steam pressure. Thus, the cooling jacket will simply behave as a normal vapour generator.

Waste heat contained in steam produced in the cooling jacket is transported to the heat exchanger by means of natural circulation in a particular type of heat pipe called the thermosyphon loop (see, figure 3.1). In a natural circulation loop, the fluid flow is driven by the buoyancy forces arising from the density gradient in the working fluid between the cooling jacket and the condenser sections of the loop. There are no moving parts needed to induce the fluid circulation in the loop (Mori et al., 1993). The only driving force source is the heat input and output. When heat is gradually added to a fluid in the cooling jacket, the fluid temperature will increase by convection until it reaches a temperature slightly above the fluid saturation temperature, from which nucleation and boiling can commence.

During nucleation and boiling, the fluid flow will be characterised by two phases, namely vapour and liquid (Dobson, 1993). The number of phases of the working fluid defines the operating mode of the thermosyphon. There are three operating modes of thermosyphon. The first is when the working fluid exits only in a single phase, the second is when two-phase flow is produced in the system, and the third is the so called heat pipe mode. In heat pipe mode, the loop is completely closed without an expansion tank and half filled with the working fluid.

Because of natural means and no use of moving parts, this system is relatively noiseless and less likely to fail. It eliminates the cost and maintenance problems of pumps, as in forced convection systems. However, one of the major problems in natural circulation systems is the occurrence of various types of instabilities. Instabilities are known to occur depending on the system geometry and operating conditions. Instabilities can cause mechanical failures of the system operation (Aritomi et al., 1992; Kakac and Liu, 1991; Kim and Lee, 1999). Figure 3.1 shows the two main lines of the thermosyphon loop, which do not work at the same time. The primary line comprises of a cooling jacket and a heat exchanger, while the secondary line comprises a cooling jacket and a natural convection air-cooled condenser. This is also an emergency line fail-safe, to ensure that the fuel tank is cooled when the power conversion unit has to be switched off for maintenance, or if it fails. The thermostatically controlled valve provides a reliable, automatic control of the operating pressure of the system and regulates the work of a specific line according to the working conditions of the system. The system working conditions are dependent on the primary line working pressure. An increase in pressure or temperature in the primary line due, for example, to a sudden failure of the heat exchanger will be sensed by the thermostatically controlled valve, which will then open the secondary line and the fuel tank cooling process continues without interruption.

Two-phase flow heat exchangers are used to save energy by direct condensation of a vapour into a liquid. During direct condensation of a vapour into a liquid energy is stored in the cooling

jacket. When energy is needed again, the liquid is depressurised and flashing occurs, which results in vapour production. Not only does condensation reduce the volume of working fluid that has been supplied and treated, but the heat contained in the condensate is also recovered.

3.2 The PBMR used fuel tank cooling design considerations

One of the main design criteria of a PBMR is that the design should be inherently safe, preferably using passive systems. The PBMR design criteria are also applicable to the used fuel tank cooling system, which in this thesis is called the WHR&U system. The design criteria options of the WHR&U system of a PBMR used fuel tank are now described.

3.2.1 Defence-in-depth

Safety is the main concern in nuclear reactor engineering particularly in the WHR&U systems of a PBMR. Safety emphasises the concept of defence-in-depth. Defence-in-depth requires that more than one totally independent cooling system is available and capable of cooling the fuel tank should one or the other not function. To achieve this, two lines regulated automatically by a thermostatically controlled valve are used in this design. This valve will reduce the risk that a primary line failure could interfere with the cooling process of the fuel tank. Using natural circulation and convection in an air-cooled condenser, the design allows the cooling process to continue automatically should a failure in the primary cooling process occur.

3.2.2 Hazard mitigation

Human error, mechanical failure or risk factors in a nuclear power plant are the most significant variables concerning possible radioactive release into the environment. Nuclear power plants, worldwide, are exposed to natural hazards such as hurricanes, floods, fires, volcanoes, etc. Damages caused by natural disasters can reach catastrophic proportions, making natural hazard mitigation an important national policy issue in nuclear engineering. The following recommendations seek to help strengthen natural hazard mitigation policy and practice, serving to reduce risk on a fuel tank cooling process site:

- Extreme natural forces should be taken into consideration on the fuel tank site.
- Contamination of the cooling working fluid should be avoided with a well and strictly regulated isolation between the nuclear fuel line and the cooling fluid.
- Safety control devices, such as pressure safety valves, should be used to control the working fluid operating pressure. This will prevent an eventual explosion due to an over pressure of the working fluid.

3.3 Geometrical design modelling

A scale model of the fuel tank cooling system design geometry will now be discussed.

3.3.1 Cooling jacket

Figure 3.2 shows details of the cooling jacket. Figure 3.2(b) shows that the cooling jacket is a cylindrical steel pressure vessel with a larger diameter section at the top to ensure that only dry saturated vapour will leave the cooling jacket. Figure 3.2(c) shows that the cooling jacket is concentric to the fuel tank. Applying Newton's law of cooling to the cooling jacket section as shown in figure 3.2(a), the heat removed to the fuel tank may be found as follows:

$$\dot{Q}_{ft,cj} = A_{z,ft} h_{ft,cj} (T_{ft} - T_f) \quad (3.3.1)$$

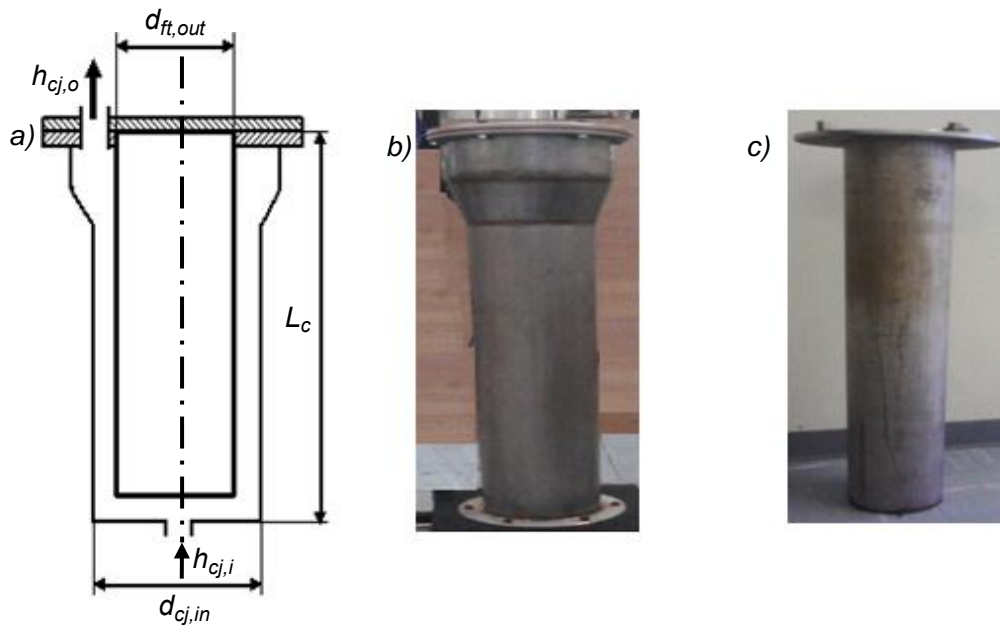


Figure 3.2: Cooling jacket details, (a) section, (b) cooling jacket, and (c) fuel tank

The convective heat transfer coefficient $h_{ft,cj}$ is given as a function of the Nusselt number Nu , the fluid thermal conductivity k_f and the cooling jacket characteristic length L_c as (Mills, 1999):

$$h_{ft,cj} = k_f (Nu/L_c) \quad (3.3.2)$$

The Nusselt number is defined in terms of the Rayleigh number Ra_L as $Nu = CRa_L^n$, with the Rayleigh number a function of the Grashof Gr_L and Prandtl number Pr (Cengel, 2003):

$$Ra_L = Gr_L Pr = \frac{g\beta(T_{ft} - T_f)}{(\mu/\rho)^2} L_c^3 Pr \quad (3.3.3)$$

When the diameter of a cylinder is sufficiently large, the effect of curvature may be neglected.

Thus the heat transfer effects will be similar to those for vertical plates if $d \geq (35L_c/Gr_L^{1/4})$ (Barron, 1999; Cengel, 2003). Mills (1999) recommends the Churchill and Chu correlation for the average Nusselt number for laminar flow ($Ra_L \leq 10^9$) as

$$Nu = 0.68 + 0.67(Ra_L \psi)^{1/4} \quad (3.3.4)$$

and for turbulent flow ($10^9 \leq Ra_L$)

$$Nu = 0.68 + 0.67(Ra_L \psi)^{1/4} \left(1 + 1.6 \times 10^{-8} Ra_L \psi\right)^{1/12} \quad (3.3.5)$$

where

$$\psi = \left[1 + \left(\frac{0.492}{Pr}\right)^{-16/9}\right] \quad (3.3.6)$$

The heat transfer area defined as a function of the wetted perimeter p_{we} and the cylinder characteristic length L_c is $A_{z,ft} = p_{we} L_c = \pi d_{we} L_c$, where the wetted diameter d_{we} is a function of the fuel tank outer diameter $d_{ft,out}$ and the cooling jacket inner diameter $d_{cj,in}$. Thus

$$A_{z,ft} = \pi(d_{cj,in} - d_{ft,out})L_c \quad (3.3.7)$$

Substituting equations (3.3.3)-(3.3.7) in (3.3.1) and rearranging, the required cooling jacket inner diameter is

$$d_{cj,in} = d_{ft,out} + \frac{\dot{Q}_{ft,cj}}{\pi k_f Nu (T_{ft} - T_f)} \quad (3.3.8)$$

The cooling jacket wall thickness is defined by the internal pressure, the temperature, the longitudinal stress and the thermal stress of the working fluid on the cylinder wall. When the internal pressure is contained by the pressure vessel itself, the longitudinal stress σ_l and thermal stress σ_{th} in the cooling jacket wall may be found as follows (Shigley et al., 2003):

$$\sigma_l = (d_{cj,in}^2 P) / (d_{cj,out}^2 - d_{cj,in}^2) \quad (3.3.9)$$

The thermal stress σ_{th} in the pressure vessel is

$$\sigma_{th} = \frac{\alpha (T_f - T_a) E}{(1 - \nu_p)} \quad (3.3.10)$$

The safety factor s is defined by the working point of the cooling jacket, with σ_{max} the yield stress, defined by the material properties at the working temperature, as follows:

$$s = \frac{\sigma_{max}}{\sigma_l + \sigma_{th}} \quad (3.3.11)$$

Substituting equations (3.3.9) and (3.3.10) in (3.3.11) and rearranging, the required cooling jacket outer diameter is

$$d_{cj,out} = d_{cj,in} \sqrt{1 + \frac{s(1 - \nu_p)}{(1 - \nu_p)\sigma_{max} + \alpha s(T_{ft} - T_f)E}} \quad (3.3.12)$$

The cooling jacket wall thickness is

$$W = (d_{cj,out} - d_{cj,in})/2 \quad (3.3.13)$$

3.3.2 Heat transport design

The heat transport system is characterised by the pipe-work diameters and components such as valves, tees, bends or any other devices that may induce minor losses into the system. Components and elements are linked at junctions. Pipe sizes are chosen based on the nature and the velocity of the working fluid in the system, or pressure drop in the system piping. Practical results define a velocity range between 25 and 35 ms^{-1} for dry saturated steam (Dobson, 2006). The transported fluid mass flow rate is

$$\dot{m} = \bar{\rho} A_p \dot{x}_p \quad (3.3.14)$$

The heat removed from the fuel tank should also be equal to the amount of heat sufficient to produce vapour in the cooling jacket. Therefore, the heat removed from the fuel tank is (Mills, 1999)

$$\dot{Q}_{ft,cj} = \dot{m}h'_{fg,i} \quad (3.3.15)$$

where $h'_{fg,i}$ is the latent heat of evaporation. The cross-section area of the pipe will be found by substituting equation (3.2.14) in (3.2.15) and rearranging, the inner pipe diameter found as a function of the power input into the system is

$$d_{p,in} = \sqrt{\frac{4\dot{Q}_{ft,cj}}{\pi\bar{\rho}_i h'_{fg,i}}} \quad (3.3.16)$$

3.3.3 Heat transfer process component design

The general theories related to condenser and evaporator design are now discussed and developed. Mueller (1983) and Taborek (1991) developed a number of requirements to be considered where the selection and design of condensers is concerned. Condensers are designed assuming film-wise condensation. Although drop-wise condensation gives higher heat transfer coefficients, it is not possible to sustain this condensation mode for a long period of time on individual condensers. The flow regime applicable along the flow path should be calculated depending on the flow characteristics of the vapour and condensate. At low vapour velocity the so-called gravity-controlled or Nusselt flow regime will be considered, while at high vapour velocity shear-controlled vapour will predominate (Kakac and Liu, 2002).

The heat exchanger was designed based on the guidelines and practices to be considered for the design of a well functioning condenser, as reported by Kakac and Liu (2002), namely a vertical in-tube heat exchanger. Vertical in-tube condensation is very effective, but the tube length is limited because it may fill with condensate. Thus the size of such a condenser is restricted; otherwise a large shell diameter would be required. The air-cooled condenser is a horizontal tube-side condenser. In a horizontal tube-side condenser, condensation is less effective and much more difficult to calculate because of the stratification of the condensate. Positive tube inclination must be used. Horizontal shell-side condensation is very popular because it is well documented and permits the use of large heat transfer areas.

3.3.3.1 Natural convection air-cooled condenser

The air-cooled condenser designed as described in this section is made of finned tubes, with fins on the air-side, while the steam flows through copper tubes. Aluminium fins are used to enhance the air-side heat transfer area. As seen in figure 3.3, the total heat removed by the finned tubes is (Mills, 1999)

$$\dot{Q}_{co,a} = n_{fin}(\dot{Q}_{co,unfin} + \dot{Q}_{co,fin}) \quad (3.3.17)$$

The heat transfer from the non-finned area $\dot{Q}_{co,unfin}$ is

$$\dot{Q}_{co,unfin} = U_{unfin}A_{unfin}(\bar{T}_{acc} - \bar{T}_{acc,air}) \quad (3.3.18)$$

where, the product $U_{unfin}A_{unfin}$ is

$$U_{unfin}A_{unfin} = \left((h_{unfin,out}A_{unfin,out})^{-1} + R_{co,wp} + (h_{unfin,in}A_{unfin,in})^{-1} \right)^{-1} \quad (3.3.19)$$

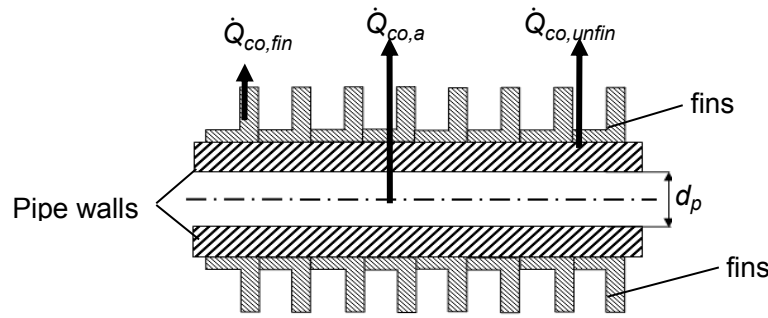


Figure 3.3: Air-cooled condenser finned section

The pipe wall conduction thermal resistance is

$$R_{co,wp} = \ln((d_p + 2t_p)/d_p)/2\pi L_p k_{cu} \quad (3.3.20)$$

The outside heat transfer coefficient $h_{unfin,in}$ combines two heat transfer mechanisms, convection and radiation, characterised by their respective heat transfer coefficients such as

$$h_{unfin,out} = h_{rad} + h_{conv,out} \quad (3.3.21)$$

The radiation heat transfer coefficient h_{rad} is (Mills, 1999)

$$h_{rad} = \varepsilon\sigma(\bar{T}_{acc,air}^2 + T_{acc,op}^2)(\bar{T}_{acc,air} + T_{acc,op}) \quad (3.3.22)$$

The convective heat transfer coefficient is (Mills, 1999)

$$h_{conv,out} = Nu_a k_{op}/d_{op,co} \quad (3.3.23)$$

The Nusselt Number Nu_a is (Mills, 1999)

$$Nu_a = \left(0.6 + \frac{0.387Ra^{1/6}}{(1 + (0.559/Pr_a)^{9/16})^{8/27}} \right)^2 \quad (3.3.24)$$

The Rayleigh number is (Mills, 1999)

$$Ra_d = \frac{g\beta(\bar{T}_{acc} - \bar{T}_{acc,air})}{(\mu/\rho)^2} d_{acc,op}^3 Pr_{air} \quad (3.3.25)$$

The convective heat transfer coefficient is calculated by substituting equations (3.2.25) and (3.2.24) in (3.2.23). In equation (3.3.19), the air-cooled condenser heat transfer area of the non-finned outer and inner pipes are found as $A_i = \pi d_i L_i$.

During condensation, inside the air-cooled condenser pipes, different flow patterns may exist and considerably affect the overall heat transfer coefficient of the heat exchanger. Thus, the heat transfer coefficient must be calculated along the length of the tube (Kakac and Liu, 2002). The inner pipe convective heat transfer coefficient is (Shah, 1979)

$$h_{unfin,in} = h_l(1 + 3.8Z^{-0.95}) \quad (3.3.26)$$

where the non-dimensional parameter Z is

$$Z = \left(\frac{1-x}{x} \right)^{0.8} Pr^{0.4} \quad (3.3.27)$$

and the liquid only heat transfer coefficient h_l is (Kakac and Liu, 2002)

$$h_l = Nu_l k_l / d_{co,ip} \quad (3.3.28)$$

The liquid-only Nusselt number Nu_l may be computed using the Dittus-Boelter equation (Mills, 1999) as

$$Nu_l = 0.023Re_l^{0.8}Pr_l^{0.4} \quad (3.3.29)$$

The liquid-only Reynolds number Re_l is

$$Re_l = G_{max}(1-x)d_{co,ip}/\mu_l \quad (3.3.30)$$

Where, the maximum mass velocity is

$$G_{max} = \bar{\rho}\dot{x}_{max} \quad (3.3.31)$$

As shown in figure 3.4(a) and figure 3.4(b), the maximum velocity in the condenser pipes is a function of the manifold inlet pipe geometry, the manifold distributing header cross-section and the manifold outlet pipes geometry, where the condenser pipes inner diameter $d_{co,ip} = d$ the working fluid velocity in the manifold is such that

$$\dot{x}_{mon} = (A_{mon,pipe}/A_{mon})\dot{x}_{co,ip} \quad (3.3.32)$$

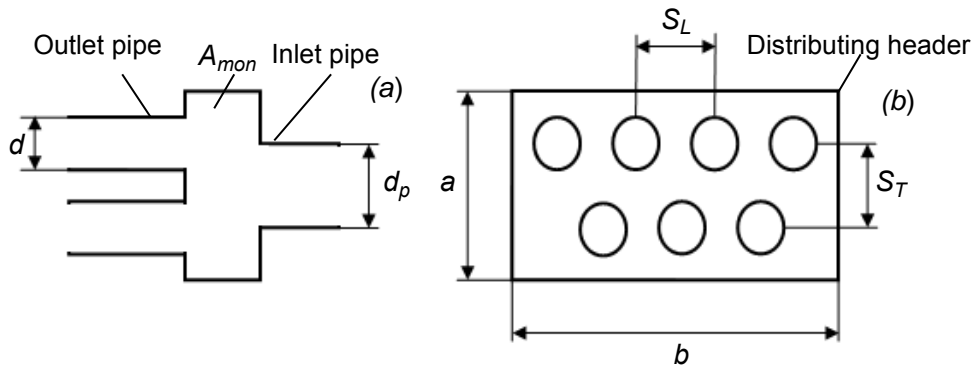


Figure 3.4: Manifold (a) geometry, (b) in and out cross-section

From figure 3.4, the manifold inlet pipe cross-section is $A_{mon,pipe} = \pi d_p^2/4$ and the manifold cross section is $A_{mon} = ab$. The maximum velocity in the condenser pipes is (Mills, 1999)

$$\dot{x}_{max} = \dot{x}_{mon} \max \left\{ \frac{S_T}{S_T - d}, \frac{S_T/2}{[S_L^2 + (S_T/2)^2]^{1/2} - d} \right\} \quad (3.3.33)$$

The homogenous density (see equation 3.3.31) $\bar{\rho}$ is (Mills, 1999)

$$\bar{\rho} = \left(\frac{x}{\rho_g} + \frac{1-x}{\rho_l} \right)^{-1} \quad (3.3.34)$$

The heat transfer rate from the tube fins is

$$\dot{Q}_{co,fin} = U_{fin}A_{fin}(\bar{T}_{acc} - \bar{T}_{acc,air}) \quad (3.3.35)$$

where the product $U_{fin}A_{fin}$ is

$$U_{fin}A_{fin} = \left[(h_{unfin,in}A_{unfin,in})^{-1} + R_{co,wp} + (n_{fin}\eta_{fin}\rho_{fin}a h_a)^{-1} \right]^{-1} \quad (3.3.36)$$

The fin perimeter ρ_{fin} and the convective finned heat transfer area which should include both sides of the fin as well as the inside area of the pipe, are (Mills, 1999)

$$\rho_{fin} = A_{fin}/a \quad (3.3.37)$$

$$A_{fin} = abn_{fin} \left[1 - \frac{\pi d^2}{2S_T S_L} + \frac{\pi d t_{fin}}{S_T S_L} \right] \quad (3.3.38)$$

The fin cross section is (Mills, 1999)

$$A_c = b t_{fin} n_{fin} (1 - \epsilon_{fin}) \quad (3.3.39)$$

The fins volume void fraction is (Mills, 1999)

$$\varepsilon_{fin} = \pi d^2 / (4S_T S_L) \quad (3.3.40)$$

The fin efficiency is (Mills, 1999):

$$\eta_{fin} = \tanh(a\beta) / (a\beta) \quad (3.3.41)$$

The fin parameter β is (Mills, 1999):

$$\beta = (h_a P_{fin} / (k_{fin} A_{o,fin}))^{1/2} \quad (3.3.42)$$

The number of pipes in the condenser is

$$n_{pipe} = 4A_{mon} / (\pi d^2) \quad (3.3.43)$$

The length of pipes is:

$$L_{pipe} = n_{fin} / n_{pipe} \quad (3.3.44)$$

3.3.3.2 Heat exchanger

The heat exchanger is a type of water-cooled condenser that delivers ways of saving water by combining the condenser pipes and the cooling pipes into one piece of equipment. This heat exchanger is a vertical shell-and-tube heat exchanger, with steam condensing on the inner tubes and cooling water circulating inside the shell. As shown in figure 3.5(a), the heat removed to the system from the evaporator is

$$\dot{Q}_{he} = U_{he} A_{z,he} F \Delta T_{In} \quad (3.3.45)$$

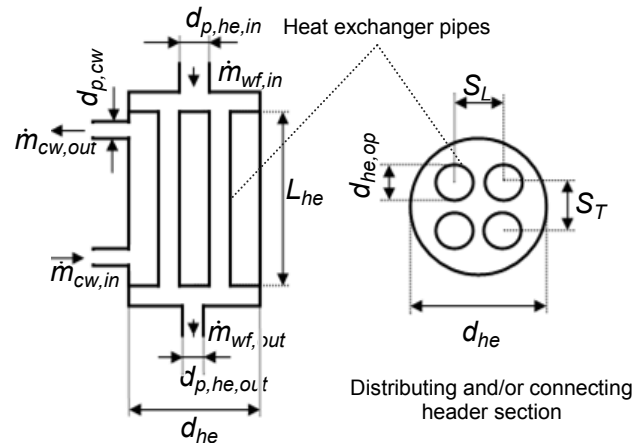


Figure 3.5: Heat exchanger configuration

The thermal resistance of the heat exchanger, considering its geometrical configuration as shown in figures 3.5(a) and 3.5(b) is

$$U_{he} A_{z,he} = \pi L_{he} \left[(d_{he,ip} h_{he,ip})^{-1} + (\ln(d_{he,op} / d_{he,ip}) / 2k_{cu}) + (d_{he,op} h_{he,op})^{-1} \right]^{-1} \quad (3.3.46)$$

The heat exchanger inner pipe heat transfer coefficient $h_{he,ip}$ is calculated as described in section 3.3.3.1. The heat exchanger outer pipe heat transfer coefficient $h_{he,op}$ is computed by taking into consideration the fact that, when evaporation occurs at a solid liquid interface, it is boiling (Kakac and Liu, 2002). The boiling process occurs when the temperature of the solid surface exceeds the liquid saturation temperature. The Shah correlation, as reported by Kakac and Liu (2002), gives the outer pipe evaporative heat transfer coefficient as

$$h_{he,op} = \psi h_{he,l} \quad (3.3.47)$$

The liquid only evaporative heat transfer coefficient $h_{he,l}$ is computed as described in section 3.3.3.1. As shown in Appendix B.2.1, the dimensionless evaporative parameter $\psi = \max(\psi_{cb}, \psi_{nb}, \psi_{bs})$ is given by Kakac and Liu (2002) as a function of other dimensionless numbers, such as the convection number, the boiling number and the Froude number. The logarithmic temperature difference of the heat exchanger in equation (3.3.45) is computed using the following equation:

$$\Delta T_{ln} = \left(\frac{((T_{hot,in} - T_{hot,out}) - (T_{cold,out} - T_{cold,in}))}{\ln((T_{hot,in} - T_{hot,out}) / (T_{cold,out} - T_{cold,in}))} \right) \quad (3.3.48)$$

3.3.4 Expansion tank

In order to stabilise the flow in the thermosyphon loop, an expansion tank was designed. The expansion tank design is determined by the height of the tank. Applying a one-dimensional momentum equation to the expansion tank, its characteristic equation is

$$P_{atm}A_t + P_{sat}A_p = \rho ghA \quad (3.3.49)$$

Assuming a constant cross section over the tank height, or $A_t = A_p = A$, the expansion tank height is

$$h = (P_{sat} + P_{atm}) / \rho g \quad (3.3.50)$$

3.4 Mathematical modelling

This section describes a mathematical model of the WHR&U system that predicts the dynamic behaviour and heat transfer processes in a two-phase flow thermosyphon loop. Due to numerical instabilities in two-phase flow systems, additional mathematical correlations such as the friction factor, the heat transfer coefficient, the void fraction and the two-phase multiplier (see Appendix B.2.2) are used to complete the mathematical model. Simplifying assumptions to overcome numerical instabilities are discussed first. Then the governing equations interpreting the flow behaviour are derived from the basic laws of thermo and fluid-dynamics.

3.4.1 Simplifying assumptions

In this project the mathematical model of the WHR&U system thermosyphon loop is simplified by assuming a one-dimensional, incompressible (for both the liquid and vapour phases) and quasi-static flow. The quasi-static assumption is because the average velocity of the working fluid in the loop is two to three orders less than the speed of sound in the fluid. Therefore, pressure waves move much faster through the working fluid than the rate of mass and heat flow in the loop. This implies that the dynamic behaviour of the flow in the loop may be analysed as a steady state flow at each time step (Aritomi et al., 1993; Dobson, 1993). The incompressibility of both the liquid and vapour phases is assumed because no significant variation of pressure is observed around the loop, thus the loop working pressure remains close to one atmosphere. However, since the density of the vapour changes with temperature, this assumption introduces some errors. These errors are offset by the simplicity this

assumption offers for the solution algorithm. Welander (1967) suggests that the following assumptions should also be made:

- The Boussinesq approximation.
- The tangential force on the working fluid is proportional to the square of the flow rate.
- The temperature of the working fluid in the thermosyphon pipe is uniform over its cross section.

The Boussinesq approximation is used in the theoretical model of the thermosyphon and it assumes that, the density and the viscosity variations are small and affect only the force term of the momentum balance equation (Agrawal, 2006). The reason why the density cannot be assumed to be a constant in the force or buoyancy term of the momentum equation is because the buoyancy force is the dominant force that drives the flow in the loop. The density varies with temperature as

$$\rho = \rho_{ref}(1 + \beta(T - T_{ref})) \tag{3.4.1}$$

where β is the thermal volumetric expansion rate of the fluid at density ρ_{ref} and temperature T_{ref} in °C

3.4.2 Conservation equations

In order to apply the conservation equations to the WHR&U system (referring to the typical two-phase flow WHR&U schematic diagram in figure 3.1), the system is first divided into a number of control volumes as shown in figure 3.6.

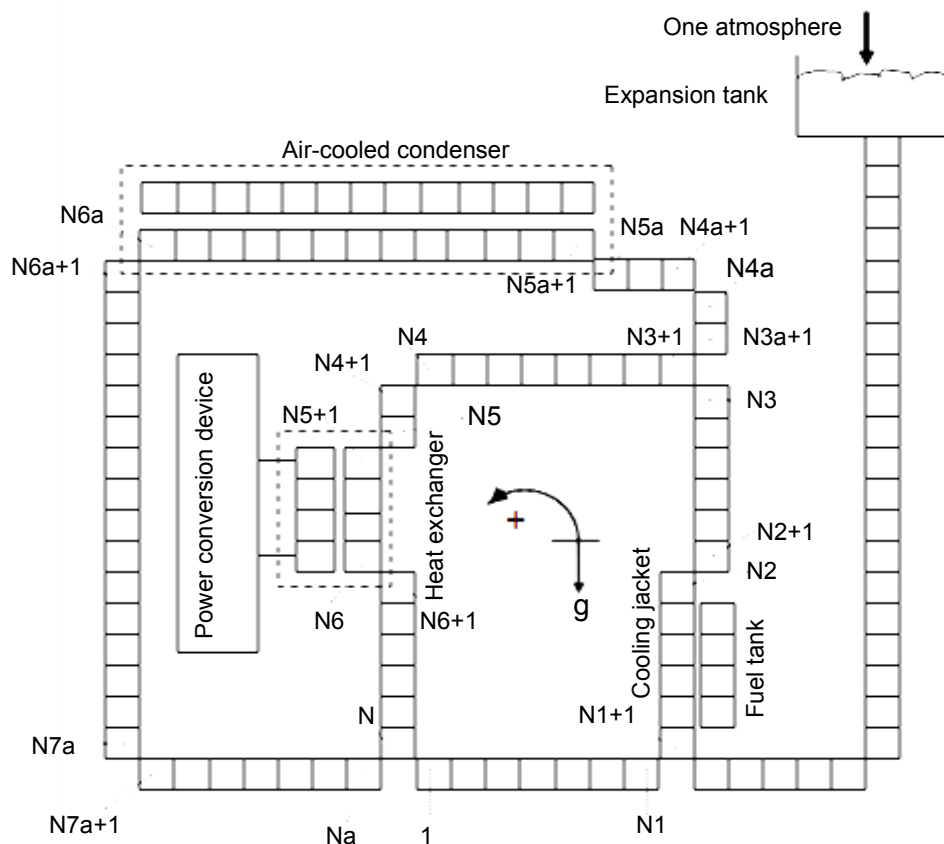


Figure 3.6: Discretisation scheme for the waste heat recovery and utilisation system

The conservation equations, written according to the laws of mechanics are applied to each specific control volume as shown in Figure 3.7, with all the fluid properties located at the centre of the control volume (Dobson, 2007).

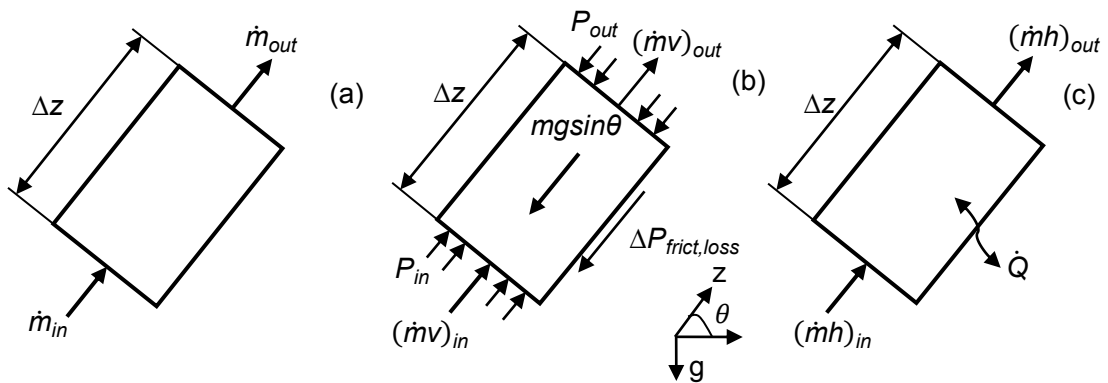


Figure 3.7: Conservation equations control volumes, (a) Mass, (b) Momentum, (c) Energy

Conservation of mass (see figure 3.7(a))

$$\frac{\Delta m}{\Delta t} = \dot{m}_{in} - \dot{m}_{out} \quad (3.4.2)$$

Conservation on momentum (see figure 3.7(b))

$$\frac{\Delta}{\Delta t}(mv) = (\dot{m}v)_{in} - (\dot{m}v)_{out} + \sum F_{syst} \quad (3.4.3)$$

Conservation of energy (see figure 3.7(c))

$$\frac{\Delta}{\Delta t}(mc_v T) = (\dot{m}h)_{in} - (\dot{m}h)_{out} \pm \dot{Q} \quad (3.4.4)$$

3.4.3 Heat transfer equations

Heat is removed from the fuel tank by the thermosyphon through the cooling jacket. The working fluid transport within the thermosyphon is due to the heat transfer process taking place in heat exchangers. An electrical resistance analogy is used for to illustrate the different heat transfer equations (Mills, 1999).

3.4.3.1 Heat removed from the fuel tank by the cooling jacket

Heat removed from the fuel tank by the cooling jacket may be illustrated as shown in figure 3.8.

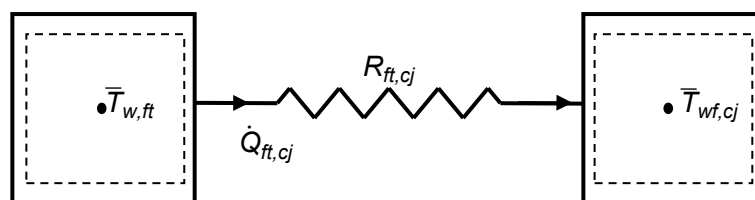


Figure 3.8: Heat removed from the fuel tank by the cooling jacket

The convection thermal resistance on the fuel tank is

$$R_{ft,cj} = \frac{1}{2\pi d_{ft,out} L_c h_{ft,cj}} \quad (3.4.5)$$

The heat removed from the fuel tank is

$$\dot{Q}_{ft,cj} = \frac{\bar{T}_{w,ft} - \bar{T}_{wf,cj,i}}{R_{ft,cj}} = \dot{Q}_{elek} = \frac{V_{sup}^2}{R_{elek}} \quad (3.4.6)$$

3.4.3.2 Heat removed from the loop by the air-cooled condenser

Heat removed from the thermosyphon through the air-cooled condenser as shown in figure 3.9 is

$$\dot{Q}_{acc,air} = \frac{\bar{T}_{acc} - \bar{T}_{acc,air}}{R_{tot}} \quad (3.4.7)$$

The air-cooled condenser total thermal resistance (Mills, 1999) is

$$R_{tot} = R_{co,ip} + R_{co,wp} + R_{th} \quad (3.4.8)$$

The convective thermal resistance between the working fluid and the pipe inner area is

$$R_{co,ip} = \frac{1}{2\pi L_{co,p} d_{do,ip} h_{unfin,in}} \quad (3.4.9)$$

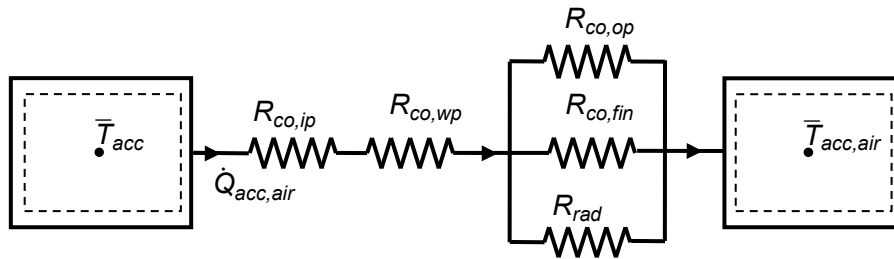


Figure 3.9: Heat removed through air-cooled condenser

The conduction thermal resistance through the pipe wall is

$$R_{co,wp} = \frac{\ln(d_{co,op}/d_{co,ip})}{2\pi L_{co,p} k_{cu}} \quad (3.4.10)$$

The air-cooled condenser air side thermal resistance is

$$R_{th} = \left[\frac{1}{R_{co,op}} + \frac{1}{R_{co,fin}} + \frac{1}{R_{rad}} \right]^{-1} \quad (3.4.11)$$

The convective thermal resistance between the pipe outer area and the environment is

$$R_{co,op} = \frac{1}{2\pi L_{co,p} d_{co,op} h_{unfin,out}} \quad (3.4.12)$$

The convective thermal resistance between the fin and the environment $R_{co,fin}$ is given by equation (3.3.35). The radiation thermal resistance as proposed by Mills (1999) is

$$R_{rad} = \frac{1}{\sigma} \left[\frac{1 - \epsilon_p}{\epsilon_p A_{z,p}} + \frac{1}{F_{p,fin} A_{z,p}} + \frac{1 - \epsilon_{fin}}{\epsilon_{fin} A_{z,fin}} \right] \quad (3.4.13)$$

3.4.3.3 Heat removed from the loop by the heat exchanger

Heat removed from the thermosyphon through the evaporator as illustrated in figure 3.10 is

$$\dot{Q}_{he,cw} = \frac{\bar{T}_{he} - \bar{T}_{cw}}{R} \quad (3.4.14)$$

The evaporative thermal resistance R is computed as given in equation (3.3.46).

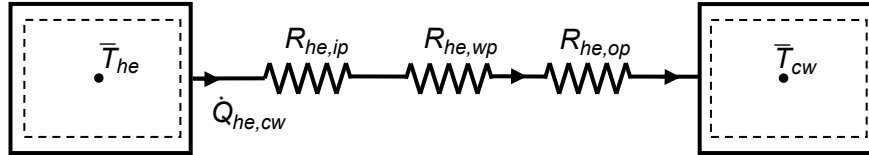


Figure 3.10: Heat removed through heat exchanger

3.4.3.4 Energy transported by the working fluid transport

Energy displaced through the working fluid transport may be seen in figure 3.7(c) and is interpreted in equation (3.4.3). The term \dot{Q} represents the heat added to or removed from the control volume, as indicated by its position in the loop. No axial conduction effect is taken into account (Ruppertsberg, 2008). According to the first law of thermodynamics, the only way of transferring energy is either by heat or by work. In the heat transfer section of the loop the heat term \dot{Q} represents not only heat losses, but also gains due to convection to and or from the environment. Work comprises machine work, surface work due to the frictional pressure drop, and shear work due to viscous stress. When substituting equation (3.4.4) in (3.4.3), as shown in Appendix B.1, it can be seen that at the control volumes boundaries, the pressure work merges with the internal energy to form the fluid enthalpy property. Other forms of energy terms, such as viscous dissipation, kinetic and potential energy are neglected since their effects are negligible compared to the internal energy.

3.4.4 Integration of conservation equations

Explicit equations describing the flow behaviour of the working fluid in any control volume of the thermosyphon will be integrated from conservation equations. Analysing a transient model of a thermosyphon, Dobson (1993) found that the explicit finite difference method was a convenient mathematical method to integrate conservation equations as far as a thermosyphon is concerned. This integration required all boundary conditions such as all forces acting on a control volume, as shown in figure 3.7(b), to be taken into account. From the conservation of momentum equation, the mass flow rate of the working fluid in the thermosyphon and the interface pressure between control volumes may be integrated as follows:

$$\sum F_{syst} = (P_{in} - P_{out})A_i - mg \sin \theta - \Delta P_{frict,loss} A_j \quad (3.4.15)$$

Substituting equation (3.4.15) in (3.4.2)

$$\frac{\Delta}{\Delta t}(mv) = (\dot{m}v)_{in} - (\dot{m}v)_{out} + (P_{in} - P_{out})A_i - mg \sin \theta - \Delta P_{frict,loss} A_j \quad (3.4.16)$$

The frictional pressure gradient $\Delta P_{frict,loss}$ takes into account all the losses due to friction as well as minor losses affecting the control volume such as inlet, bend, valve and, outlet losses, etc. It may be convenient to include minor losses as equivalent lengths of control volumes of the same diameter $\Delta Z = \Delta Z + \Delta Z_{eq}$ (Dobson, 2007). Thus the frictional loss is computed as

$$\Delta P_{frict,loss} = \frac{f\Delta Z}{2d} \rho v^2 = \frac{f(\Delta Z + \Delta Z_{eq})}{2d} \rho v^2 = \left(\frac{f\Delta Z}{d} + \sum k_j \right) \frac{\rho v^2}{2} \quad (3.4.17)$$

where, f is the friction coefficient and $\sum k_j$ the sum of the different characteristic minor losses coefficients. The general form of equation (3.4.17) is

$$\Delta P_{frict,loss} = (C_f + K) \frac{\rho v^2}{2} \quad (3.4.18)$$

Rearranging equation (3.4.16)

$$v \frac{\Delta m}{\Delta t} + m \frac{\Delta v}{\Delta t} = (\dot{m}v)_{in} - (\dot{m}v)_{out} + (P_{in} - P_{out})A_i - mg \sin \theta - \Delta P_{frict,loss} A_j \quad (3.4.19)$$

$m = \rho V = \rho A_i \Delta Z$, and $\dot{m} = \rho A_i v$, thus $\dot{m} = (mv)/\Delta Z$, equation (3.4.19) takes the form

$$\frac{m}{\rho A_i} \frac{\Delta \dot{m}}{\Delta t} = (\dot{m}v)_{in} - (\dot{m}v)_{out} + (P_{in} - P_{out})A_i - mg \sin \theta - \Delta P_{frict,loss} A_j - \frac{\dot{m}}{\rho A_i} \frac{\Delta m}{\Delta t} \quad (3.4.20)$$

Based on equation (B.1.4) in Appendix B, the quasi-static and incompressible assumptions, equations (3.4.20) may be rewritten as

$$\frac{m}{\rho A_i} \frac{\Delta \dot{m}}{\Delta t} = \dot{m} \left(\frac{\dot{m}}{\rho_{in} A_i} + \frac{\dot{m}}{\rho_{out} A_i} \right) + (P_{in} - P_{out})A_i - mg \sin \theta - \Delta P_{frict,loss} A_j - \frac{\dot{m}}{\rho A_i} \frac{\Delta m}{\Delta t} \quad (3.4.21)$$

Considering that, the pressure is nearly constant around the loop

$$\frac{m}{\rho A_i} \frac{\Delta \dot{m}}{\Delta t} = \frac{\dot{m}^2}{A_i} \left(\frac{1}{\rho_{in}} + \frac{1}{\rho_{out}} \right) - \rho A_i \Delta Z g \sin \theta - \Delta P_{frict,loss} A_j - \frac{\dot{m}}{\rho A_i} \frac{\Delta m}{\Delta t} \quad (3.4.22)$$

Integrating equation (3.4.22) around the loop in the interval $[t, t+\Delta t]$, and for each control volume k , in quasi-static and incompressible flow, the actual mass flow rate is:

$$\dot{m}^{t+\Delta t} = \dot{m}^t + \Delta t \left[\frac{-\sum_{k=1}^N \frac{\dot{m}_k^2}{A_{i,k}} \left(\frac{1}{\rho_{k,1/2}} - \frac{1}{\rho_{k+1/2}} \right) - \sum_{k=1}^N \rho_k A_{i,k} \Delta Z_k g \sin \theta_k - F_{frict}}{\sum_{k=1}^N \frac{m_k}{\rho_k A_{i,k}}} \right] \quad (3.4.23)$$

where, $F_{frict} = \sum_{k=1}^N \Delta p_{frict,loss,k} A_{j,k}$

$$\sum_{j=1}^N \Delta p_{frict,loss,j} = \sum_{j=1}^N \frac{1}{2} \left(\frac{C_{f,j} + k_j}{\rho_j} \right) \frac{(\dot{m}^t)^2}{A_{i,j}^3} \quad (3.4.24)$$

The integration of the conservation of energy equation allows the computation of the working fluid temperature in each control volume and the thermodynamic quality of the working fluid. Therefore, as shown in Appendix B.1 it may be seen that

$$u^{t+\Delta t} = u^t + \frac{\Delta t}{m^t} [\dot{m}^t (h_{in} - h_{out}) \pm \dot{Q}] \quad (3.4.25)$$

where, \dot{Q} is positive when heat is added to and negative when removed from the control volume.

$$\text{If } u_n^{t+\Delta t} < u_f \text{ then } T_n^{t+\Delta t} = u_n^{t+\Delta t} / c_v \text{ and } x_n^{t+\Delta t} = 0 \quad (3.4.26)$$

$$\text{If } u_n^{t+\Delta t} > u_f \text{ then } T_n^{t+\Delta t} = T_{sat} \text{ and } x = (u_n^{t+\Delta t} - u_{f,n}^{t+\Delta t}) / u_{fg,n}^{t+\Delta t} \quad (3.4.27)$$

where, $u_{f,n}^{t+\Delta t} = c_v T_{sat,n}^{t+\Delta t}$

4 Use of Stirling engine for utilisation waste heat from a PBMR fuel tank

Stirling engines (SEs) have been identified as being capable of utilising high-temperature waste heat from PBMR fuel tanks. In particular, a free-piston SE has been selected due to its having no mechanical links between moving components, and its high reliability. A description of free-piston SE components, followed by conceptual theories accounting for the geometrical design, building, manufacture and construction of a heat exchanger for use in a free-piston SE will be presented first. Thereafter the so-called *lumped parameter* modelling of a Stirling engine heat exchanger will be developed.

4.1 Free-piston Stirling engine

A free-piston SE is a mechanical device in which the motion of the working fluid and reciprocating elements perform a thermodynamic cycle. The SE thermodynamic cycle is sustained by fluid forces and dynamic fluidic interaction between the engine components. There is no need for mechanical linkages coupling the reciprocating elements consisting of pistons and/or displacers. There are many types of free-piston SEs, each specified in terms of the mechanical configuration characterised by the reciprocating elements, heat exchangers and working space arrangements (Walker, 1980).

A number of reciprocating elements may be needed to define a specific mechanical configuration of a free-piston SE. Figure 4.1 shows the arrangement of a free-piston SE with a piston and displacer in the same cylinder. Piston and displacer are separated by a working space 2 which at ambient temperature is the compression space. The working space 3, at the right of the displacer, is the high-temperature expansion space. Compression and expansion spaces are in mutual communication through a heater, regenerator and cooler. Space 1 at the left of the piston acts as a mechanical gas spring.

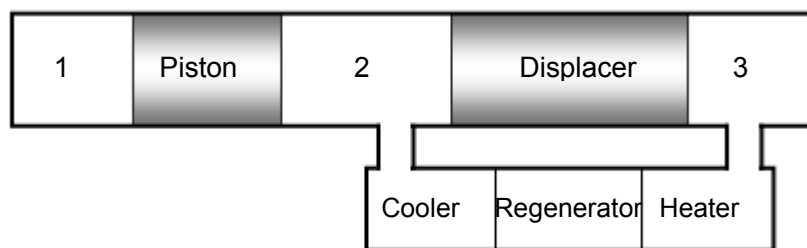


Figure 4.1: Diagram of a free piston Stirling engine

4.2 Free-piston Stirling engine components

In free-piston SEs, the most important elements are the two working spaces, whose volumes vary cyclically at the same frequency, but with phase differences. Therefore, depending on the reciprocating elements positions, a volume variation of the expansion space determines the

variation in the compression space (Walker and Sent, 1985). Heat is exchanged from the heat source to the engine, and then from the engine to the environment through the heat exchanger.

4.2.1 Reciprocating elements

Two types of reciprocating elements, the piston and displacer, are used to define the mechanical configuration of a free-piston SE. The piston is a heavy structural element with gas seals to contain the working fluid. It is used to convert the gaseous energy of the working fluid to mechanical work. It drives the engine load by means of the pressure difference between the compression and the gas spring spaces. The temperature of these spaces is almost the same, therefore, there is a high-pressure and zero-temperature gradient between them (Thombare and Verma, 2006).

The displacer is a lightweight component compared to the piston. It is essentially a zero-work element located between the expansion and the compression spaces. It is hollow and contains radiation shields and also acts as an insulating barrier between the compression and the expansion spaces. A small pressure difference does exist across the displacer due to the pressure drop across the regenerator and associated heat exchangers. It is therefore constructed to work using only low pressure and inertia forces with minimum thermal conduction loss (Thombare and Verma, 2006).

4.2.2 Heat exchangers

Heat exchangers are key components of SEs. Three heat exchangers, namely, the heater, the regenerator and the cooler are used in a free-piston SE. The heater transfers heat from an external source to the working fluid contained in the expansion space. The cooler absorbs heat from the engine working fluid in the compression space and rejects it into the atmosphere through a coolant. Regenerators act as thermal sponges by alternatively accepting heat from the working fluid and rejecting heat back into the working fluid. The working fluid flows through the heater, regenerator and cooler in an irreversible process, because, it is largely affected by the pumping losses (Urieli, 1977). Pumping losses are generally described in terms of the flow's viscous friction (Minassians, 2007). Heat exchangers comprise the dead volume of the engine. They reduce the nominal output power by decreasing the engine compression ratio. Hence, much attention should be paid to improving SE heat exchanger design, to ensure better overall engine performances.

4.2.3 Flow friction effects in a Stirling engine heat exchanger

Flow friction effects in SE heat exchangers are very important. They determine the pumping losses of the engine in terms of the pressure drop. The pressure drop determines the flow dissipation, which decreases the engine power output. As shown in equation (3.4.17), the flow dissipation effects are fully dependent on the geometry of the working fluid path, the friction

factors and fluid properties. In a SE, friction factors are usually defined by empirical expressions obtained from experimental data. Minassians (2007) generalised an expression for the friction factor as a function of the skin friction coefficient C_{sf} , the drag friction coefficient C_{df} and the Reynolds number Re as

$$C_f = \frac{C_{sf}}{Re^n} + C_{df} \quad (4.2.1)$$

The skin and drag frictions are functions of the nature of the flow, which is characterised by the value of the Reynolds number. For laminar flow and transition from laminar to turbulent flow $C_{sf}=16$ and $C_{df} = 0$ respectively.

The pressure drop due to the heater, regenerator and cooler geometry, that is characterised by a sudden expansion, an enlargement, and a sudden compression is:

$$\Delta P_{i,j} = K_i \frac{1}{2} \rho_i \dot{x}_i + \Delta P_e + K_j \frac{1}{2} \rho_j \dot{x}_j \quad (4.2.2)$$

where, K_i and K_j are the pressure factors due to a sudden expansion and compression, respectively. The enlargement pressure drop ΔP_e is a result of the geometry of the heat exchanger and the change in density during heating and cooling, which cause the momentum to increase from j to i . The change in the longitudinal momentum must be balanced by the pressure difference applied due to the acceleration of the gas between the inlet and the outlet of the heat exchanger passage. The enlargement pressure drop is found for each section of the heat exchanger as given in equation (4.3.32). Finally, the fluid flow dissipation is given as

$$\dot{W}_{flow} = \Delta P \dot{V} \quad (4.2.3)$$

4.2.4 Oscillating flow in free piston Stirling engine heat exchanger

The SE working space volume varies according to a harmonic law. This volume variation assumption was first made by Schmidt in 1871. The Schmidt assumption concerned only an Alpha-type engine, which is the simplest SE configuration. Berchowitz and Ureili (1984), and later Walker and Sent (1985), presented their volume variation assumptions for both the Beta- and Gamma-type engines. This project is concerned with a Beta-type free-piston SE configuration.

The volume variation of the compression space is

$$V_c = V_{cl,c} + \frac{V_{swept,c}}{2} (1 + \cos(\theta + \delta)) \quad (4.2.4)$$

The volume variation of the expansion space is

$$V_e = V_{cl,e} + \frac{V_{swept,e}}{2} (1 + \cos(\theta + \alpha + \delta)) \quad (4.2.5)$$

The phase advance of the compression space volume with respect to the piston is

$$\delta = \tan^{-1} \left(\frac{V_{da} \sin \phi}{V_{da} \cos \phi - V_{pa}} \right) \quad (4.2.6)$$

The phase advance of the expansion space volume with respect to the compression space volume is

$$\alpha = \pi + \phi + \delta \quad (4.2.7)$$

where, $V_{pa} = A_p x_p$ is the volume in the compression space due to the piston movement and $V_{da} = A_d x_d$ is the displacer movement, θ is the cycle angle, ϕ the phase advance of the displacer with respect to the piston.

Equations (4.2.5) and (4.2.6) show that in SE the working fluid is moved back and forth by the action of the piston-displacer through heat exchangers according to an oscillating law. The displacer and the piston steady state motions are given as follows:

$$x_d = \frac{V_{swe}}{2A_p} (1 + \cos(\theta + \alpha + \delta)) \quad (4.2.8)$$

$$x_p = \frac{V_{swc}}{2A_p} (1 + \cos(\theta + \delta)) \quad (4.2.9)$$

As the SE cycle angle is a function of the number of displacer's cycles per second or frequency $\omega = 2\pi f = 2\pi/T$, the free-piston SE cycle angle is

$$\theta = \omega t \quad (4.2.10)$$

In an oscillating flow regime, the average cycle pressure drop of the oscillating flow is usually four to six times higher than that of a uni-direction steady flow of the same Reynolds number. The pressure drop across the heat exchanger for an oscillating flow is (Minassians 2007)

$$\Delta P = \Delta P_{max} \cos \theta \quad (4.2.11)$$

4.3 Stirling engine heat exchanger geometrical design

An efficient SE should have a heat exchanger that provides high heat transfer performance; hence, a SE heat exchanger optimal design is always required. Most published models for the thermodynamic performance of SE heat exchangers are one-dimensional, and are based on the known characteristics of flow resistance and heat transfer coefficient (Park et al, 2002). The heat transfer to the working fluid in the heat exchanger is a function of the temperature difference between the wall temperature T_w and the working fluid temperature T that passes through the heat exchanger wetted area A_{we} and the heat transfer coefficient h

$$\dot{Q} = A_{we} h (T_w - T) \quad (4.3.1)$$

The heat transfer coefficient can be computed from the Nusselt number Nu , which is a function of the Stanton number St , the Prandtl number Pr and the Reynolds number Re as follows:

$$h = Nu k/d_h = St Re Pr k/d_h \quad (4.3.2)$$

Nusselt numbers are obtained from experimental data and presented either graphically or as an algebraic expression for various heat exchanger geometries. Yuan and Dybbs (1992) reported that the heat transfer coefficient is more significant in an oscillating flow regime compared to a uni-directional flow. Therefore in an oscillating flow regime the Reynolds number is

$$Re_{ave} = \rho d_h \dot{x}_{ave} / \mu \quad (4.3.3)$$

The average velocity is

$$\dot{x}_{ave} = 2\dot{x}_{max} / \pi \quad (4.3.4)$$

The Prandtl number Pr is (Mills, 1999)

$$Pr = \mu c_p / k \quad (4.3.5)$$

The Stanton number is (Mills, 1999)

$$St = h / (\rho \dot{x}_{ave} c_p) \quad (4.3.6)$$

4.3.1 Heater and cooler design

The heater and cooler are designed in the same configuration. They are made up of a shell of tubes within a tube, with the coolant flowing through the shell tube while the working gas flows through the inner pipes. The external tube is a stainless steel tube filled with copper pipes arranged in a staggered configuration. The shell tube and the inner shell copper pipes are filled with woven wire mesh to increase the heat exchanger efficiency. Woven wire mesh screens will play a role of enhancing the heat exchanger heat transfer area. They were simulated as the heat exchanger copper pipes inner and outer fins. First the heat exchanger fins modelling, during which wire mesh was modelled as fins, will be presented, followed the analysis of the heat transfer and pressure drop correlations due to the use of fins consisting of woven wire mesh, and then computation of the actual heat transfer coefficient and the effective pressure drop in the heat exchanger.

4.3.2 Heat exchanger fin modelling

Besides the flow resistance and heat transfer coefficient, the geometry of the heat exchanger is one of the main factors defining the heat transfer rate of the heat exchanger. In this project, the dimension of the heat exchanger is dependent on the size of the mesh and the diameters of the shell tube and inner pipes which determine the exchanger heat transfer area. Therefore plain-weave screens are stacked together to form a laminating screen. Each screen is characterised by the mesh size, which defines the woven wire diameter d_{wi} . Park et al (2002) estimated the laminating screen thickness is

$$L_w = C_f N_{scr} (d_{wy} + d_{wz}) \quad (4.3.7)$$

The compression factor, C_f takes into consideration the spacing between the wire crimping at the wire intersection and the interval of the wires of adjacent screens. Successive screens are arranged in staggered configuration, where alternate screen layers are offset in y and z directions by $0.5 Mesh^{-1}$. In this project an isotropic laminating screen is considered in which

$$d_{wz} = d_{wy} = d_{wi} \quad (4.3.8)$$

The compression factor as described by Park et al (2002) is approximated as

$$C_{f,j} = (-3.906 \times 10^{-4} C \pi d_{wi,j} M_j) / (1 - \varepsilon_j) \quad (4.3.9)$$

The porosity ε is

$$\varepsilon_j = \frac{V_{tot,j} - V_{m,j}}{V_{tot,j}} \quad (4.3.10)$$

Park et al (2002) defined the compression corrective factor C as

$$C_j = 123(d_{wi,j} M_j)^4 - 384(d_{wi,j} M_j)^2 - 640 \quad (4.3.11)$$

The woven wire mesh laminating screen can be considered as a collection of heat fins if one assumes a symmetric heat distribution in the wire matrix around the centre of the tube. Each mesh wire is then approximated as a heat fin. This can be visualized by considering all the mesh wires of a mesh screen to be loose at one end and soldered to the pipe wall on the

opposite end and unfolding the tube from the unsoldered side (see figure 4.2(a)). When this is done, each wire will be extracted to stand separately, as shown in figure 4.2(b). The pipe and screens can now be represented as a flat plate of length equal to the perimeter of the pipe, with fins attached on both side as shown in figure 4.2(b). The inner and outer surface areas of pipes will then be considered as finned, with cylindrical mesh wires as fins. The fin's geometrical dimensions are defined from the mesh characteristics dimensions as shown in figure 4.2(c).

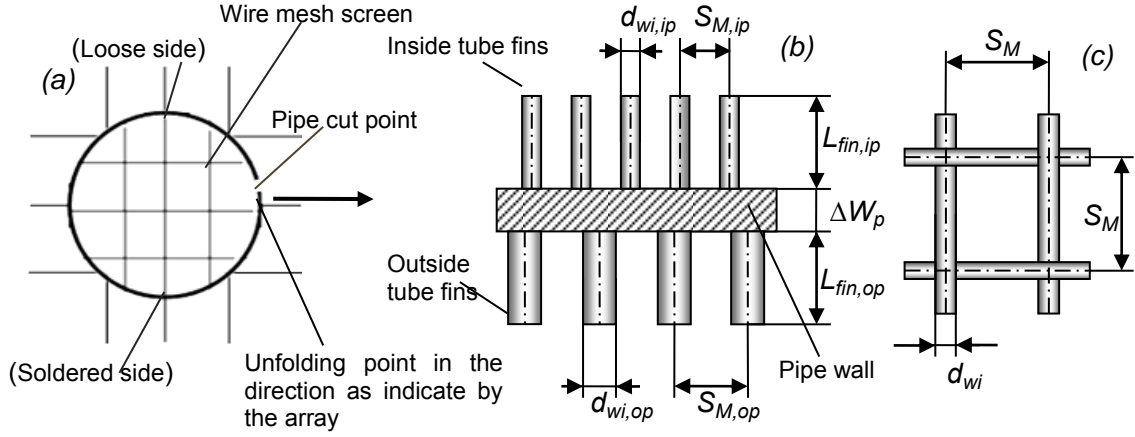


Figure 4.2: Wire mesh in a pipe; (a) loose and soldered sides representations, (b), Inner and outer pipe fins dimensions, (c) mesh dimensions

The fins inner and outer pitches are

$$S_{M,j} = 0.0254 / Mesh_j \quad (4.3.12)$$

The inner and outer mesh numbers are

$$M_j = Mesh_{ip} / 0.0254 \quad (4.3.13)$$

The inner mesh number of holes is

$$N_{holes,ip} = \pi M_{in}^2 N_{scr,j} (d_{op} - \Delta W_p)^2 / 4 \quad (4.3.14)$$

The outer mesh number of holes is

$$N_{holes,op} = \pi M_o^2 N_{scr,j} ((d_{op} - \Delta W_p)^2 - N_p d_{op}^2) / 4 \quad (4.3.15)$$

The heat transfer areas per holes in the inner and outer mesh are

$$A_{z,perhole,j} = 2\pi (S_{M,j} - d_{wi,j}) d_{w,j} \quad (4.3.16)$$

The heat transfer areas in the inner and outer mesh are

$$A_{z,j} = N_{holes,j} A_{z,perhole,j} \quad (4.3.17)$$

The inner and outer mesh cross-sectional areas per hole are

$$A_{perhole,j} = (S_{M,j} - d_{wi,j})^2 \quad (4.3.18)$$

The inner and outer total mesh areas are

$$A_j = N_{holes,j} A_{perholes,j} \quad (4.3.19)$$

From equation (4.3.19) the inner and outer wire mesh volumes are

$$V_{m,j} = 2 \left[\pi N_{scr,j} ((d_j - 2\Delta W_j)^2 / 4) - A_j \right] d_{wi,j} \quad (4.3.20)$$

The geometrical inner pipe volume is

$$V_i = \pi L_p N_p (d_{op} - \Delta w_p)^2 / 4 \quad (4.3.21)$$

The geometrical outer pipe volume is

$$V_o = \pi L_p ((d_o - \Delta w_h)^2 - N_p d_{op}^2) / 4 \quad (4.3.22)$$

The heat exchanger working fluid and the coolant volume are

$$V_{wf,j} = V_j - V_{m,j} \quad (4.3.23)$$

The porosity in the inner and outer pipe mesh are

$$\varepsilon_j = V_{wf,j} / V_j \quad (4.3.24)$$

The number of mesh screen layer in the pipe and outer mesh are

$$N_{scr,j} = N_p L_p / t_{scr,j} \quad (4.3.25)$$

The inner and outer pipe laminate thicknesses are:

$$L_{lam,j} = 2C_{f,j} N_{scr,j} d_{wi,j} \quad (4.3.26)$$

The number of fins may be calculated as follows:

The inner pipe mesh number of fins is

$$N_{fin,in} = (\pi L_p (d_{op} - \Delta w_p) / S_{M,ip}) N_{scr,i} N_p \quad (4.3.27)$$

The outer pipes mesh number of fins is

$$N_{fin,o} = \pi ((L_{fin,o} L_p) / S_{M,op}) N_{scr,o} N_p \quad (4.3.28)$$

The inner and outer pipe fins heat transfer areas are

$$A_{fin,j} = \pi d_{wi,j} L_{fin,j} \quad (4.3.29)$$

The total inner and outer pipe fins heat transfer area are

$$A_{fin,tot,j} = N_{fin,j} A_{fin,j} \quad (4.3.30)$$

The fins heat transfer coefficients as well as the pressure drop in the heat exchanger are porosity dependent. They will be calculated using their numerical correlations, respectively. Park et al., (2002) proposed the following expressions to calculate the heat transfer correlation, respectively, the pressure drop in an internally finned tube or in the inner pipe mesh for a staggered configuration as

$$j = StPr^{2/3} = 5.86Re^{-0.68} \left(\frac{1 - \varepsilon}{\varepsilon} \right)^{0.2} \frac{d_{wi}}{L_{wi}} \quad (4.3.31)$$

$$\Delta P_e = f \frac{G^2 B L_{lam}}{2\bar{\rho}} \left(\frac{\varepsilon}{1 - \varepsilon} \right)^{0.4} + G^2 \left(\frac{1}{\rho_i} - \frac{1}{\rho_j} \right) \quad (4.3.32)$$

where, $Re = (Gd_h) / \mu$ is the Reynolds number, $G = G_i / \varepsilon$ is the internal mass velocity, $B = 4(1 - \varepsilon) / d_h$ the specific surface area and $d_h = \varepsilon d_{wi} / (1 - \varepsilon)$, with d_h the mesh hydraulic diameter (defined as a function of porosity ε and the mesh wire diameter d_{wi}) and $G_i = \rho_i \dot{x}_{mean,i}$ the internal mass velocity per hole. The mean density $\bar{\rho} = (\rho_i + \rho_j) / 2$, with ρ_i and ρ_j , the densities of the hot and cold sections of the heat exchanger, respectively. The heat transfer and pressure drop correlations in the outer pipe mesh may then be approximated according to the fins geometry and the tubes configuration. Referring to Webb (1994), the recommended correlations in a staggered tube layout configuration is found as follows:

$$j = 0.292Re^n \left(\frac{\Delta Sd}{d_{op}} \right)^{0.45} \left(\frac{\Delta Sd}{L_{fin,o}} \right)^{0.26} \left(\frac{d_{wi,o}}{d_{op}} \right)^{0.67} \left(\frac{d_{op} + L_{fin,o}}{d_{op}} \right)^{0.47} \left(\frac{d_{op} + L_{fin,o}}{d_{wi,o}} \right)^{0.77} \quad (4.3.33)$$

where, the pitch wire diameter difference is $\Delta Sd = S_{Mo} - d_{wi,o}$. The power constant of equation (4.3.33) n is (Webb, 1994)

$$n = -0.415 + 0.00346((d_{wi,o})/S_{Mo}) \quad (4.3.34)$$

The friction factor

$$f = 3.805Re^{-0.234} \left(\frac{\Delta Sd}{d_{op} + L_{fin,o}} \right)^{0.25} \left(\frac{L_{fin,o}}{\Delta Sd} \right)^{0.76} \left(\frac{d_{op}}{d_{op} + L_{fin,o}} \right)^{0.73} \left(\frac{d_{op}}{S_T} \right)^{0.71} \left(\frac{S_T}{S_L} \right)^{0.77} \quad (4.3.35)$$

The Colburn factor J is defined in terms of the Stanton number St and the Prandtl number Pr as

$$J = StPr^{2/3} \quad (4.3.36)$$

Mills (1999) defined the Stanton number as a function of the heat transfer coefficient h as given in equation (4.3.6). Therefore, from equation (4.3.6) the fin heat transfer coefficient is

$$h_{fin} = \rho \dot{x}_{mean} c_p St = Gc_p St \quad (4.3.37)$$

The fin efficiency is Mills (1999)

$$\eta_{fin} = \tanh(\sqrt{2}\beta L_{fin}) / (\sqrt{2}\beta L_{fin}) \quad (4.3.38)$$

where, the coefficient $\beta = \sqrt{(h_{fin}P_{fin})/(kA_{fin})}$, the fin perimeter is $P_{fin} = \pi d_{wi}$, and the fin cross-sectional area is $A_{fin} = (\pi d_{wi}^2)/4$. The heat transfer coefficient between the heat sources working fluid and the engine working gas is also function of the inner and outer thermal resistances. Figure 4.3 shows all the heat exchanger thermal resistances. The inner and outer pipe total thermal resistance $R_{j,pipe}$ is

$$R_{j,pipe} = (R_{fin,j}^{-1} + R_j^{-1})^{-1} \quad (4.3.39)$$

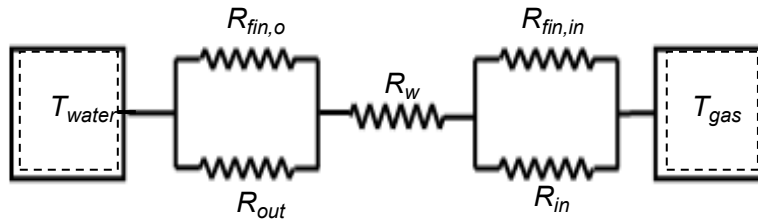


Figure 4.3: Heat exchanger thermal resistances

The pipe Wall thermal resistance is

$$R_w = \ln((d_{op} + 2\Delta w_p)/d_{op}) / (2\pi k L_p N_p) \quad (4.3.40)$$

The inner and outer pipe total thermal resistance R_j is

$$R_j = (A_{z,j} h_j)^{-1} \quad (4.3.41)$$

The inner pipe fins thermal resistance is

$$R_{fin,ip} = (\eta_{fin,ip} N_p A_{fin,tot,ip} h_{fin,g})^{-1} \quad (4.3.42)$$

The outer pipe fins thermal resistance is

$$R_{fin,op} = (\eta_{fin,op} N_p A_{fin,tot,op} h_{fin,wf,op})^{-1} \quad (4.3.43)$$

The overall thermal resistance in the heat exchanger is

$$R_{tot} = \sum_{j=in,p}^{out,p} R_{j,pipe} + R_w \quad (4.3.44)$$

The heat transfer to the engine from the heat source is

$$\dot{Q}_{hot} = \frac{T_{hot} - T_{wf}}{R_{tot}} \quad (4.3.45)$$

The heat removed from the engine to the heat sink is

$$\dot{Q}_{cold} = \frac{T_{wf} - T_{cold}}{R_{tot}} \quad (4.3.46)$$

The heat transfer coefficients of equation (4.3.41) for other working fluids such as water may be calculated using the equations presented in section 3.3.3.1. Thombare and Verma (2006) published a research on technological developments in SE cycle. They found that it is not easy to estimate the heat transfer coefficient of a cooler, not only because of the exchanger geometry, but also because the heat transfer coefficient in the cooler is fully dependent on the nature of the coolant used. They presented an expression for a heat transfer coefficient using water as coolant as

$$h_{wa} = 0.35Re^{0.55}Pr^{0.33}k_{wa}d_o \quad (4.3.47)$$

4.3.3 Regenerator design

The regenerator is designed as a stainless steel pipe filled with plain-woven wire mesh. Mesh screens are stacked together to form a laminating screen, exactly in the same configuration as in the cooler and heater pipes. Specifications of the mesh characteristics are as mentioned in the previous sections. A regenerator cyclically stores and releases energy. This dual function determines different values of heat transfer coefficients and friction factors compared to those presented for the heater and cooler (Thombare and Verma, 2006). Barron (1999) reported the heat transfer coefficients correlation for woven screen matrices in the regenerator as

$$j_R = CRe^{-n} = \frac{h_{fin}Pr^{2/3}}{c_p G} \quad (4.3.48)$$

where, the values of constant C and n are related to the porosity ε

$$n = 0.483 - 0.236(1 - \varepsilon) \quad (4.3.49)$$

$$C = 1.415 - 2.490(1 - \varepsilon) \quad (4.3.50)$$

Kays and London (1984) reported the friction factor correlation in the regenerator as

$$f = \frac{C_1}{Re} (1 + C_2 Re^{0.88}) \quad (4.3.51)$$

where values, for the constant C_1 and C_2 for various values of porosity are given in references by Barron (1999).

4.4 Lumped parameter modelling of a Stirling engine heat exchanger

A lumped parameter model may be used to describe the thermo-fluid dynamic behaviour of the SE shown in figure 4.4. The thermo-fluid dynamic behaviour of a SE does not depend only on the nature of the working fluid, but also on its heat exchanger performances. A lumped parameter modelling of a SE heat exchanger will be developed by applying the boundary conditions defining its working conditions in the engine assembly.

Third order modelling methods are used to model a SE. The first method assumes an isothermal cooling, heating, compression and expansion processes. This approach is often used in the preliminary design of a SE and is mainly known as the Schmidt analysis (Urieli,

1977). The second method assumes an isothermal cooling and heating processes, while the compression and expansion processes are assumed adiabatic. This approach is closer to an actual engine as it analyses different types of losses in the engine (Walker, 1980). The third method applies the equations of change, mass momentum and energy to the engine system consisting of a number of one-dimensional lumped control volumes. This is the approach that will be used in this project to theoretically model the SE heat exchanger.

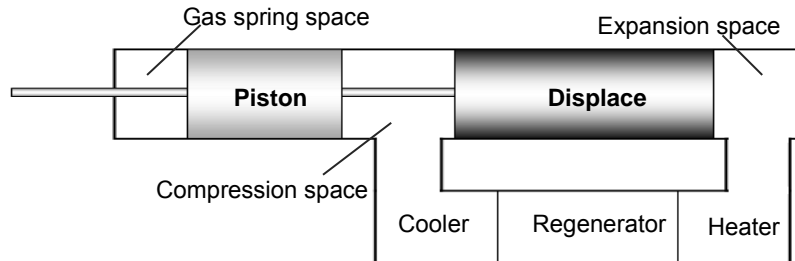


Figure 4.4: A free piston Stirling engine

The following topics were addressed, in order to elaborate on the third order modelling approach: identification of different types of energy losses in the SE (see section 4.4.1); a Schmidt analysis (section 4.4.2), and the way in which the control volumes are addressed as nodal analysis according to Finkelstein (Walker, 1980) (section 4.4.3). Finally, a nodal analysis approach to the heating, regenerative and cooling heat exchanger will be developed and presented.

4.4.1 Energy losses through the Stirling engine heat exchanger

Stirling engine heat exchangers define the engine performance. The heat exchanger energy losses were analysed based on the SE energy losses. In a SE the energy losses are due to the mechanical and thermodynamic processes involved during the engine operation. Compression and expansion are not adiabatic. Heat exchangers are not ideal since the pressure drops in the engine across the heat exchanger and losses of heat in the exchangers exist. An accurate prediction of the engine performances requires an understanding of the factors causing losses, such as: the flow losses, the gas leakage, the heat transfer losses, and the regenerator losses. Consideration of their effects on the SE heat exchangers follows the third order method analysis of a SE heat exchanger which is the aim of this modelling.

4.4.1.1 Energy loss due to flow friction effects

The pressure drop due to friction in the engine is described in section 4.2.3. The internal energy generated when the working fluid is forced to flow against the frictional drag force is

$$\Delta\dot{Q}_{frict,j} = -(\dot{m}_j\Delta P_j)/\rho_j \quad (4.4.1)$$

The total heat generated by pressure drop in the different exchangers is

$$\Delta\dot{Q}_{frict,tot} = \Delta\dot{Q}_{frict,c} + \Delta\dot{Q}_{frict,r} + \Delta\dot{Q}_{frict,h} \quad (4.4.2)$$

4.4.1.2 Energy loss due to working fluid leakage effects

A SE must seal up the working fluid in order to prevent it from escaping from the working spaces. Gas leakage results in significant engine power loss. During a gas leak, a certain amount of energy is dissipated that is not accounted for in an adiabatic or isothermal model. This irreversible loss, mainly encountered in the compression and expansion space, is given as follows (Walker and Sent, 1985)

$$\Delta\dot{Q}_{leak} = \frac{\pi\lambda^3 d}{24\mu L} \rho_{max}^2 \quad (4.4.3)$$

4.4.1.3 Energy loss due to internal conduction

All materials conduct heat at a rate that depends on their thermal conductivity. Thermal conductivity is very important in SEs due to the heat flowing out of the system by conduction from the heater to the cooler along the cylinder and displacer walls. The cylinder and displacer walls are made as thin as possible to reduce conduction. Energy loss from each control volume is (Tlili, 2002)

$$\Delta\dot{Q}_{int,cond,j} = \frac{k_{wall}A_{z,wall}}{L} (T_{wall,j} - T_j) \quad (4.4.4)$$

4.4.1.4 Energy loss due to radiation and convection

The SE heat exchanger is subject to various thermal energy losses through radiation and convection, occurring whenever the potential arises. They are mostly avoided by the use of radiation shields and enclosures or convective spoilers (Walker and Sent, 1985).

4.4.1.5 Energy loss due to external conduction

The SE heat exchanger is subject to various thermo-fluid losses, such as energy lost through fluid friction in the regenerator matrix, heat conduction due to the temperature gradient along the matrix length, and heat flux returning to the working fluid in reverse flow, which is always less than the heat to the matrix hot side. Therefore, there is a net enthalpy flux in the matrix from the hot side to the cold side. Energy lost by external conduction is found in the regenerator, which is not adiabatic. These losses are specified by the regenerator effectivity, $\varepsilon \leq 1$, defined as a ratio of the heat given up in the regenerator by the working fluid during its passage towards the compression space; to the heat received in the regenerator by the working fluid during its passage towards the expansion space (Tlili and Timouni, 2006). Thus, energy stored by the regenerator at the time of the passage of working fluid from the expansion space to the compression space is not completely restored at the time of the working fluid's return, even in an ideal case where the regenerator is perfectly insulated, i.e. $\varepsilon = 1$. In many second-order models, the effectivity of the regenerator is considered as a function of a number of transfer units (Ntu). The later are again a function of a number of relevant characteristics. Urieli (1977) and later Kolin (1991) proposed that the effectiveness ε can be calculated as

$$\varepsilon = \frac{Ntu}{1 + Ntu} \quad (4.4.5)$$

$$Ntu = \frac{hA_z}{\dot{m}c_p} \quad (4.4.6)$$

The energy lost by external conduction is (Tlili, 2002)

$$\Delta\dot{Q}_{ext} = (1 - \varepsilon)(\Delta\dot{Q}_r) \quad (4.4.7)$$

From equation (4.4.7) it is clearly that the energy lost in the regenerator is the contribution of the energy lost in the hot and cold sides. It is calculated as

$$\Delta\dot{Q}_r = \Delta\dot{Q}_{r1} + \Delta\dot{Q}_{r2} \quad (4.4.8)$$

4.4.1.6 Energy loss due to the shuttle effect

In a SE, thermal loss due to the shuttle effect is characterised by a difference between the operating temperature profile of the moving displacer from the hot to the cold side of the cylinder, and its wall temperature profile from the hot cylinder wall to the cold cylinder wall. It has an effect of increasing the apparent thermal loss. The shuttle effect can be very important, particularly in small SEs. Various studies have been done on the shuttle effect, and it has been found that the shuttle effect increases the thermal conductance loss. This thermal conductance loss is difficult to estimate before the engine design is complete (Tlili and Timouni, 2006). Therefore, for a preliminary design, Walker (1980) proposed that it is convenient to use the Martini recommendations, which lead to the following approximation of the shuttle heat

$$\Delta\dot{Q}_{sh} = 0.4x_d^2kd \frac{(T_h - T_c)}{SZ} \quad (4.4.9)$$

4.4.2 The Schmidt assumptions

The Schmidt theory is one of the isothermal calculation methods for SEs. This theory provides a harmonic motion for the reciprocating elements, but retains the major assumptions of isothermal compression and expansion, and perfect regeneration (Urieli, 1977). It, thus, remains highly idealised, but certainly more realistic than the ideal Stirling cycle (Tlili, 2002). The assumption of simple-harmonic volume variation permits the pressure, P to be expressed as a function of crank angle, ω and leads to closed-form solutions for work per cycle (Tlili and Timouni, 2006). The Schmidt formula may be shown in various forms, depending on the notations used, and can be arranged for a Beta-configuration SE (Walker and Sent, 1985). In the first-order method analysis, when applying the Schmidt theory, the internal temperatures of expansion and compression spaces are isothermal. The working fluids in each control volume obey the perfect gas law, and there is a perfect mixing of the working space content (Urieli, 1977)

$$P_j V_j = m_j R T_j \quad (4.4.11)$$

The mass of the working fluid through the heat exchanger and the working spaces remains constant, so it is assumed that, there is no leakage

$$m_1 + m_h + m_r + m_c + m_2 = m \quad (4.4.12)$$

Applying equation (4.4.11) to each control volume and substituting the result obtained in equation (4.4.12), then rearranging, the instantaneous working fluid pressure is constant through the work spaces

$$P = mR \left(\frac{V_1}{T_1} + \frac{V_h}{h} + \frac{V_r}{T_r} + \frac{V_c}{T_c} + \frac{V_2}{T_2} \right)^{-1} \quad (4.4.13)$$

The Schmidt theory assumes that the temperature gradient in the regenerator is null and, therefore, the temperature in the regenerator is given as a function of the heater and the cooler temperatures T_h and T_c

$$T_r = (T_h - T_c) / \ln(T_h / T_c) \quad (4.4.14)$$

The harmonic variation of the working spaces volumes is calculated using equations (4.2.4) and (4.2.5).

4.4.3 Nodal analysis

In 1960, Finkelstein developed an ideal adiabatic analysis of a SE (Walker, 1980). He repeated the Schmidt assumptions, as discussed above, and retained the assumption of an adiabatic and not isothermal process in the working spaces. Finkelstein then proposed that the process remains isothermal in the heater and cooler. Nevertheless, the possibility of a non-isothermal process represents an operating process close to the real engine. From the ideal adiabatic analysis, Finkelstein pioneered nodal analysis in 1975 but, later, several other nodal analyses were made independently (Walker, 1980). This project will also use nodal analysis to mathematically model the dynamic behaviour of the working fluid in the SE heat exchanger. This will be achieved by solving conservation of mass, momentum and energy equations for each node's control volume, assuming that all the fluid properties are located on the cell centre points, called nodes. The operating conditions must be specified; these include the changing pressure, and the temperature of the heat source and sink (Walker, 1980). The output of the simulation is the pressure, temperature and mass distribution in the engine at the end of each time step. The aerodynamic friction equations will be taken into account as well as the equations of state of the working fluid. From figure 4.5, the conservation equation may be written as follows:

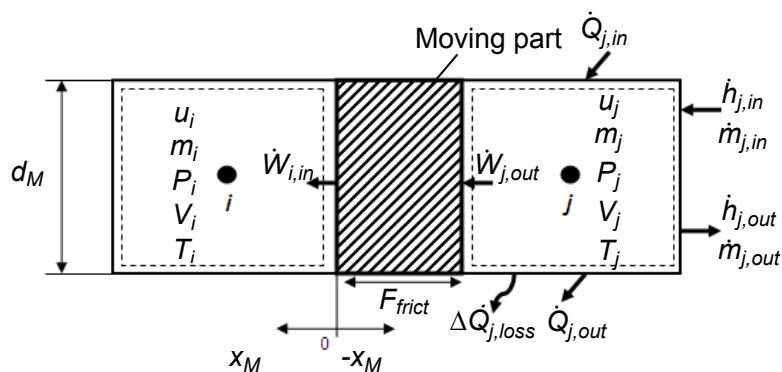


Figure 4.5: Engine control volume

Conservation of mass equation

$$\frac{dm_j}{dt} = \dot{m}_{j,in} - \dot{m}_{j,out} \quad (4.4.15)$$

Conservation of momentum equation

$$\frac{d}{dt}(m_j \dot{x}_j) = (P_j - P_i)A_M - F_{frict} \quad (4.4.16)$$

Conservation of energy equation

$$\frac{du_j}{dt} = \dot{Q}_{j,in} - \dot{Q}_{j,out} + h_{j,in} - h_{j,out} + \dot{W}_{i,in} - \dot{W}_{j,out} - \Delta \dot{Q}_{j,loss} \quad (4.4.17)$$

where $A_M = \pi d_M^2/4$, and from equation (4.4.11) $m_j = P_j V_j / RT_j$, and substituting for m_j into equation (4.4.15) then, rearranging into a form suitable for an explicit numerical solution method, gives the node new pressure as

$$P_j^{t+\delta t} = \left[\left(\frac{P_j V_j}{RT_j} \right)^t + \delta t (\dot{m}_{j,in}^t - \dot{m}_{j,out}^t) \right] \left(\frac{RT_j}{V_j} \right)^{t+\delta t} \quad (4.4.18)$$

The new volume is

$$V_j^{t+\delta t} = V_j^t + A_M x_j^{t+\delta t} \quad (4.4.19)$$

The adiabatic assumption results in a change of the specific internal energy in a closed control volume as

$$u = c_v \Delta T \quad (4.4.20)$$

A change of the specific enthalpy in an opened control volume is

$$h = c_p \Delta T \quad (4.4.21)$$

The instantaneous pressure equation can be obtained in a similar manner as for the isothermal model. This is given in equation (4.4.13). From equation (4.4.20) the internal energy of a node of mass m_j is $u_j = C_v m_j dT_j$, and substituting for u_j into equation (4.4.17) and rearranging, into a form suitable for an explicit numerical solution, gives the node new temperature as

$$T_j^{t+\delta t} = \frac{c_v^t m_j^t T_j^t + \delta t (\dot{Q}_{j,in} - \dot{Q}_{j,out} + h_{j,in} - h_{j,out} + \dot{W}_{j,in} - \dot{W}_{j,out} + \Delta \dot{Q}_{j,loss})}{c_v^{t+\delta t} m_j^{t+\delta t} T_j^{t+\delta t}} \quad (4.4.22)$$

The node new mass is

$$m_j^{t+\delta t} = (P_j^{t+\delta t} V_j^{t+\delta t}) / (RT_j^{t+\delta t}) \quad (4.4.23)$$

The node new mass flow rate is

$$\dot{m}_j^{t+\delta t} = (m_j^{t+\delta t} - m_j^t) / \delta t \quad (4.4.24)$$

The new pressure for the i^{th} node control volume is obtained by rearranging equation (4.4.16), to give

$$P_i^{t+\delta t} = P_j^{t+\delta t} - \frac{1}{A_M} \left[\frac{(m_j \dot{x}_j)^{t+\delta t} - (m_j \dot{x}_j)^t}{\delta t} - F_{frict} \right] \quad (4.4.25)$$

Continuing with the nodal analysis with reference to figure 4.6 the following equations are now derived to complete the SE heat exchanger mathematical model. The displacements of the moving parts are

$$x_p = 0, \text{ and } x_d = x(t) \quad (4.4.26)$$

The enthalpy and power crossing the boundaries of the expansion space e are

$$\text{if } \dot{m}_{e,h} \geq 0 \text{ then } h_{e,h} = -c_p T_e \text{ else } h_{e,h} = c_p T_h \quad (4.4.27)$$

$$\dot{W}_{d,e} = P_e A_d \dot{x}(t) \quad (4.4.28)$$

With reference to section 4.4.1, the energy loss from the expansion space e and compression space co is

$$\Delta\dot{Q}_{j,loss} = \Delta\dot{Q}_{leak,j} + \Delta\dot{Q}_{int,cond,j} + \Delta\dot{Q}_{sh,j} \quad (4.4.29)$$

The enthalpy and power crossing the boundaries of the heater h are

$$\text{if } \dot{m}_{e,h} \geq 0 \text{ then } h_{h,rh} = c_p(T_e - T_h) \text{ else } h_{h,rh} = c_p(T_{rh} - T_h) \quad (4.4.30)$$

$$\dot{Q}_{hot} = AU|_h(T_{hot} - T_h) \quad (4.4.31)$$

With reference to section 4.4.1, the energy loss from heater h and cooler c is

$$\Delta\dot{Q}_{j,loss} = \Delta\dot{Q}_{leak,j} + \Delta\dot{Q}_{int,cond,j} + \Delta\dot{Q}_{frict,j} \quad (4.4.32)$$

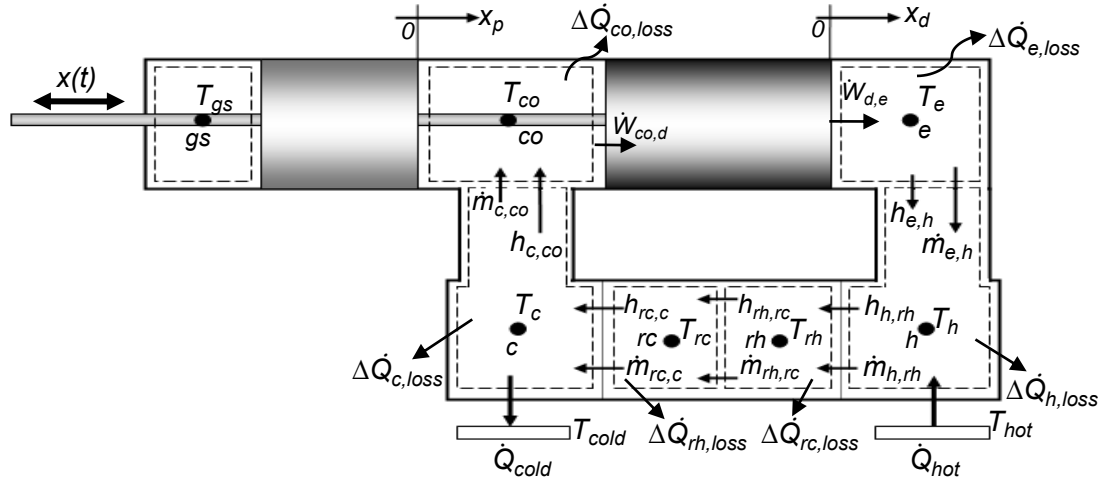


Figure 4.6: A Stirling engine mathematical model control volume layout

The enthalpy and power crossing the boundaries of the hot side regenerator rh are

$$\text{if } \dot{m}_{e,h} \geq 0 \text{ then } h_{rh,rc} = c_p(T_h - T_{rh}) \text{ else } h_{rh,rc} = c_p(T_{rc} - T_{rh}) \quad (4.4.33)$$

$$\dot{Q}_{rh} = AU|_{rh}(T_{rh} - T_r) \text{ with } T_r = (T_{hot} - T_{cold}) / \ln(T_{hot}/T_{cold}) \quad (4.4.34)$$

With reference to section 4.4.1, the energy loss from the hot side rh and cold side rc of the regenerator

$$\Delta\dot{Q}_{j,loss} = \Delta\dot{Q}_{j,+} = \Delta\dot{Q}_{leak,j} + \Delta\dot{Q}_{int,cond,j} \quad (4.4.35)$$

The enthalpy and power crossing the boundaries of the cold side regenerator rc are

$$\text{if } \dot{m}_{e,h} \geq 0 \text{ then } h_{rc,c} = c_p(T_{rh} - T_{rc}) \text{ else } h_{rc,c} = c_p(T_c - T_{rc}) \quad (4.4.36)$$

$$\dot{Q}_{rc} = AU|_{rc}(T_r - T_{rc}) \text{ with } T_r = (T_{hot} - T_{cold}) / \ln(T_{hot}/T_{cold}) \quad (4.4.37)$$

The enthalpy and power crossing the boundaries of the cooler c are

$$\text{if } \dot{m}_{e,h} \geq 0 \text{ then } h_{c,co} = c_p(T_{rc} - T_c) \text{ else } h_{c,co} = c_p(T_{co} - T_c) \quad (4.4.38)$$

$$\dot{Q}_{cold} = AU|_c(T_c - T_{cold}) \quad (4.4.39)$$

The enthalpy and power crossing the boundaries of the compression space co are

$$\text{if } \dot{m}_{e,h} \geq 0 \text{ then } h_{c,co} = c_p T_c \text{ else } h_{c,co} = -c_p T_{co} \quad (4.4.40)$$

$$\dot{W}_{d,e} = -P_{co} A_d \dot{x}(t) \quad (4.4.41)$$

5 Waste heat recovery experimental and theoretical results

The aim of the WHR experiment is to verify the theoretical model simulating the heat transfer of the recovered heat from the fuel tank to the heat exchanger and/or the air-cooled condenser. Analysis of the WHR experimental and theoretical results will now be described. The experimental set-up is explained first, followed by the experimental testing procedure, thereafter experimental and theoretical results will be presented and discussed.

5.1 Experimental setup

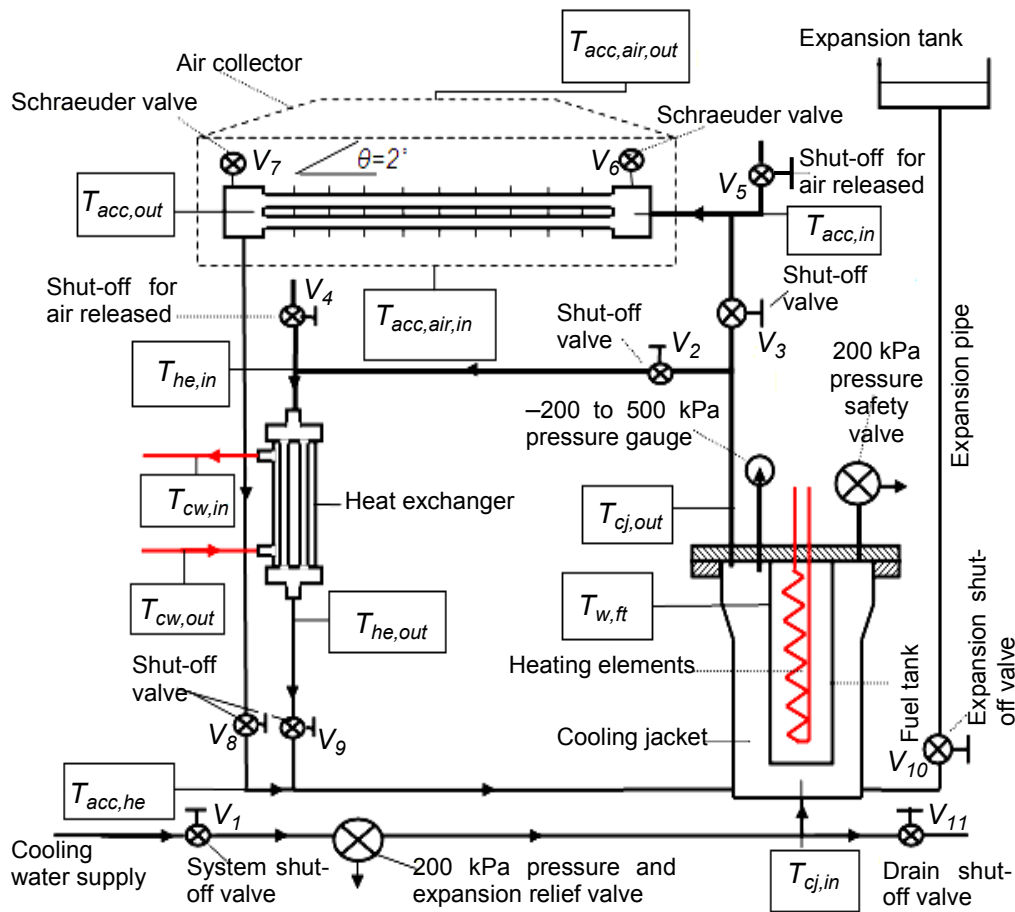


Figure 5.1: Schematic diagram of the experimental set-up

Figure 5.1 shows a schematic diagram of a thermosyphon loop designed and constructed to demonstrate the recovery of waste heat from a PBMR spent/used fuel tank. The thermosyphon loop consists of a primary and secondary line, manually regulated by four shut-off valves, V_2 , V_3 , V_8 , and V_9 . The primary line comprises the cooling jacket and the heat exchanger, while the secondary line comprises the cooling jacket and the air-cooled condenser. The cooling jacket is concentric to a fuel tank containing electrical heating elements that are used to simulate the heat transferred to the cooling jacket through the fuel tank walls. The heated-up fuel tank walls will raise the temperature of the water in the cooling jacket. If the temperature of water is raised beyond its saturation point, then vapour is produced. The flow in the loop will then be characterised by a two-phase mixture of vapour

and liquid. Therefore, three modes of operation, namely single phase, single to two-phase, and heat pipe mode, may be considered.

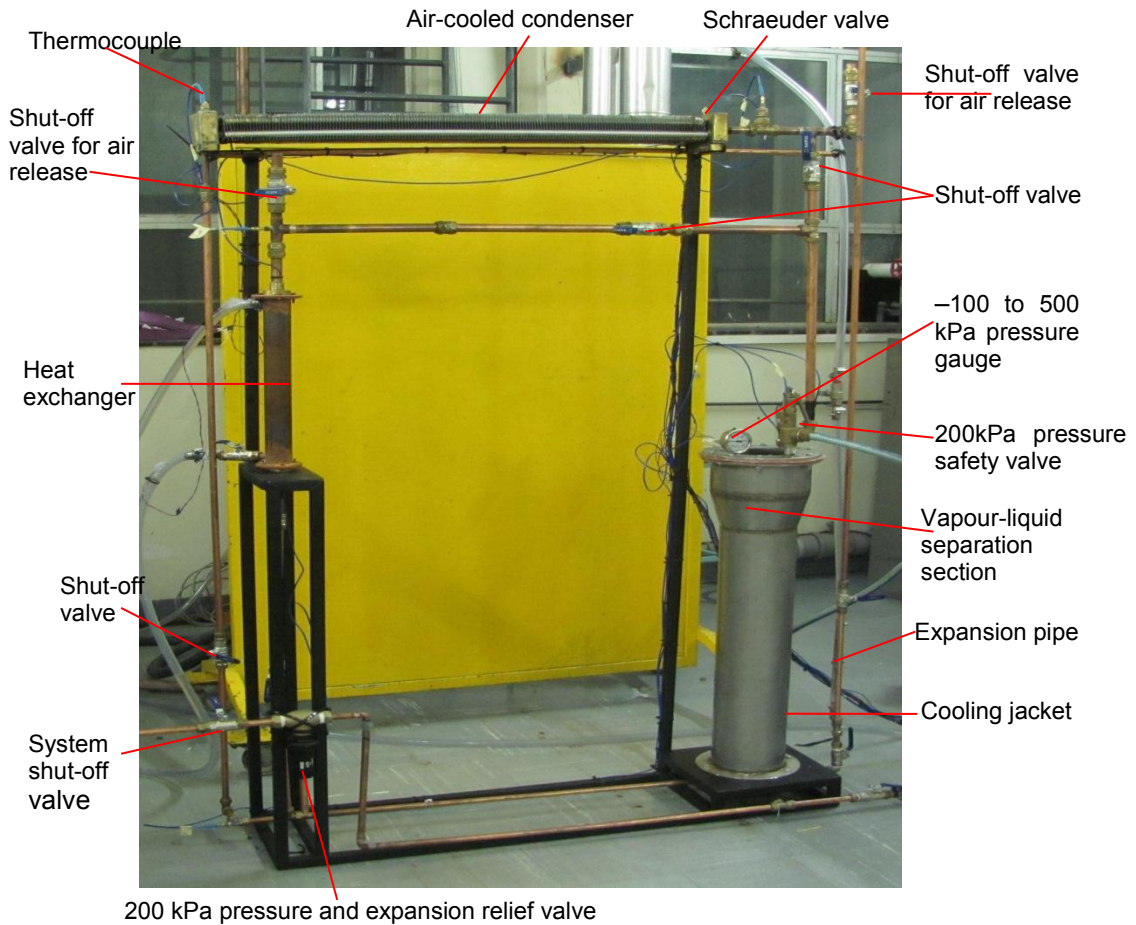


Figure 5.2: Waste heat recovery and utilisation system experimental set-up (without the air collector)

For the single-phase mode, the system is filled with water and the flow remains single throughout the operation. The system pressure will not only be dictated by the heat input to the system but also by the level of water above the cooling jacket. Although the system has a header tank to maintain a safe working pressure, a 200 kPa pressure safety valve, and a 200 kPa pressure and expansion relief valve is used to regulate the system pressure (see figure 5.1). An over-pressure, due to the level of water above the cooling jacket, will be balanced by the action of the expansion tank linked to the bottom of the cooling jacket. The expansion tank is linked to the cooling jacket by an expansion pipe through an expansion shut-off valve V_{10} that will remain open during the single-phase mode operation. In the single-to two-phase mode, the flow begins in single-phase mode but turns to a two-phase mode due to an addition of heat input to the system. In the heat pipe mode, the system starts off with a loop partially filled with water. The expansion shut-off valve V_{10} is closed. As heat is supplied to the cooling jacket through the fuel tank walls, boiling will commence when the water saturation point is reached. As the loop is partially filled with water, when boiling commences, the flow will be characterised by an oscillatory two-phase flow and a high heat transfer rate is established between the evaporator and condenser sections of the loop. The system pressure is measured using a -100 to 500 kPa pressure gauge on top of the cooling jacket. A 200 kPa

pressure and expansion relief valve, after the system shut-off valve V_1 , are used to regulate the system pressure to a value not exceeding 200 kPa.

The system temperatures were measured using T-type thermocouples, except in the fuel tank where K-type thermocouples were used. In figure 5.1, all temperature measuring points are represented by square boxes. For air temperature and air velocity measurements on the air-cooled condenser side an air collector was used to channel the air over the heat exchanger and to facilitate air-flow velocity measurements. Figure 5.2 shows a photograph of the WHR&U system experimental set-up thermosyphon loop without the air collector. The thermosyphon loop was made with copper pipes. Copper pipes of 22 mm OD and 1 mm wall thickness were used in the hot fluid lines between the fuel tank and the air-cooled condenser and heat exchanger inlets. Copper pipes of 15 mm OD and 1 mm wall thickness were used for the cold liquid (condensate) return lines to the fuel tank.

5.1.1 Fuel tank

The fuel tank was manufactured from stainless steel pipe of 140 mm OD, 915 mm length and 6 mm wall thickness. An analogue pressure gauge and a pressure safety valve were mounted on the fuel tank top flange, as shown in figure 5.2. To simulate the heat generated by the PBMR fuel in the fuel tank, two incalloy 825 heaters, 3 kW and 230 V each, were used as shown in figure 5.1. The heaters were surrounded with copper mesh to enhance the heat transfer rate from the heating elements to the fuel tank wall internal area.

5.1.2 Cooling Jacket

The cooling jacket was manufactured from a two part assembly. The bottom part is a 168 mm OD stainless steel pipe of 720 mm length and 2 mm wall thickness. The top part is a 218 mm OD stainless steel pipe of 150 mm length and 2 mm wall thickness. As seen in figure 5.2, these two parts are welded together through a stainless steel conical reducer, called the vapour-liquid separation section. The cooling jacket's bottom end was welded onto a stainless steel plate of 10 mm thickness, fitted on its support with M8 stainless steel bolts. The top end flange was fitted to the fuel tank flange with M10 stainless steel bolts. The fuel tank and cooling jacket flanges are air sealed with a 40 durometer, peroxide-cured, and high-temperature-resistant silicone rubber compound.

5.1.3 Air-cooled condenser

The air-cooled condenser was manufactured from seven copper pipes assembled in a two-row staggered configuration with a 26 mm transversal pitch and 32 mm longitudinal pitch. Each pipe has a 15 mm OD, 1100 mm length and 1 mm wall thickness, and they were finned with aluminium fins of 120 mm length, 65 mm width and 0.78 mm thickness. The aluminium fins are spaced 5 mm from one another. At the inlet, the vapour is distributed to the pipes via a

brass manifold, and a similar manifold at the other end collects the condensate and channels it to the downcomer.

5.1.4 Heat exchanger

The heat exchanger is a vertical shell and tube heat exchanger with steam condensing in the tubes and cooling water circulating in the shell. The shell is a copper pipe of 54 mm OD, 420 mm length and 2 mm wall thickness, while the inner tubes are four copper pipes of 15 mm OD, 420 mm length and 1 mm wall thickness. The distributing and the collecting headers were machined from brass of 100 mm ID, 20 mm width and 3 mm wall thickness. The header flanges were bolted with M6 stainless steel bolts with a seal made of a high-temperature-resistant silicone rubber compound.

5.2 Experimental testing procedure

Referring to figure 5.1, the experimental testing was conducted according to the following procedural steps. Open the shut off valves V_1 , V_2 , V_3 , V_4 , V_5 , V_{10} and V_{11} to supply the system with water. These valves remain open until the system is filled with water so that the entrapped air is released, while filling the system. Air is displaced out of the system by the rising water through the shut-off valves for air release (V_4 and V_5) and the Schraeuder valves (V_6 and V_7). Only when the system is full of water, close first the shut-off valves for air release V_4 and V_5 and thereafter the main shut-off valve V_1 . Check the entire system for any water leaks. Through the transparent plastic expansion pipe and using the expansion shut-off valve V_{10} and the drain valve V_{11} , check and adjust the water level in the system. The primary line is selected by leaving open the shut-off valves V_2 and V_9 while the shut-off valves V_3 and V_8 are closed. For the secondary line the shut-off valves V_3 and V_8 are opened while the shut-off valves V_2 and V_9 are closed. A hand operated variable voltage source is used to adjust the electrical power supplied to the heating elements. Heat is added to the system and the water temperature rises. When the temperature of water reaches its saturation point, boiling begins: the working fluid in the system will be characterised by a vapour-liquid mixture. Once this procedure has been completed, the single, single to two-phase and heat pipe operating modes may be considered.

For single-phase and single to two-phase operating modes, the expansion tank shut-off valves V_{10} , V_4 and V_5 remain open while all the other valves are closed. The system is filled with water to its maximum capacity as described in the previous paragraph. The shut-off valves for air release V_4 and V_5 remain open until the water boils. Two minutes after boiling commences, close the valves V_4 and V_5 . A simple test to gauge the amount of air in the system involves two temperature measurements from the inlet and outlet of the air-cooled condenser ($T_{acc,in}$ and $T_{acc,out}$) through the manifolds. If there is air in the system it will accumulate in the connecting manifold, and the temperature of the working fluid in the connecting manifold will be less than the saturated temperature of the working fluid. After the air is removed from the system, the power is switched off and the loop allowed to cool down completely. During the cooling

process of the loop, heat is removed from the system by the air-cooled condenser; hence the system's pressure decreases. A complete cooling of the system was gauged by a pressure reading on the -100 to 500 kPa pressure gauge. The value of the pressure should be ≤ 100 kPa to ensure that the system is completely cooled. Thereafter, the power is switched on again to start the single to two-phase operating mode test.

For the heat pipe operating mode, the system is filled with water and the level adjusted (to a level slightly above the cooling jacket) following the same procedure as described in the first paragraph of this section. The air trapped in the water must be removed. If left unchecked, this air will create an insulating layer in the condenser section, which negatively affects the heat transfer coefficient in the loop cooling sections. Air is removed from the system by boiling water. The shut-off valves for air release V_4 and V_5 are opened until only vapour is released from the system. After a few seconds, close the shut-off valves for air release V_4 and V_5 , then open the Schraeuder valves V_6 and V_7 to check again if only vapour is released. This ensures that air is completely removed from the system. The removal of air from the system in the heat pipe operational mode may be gauged by taking three temperature measurements. The temperature at the inlet of the air-cooled condenser $T_{acc,in}$ and the temperature at the inlet of the heat exchanger $T_{he,in}$ should equal the temperature at the outlet of the cooling jacket $T_{cj,out}$.

5.3 Experimental and theoretical results

The experimental results obtained from the experimental set-up shown in section 5.1 are now discussed with the aid of a number of different sets of representative test data. Theoretical results obtained from the WHR&U system mathematical model, developed in section 3.3, are also discussed, and compared to the experimental results. In order to gauge the validity of the experimental results, a sensitivity analysis investigating the parameters that influence the theoretical results was also conducted. A summary of the sensitivity analysis done on the theoretical model is presented first, and thereafter experimental and theoretical results are presented and discussed.

5.3.1 Sensitivity analysis of the WHR&U system theoretical model

In this section, a sensitivity analysis of the WHR&U system theoretical model was undertaken to investigate the more important parameters affecting the theoretical results. The experimental results were set as a reference base line for the theoretical model. It was necessary to analyse in which way changes in the flow and geometrical variables of the cooling sections of the WHR&U system loop affect theoretical results. The flow variables considered in this analysis are the air and working fluid mass flow rate (\dot{m}_a , \dot{m}_{wf}), dynamic viscosity (μ_a , μ_{wf}), density (ρ_a , ρ_{wf}), thermal conductivity (k_a , k_{wf}) and specific heat constant (c_a , c_{wf}). The geometrical variables considered are the heat transfer area (A_z), the diameter of the heat exchanger tubes (d_p), the number of tubes (N_p), the tube transversal pitch (S_T), the tube longitudinal pitch (S_L), and the tube layout. Referring to equation (3.4.7) and (3.4.14), it was found that the flow and geometrical variables influencing the theoretical results are

captured in the thermal resistances of the air-cooled condenser and heat exchanger, respectively. It was then, convenient to investigate how changes in the air-cooled condenser and heat exchanger thermal resistance affect the theoretical results.

As given in equation (3.4.8), the air-cooled condenser total thermal resistance consists of the inner convective thermal resistance $R_{co,ip}$, the wall conduction thermal resistance $R_{co,wp}$, and the air-side thermal resistance R_{th} . The air-side thermal resistance consists of the convective air thermal resistance $R_{co,op}$, the fin thermal resistance $R_{co,fin}$, and the radiation thermal resistance R_{rad} . The sensitivity analysis process involved an investigation on each specific thermal resistance, analysing the way it affects results. It was found that, the radiation thermal resistance $R_{rad} = 715831264.40004 \text{ K/W}$ is high, and therefore does not influence the results. The wall conduction thermal resistance $R_{co,wp} = 4.77271 \times 10^{-5} \text{ K/W}$ is low, and therefore allows a good heat transfer between the inner and outer pipes' heat transfer areas. It is for this reason that, during this investigation, the conduction thermal resistance was not considered as a parameter affecting theoretical results. Changes in the convective air thermal resistance $R_{co,op} = 0.10596 \text{ K/W}$ least affects results. This is because the convective heat transfer coefficient from unfinned air-cooled condenser tubes is not good. It is for this reason that fins are used to enhance the heat transfer area of the air-cooled condenser to the air. The inner convective thermal resistance $R_{co,ip} = 0.00078 \text{ K/W}$, and the fin thermal resistance $R_{co,fin} = 0.00176 \text{ K/W}$ remained the main parameters influencing theoretical results. These thermal resistances were calculated using Nusselt number correlations capturing their respective heat transfer coefficients (see section 3.3.3).

The computer simulation temperatures with a theoretically calculated total air-cooled condenser thermal resistance $R_{tot,acc,t} = 0.00256 \text{ K/W}$ gave the heat transferred out of the steam and into the air as $\dot{Q}_{acc,t} = \Delta T_{In,acc,t} / R_{tot,acc,t} = 7190.04402 \text{ W}$. However, the experimentally calculated heat transfer rate based on the conservation of energy for the air through the air-cooled condenser fins is $\dot{Q}_{acc,e} = 2386.92001 \text{ W}$ (see Appendix C.2.2). As shown in Appendix C.2.2, assuming that the experimentally determined heat transfer rate is $\dot{Q}_{acc,e} = 2386.92121 \text{ W}$, an experimentally determined air-cooled condenser total thermal resistance is $R_{tot,acc,e} = 0.00831 \text{ K/W}$. This thermal resistance of 0.00831 K/W is considerably greater than the theoretically determined value of 0.00256 K/W . This means that the theoretical model value of heat transfer coefficient that was used was too high. The result of this was that the inlet working fluid $T_{acc,in}$ and outlet air and working fluid temperatures, $T_{acc,air,out}$ and $T_{acc,out}$, respectively, were over-predicted. This could be expected, as the theoretical correlation used may have not truly represented the as-manufactured and tested air-cooled condenser.

Yang et al. (2006) suggest that, in cases like this, the theoretically determined total thermal resistance may be adjusted accordingly as

$$R_{tot,actual} = R_{tot,t} Ra_e^{-n} \quad (5.3.1)$$

where, $R_{tot,actual}$ is the actually determined total thermal resistance, $R_{tot,t}$ is the theoretically determined total thermal resistance, Ra_e the experimentally determined Raleigh number, and n is an experimentally determined constant. In this case the experimentally determined total thermal resistance $R_{tot,acc,e}$ is assumed to be the actual total resistance $R_{tot,actual}$, while the constant n may be calculated as

$$n_{acc} = \frac{\ln\left(\frac{R_{tot,t}}{R_{tot,actual}}\right)}{\ln(Ra_e)} = \frac{\ln\left(\frac{R_{tot,t}}{R_{tot,acc,e}}\right)}{\ln(Ra_{e,acc})} = \frac{\ln\left(\frac{0.00256}{0.00830}\right)}{\ln(14706881.91)} = -0.07137 \quad (5.3.2)$$

Substituting n in equation (5.3.1), with the calculated n_{acc} from equation (5.3.2), the actual total thermal resistance used in the theoretical model for the air-cooled condenser line is

$$R_{tot,actual,acc} = R_{tot,t} Ra_e^{-n_{acc}} = 0.00256 (14706881.91)^{0.071371} = 0.00831 \text{ K/W} \quad (5.3.3)$$

Extending the same analysis to the heat exchanger, it was found that the theoretically calculated heat exchanger total thermal resistance $R_{he,t} = 0.00423 \text{ K/W}$ was considerably less than the experimentally determined thermal resistance $R_{tot,he} = 0.00851 \text{ K/W}$ (see Appendixes C.2.3 and C.2.4). The results of this were that the heat exchanger working fluid and cooling water outlet temperatures $T_{he,out}$ and $T_{cw,out}$, respectively, were over-predicted. This was also expected, for the same reasons as outlined in the previous paragraph. The theoretically determined thermal resistance was also adjusted using equation (5.3.1), with the constant n given as

$$n_{he} = \frac{\ln\left(\frac{R_{tot,t}}{R_{tot,actual}}\right)}{\ln(Ra_e)} = \frac{\ln\left(\frac{R_{he,t}}{R_{tot,he}}\right)}{\ln(Ra_{he})} = \frac{\ln\left(\frac{0.0042}{0.00850}\right)}{\ln(458213314.64)} = -0.03504 \quad (5.3.4)$$

Substituting n in equation (5.3.1) with the calculated n_{he} from equation (5.3.4), the actual total thermal resistance used in the theoretical model for the heat exchanger line is

$$R_{tot,actual,he} = R_{he,t} Ra_{he}^{-n_{he}} = 0.0042 (458213314.64)^{0.0354} = 0.00853 \text{ K/W} \quad (5.3.5)$$

The experimentally adjusted values of the total thermal resistance $R_{tot,actual,acc}$, and $R_{tot,actual,he}$ were used in the theoretical model to simulate the WHRS loop temperatures. Results are given in section 5.3.2. It was noticed that, the heat input to the system greatly influences the flow variables of the system such as the working fluid mass flow rate \dot{m}_{wf} and the dynamic viscosity μ . These variables are captured in the Reynolds number. The Reynolds number as a function of the working fluid mass flow rate is

$$Re = \frac{4\dot{m}_{wf}}{\pi\mu d} = \frac{4}{\pi\mu d} \frac{\dot{Q}_{in} - \dot{Q}_{loss}}{h_{fg}} \quad (5.3.5)$$

In equation (5.3.5), the terms $\dot{Q}_{in} - \dot{Q}_{loss}$ represents the heat removed from the system by the air-cooled condenser $\dot{Q}_{acc} = \dot{Q}_{in} - \dot{Q}_{loss}$ and/or the heat exchanger $\dot{Q}_{he} = \dot{Q}_{in} - \dot{Q}_{loss}$. The h_{fg} is the latent heat of vapourisation. It is seen that if the heat input to the system increases the mass flow rate increases proportionally and therefore the Reynolds number increases. Figure 5.3(a) shows how the heat exchanger and the air-cooled condenser thermal resistances (used in the adjusted theoretical model) change as a function of the Reynolds numbers. For improved clarity of figure 5.3(a), especially for Reynolds numbers ≥ 3000 , the heat exchanger and the air-cooled condenser heat transfer rates per degree are given in figure 5.3(b).

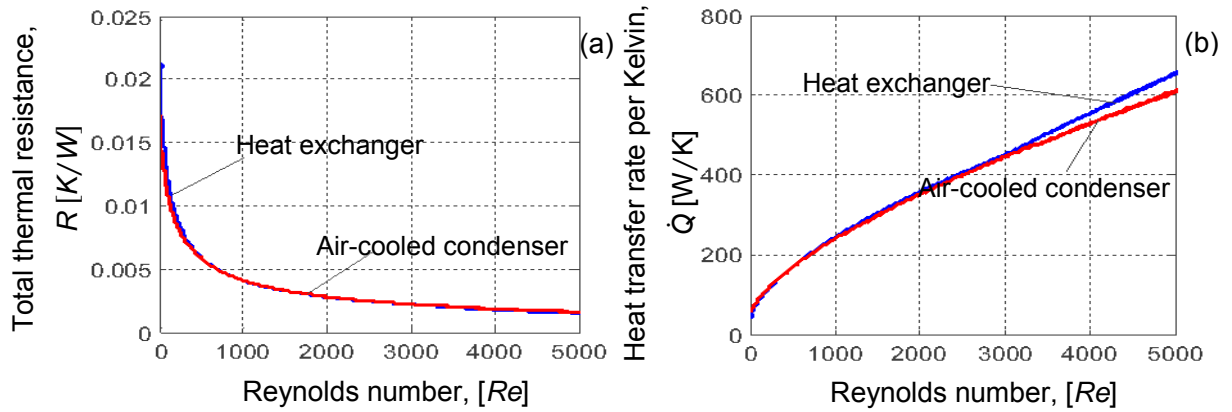


Figure 5.3: Heat exchanger and air-cooled condenser: (a) total thermal resistance, (b) heat transfer rate per degree unit

5.3.2 Results

Figure 5.4 shows a typical single to two-phase mode experimental, e , and theoretical, t , set of results for the air-cooled condenser. Figure 5.4(a) shows the air-cooled condenser working fluid and coolant inlet and outlet temperatures, $T_{acc,in}$, $T_{acc,out}$, $T_{acc,air,in}$ and $T_{acc,air,out}$ as a function of time. Figure 5.4(b) shows the inlet and outlet cooling jacket fluid temperatures, $T_{cj,in}$ and $T_{cj,out}$ and the fuel tank wall temperatures, $T_{w,ft}$ as a function of time.

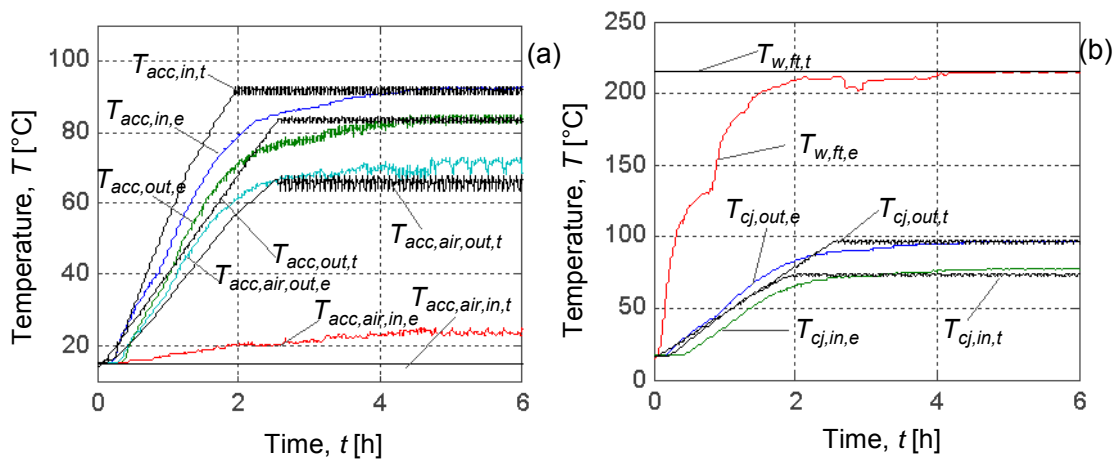


Figure 5.4: Single to two-phase mode: (a) air-cooled condenser temperatures, (b) fuel tank wall and cooling jacket temperatures.

Figure 5.4(a) shows that, the $T_{acc,in,e}$ increases rapidly to 80 °C within 2 hours. Thereafter the temperature increases slowly to 92 °C after 4 hours when steady state is reached. Its corresponding predicted value $T_{acc,in,t}$ reached a steady state 2 hours earlier because of the power input to the system that was quickly removed from the system by the air-cooled condenser. The air-cooled condenser was initially designed to remove from the system a power input in the range 3-6 kW. The power input to the system was set to its maximum constant value in the theoretical model, but it increased slowly during experiments. Therefore, the working fluid temperature takes a long time (2 hours) to reach its saturation temperature in the experimental results. The $T_{acc,air,e}$ increases from 15 °C to 24.35 °C, because the

thermocouples used to measure $T_{acc,air,e}$ were situated in an environment that was affected by the radiation heat ($\dot{Q}_{rad} = (\bar{T}_{acc} - \bar{T}_{air})/R_{rad} = 95 \times 10^{-9} W$) from the air-cooled condenser fins.

The $T_{acc,air,out,e}$, increases to 63 °C after 2 hours, and then to 69 °C after 5 hours. The corresponding predicted temperature $T_{acc,air,out,t}$ is close to $T_{acc,air,out,e}$ with a difference of approximately 5 °C. At the air-cooled condenser outlet the pressure is at its lowest, but it gradually increases up to a maximum point and manifests itself as an oscillating temperature with an amplitude of 1 °C: the amplitude of oscillation increases up to 6 °C in the experimental results. In the theoretical model the air-cooled condenser outlet working fluid oscillates with a maximum amplitude of oscillation of 2 °C. These temperature oscillations are due to the condensing process described by the fact that when the fluid condenses in the condenser, energy is taken out of the system, therefore the fluid temperature decreases. Then, after, energy in a form of latent heat of vaporisation is brought back into the condenser from the cooling jacket, the temperature increases again. The experimental amplitude of oscillation of the working fluid at the outlet of the air-cooled condenser is greater than its corresponding theoretical value due to sub-cooling. The theoretical model did not make provision for sub-cooling, only bulk boiling.

Figure 5.4(b) shows that the cooling process of the fuel tank is sustained by the bulk fluid temperature at the inlet $T_{cj,in,e}$ and outlet $T_{cj,out,e}$ points of the cooling jacket, it keeps $T_{w,ft,co,e}$ at about 215 °C. The $T_{cj,in,t}$ and $T_{cj,out,t}$ were predicted accurately. This shows that although when operating at red hot conditions the incoloys heating element can reach 650 °C, the cooling process undertaken by the presence of water in the cooling jacket keeps the fuel tank temperature around 215 °C. This is due to heat removed from the system by the air-cooled condenser. These results show that, by keeping the temperature of the fuel tank wall around 215 °C, its cooling process is achieved.

Figure 5.5(a) shows the predicted and the calculated single to two-phase operating mode mass flow rate as a function of time. In the experimental model the pressure difference within the system between the heating and cooling section characterised the fluid driving force, and hence defined the mass flow rate calculated in terms of the power input and the fluid properties at the inlet and outlet points of the heating section (see equation (5.3.5)). It is seen that the predicted mass flow rate $\dot{m}_{wf,t} = 38.32176 g/s$ (see Appendix C.2.1.2) as calculated from equation (3.4.23) increases rapidly to its maximum steady state value after 2.5 hours. The experimentally calculated mass flow rate $\dot{m}_{wf,e} = 34.6754 g/s$ (see Appendix C.2.2) increases slowly to its maximum steady state after 4.5 hours. This is because the theoretical model set the power input to the system to its maximum value, while in the experimental model the power was gradually supplied to the heating elements. The result of this is that boiling starts earlier in the theoretical model than in the experiments.

Figure 5.5(b) shows the experimental and theoretical heat transfer rates as a function of time for the air-cooled condenser line. The accurately predicted electrical energy input to the

system $\dot{Q}_{elek} = \dot{Q}_{in} = V_{sup}^2 / R_{elek} = 3008.333 \text{ W}$ is balanced by the heat output from the system through the air-condenser $\dot{Q}_{acc,e} = 2386.92 \text{ W}$ and the experimentally calculated power lost in the system $\dot{Q}_{loss} = \dot{Q}_{elek} - \dot{Q}_{acc} = 621.413 \text{ W}$. These results show that the heat added to the system by the heating elements through the fuel tank walls is carried out of the system by the air-cooled condenser, excluding some losses from the interconnecting pipe-work. There is still a slight difference between the power input to the system and the heat removed from the system plus the calculated heat lost ($\dot{Q}_{acc} + \dot{Q}_{loss}$) = 2752 W. This is explained by the fact that other possible heat lost from the system, such as the heat lost by the system through its support structure, was neglected. The system's losses of heat through its support structure is due to the heat transfer mechanism, such as conduction from the cooling jacket to the support and then convection from the support to the environment.

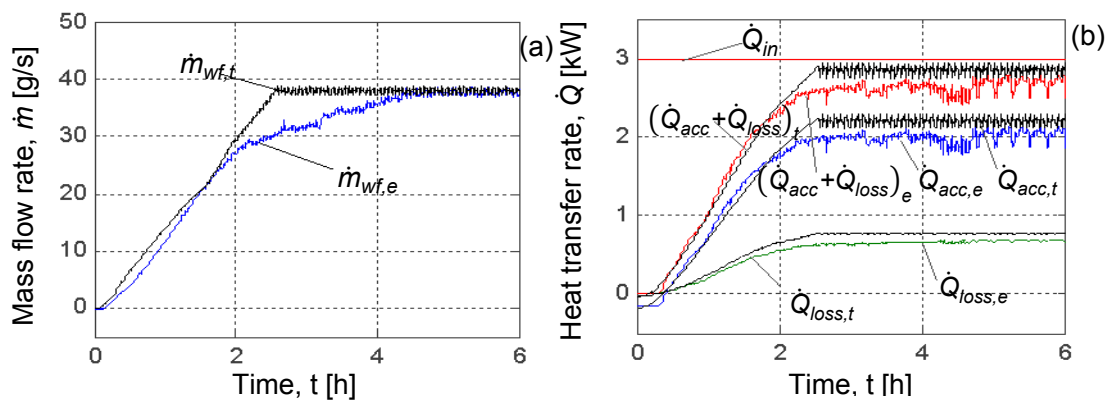


Figure 5.5: Single to two-phase mode for air-cooled condenser line: (a) mass flow rate, (b) energy balance

Figure 5.6 shows a typical set of single to two-phase mode experimental and theoretical results for the heat exchanger line. Figure 5.6(a) shows an accurately predicted temperature rise of the working fluid in the heat exchanger. The $T_{he,in,e}$ increases rapidly to a maximum temperature of 92 °C after 2.585 hours, thereafter it decreases slightly to 90 °C after a further 2.625 hours. It is constant around 90 °C for about 50 min and then drops by 1 °C when steady state is reached around 89 °C in the top section of the heat exchanger. The $T_{he,in,t}$ increases in the same range as $T_{he,in,e}$, but reaches steady state around 90 °C, one hour earlier than $T_{he,in,e}$. The $T_{he,in,e}$ and $T_{he,in,t}$ oscillate steadily, with an oscillating amplitude of 1 °C and 1.25 °C, respectively. The $T_{he,out,t}$ and $T_{cw,out,t}$ are accurately predicted and they oscillate around 61 °C and 33 °C with an oscillating amplitude of 3 °C and 2 °C, respectively, due to the mass flow rate oscillation.

Figure 5.6(b) shows that, the cooling process maintains $T_{w,ft,e}$ around 193.54 °C. The $T_{cj,in,t}$ and $T_{cj,out,t}$ were accurately predicted. They reach steady state earlier than $T_{cj,in,e}$ and $T_{cj,out,e}$. These results show that cooling the fuel tank by the heat exchanger keeps its temperature below 215 °C, when steady state is reached, as in the air-cooled condenser. This is due to a good average heat transfer coefficient of the heat exchanger compared to the air-cooled

condenser. When steady state is reached a maximum amount of heat is added to the system. This offers much better cooling of the fuel tank.

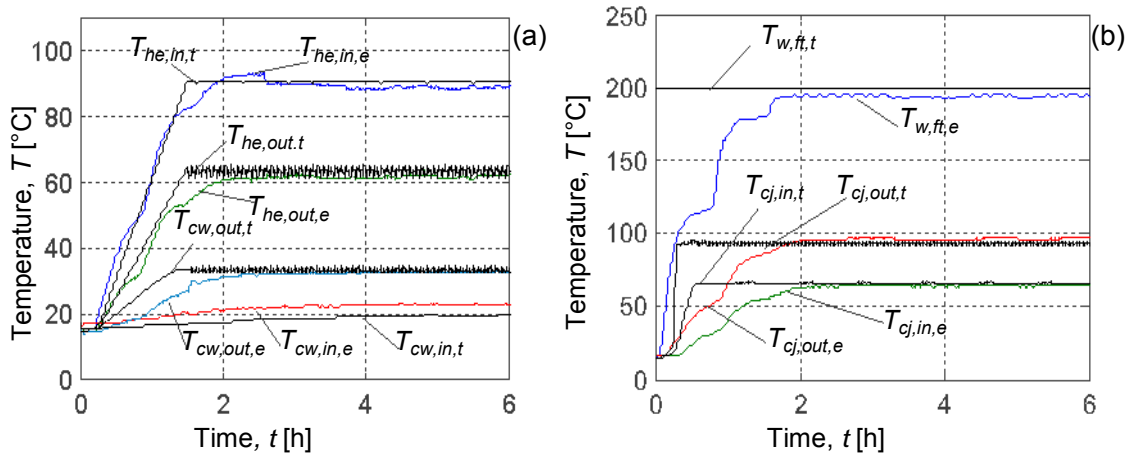


Figure 5.6: Single to two-phase mode heat exchanger line: (a) heat exchanger temperatures, (b) fuel tank wall and cooling jacket temperatures

Figure 5.7(a) shows the predicted and the calculated mass flow rates as a function of time. The predicted mass flow rate $\dot{m}_{wf,t} = 39.1645 \text{ g/s}$, calculated from equation (3.4.23), increases rapidly to its maximum steady state value after 2.8 hours. The experimentally calculated mass flow rate increases less rapidly to its maximum steady state of $\dot{m}_{wf,e} = 40.0341 \text{ g/s}$ after 4 hours. Before steady state is reached, the theoretical and experimental calculated mass flow rates converge to the same values and increase with the same slope after 1.675 hours for about 1.078 hours. This is due to a well-predicted heat transfer coefficient that allows heat removal in the range of 2.0 to 2.1171 kW in both the theoretical and experimental cases as seen in figure 5.7(b).

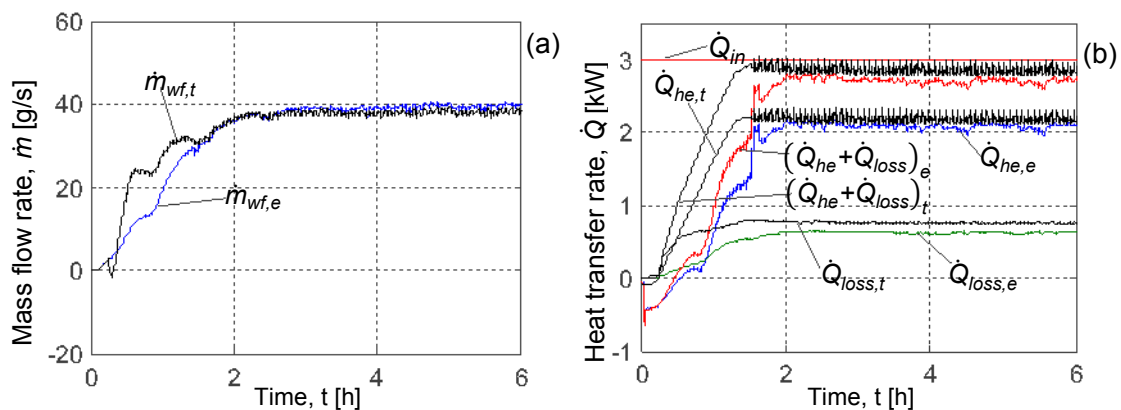


Figure 5.7: Single to two-phase mode for heat exchanger line: (a) mass flow rate, (b) energy balance

The $\dot{m}_{wf,t}$ oscillates early, with an oscillation amplitude of 0.1 g/s after 50 min. Thereafter, the oscillation amplitude increases to 2.2012 g/s after 2.6221 hours. This sudden larger increase of the oscillation amplitude shows a nett transition from single to two-phase flow. The $\dot{m}_{wf,e}$ oscillation with an amplitude of 1.0451 g/s starts 1.848 hours after $\dot{m}_{wf,t}$. There may be three

reasons for the late $\dot{m}_{wf,e}$ oscillation. The first is the gradual power input to the system. The second is the liquid carried over in the vapour-liquid mixture flow. The third is the change in water level in the heat exchanger caused by the vapour-liquid mixture that condenses. This will cause the heat exchanger inlet thermocouple to be periodically immersed in hot water from the cooling jacket and then cooler water rising from the heat exchanger.

Figure 5.7(b) shows the heat exchanger line heat transfer rates as a function of time, calculated from theoretical and experimental results. It is seen that an accurate prediction of how the energy input to the system $\dot{Q}_{elek} = \dot{Q}_{in} = V_{sup}^2 / R_{elek} = 3008.33313 \text{ W}$ is balanced by the action of the heat output from the system through the heat exchanger $\dot{Q}_{he,e} = 2113.92001 \text{ W}$ and the heat lost in the system $\dot{Q}_{loss} = \dot{Q}_{elek} - \dot{Q}_{he} = 623.37103 \text{ W}$. There is still a slightly difference between the power input to the system and the heat removed from the system plus the calculated heat lost $(\dot{Q}_{he} + \dot{Q}_{loss}) = 2737.33113 \text{ W}$. This is for the same reason of additional heat lost from the system as explained in the previous paragraph. It is also seen that, the power output from the system by the water-cooled condenser is negative for the first 30 min. This is because when the process starts, depending on the cooling water mass flow rate, more heat is removed from the system than it is added. Although the same amount of heat is added by the heating element to the system through the cooling jacket, for the first 30 min the power output of the system is negative. These results show that the heat added to the system is recovered by the heat exchanger through the cooling water at a temperature of 36 °C.

In heat pipe operating mode, when the heat input is approximately the same as the heat output, the working fluid boils, and at the same time the vapour saturation temperature increases far from the temperature at the vapour liquid interface, hence increasing the system pressure, while the density of the working fluid decrease at the heat source. Simultaneously, some of the vapour is condensing, and therefore increasing the density of the working fluid at the heat sink. The difference in the density of the working fluid between the heat source and the heat sink generates a buoyancy force, causing a positive flow rate of the working fluid and sending the cooler liquid from the heat sink back to the heat source. This will cause boiling to cease temporarily. Then, after some time, the temperature of the working fluid will increase up to the boiling point, and the cycle continues with the temperature and the pressure continually rising. Depending on the heat transfer rate of the heat source and sink, vapour generation and condensation will be approximately equal, and the system pressure and temperature will stabilise.

Figure 5.8 shows the heat pipe operating mode experimental and theoretical results for a 75% working fluid fill ratio using the air-cooled condenser line. When the loop is filled at 75% filling ratio the level of the working fluid is slightly above the cooling jacket. The fuel tank is entirely emerged in the working fluid. As seen in figure 5.8(a), results indicate that the $T_{acc,out,t}$ and $T_{acc,air,out,t}$ predict well the experimental corresponding values $T_{acc,out,e}$ and $T_{acc,air,out,e}$, respectively.

At steady state, the air cooled condenser outlet working fluid and coolant converge to the same values of 83 °C and 86 °C for the theoretical and experimental results. This is because the average heat transfer coefficient of the air-cooled condenser is much better in two-phase than in single and single to two-phase flow. Looking at figure 5.8(b) it is noticed that a good overall heat transfer coefficient for the air-cooled condenser in heat pipe operating mode accurately predicts $T_{cj,out,t}$ and $T_{cj,in,t}$. This result keeps $T_{w,ft,e}$ around 193.84 °C. This is an improvement in the fuel tank cooling temperature compared to the single and single to two-phase operating mode.

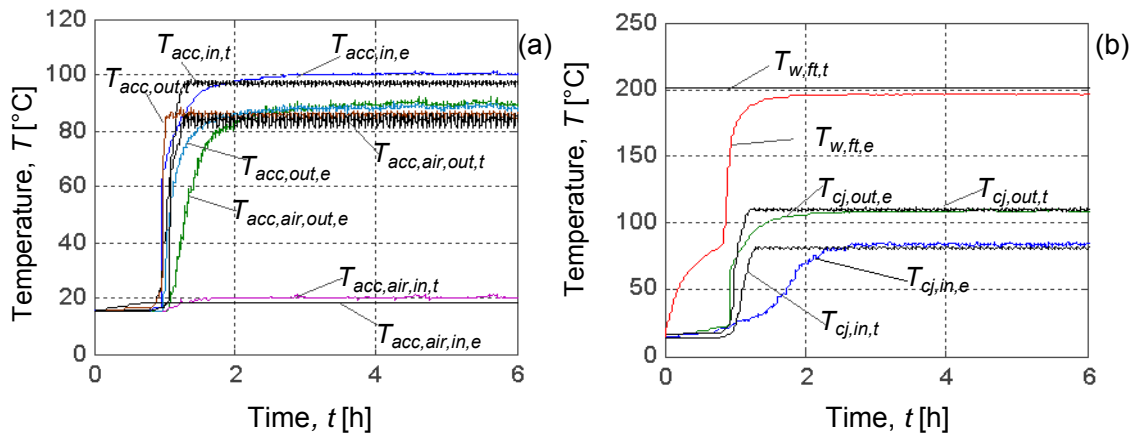


Figure 5.8: Heat pipe mode with loop filled with 75% of working fluid: (a) air-cooled condenser temperatures, (b) fuel tank wall and cooling jacket temperatures

Figure 5.9 shows that the heat transfer coefficient is much better in the heat pipe operating mode. The calculated mass flow rates increase and reach steady state fast as seen in figure 5.9(a). The heat transfer process takes place rapidly in two-phase due to a high heat transfer rate, dictated by a good heat transfer coefficient. This is also the reason why the mass flow rates are high and the calculated power well balanced in the system as shown in figures 5.9(a) and 5.9(b), respectively. In the time range 1 to 2 hours the predicted mass flow rate increases rapidly compare to experimental mass flow rate. This is again due to the gradual increase in the power for the experiments, as also outlined in previous paragraphs.

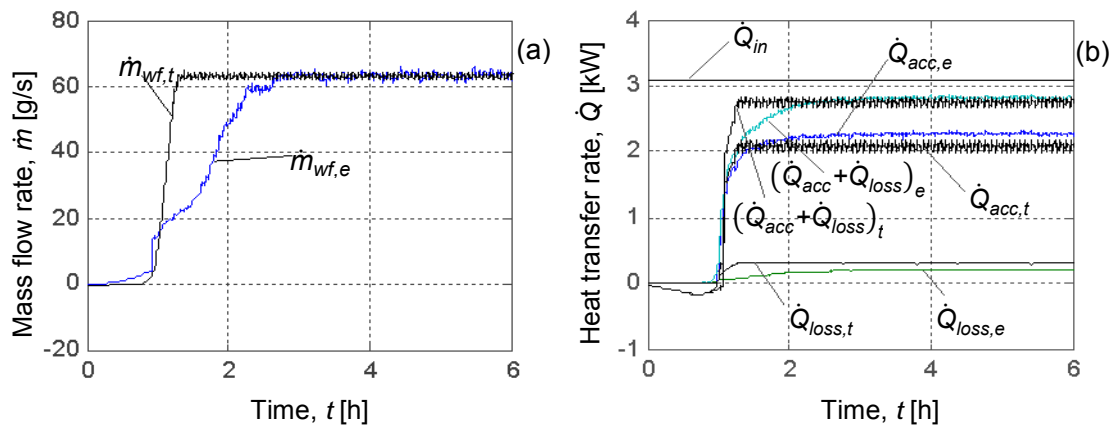


Figure 5.9: Heat pipe mode with loop filled with 75% of working fluid air-cooled condenser line: (a) mass flow rate, (b) energy balance

Figure 5.10 shows experimental and predicted results of a typical set of heat pipe operating mode heat exchanger line temperatures for a 75% working fluid filling ratio. For clarity, figure 5.10(a) showing the heat exchanger set of temperatures as a function of time, is split in figure 5.10(b) and figure 5.10(c). Figure 5.10(b) shows the heat exchanger inlet and outlet working fluid temperatures as a function of time. Figure 5.10(c) shows the heat exchanger inlet and outlet cooling water temperatures as a function of time. Figure 5.10(d) shows the cooling jacket inlet and outlet working fluid and fuel tank temperature as a function of time. The heat exchanger is supplied with a steady stream of water and the electrical power is switched on. Boiling is seen to start at about 45 min after the power is switched on, as seen by the characteristic start-up mass flow rate transient of up to 400 g/s whereafter it quickly settles down to a reasonably steady 100 g/s, after the shut-off valve V_4 is closed (see figure 5.10(e)).

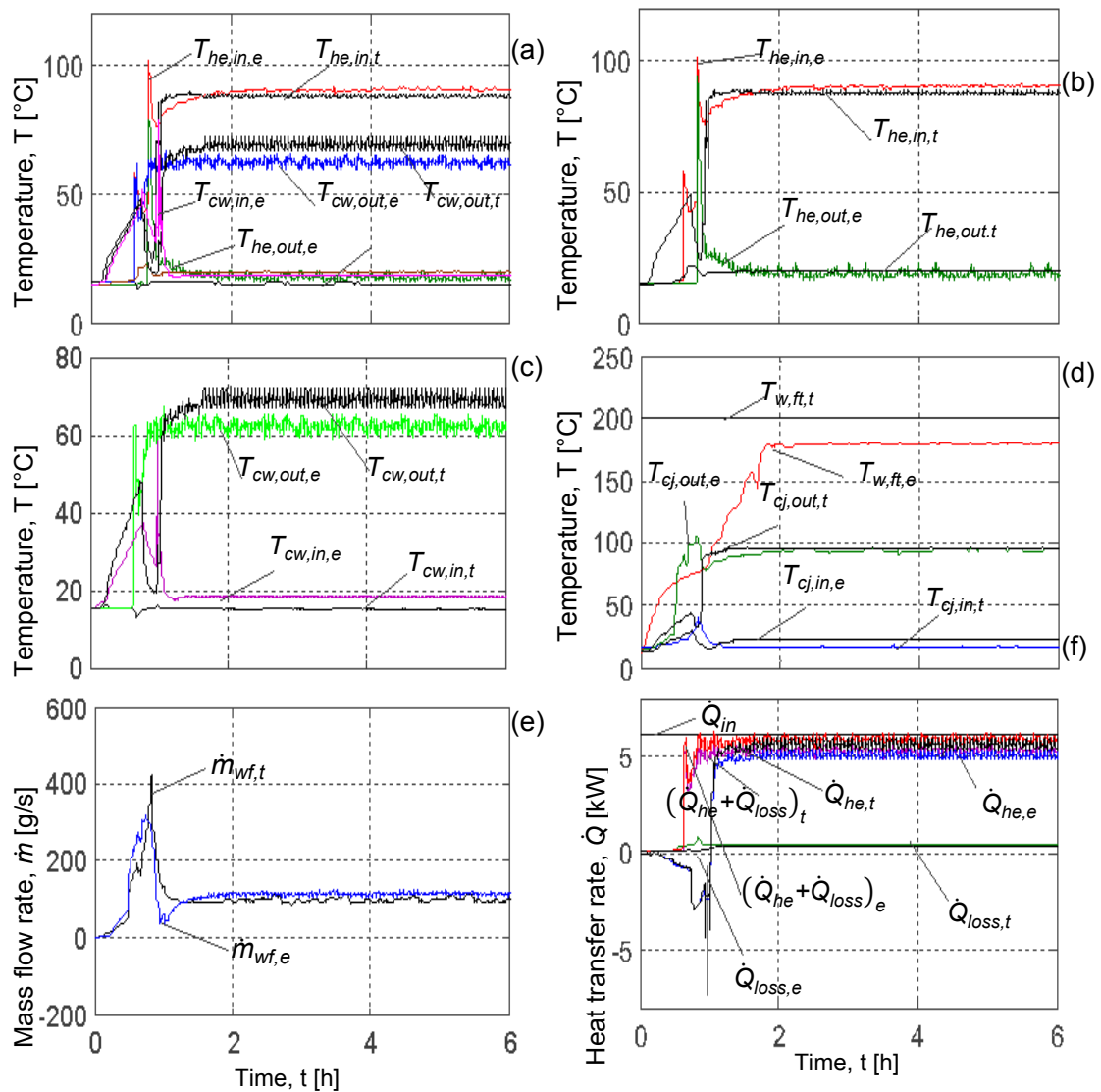


Figure 5.10: Heat pipe operating mode heat exchanger line: (a) heat exchanger temperatures, (b) heat exchanger inlet and outlet temperatures, (c) cooling water inlet and outlet temperatures, (d) fuel tank wall and cooling jacket temperatures, (e) mass flow rate, (f) power balance

As seen in figure 5.10(a), experiments indicate that when boiling starts, the inlet heat exchanger temperature increases rapidly to a maximum value of 100 °C then decreases to 78 °C before steady state is reached at 90 °C. This is because when the experiment starts, the shut-off valve for air released (V_3 , see figure 5.1) is opened to release all the air from the system by boiling. Boiling starts at 100 °C, which is the saturated temperature corresponding to the atmospheric pressure. Figures 5.10 (a), (b), (c), (d), (e) and (f) all show a reasonable correspondence between the theoretical and the experimental results. This is especially so when a steady heat pipe operating mode has been achieved.

6 Stirling engine heat exchanger experimental and theoretical results

The aim of the SE heat exchanger experiment is to verify the theoretical model that simulates the heat transferred from the heat source to the engine. In this project the heat source is the heat recovered from the fuel tank by the heat exchanger in the WHR&U system thermosyphon loop (see figure 5.1). The SE heat exchanger experimental and theoretical results will now be analysed. The experimental set-up is explained first, followed by the experimental testing procedure and an analysis investigating the most important parameters influencing the heat exchanger theoretical flow resistance and heat transfer coefficients. Thereafter, experimental and theoretical results will be presented and discussed.

6.1 Experimental setup

A photograph and a schematic diagram of the SE heat exchanger experimental set-up assembly are shown in figures 6.1 and 6.2.

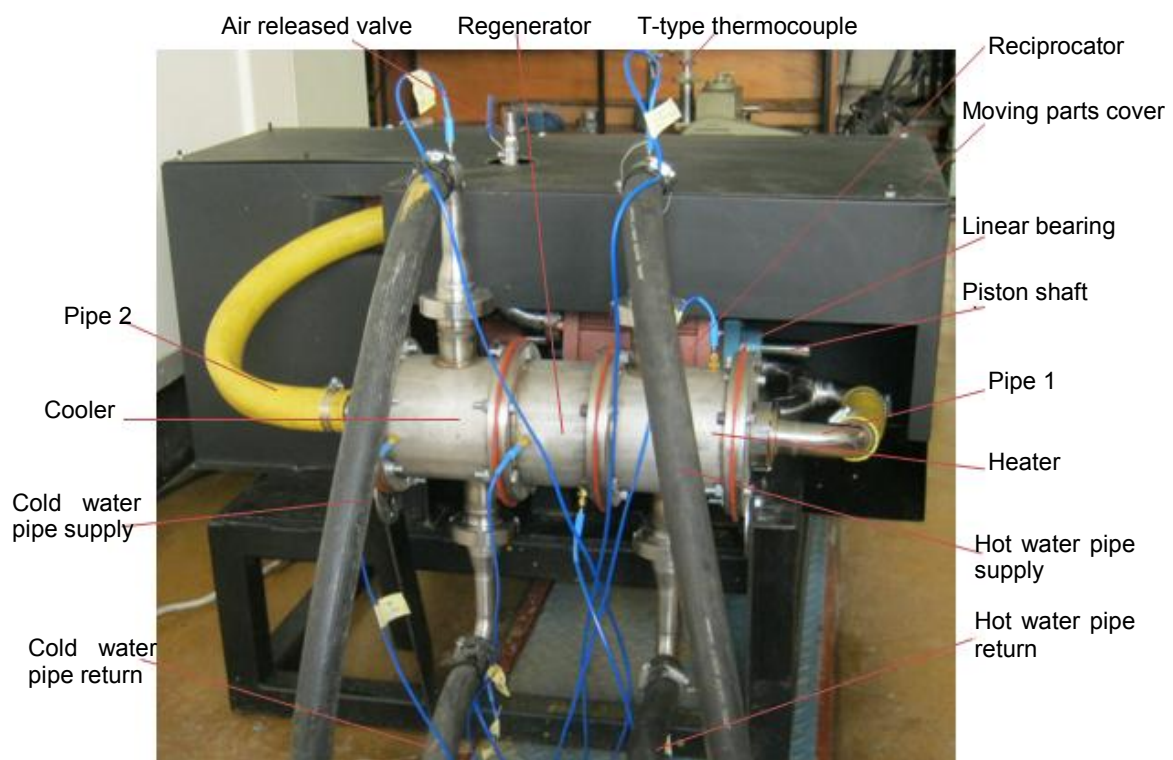


Figure 6.1: regenerative heat exchanger experimental set-up

The experimental set-up simulates the SE heat exchanger behaviour. This assembly was used to evaluate the experimental heat exchanger flow resistance and heat transfer coefficients of the SE heat exchanger. The assembly comprises a heat exchanger and a reciprocator. In addition to the heat exchanger design, the reciprocator was designed to simulate the SE oscillating flow behaviour through the heat exchanger.

The reciprocator displaces air back and forth through the heater's inner copper pipe wire matrix (60-mesh) where it exchanges heat with hot water. The hot water is supplied to the heat exchanger by the hot water pipe supply (see figure 6.1). After exchanging heat with the air, hot water exits the heat exchanger through the hot water pipe return. The heated air leaving the heater enters the hot side of the regenerator at an average temperature of $\bar{T}_h = (T_{h,i} + T_{h,o})/2$. The hot air releases heat to the 60-mesh copper wire matrix in the hot side of the regenerator. The hot side wire matrix absorbs heat from air at a temperature $T_{r,h}$, as the air moves through the regenerator to the cold side. The regenerator cold side wire matrix absorbs heat from the air before it moves to the cooler at an average temperature of $T_{r,c}$. In the cooler, heat is absorbed from the air by the cold water. The cold water at $T_{c,i}$ is supplied to the cooler by the cold water supply pipe and leaves the heat exchanger at a temperature $T_{c,o}$. The cold air from the cooler moves to the compression space to complete its first cycle. During the second cycle, the cold air leaves the compression space at a temperature T_{co} as it enters the cooler. In the cooler, the energy that the air had received in the compression space due to compression is absorbed and rejected to the cooling water. The cold air at an average temperature of $\bar{T}_c = (T_{co} + T_{r,c})/2$ leaves the cooler and then moves to the cold side of the regenerator. The regenerator cold side wire matrix rejects heat back to the air at a temperature $T_{r,c}$. As the air moves through the regenerator, more heat is transferred back to the air. The air then leaves the regenerator hot side at the temperature $T_{r,h}$ and enters the heater where it is heated again by the hot water. The heated air at an average temperature of \bar{T}_h enters the expansion space at T_e to complete the cycle.

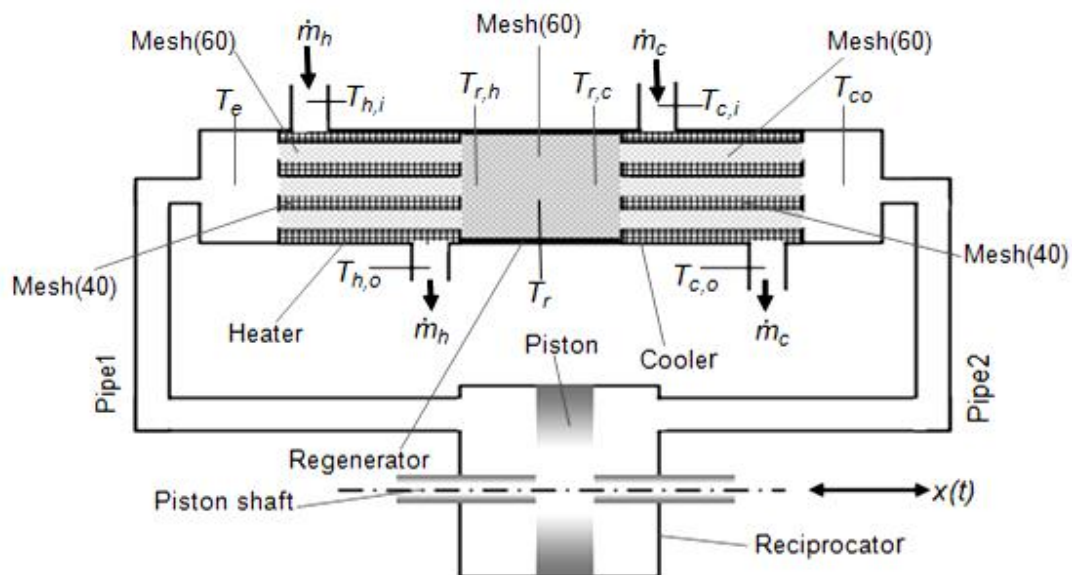


Figure 6.2: Schematic diagram of regenerative heat exchanger experimental set-up

6.1.1 Heat exchanger

The heat exchanger is a heater-regenerator-cooler assembly. The heater and cooler were manufactured and assembled in the same configuration. The heater and cooler are made of a grade 304 stainless steel shell tube of 133 mm external diameter, 135 mm length and 5 mm wall thickness (see figure 6.3). The shell tube contains 10 copper pipes of 20 mm internal

diameter, 100 mm length and 1 mm wall thickness. The copper pipes are arranged in a staggered configuration of 32 mm longitudinal pitch and 16 mm transversal pitch through brass flanges of 130 mm diameter and 3 mm wall thickness. Each copper pipe of the heat exchanger is filled with 303 laminating screens of 60-mesh woven copper wire, while the space surrounding the pipes of same length as the copper pipes in the shell tube with 191 laminating screens of 40-mesh woven copper wire. All the woven wire mesh laminating screens holes in the heat exchanger are offset relatively to each other, so as to ensure a well-mixed flow. In the heater and cooler, the woven wire mesh laminating screens are held together by two circlips at the end of each copper pipe and by brass flanges in the shell tubes. Depending on the direction of the flow, distributing space on one side and collecting space on the other side were provided in the heater and cooler, respectively. It is for this reason that the heater and cooler copper pipes length are 35 mm smaller than the shell tube length. The brass flanges and the collecting and/or distributing spaces are air-sealed with rubber O-rings. The O-ring is held against the shell tube by a high-temperature-resistant plastic spacer of 120 mm internal diameter, 35 mm length and 5 mm wall thickness.

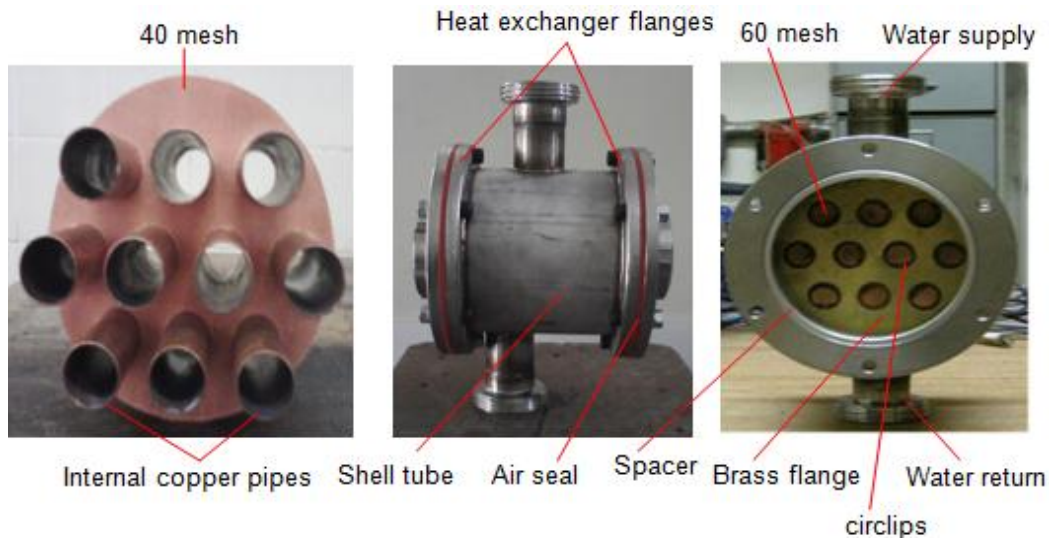


Figure 6.3: Heater and cooler details

The regenerator is made of a grade 304 stainless steel tube of 125 mm internal diameter, 100 mm length and 7.5 mm wall thickness. The regenerator is filled with 303 60-mesh offset woven copper wire laminating screens. The heater, cooler and regenerator flanges are bolted together with M8 stainless bolts. All flanges have a 40-durometer, peroxide cured, and high-temperature-resistant silicone rubber compound gasket sandwiched between them. The heat exchanger is fitted to the assembly support with M8 bolts, through a bracket.

6.1.2 Reciprocator

To test the heat exchanger, a reciprocator simulating the SE oscillation flow through the heat exchanger was designed, constructed and manufactured. The reciprocator was made using a stainless steel pipe of 300 mm internal diameter, 180 mm length and 10 mm wall thickness and containing an aluminium piston of 300 mm diameter and 45 mm width (see figure 6.4). The reciprocator piston was designed to displace 4 litres of air through the heat exchanger at

a maximum operating frequency and pressure of 40 Hz and 300 kPa, respectively. The piston shaft is supported by the reciprocator closures through two SKF YAR2082F linear bearings. The closure flanges and reciprocator cylinder are bolted together with M8 mild steel bolts.

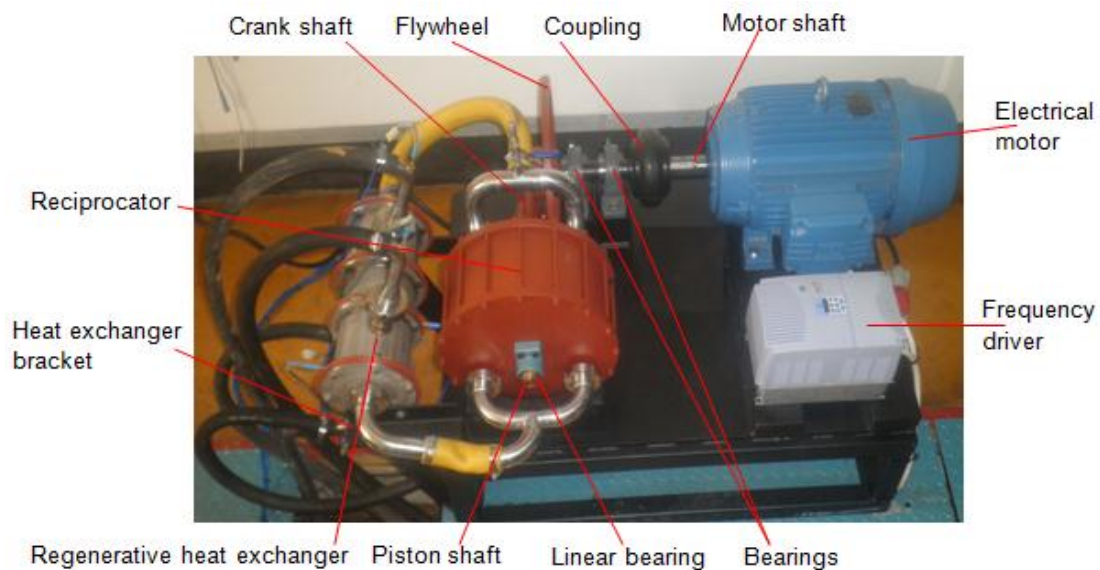


Figure 6.4: Reciprocator view assembly

The linear motion of the piston shaft is obtained using an eight pole, 380 V/ 415 V or 525 V, three-phase, 50 Hz and 7.5 kW squirrel cage electrical motor (Weg made in Brazil, permit number: 4754/6862) through a crankshaft mechanism, mechanically linked to the flywheel. The flywheel shaft is supported by two SKF SYK40TR bearings fitted in housing units, and mechanically linked to the electrical motor shaft through an Arpex ARF-6 coupling. The crankshaft then converts the angular motion received from the flywheel into a linear motion directly transmitted to the piston shaft through a connector.

6.2 Heat exchanger testing experimental procedure

The heat exchanger testing was conducted according to the following procedure. Check and ensure that any moving parts are intact and secure the moving parts cover. Ensure there is no leakage from the system and all water pipes are well clamped. This check is to be done with cold water. Check that all hot water pipes are double-clamped. Attend to any possible system water leaks. Check all the cover connections on the structure support before commencing the operation. Check that the levels of water in the cold and hot water supply reservoirs are filled to capacity. Check that the valves supplying water in all other laboratories from the same reservoirs are all closed. With cold water, check that, there is no leak in the water supply and return lines (especially on the hot water side). Fully open all return valves. Open, half-way all supply valves to overcome the pressure that may build up in the water system. Switch on all water pumps. Then set the hot water temperature to the desired temperature. Switch on the electrical motor. Set the desired frequency for a specific test. All temperature measurements were made using T-type thermocouple. The thermocouple signals are converted into temperature using a Hewlett Packard 34970A data logger serial number MY41116811 and a computer. The pressure measurements were taken using an Endress+Hauser deltabar

PMD230-CU1B2ED1A, serial number 6FQ0142 pressure transducer; while the mass flow rates were measured using a Festo MS6-SFE flow sensor.

6.3 Heat exchanger theoretical model adjustment

In order to validate the SE heat exchanger theoretical model that predicts the engine thermo-flow characteristics, an experimental investigation was conducted. The heat exchanger experimental investigation was conducted in a preliminary phase, which gives results from unidirectional flow data measurements, and then a main testing phase from which results from fluctuating flow data measurements were obtained. Results obtained from the preliminary phase of experiments were used to adjust the theoretical model that predicts the heat exchanger heat transfer coefficients and pressure drops. A description of how the theoretical model was adjusted to simulate the experiments is now presented.

During the preliminary phase of experiments results of which are shown in section 6.4, a deviation of the predicted results compared to the experimental results was noticed. This deviation was due to the fact that, for an enhanced-fin heat exchanger, especially when woven wire mesh is used, there is little published work available and little progress has been made in attempts to analytically or numerically predict the heat transfer coefficient and friction factor. There are no rules for selecting the appropriate heat transfer coefficient and friction factor correlations. Therefore, in order to gauge experimental data, the theoretical result was adjusted so that it simulated the heat exchanger. This was undertaken by identifying the most important parameters affecting the theoretical results. It was found that the exchanger heat transfer coefficient and friction factor are affected by the flow and geometrical variables (see section 4.3). The most important flow variables affecting the theoretical results are the air velocity, the viscosity, the density, the thermal conductivity and the specific heat. The geometrical variables affecting the theoretical results are the heat transfer area, the diameter of the exchanger tubes, the number of tubes, the transversal tube pitch, the longitudinal tube pitch, the tube layout, the woven wire mesh characteristics, and the mesh layout. In a compact heat exchanger, a large heat transfer area to the exchange volume ratio will increase the performance of the heat exchanger. A woven wire matrix having a large surface area to the volume ratio and high effective thermal conductivity results in a very effective heat transfer area.

The analysis of the flow and geometrical variables affecting the heat exchanger performances has led to seeking the most important dimensionless parameters affecting the theoretical results. It was found that the most important dimensionless parameters affecting the heat exchanger performance are the porosity, the fins efficiency and the Prandtl number. The porosity captures all geometrical variables and the Prandtl number all flow variables, while the fins efficiency bridges between the flow and geometrical variables. Referring to equation (4.3.44) it was seen that the effect of the porosity, the fin efficiency and the Prandtl number may be captured in the heat exchanger thermal resistance. It was found that change in the Prandtl number and the fin efficiency had a smaller effect on the heat exchanger thermal

resistance. The most important parameter affecting the exchanger thermal resistance is the porosity. It was then convenient to investigate how changes in the porosity affect the heater, cooler and regenerator thermal resistances. Based on the findings of the above investigation, the heater, cooler and regenerator porosities were adjusted so that the theoretically determined heat exchanger thermal resistances and friction factors simulate the experimentally determined thermal resistances and friction factors respectively.

The heater porosity $\varepsilon_h = 0.37241$ (see Appendix C.3.1.6), the computer simulation temperatures and the heater thermal resistance $R_{h,t} = 1.45901 \times 10^{-4} \text{ K/W}$ (see Appendix C.3.6) give the heat transferred from the hot water to the air $\dot{Q}_{a,h,t} = (\bar{T}_{hot} - \bar{T}_{hot,g})/R_{h,t} = 52679.92014 \text{ W}$. Similarly, the cooler and regenerator porosities $\varepsilon_c = 0.37241$ and $\varepsilon_r = 0.34412$ respectively, the cooler and regenerator theoretically determined thermal resistances $R_{c,t} = 1.48201 \times 10^{-4} \text{ K/W}$ and $R_{r,t} = 8.03101 \times 10^{-6} \text{ K/W}$, respectively, gave the heat transferred from the air to the cold water (see equation (4.3.46)) $\dot{Q}_{cold,t} = (\bar{T}_{cold,g} - \bar{T}_{cold})/R_{c,t} = 41045.88311 \text{ W}$ in the cooler and from the air to the wire matrix $\dot{Q}_{a,r,t} = (\bar{T}_{r,g} - \bar{T}_{r,m})/R_{r,exp} = 5493.13113 \text{ W}$ in the regenerator (Newton law of cooling). Their corresponding experimentally calculated heat transfer rates, based on the conservation of energy equation for the hot and cold water through the heater and cooler, are $\dot{Q}_{a,h} = 13786.67704 \text{ W}$ and $\dot{Q}_{a,c} = 10536.24122 \text{ W}$, respectively (see Appendix C.3.3). The experimentally calculated heat transfer rate based on the conservation of energy equation for the air between the regenerator hot side and cold side is (this is should be equal to the heat absorbed in the wire matrix) $\dot{Q}_{a,r} = \rho_{a,r}(@\bar{T}_r)V_{a,r}\pi d_p^2 c_{p,a,r}(T_{r,h} - T_{r,c})/4 = 3063.07961 \text{ W}$ (see Appendix C.3.3). The heater, cooler and regenerator theoretically determined thermal resistances of $R_{h,t} = 1.45901 \times 10^{-4} \text{ K/W}$, $R_{c,t} = 1.48201 \times 10^{-4} \text{ K/W}$ (referring to equations (4.3.45 and 4.3.46) and $R_{r,t} = 8.03101 \times 10^{-6} \text{ K/W}$, respectively (see appendix C.3.8), are considerably smaller than their corresponding experimentally determined thermal resistances of $R_{h,exp} = 3.00011 \times 10^{-4} \text{ K/W}$, $R_{c,exp} = 2.43017 \times 10^{-4} \text{ K/W}$ and $R_{r,exp} = 1.43001 \times 10^{-5} \text{ K/W}$, respectively (see Appendix C.3.9). This means that the theoretical model used values of heat transfer coefficients in the heater, cooler and regenerator that were too high, and therefore over-predicted results. To adjust the theoretical thermal resistances, the heater, cooler and regenerator experimentally determined thermal resistances were used as reference to correlate the corrected porosity. The corrected porosity is calculated as (see Appendix C.3.10)

$$A_z \frac{0.023(\bar{\rho}\bar{x})^{0.8}(1-\varepsilon)^{0.2}(Pr)^{0.4}k}{\varepsilon(d_w)^{0.2}(\mu)^{0.8}} + \eta_{fin} A_{fin} c_p \frac{5.86(\bar{\rho}\bar{x})^{0.32}(1-\varepsilon)^{0.88}(\mu_g)^{0.68}}{(\varepsilon)^{1.2}(Pr)^{-2/3}} \frac{(d_w)^{0.32}}{L_{fin}} = \Delta \quad (6.3.1)$$

The thermal resistance parameter Δ is also given by

$$\Delta_j = \left[R_{j,exp} - \frac{\ln(d_{op}/(d_{op} - 2\Delta W_p))}{2\pi k_{cu} N_p L_p} \right]^{-1} \quad (6.3.2)$$

where, $R_{j,exp}$ is the thermal resistance experimentally determined. The mean velocity calculated from the experimental pressure drop across each heat exchanger is given by

$$\bar{x} = \sqrt{2\Delta P_j / C_{f,j} \bar{\rho}} \quad (6.3.3)$$

The experimentally calculated coefficient factor is

$$C_{f,j} = [\bar{\rho}(\pi d_p)^2 \Delta P_j] / (8m_{a,j}) \quad (6.3.4)$$

The fin efficiency η_{fin} , the mesh holes total heat transfer area A_z and the fins total heat transfer area A_{fin} are calculated as given in equations (4.3.38), (4.3.17) and (4.3.29), respectively. Although change in the fin efficiency had a smaller effect on the thermal resistance, it was more convenient to investigate the fin efficiency changes as a function of the fin length. Figure 6.5 shows how the fin efficiency varies with the length of the fin.

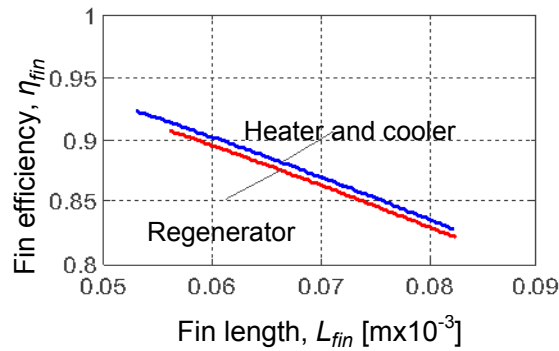


Figure 6.5: Fin efficiency as a function of the fin length

Using the corrected porosities obtained by solving equation (6.3.1), the corrected volume of the wire matrix in the heater, cooler and regenerator are calculated as

$$V_{m,j} = (1 - \varepsilon_j) V_{tot,j} \quad (6.3.4)$$

Substituting equation (6.3.4) in equation (4.3.20) and rearranging, the corrected number of screens in the heater, cooler and regenerator are calculated as

$$N_{scr,j} = \frac{4V_{m,j}}{2d_w [\pi(d_j - 2\Delta W_j)^2 - 4N_{holes,pers,j} A_{perholes,j}]} \quad (6.3.5)$$

Table 6.1 gives the corrected values of the porosity, the total volume the wire matrix or metal volume and the number of woven wire mesh laminating screens. These values were used in the theoretical model for the heater, cooler and regenerator respectively to simulate the experiment.

Table 6.1: The corrected values of the porosity, volume and number of screens

Designation	Heater	Cooler	Regenerator
Porosity	0.596	0.576	0.507
Diameter screen, d_{scr} [m]	0.0195	0.0195	0.1225
Total volume, V_{tot} [m^3]	0.0003142	0.0003142	0.00112
Metal volume, V_m [m^3]	0.0001269	0.0001018	0.0003136
Number of inner pipes, N_p	10	10	0
Number of screens, N_{scr}	1900	1980	224

6.4 Heat exchanger experimental and theoretical results

Figure 6.6 shows a typical set of experimental and theoretical results for the heat exchanger temperatures as a function of time from start-up to steady state. Figure 6.6(a) shows the heat exchanger hot and cold water experimental and predicted results, while figure 6.6(b) shows the heat exchanger air experimental and predicted results. Figures 6.6(a) and 6.6(b) show, that steady state is reached after one hour on the hot water side, and after two hours on the expansion space side. The heat exchanger temperatures on the hot side are over-predicted but under-predicted on the cold side. After applying the corrected values of porosity, as given in table 6.1, it is seen in figures 6.6(c) and 6.6(d) that the theoretical results correlate much better with the experimental results.

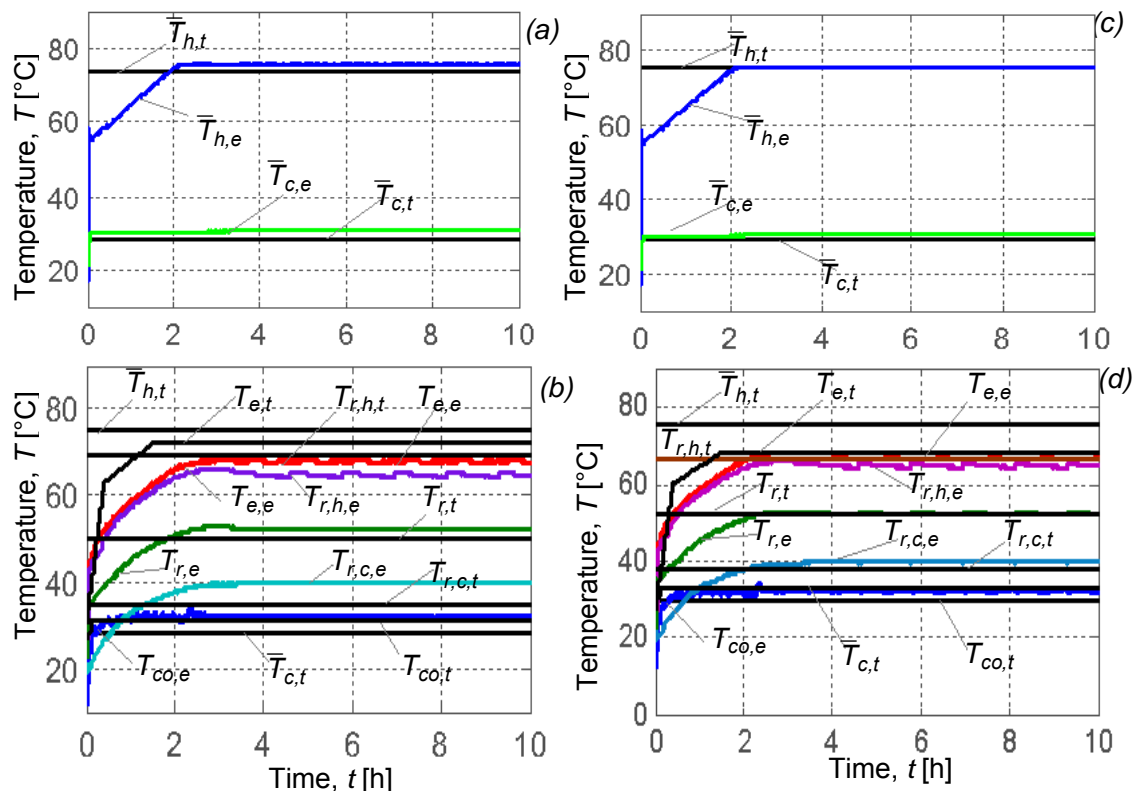


Figure 6.6: The predicted and experimental heat exchanger temperatures, from start-up to steady state: (a) hot and cold water experimental and predicted, (b) air experimental and predicted, (c) hot and cold water experimental and prediction adjusted, (d) air experimental and prediction adjusted

Figure 6.6(d) shows that after steady state is reached, the theoretical temperatures in the regenerator $T_{r,h,t}$, $T_{r,t}$ and $T_{r,c,t}$ predict their corresponding experimental $T_{r,h,e}$, $T_{r,e}$ and $T_{r,c,e}$ with a deviation of 5 °C, 3 °C and 4 °C, respectively. This is because the regenerator does not involve two distinct working fluids, such as hot or cold stream and air. Heat is transferred from the hot stream to air in the heater, and absorbed from the air to the cold water in the cooler. Hot air from the heater and/or cold air from the cooler enter the regenerator at a high and/or low temperature, and leaves at a much lower and/or higher temperature. The regenerator matrix absorbs heat from the hot air or releases it back to the cold air in a normal direction to the axial flow direction by convection. This decreases the temperature of the air

along the regenerator axial direction by conduction. The theoretical model did not take into account the axial conduction in the regenerator.

Figure 6.7 gives the heater, cooler and regenerator heat exchanger overall heat transfer coefficients as a function of the Reynolds number. As can be seen, the theoretical values for the heater, cooler and regenerator (h,t), (c,t) and (r,t), respectively, over-predicted the experimental values (h,e), (c,e) and (r,e) (see figure 6.7(a)). However, when applying the corrected porosity, it is seen that when using for the heater, cooler and regenerator corrected porosity of $\varepsilon_h=0.596$, $\varepsilon_c=0.576$ and $\varepsilon_r=0.507$ the corrected theory now better-predicts the experimental values (see figure 6.7(b)).

Figure 6.7(b) shows that, for the same Reynolds number, the overall heat transfer coefficient is much greater in the cooler than in the heater. The corrected overall heat transfer coefficients in figure 6.7(b) drop by about 12%, 10% and 2% of the overall heat transfer coefficients in figure 6.7(a) in the cooler, heater and regenerator, respectively. There are two reasons for this. The first is that the cooler metal fraction of $1 - \varepsilon_c=0.424$ is greater than the heater metal fraction of $1 - \varepsilon_h=0.404$ for the same mesh number M_i and mesh wire diameter d_{wi} product of $M_i d_{wi}=0.388$. This means, the heat transfer area in the cooler is much better than in the heater. The second reason involves the air properties. The density of air in the cooler is slightly larger than that of the air in the heater. Hence, the heat transfer coefficient is much better with heavier air than lighter air.

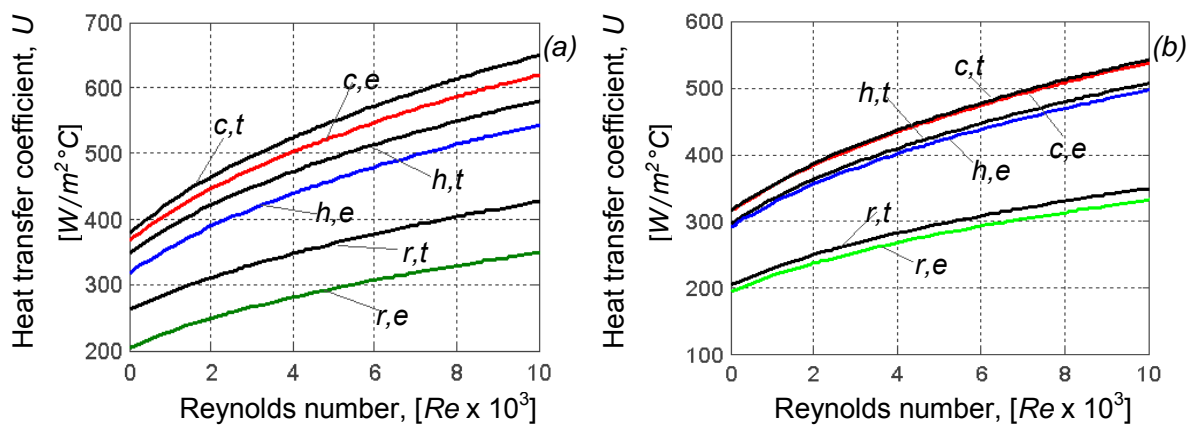


Figure 6.7: The average heat transfer coefficient as a function of the Reynolds number: (a) as measured and predicted, (b) as measured, but prediction adjusted

The experimental and predicted pressure drop across the heater, cooler and regenerator as a function of the Reynolds number are shown in figure 6.8. Figure 6.8(a) shows the pressure drop in the heater cooler and regenerator as measured and predicted. Using the corrected values for the porosity, it is seen in figure 6.8(b) that the pressure drop is now better-predicted. When comparing figures 6.8(a) and 6.8(b), it is seen that, due to the correction in the cooler, heater and regenerator porosities, the corrected pressure drops of figure 6.8(b) decrease by about 20%, 12.5% and 2.5% of the pressure drops in figure 6.8(a) for the cooler, heater and regenerator respectively. This is also due to the metal fractions reason outlined in the previous paragraph.

Figure 6.8 shows that, although designed and manufactured in the same configuration, the pressure drop in the cooler is not the same as the pressure drop in the heater, and the pressure drop in the regenerator is one-third less the pressure drop in the heater. There are two reasons for the pressure drop differences between the heater, cooler and regenerator seen in figures 6.8(a) and 6.8(b). The first reason involves the pressure loss due to the geometry of the heater, cooler and regenerator. The inlet and outlet losses of the heater and cooler increase the pressure drop in the cooler and heater, compared to the regenerator. The second reason involves the metal fraction of the heater and cooler. A high metal fraction of the cooler $1 - \epsilon_c$ compared to the heater metal fraction $1 - \epsilon_h$ means that the cooler is more porous than the heater. Therefore, the pressure drop in the cooler is higher than the pressure drop in the heater.

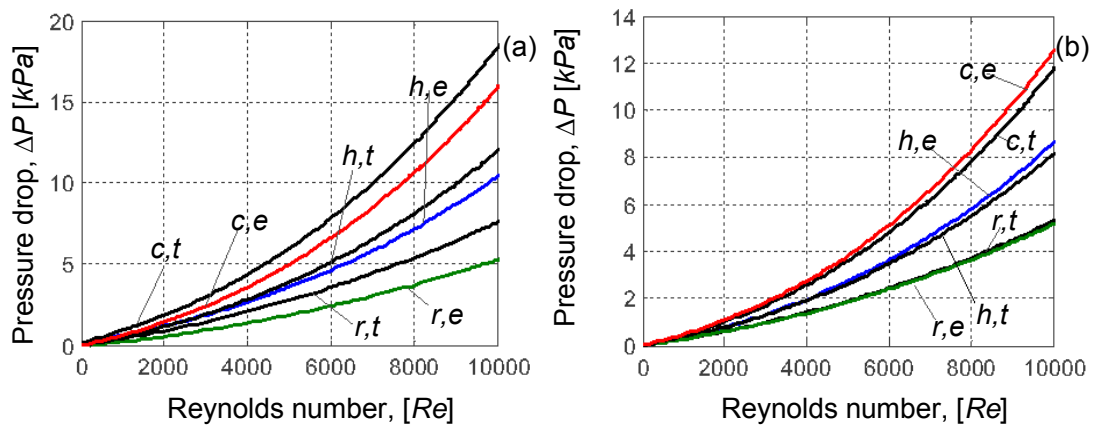


Figure 6.8: The pressure drop as a function of the Reynolds number: (a) as measured and predicted, (b) as measured, but prediction adjusted

Figure 6.9(a) gives a better-predicted friction factor as a function of the Reynolds number. Figure 6.9(b) shows a better-predicted Colburn factor as a function of the Reynolds number. It is seen that, on a logarithmic scale, the friction factors decrease almost exponentially with the Reynolds number, while the Colburn factors decrease linearly with the Reynolds number.

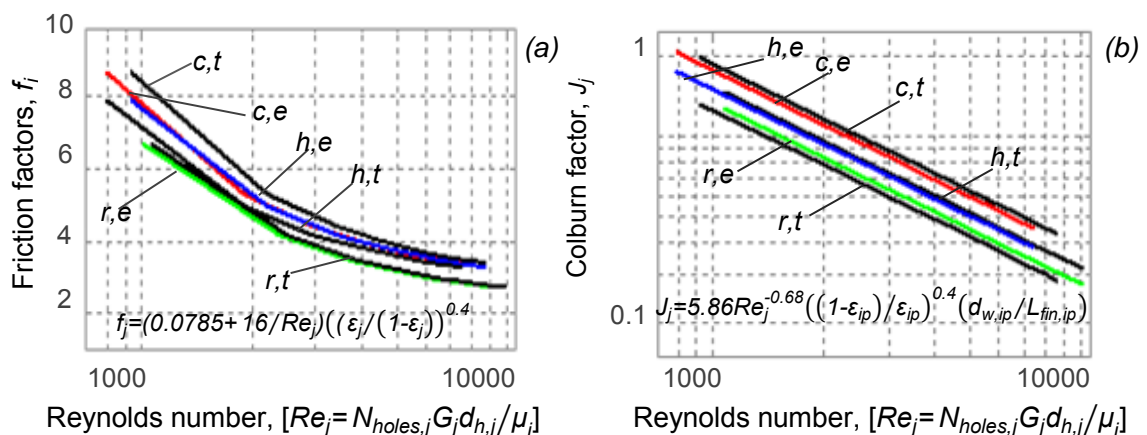


Figure 6.9: Dimensionless factors as measured and predicted: (a) friction factors, (b) colburn factors

Figure 6.10 shows a typical set of oscillating flow experimental results in the heater, cooler and regenerator. Figure 6.10(a) gives the heat exchanger temperatures as a function of time from start up to steady state for a frequency of 10 Hz, while figure 6.10(b) gives results for a frequency of 5 Hz. When comparing figure 6.10(a) to figure 6.10(b), it is seen that steady state in the heat exchanger working fluid temperatures is reached earlier when the heat exchanger flow frequency is high. Having a close look on figure 6.10, it is not easy to analyse the detailed flow behaviour in the heat exchanger working spaces as it gives results for three hours. Knowing that, a frequency is the number of cycles per second, it was then decided to restrict the results period from three hours to one second, after steady state has been reached. From a period of one second, the flow behaviour in each of the heat exchanger working spaces may be better analysed. Hence, figure 6.11 gives the steady state predicted and measured heat exchanger temperatures, but on a much smaller time scale (period of one second), after 60 min.

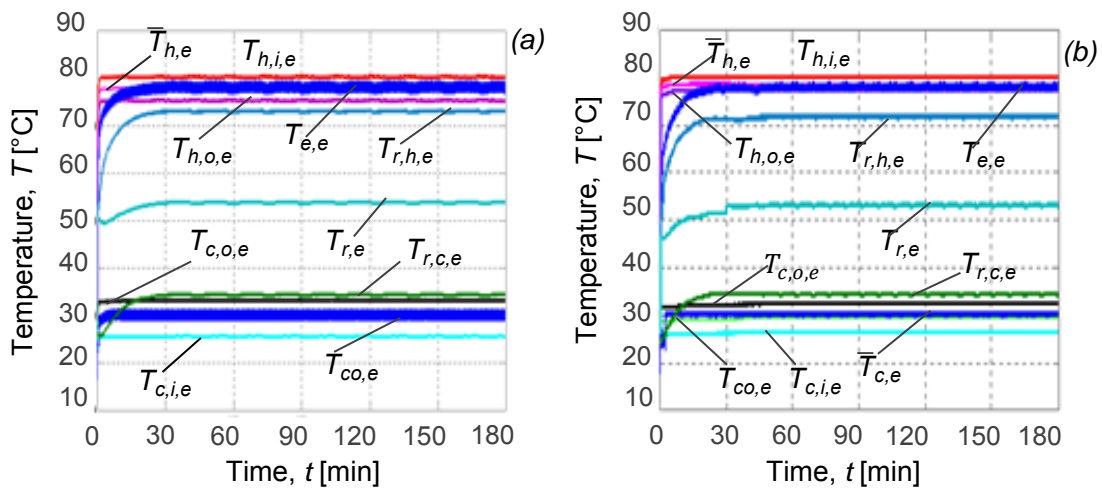


Figure 6.10: The heat exchanger temperatures, as measured in an oscillating flow, from start-up to steady state: (a) frequency of 10 Hz, (b) frequency of 5 Hz

Figure 6.11 shows the steady state heat exchanger working fluid temperatures as a function of time for an operating frequency of 10 Hz (figure 6.11(a)) and 5 Hz (figure 6.11(b)). It is seen that all heat exchanger working space temperatures are accurately predicted. When analysing figure 6.11, two main observations are made for the results interpretation as follow: In figure 6.11(a) the mean temperatures in the expansion \bar{T}_e and compression \bar{T}_{co} spaces are equal to the mean hot \bar{T}_h and mean cold \bar{T}_c temperatures respectively. The heat transfer rate between the hot and/or the cold streams and the heat exchanger for an operating frequency of 10 Hz, $\dot{Q}_{h,e}=(UA)_{h,e}(\bar{T}_h-\bar{T}_e)\approx 0$ and $\dot{Q}_{co,c}=(UA)_{co,c}(\bar{T}_{co}-\bar{T}_c)\approx 0$, respectively, are close to zero. This means there is no heat transferred between the heat source and the heat exchanger, as well as the heat exchanger and the heat sink. This retains the heat exchanger adiabatic working spaces assumption (see section 4.4). In figure 6.11(b) the mean temperatures in the expansion \bar{T}_e and compression \bar{T}_{co} spaces are different to the mean hot \bar{T}_h and mean cold \bar{T}_c temperatures, respectively. The heat transfer rate between the hot and/or the cold streams and the heat exchanger for an operating frequency of 5 Hz $\dot{Q}_{h,e}=(UA)_{h,e}(\bar{T}_h-\bar{T}_e)\neq 0$ and $\dot{Q}_{co,c}=(UA)_{co,c}(\bar{T}_{co}-\bar{T}_c)\neq 0$, respectively, are different to zero. This means there is indefinitely

heat transferred from the heat source to the heat exchanger, as well as the heat exchanger to the heat sink. This retains the heat exchanger isothermal working spaces assumption (see section 4.4).

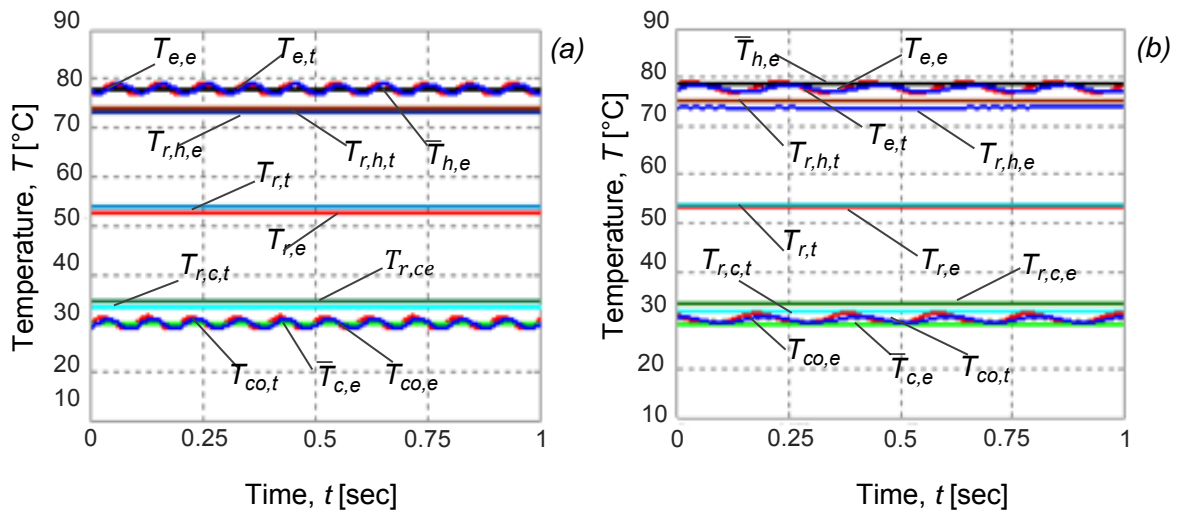


Figure 6.11: Steady state heat exchanger temperatures, as measured and predicted in an oscillating flow, a) frequency of 10Hz, b) frequency of 5 Hz

After repeatedly conducting the same experiments for the operating frequencies of 5 Hz, 7.5 Hz, 10 Hz and 15 Hz, it was found that; results for frequencies < 10 Hz, the isothermal assumption was valid, and results for frequencies ≥ 10 Hz, the adiabatic assumption was valid. From these observations, it may be understood that, the SE should be operated at a frequency of no less than 10 Hz, to develop high performance. Figure 12 shows results of the heat exchanger temperatures as a function of time, for an operating frequency of 15 Hz (figure 6.12(a)) and 7.5 Hz (figure 6.12(b)), respectively, given for half a second each.

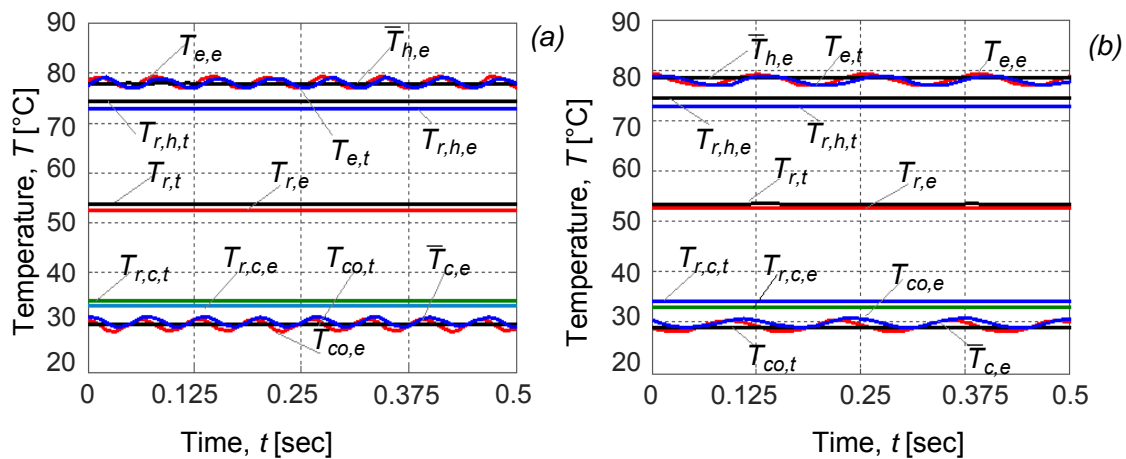


Figure 6.12: Steady state heat exchanger temperatures, as measured and predicted in an oscillating flow for half a second: (a) frequency of 15 Hz, (b) frequency of 7.5 Hz

Figure 6.13 shows the experimentally and theoretically calculated regenerator temperature profile as a function of position (from the heater to the cooler side) for an oscillating flow (figure 6.13 (a)) and a unidirectional flow (figure 6.13 (b)). These results show that, the

performance of the regenerator not only depends on the geometry of the material used to enhance its heat exchanger area, but also on the length of the regenerator itself. When analysing figures 6.13(a) and 6.13(b), it may be understood that by alternatively absorbing heat from, and/or releasing heat back to the heat exchanger working fluid, the regenerator simultaneously serves as a pre-cooler and/or pre-heater. A pre-cooler function of the regenerator can be described when the working fluid flows from the heater to the cooler whereas a pre-heater is described to flow in the opposite direction.

When comparing figure 6.13(a) to figure 6.13(b), it may be seen that the temperature drop much lower in the oscillating flow than in the unidirectional flow. This is because the heat transfer coefficient in the oscillating flow is much better than in the unidirectional flow. Heat is then removed and/or brought back from/to the hot and/or cold air much quickly in the oscillating flow than in the unidirectional flow regime.

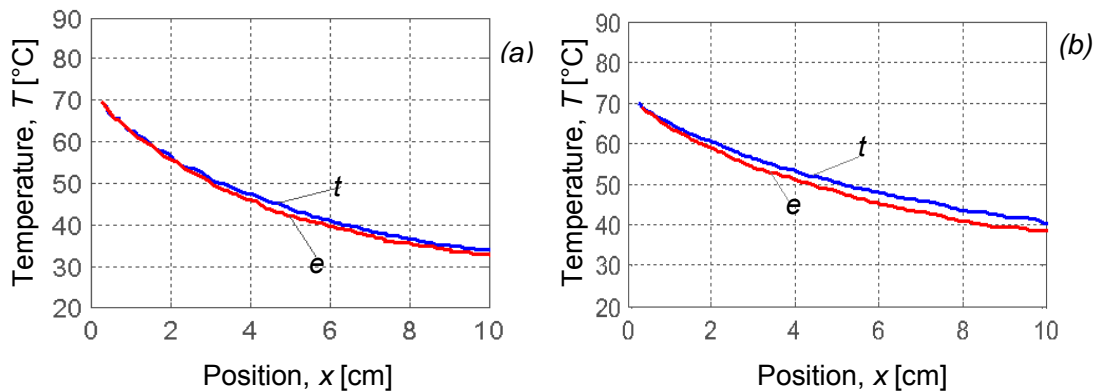


Figure 6.13: Regenerator calculated temperature as a function of position: (a) oscillating flow, (b) unidirectional flow

Figure 6.14 shows the calculated mass flow rate and the pressure in the heat exchanger working spaces as a function of time for an operating frequency of 10 Hz. Figures 6.14(a), 6.14(b) and 6.14(c) give the mass flow rate of the heat exchanger working spaces, the pressure drop across the heater, regenerator and cooler, and the heat exchanger working spaces pressures, respectively, as a function of time. Figure 6.14(d) gives the average heat transfer coefficients in the heater, regenerator and cooler as a function of the Reynolds number.

Figures 6.14(a) and 6.14(c) show that the mass flow rate and the pressure are slightly high in the expansion space compared to the mass flow rate and the pressure in the compression space. This is due to the presence of the wire matrix, which develops a drag force in the working fluid path. Furthermore a high-temperature in the heater increases the pressure in the working space adjacent to the heater, therefore decreasing the density of the working fluid in the same working space. The same situation will occur in the cooler and the working space adjacent to the cooler, but in an opposite direction. Figure 6.14(b) shows that the pressure drop across the cooler is higher than the pressure drop across the heater, and the pressure drop across the heater is higher than the pressure drop across the regenerator. Figure 6.14(d)

shows that the heat transfer coefficient in an oscillating flow regime is almost 3.3 times as high as the heat transfer coefficient in the unidirectional flow regime (see figure 6.7(b)).

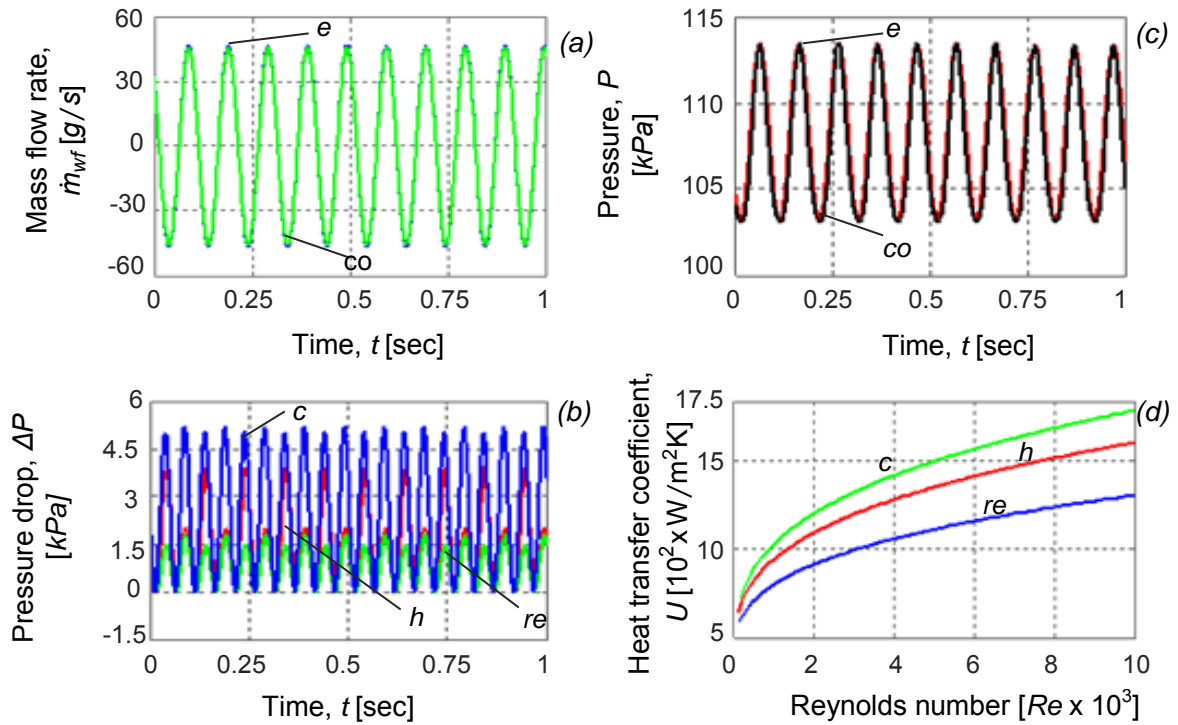


Figure 6.14: Calculated, a) mass flow rate, b) pressure drop across the heat exchangers, c) pressure in the working spaces, d) overall heat transfer coefficient in the heat exchangers

Figure 6.15 shows the pressure-volume (PV) diagram and the energy balance in the heat exchanger. Figure 6.15(a) shows that the heat exchanger will not perform any type of work as the PV area of the expansion space minus the PV area of the compression space is close to zero. Hence, the SE heat exchanger is not an engine, but an essential part of the engine that receives and rejects heat, allowing the engine to perform its thermodynamic cycle. Figure 6.15(b) shows how the average heat transfer rate between the hot source \bar{Q}_{hot} supplied to the heater balances the average heat absorbed in the regenerator \bar{Q}_r , the heat loss \bar{Q}_{loss} and the heat rejected from the heat exchanger through the cooler to the cold water \bar{Q}_{cold} .

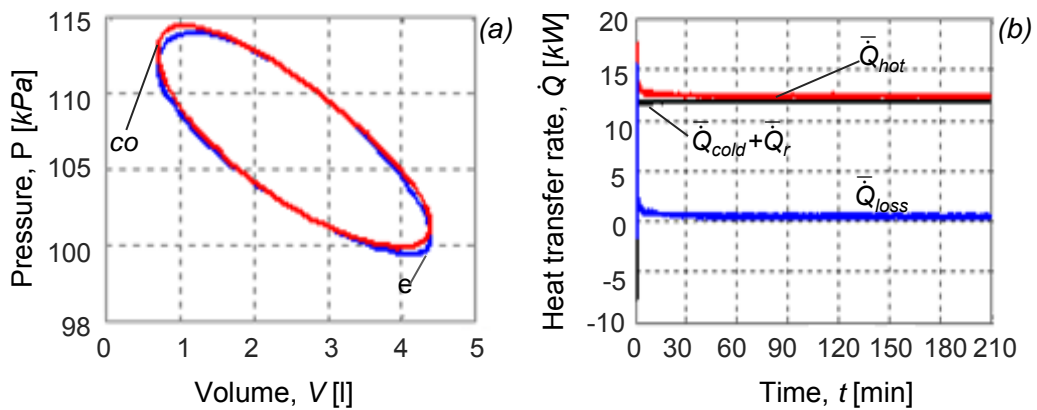


Figure 6.15: Calculated, a) P-V diagram, b) Energy balance

7 Dynamic analysis of the heat exchanger assembly

7.1 Introduction

When a mechanical component is subject to the action of external forces or torques, it deforms by developing internal stresses. These stresses may totally or partially balance the external forces. If partially balanced, a dynamic and/or thermodynamic state is reached. In this analysis it is assumed that all deformations are elastic and linear. Any dynamic behaviour is a source of vibrations in components, particularly in mechanical systems. Vibrations of mechanical systems cause noise, premature wear and fatigue (Mulapi, 2002). Fatigue of material is a process of the generation and development of cracks, leading finally the breakage of components (Del Pedro and Pahud, 1988). Due to frictions of mechanical components, fatigue causes energy dissipation that is harmful to the system efficiency (Morel, 1979). Senda (2004) reported that it is important to reduce vibrations in a system by either resisting against their effects with a passive isolation or resisting against their causes by a good design of components or, if necessary, a good design of the entire mechanical system. Resisting against vibration in a mechanical design may be elaborated as follows: Detect the main source causing vibrations of a mechanical system. Analyse the transmissions of vibration in the system, and then predict the resonance possibilities, or design ways of reducing all vibrations, if possible. The transmission of vibrations and the prediction of resonance may be done by the use of modal analysis (Courrech and Ronald, 2002).

7.1.1 Modal analysis

Modal analysis is a tool that offers knowledge of the characteristics of a machine, a structure or a mechanical system. Through modal analysis, the operating conditions and factors influencing the vibrational behaviour of a mechanical system may also be determined. It allows predicting any eventual damage of a particular component in the system and/or the entire system. At the stage of a preliminary design for a new mechanical system, modal analysis allows for the sizing and the definition of its optimal operating conditions. There are two types of modal analysis, the experimental and the analytical modal analysis. Experimental modal analysis requires the realisation of prototypes, from which, representative tests are performed to deduce a mathematical model corresponding to the theoretical model of the system. Experimental modal analysis must include vibration measurements. The analytical modal analysis establishes the theoretical or mathematical modelling for the dynamic behaviour of a mechanical system, allowing the frequencies response analysis through an appropriate mathematical tool (Del Pedro and Pahud, 1988).

7.1.2 Analytical modal analysis of a mechanical system

A mechanical system may be considered as a system of n degrees of freedom, possessing n natural frequencies. To each natural frequency there corresponds a natural vibration, the

displacements of which define normal modes of vibration (Senda, 2004). Normal modes of vibrations depend on masses, stiffness and their distributions on the system. A mechanical system may vibrate in a normal mode if only appropriate initial conditions of vibrations are reached. But if the system is subject to some external force, such as torque, vibrations comprising all system normal modes will exist (Courrech and Ronald, 2002). Forced vibrations of a mechanical system in a simple harmonic excitation occur at a frequency of excitation. If there is coincidence between one of the natural frequencies and one of the excitation frequencies, there is resonance. Resonance causes damage in any mechanical system, therefore a damper should be added to the system to reduce the amplitude of vibration by creating a phase shift of the response of the system (Del Pedro and Pahud, 1988).

7.2 Main sources of excitation in vibrations and their calculation

To comprehend the analysis of the dynamic behaviour of a mechanical system, special attention must be paid to major sources of excitation in vibration, the components of liaison and components containment of the system. In the case of the SE heat exchanger experimental set-up assembly, the main sources of excitation in vibration are: the shafts and couplings, the bearings and the electrical motor and the heat exchanger working spaces.

7.2.1 The shafts and couplings

Not only do shafts transmit vibrations, they are also sources of vibrations. Notwithstanding the care given to the construction of a mechanical system, it is not possible to align the shaft axis of rotation with the centre of gravity of each of its parts. The deformation of the shaft during rotation results in vibrations. Generally, the vibrations arise from machining defects, shaft installation or assembly. During operation, shafts may also deform due to an asymmetric heat distribution (Morel, 1979). Couplings may also be sources of vibrations due to, bad centring of plates: a defect of parallelism and a failure of alignment of axis in rotation defined by two angles. These two angles are the angle of inclination corresponding to a deviation angle in the plane of the rotation axis, and the angle of deviation in the plane normal to the previous (Blanc, 2004).

Table 7.1: Frequency of excitation in vibration of shaft and coupling

Type of component	$\omega = \frac{2\pi N}{60}$ [rads^{-1}]	2ω [rads^{-1}]	3ω [rads^{-1}]	4ω [rads^{-1}]
Shaft and coupling	149.2	298.5	447.7	596.9

The shaft and coupling failure results in vibrations of the system in rotation; it therefore vibrates at the frequency of rotation ω . Courrech and Ronald (2004) report that it is often convenient to consider the frequencies of excitation in vibration for the shafts and couplings

as equal to the double, and sometimes even to the triple and quadruple, of the frequency of rotation ω . Table 7.1 summarises the values of the frequency of excitation in vibration for the shaft and the coupling.

7.2.2 The bearings

Bearings are a compulsory passage of vibrations. The failure mode in bearings is often explained by the degradation process. Indeed, bearing degradation generally results in a subsurface or a surface fatigue of one of the ball-races. Thus fatigue cracks occur and propagate until failure occurs. Shocks due to bearings failure excite defective frequencies, which depend on the number of rolling elements N , the rotational speed $\omega=149.2 \text{ rads}^{-1}$ and the geometrical dimension of the bearing, such as, the rolling element diameter d the bearing pitch diameter D and the contact angle φ . The bearings frequencies of excitation in vibration may be determined as summarised in table 7.2 (Kilundu et al., 2009).

Table 7.2: Frequency of excitation in vibration of bearings

N	d [mm]	D [mm]	Outer race defect $\omega_1 = \frac{\omega N}{2} \left(1 - \frac{d}{D} \cos \varphi\right)$ [rads ⁻¹]	Inner race defect $\omega_2 = \frac{\omega N}{2} \left(1 + \frac{d}{D} \cos \varphi\right)$ [rads ⁻¹]	Rolling element defect $\omega_1 = \frac{\omega N d}{2 D} \left(1 - \left(\frac{d}{D} \cos \varphi\right)^2\right)$ [rads ⁻¹]
33	40	90	1514.5	3409.9	932.2

7.2.3 The electrical motor

The electromagnetic actions of parasitic induction forces in the electrical motor generally originate due to a deficiency in the gap and a failure of the stator and/or the rotor. The electrical motor failures generate vibrations with excitation frequencies as summarised in table 7.3 (Briget, 1980)

Table 7.3: Frequency of excitation of the electrical motor

Frequency f , [Hz]	Number of poles N_p	Number of pairs of poles P	Slip g [%]	Synchronous speed $N_s = \frac{60f}{P}$ [rpm]	Asynchronous speed $N = (1-g)N_s$ [rpm]	Vibration frequency $\omega = \frac{\pi N_p}{30} (N_s - N)$ [rads ⁻¹]
50	4	2	5	1500	1425	31.42

7.2.4 The heat exchanger

The excitation in vibration in the heat exchanger is due to the gas-spring effect in the heat exchanger working spaces. All dynamic gas spring spaces, including reciprocators vibrate at

the natural frequency of gas. At the point of vibration, the displacement and the resulting pressure amplitude is maximum. The frequency of vibration in the heat exchanger is summarised in table 7.4 (Smith, 2006).

Table 7.4: Frequency of excitation in vibration of the heat exchanger

Control volume	Pressure P_{max} [Pa]	Displacement X [m]	Cross Area, A_p [m ²]	Mass m [kg]	Vibration frequency $\omega = \sqrt{\frac{P_{max} A_p}{xm}}$ [rads ⁻¹]
Expansion	114000	0.03	0.1029	0.0034	10724.1
Heater	113100	0.03	0.023	0.0001	29446.7
Regenerator	111800	0.03	0.049	0.0003	24671.6
Cooler	110250	0.03	0.023	0.0002	20557.8
compression	109100	0.03	0.1029	0.0034	10491.1

7.3 Dynamic behaviour of the heat exchanger assembly

Modelling of a continuous system (mass and stiffness distributed throughout the element) provides analytical results based on continuum mechanics and analytical mechanics. These analytical results are general, but necessary in the design of a mechanical system. However, the vibrations of complex structures admit a large number of degrees of freedom and require the use of a computer program to solve their characteristic differential equations. Differential equations characterising the dynamic behaviour of a mechanical system are summarised by way of the following equations (Del Pedro and Pahud, 1988).

$$[M]\ddot{x} + [C]\dot{x} + [K]x = f(t) \tag{7.3.1}$$

Where, x , \dot{x} and \ddot{x} are the displacement, velocity and acceleration respectively. $[M]$, $[C]$ and $[K]$ are the matrix mass, damping and stiffness, respectively, and $f(t)$ is a vector representing the effect of the external forces acting on the system. The Lagrange formulations will be applied to the heat exchanger assembly model shown in figure 7.1 to develop its dynamic behaviour characteristic equations in the form of equation (7.3.1).

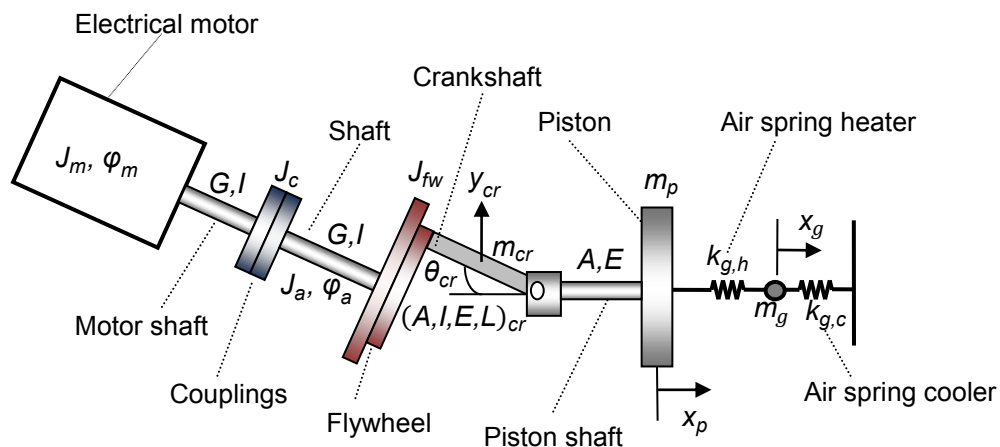


Figure 7.0.1: Dynamic model of experimental set-up of heat exchanger

Lagrange's formulation allows the derivation of all the equations of motion of the system, from three scalar equations: the kinetic energy, the potential energy and the virtual work due to non-conservative forces. From the kinetic and potential energy of each of the moving parts of the heat exchanger assembly model shown in figure 7.1, the Lagrange operator will be defined. Thereafter, from the Lagrange operator definition, a Lagrange formulation will be established to determine the dynamic behaviour equations of the system. The latter will be simplified as follows. As all shafts in rotation are short and rigid, only deformation in torsion φ will be considered. Bending deformation defined by the deformation y_{cr} and the angle of bending deformation θ_{cr} will be considered for the crankshaft. As the piston shaft is short and very rigid (see Appendix D.4), its bending deformation is neglected, and it will only be considered as a connecting element between the piston and the crankshaft, and therefore characterised only by its stiffness (Del Pedro and Pahud, 1988; Meirovitch, 2001). Table 7.5 summarises the kinetic and potential energy equation for each moving part of the heat exchanger experimental set-up model shown in figure 7.1. The mass, the mass inertia and the stiffness of the components are given in Appendix D.4.

Table 7.5: Summary of kinetic and potential energy for each component of the heat exchanger experimental set-up

Component	Kinetic energy	Potential energy
Electrical motor, and shaft	$E_{k,m} = \frac{1}{2} J_m \dot{\varphi}_m^2$	$E_{p,m} = \frac{1}{2} k_{t,m} \varphi_m^2$
Coupling	$E_{k,co} = \frac{1}{2} J_{co} (\dot{\varphi}_m^2 - \dot{\varphi}_a^2)$	$E_{p,co} = \frac{1}{2} k_{c,co} (\varphi_m - \varphi_a)^2$
Shaft	$E_{k,a} = \frac{1}{2} J_a \dot{\varphi}_a^2$	$E_{p,a} = \frac{1}{2} k_{t,a} \varphi_a^2$
Flywheel	$E_{k,fw} = \frac{1}{2} J_{fw} \left(\dot{\varphi}_a^2 - \left(\frac{L}{2} \dot{\theta}_{cr} \right)^2 \right)$	$E_{p,fw} = \frac{1}{2} k_{e,fw} \left(\varphi_a - \frac{L}{2} \theta_{cr} \right)^2$
Crankshaft	$E_{k,cr} = \frac{1}{2} m_{cr} \left(\dot{y}_{cr}^2 + \left(\frac{L}{2} \dot{\theta}_{cr} \right)^2 \right)$	$E_{p,cr} = \frac{1}{2} k_{b,cr} \left(y_{cr} + \frac{L}{2} \theta_{cr} \right)^2$
Piston	$E_{k,p} = \frac{1}{2} (m_{ps} + m_p) \dot{x}_p^2$	$E_{p,p} = \frac{1}{2} \left(\frac{k_{c,c} k_{b,ps}}{k_{c,c} + k_{b,ps}} \right) x_p^2$
Gas	$E_{k,g} = \frac{1}{2} \frac{m_g}{L_p} \int_0^{L_p} \left(\dot{x}_p + \frac{x}{L_p} (\dot{x}_g - \dot{x}_p) \right)^2 dx$ $E_{k,g} = \frac{1}{2} m_g \left(\frac{\dot{x}_g^2 + \dot{x}_g \dot{x}_p + \dot{x}_p^2}{3} \right)$	$E_{p,g} = \frac{1}{2} k_g x_g^2$

From table 7.5 the heat exchanger assembly total kinetic and potential energy are

$$E_k = E_{k,m} + E_{k,co} + E_{k,fw} + E_{k,cr} + E_{k,p} + E_{k,g} + E_{k,a} \quad (7.3.2)$$

$$E_p = E_{p,m} + E_{p,cr} + E_{p,p} + E_{p,g} + E_{p,a} + E_{p,co} + E_{p,fw} \quad (7.3.3)$$

From equation (7.3.2) and (7.3.3) the Lagrange operator is

$$L = E_k - E_p \quad (7.3.4)$$

The Lagrange formulations of the heat exchanger experimental set-up are given as

$$\frac{d}{dt} \left(\frac{\partial L}{\partial \dot{x}_j} \right) - \frac{\partial L}{\partial x_j} + \frac{\partial W}{\partial \dot{x}_j} = f_j(t) \quad (7.3.5)$$

Where ∂x_j and $\partial \dot{x}_j$ are the change in the vector displacement and velocity. ∂L , is the change in the Lagrange operator, ∂W is the change in the dissipation vector and $f_j(t)$ is a vector representing the system external forces. For a no dissipative system, the Lagrange formulations may be reduced as (Del Pedro and Pahud, 1988)

$$\frac{d}{dt} \left(\frac{\partial L}{\partial \dot{x}_j} \right) - \frac{\partial L}{\partial x_j} = f_j(t) \quad (7.3.6)$$

Substituting equation (7.3.4) in equation (7.3.6) and rearranging, the motion equations for each component of the system are given as

$$\frac{d}{dt} \left(\frac{\partial L}{\partial \dot{\varphi}_m} \right) - \frac{\partial L}{\partial \varphi_m} = (J_m + J_{co}) \ddot{\varphi}_m + (k_{t,m} + k_{c,co}) \varphi_m - k_{c,co} \varphi_a = \theta_{max} \sin(\omega t) \quad (7.3.7)$$

$$\frac{d}{dt} \left(\frac{\partial L}{\partial \dot{\varphi}_a} \right) - \frac{\partial L}{\partial \varphi_a} = (J_{fw} + J_a - J_{co}) \ddot{\varphi}_a - k_{c,co} \varphi_m + (k_{t,a} + k_{e,fw} + k_{c,co}) \varphi_a - k_{e,fw} \frac{L}{2} \theta_{cr} = 0 \quad (7.3.8)$$

$$\frac{d}{dt} \left(\frac{\partial L}{\partial \dot{\theta}_{cr}} \right) - \frac{\partial L}{\partial \theta_{cr}} = \left(\frac{L^2}{4} m_{cr} - J_{fw} \right) \ddot{\theta}_{cr} - \frac{L}{2} k_{e,fw} \varphi_a + (k_{b,cr} + k_{e,fw}) \theta_{cr} + \frac{L}{2} k_{b,cr} y_{cr} = 0 \quad (7.3.9)$$

$$\frac{d}{dt} \left(\frac{\partial L}{\partial \dot{y}_{cr}} \right) - \frac{\partial L}{\partial y_{cr}} = m_{cr} \ddot{y}_{cr} + k_{b,cr} y_{cr} + k_{b,cr} \frac{L}{2} \theta_{cr} = 0 \quad (7.3.10)$$

$$\frac{d}{dt} \left(\frac{\partial L}{\partial \dot{x}_p} \right) - \frac{\partial L}{\partial x_p} = \left(m_{ps} + m_p + \frac{1}{3} m_g \right) \ddot{x}_p + \frac{1}{6} m_g \ddot{x}_g + \frac{k_{c,c} k_{b,ps}}{k_{c,c} + k_{b,ps}} x_p = 0 \quad (7.3.11)$$

$$\frac{d}{dt} \left(\frac{\partial L}{\partial \dot{x}_g} \right) - \frac{\partial L}{\partial x_g} = \frac{1}{3} m_g \ddot{x}_g + \frac{1}{6} m_g \ddot{x}_p + k_g x_g = 0 \quad (7.3.12)$$

The determinant of the characteristic matrix of equations (7.3.7) to (7.4.12) gives the frequency equation of the system (see Appendix D.4). The first solution of the frequency equation gives the smallest system natural frequency $\omega_1 = 35000 \text{ rad/s}$.

All heat exchanger experimental set-up excitation in vibration frequencies are small compare to $\omega_1 = 35000 \text{ rad/s}$. The system vibrations will not reach resonance, therefore the design is safe. There is resonance only when there is coincidence between one of the excitation frequencies in vibration and one of the natural frequencies of the system (Meirovitch, 2001). The reason why the natural frequency is so high is that the stiffness of the materials used in the design is high. Vibrations dealt with during testing would not damage the experimental set-up. It is also noticed that the frequency of excitation in vibration for the heat exchanger working spaces is too high compared to the frequency of excitation in vibration of other moving parts. This means that high frequencies it will be required to excite the heater, cooler and regenerator working fluid in vibration, therefore vibrations at low frequency will not affect the working fluid dynamic behaviour in the heat exchanger.

8 Discussion, conclusions and recommendations

This section discusses and draws conclusions based on the objectives and findings of the project. Based on the conclusions drawn recommendations for future research are also made.

8.1 The PBMR waste heat streams

The first objective of this project was to identify the waste heat streams from a PBMR. Five waste heat streams were identified as capable of providing adequate thermal energy (section 2.2). These were the pre- and inter-cooler, the reactor cavity cooling system (RCCS), the core barrel conditioning system (CBCS), the core conditioning system (CCS) and the used and/or spent fuel tank.

Heat at temperatures in the order of 130 °C is removed from the helium working fluid of the Brayton cycle by the pre-cooler and inter-cooler cooling water. According to Slabber (2006) parasitic or residual heat at temperatures in the order of 232.5 °C must be removed through the RCCS as a temperature ≤ 400 °C must be maintained outside the RPV. A limit design temperature of ≤ 65 °C must be maintained for the concrete surfaces of the reactor cavity during normal operation. The core conditioning system removes decay heat at temperatures in the order 387 °C. The core barrel core conditioning system removes decay heat up to 1.5 MW during all anticipated normal operating conditions. Nuclear reactor used and/or spent fuel are thermally hot as well as highly radioactive, hence it is required that the temperature of the fuel within the tank should be maintained at temperatures ≤ 400 °C (Fuls and Mathews, 2006). However the carbon steel tank must be kept to below 300 °C to ensure a proper fuel tank cooling Slabber (2008).

From the above findings it can be concluded that the requirements of the first objective was met, as there is approximately a total of 9.84 MW heat in the range 130-400 °C that may be extracted from the inter-cooler, pre-cooler, RCCS, CCS, CBCS and the spent and/or used fuel tank.

8.2 Energy conversion devices

The transformation of waste heat extracted from the PBMR waste heat streams into a useful form of energy may be done by using an energy conversion device in a WHR&U system. Energy conversion devices capture the recovered waste heat and re-utilise a portion of the heat. To meet the second objective of this project, some energy conversion devices that may be used in a PBMR WHR&U system were analysed. It was understood that the WHR&U system efficiency is directly dependent on the waste heat source and the type of energy conversion device used. For different waste heat source temperatures in the range 60-800 °C a dual function absorption cycle (DFAC), an organic Rankine cycle (ORC) and a Stirling engine (SE) were identified as being particularly attractive (section 2.4).

Hence, as shown in figure 2.6 for the PBMR waste heat streams described above (section 8.1), the ORC is the system of preference because it can efficiently handle heat at temperatures in the range 100-350 °C and even higher, up to temperatures slightly below 400 °C. Furthermore ORC is a more popular energy production cycle because of the use of n-pentane as the working fluid. The latter enables the ORC to be used even in low-temperature waste heat recovery. However, for the low-heat source temperatures in the range 60-100 °C a DFAC is appropriate, not only for producing refrigeration, but also for power generation (see figure 2.7). For a high-temperature WHR&U system with heat source temperatures in the range 350-800 °C a Stirling engine is appropriate.

It is thus recommended that future studies on WHR&U systems, emphasis on DFAC power generation for low-temperature heat sources. Notwithstanding the fact that, from an energy conversion efficiency point of view SEs are not as good as ORC and DFAC for heat source temperatures ≤ 400 °C (see figure 2.6). SEs have to be considered because of their good reliability. SEs are thus indicated where excellent reliability, from a safety point of view, is necessary. Thus in further studies on WHR&U systems, emphasis on the use of a low-temperature SEs is also recommended.

8.3 The validity of utilising the waste heat from the fuel tank

The third objective of this project was to demonstrate the validity of utilising the waste heat from the PBMR used fuel tank. This requires waste heat to be recovered first, and thereafter the recovered heat may be utilised in an appropriate energy conversion device. For this consideration, the project was thus divided into two main sections: the waste heat recovery and the waste heat utilisation system. From the background theory presented in the literature survey and with the aid of Dobson (2008), a scale model WHR&U system (shown in figure 3.1) was designed, built and tested. Cooling was selected as a mechanism of waste heat recovery and utilisation process of a PBMR fuel tank. Heat was then removed from the fuel tank by the heat exchanger and/or air-cooled condenser, and then carried out of the system through the heat exchanger cooling water. Hence, the designed PBMR used and/or spent fuel tank WHR&U system was found to function well. This design used two incoloy electrical heating elements of 3 kW each to simulate the fuel tank waste heat.

The as-tested scale model of the used and/or spent fuel tank (shown in figures 5.1 and 5.2) has four shut-off valves to manually regulate the two lines of the WHR&U system, instead of an automatic thermostatic control valve. An automatic thermostatic control valve will automatically divert the steam from the cooling jacket to the secondary line should a fault or a stoppage occur in the primary cooling line as a result of a mechanical failure or planned maintenance of the power conversion system. An automatic thermostatic control valve requires specific analysis which depends upon the thermosyphon, thermo-dynamic flow response. The use of a domestic electric hot-water geyser thermostatic control valve was considered. It was however unsuitable because its over-temperature option opens at about 93 °C, whereas the design specification for the cooling jacket is 250 °C. This requires the WHR&U system loop to be established first, and thereafter the thermostatic control valve

design options may be investigated in accordance of the loop thermo-dynamic response. It is thus recommended that such a thermostatic control valve be researched in future studies.

8.4 PBMR used and/or spent fuel tank WHR&U system theoretical model

A theoretical model that simulates the heat transfer process in the as-designed WHR&U system was developed (in section 3.4), to meet the requirements of the fourth objective of this project. In order to validate the theoretical model results, an experimental investigation of the PBMR WHR&U system thermosyphon loop was performed. It was found that the theoretically and experimentally calculated heat transfer coefficients deviate. Several tests were undertaken for each of the selected operating modes. Thereafter, it was decided to set the experimental results as reference to adjust the theoretical heat transfer coefficients so that they simulate the experiments. As reported by Ruppertsberg (2008), a two-phase flow thermosyphon loop is a non-linear system where all the system parameters are interlinked so that a small change in one of the parameters may significantly influence results. The theoretical model adjustment commenced with an investigation into the most important parameters influencing the theoretical heat transfer coefficients and flow resistances. It was found that the theoretical model is influenced by the power input to the system, the flow variables and the geometrical variables of the system (section 5.3.1).

The power input and the flow variable are captured in the Reynolds number. The Reynolds number, the flow and geometrical variables (other than those captured in the Reynolds number) are all captured in the thermal resistances of the air-cooled condenser and heat exchanger, respectively. It was then, investigated how changes in the air-cooled condenser and heat exchanger thermal resistance affect the theoretical results. This led to a thermal resistance correction in accordance with a suggestion of Yang et al. (2006). The current theoretical model thus uses the heat exchanger and air-cooled condenser overall heat transfer coefficients that were adapted to their geometries from the corrected thermal resistances. This allowed better predictions of the experimental results (section 5.3). Hence, the actual theoretical model better simulates the experiment. But, as the power input and the geometrical variables of the air-cooled condenser and heat exchanger influence the theoretical results, it is thus recommend that a theoretical model validation for a larger scale PBMR used and/or spent fuel tank WHR&U system be considered in future studies.

8.5 Lumped parameter modelling of a Stirling engine heat exchanger

The fifth objective of this project was to create a mathematical model of a SE heat exchanger. A lumped parameter model was used to describe the thermo-fluid dynamic behaviour of the SE heat exchanger (section 4.4). Emphasis was placed on the third approach, the so-called *lumped parameter* modelling of a SE heat exchanger. In order to validate the SE heat exchanger theoretical model, first a preliminary experimental investigation was conducted, which gives results from unidirectional flow data measurements, and, second a main testing

phase was carried out, which gives results from fluctuating flow data measurements. Results obtained from the preliminary phase of experiments were used as a reference to validate the theoretical model that predict the heat exchanger heat transfer coefficients and pressure drops. During the preliminary phase of experiments, a deviation in the predicted results compared to the experimental results was noted. This deviation of the predicted results was due to a lack of published information and little progress made in attempts to analytically or numerically predict the heat transfer coefficients and friction factors for heat exchangers using woven wire mesh.

The theoretical model was adjusted so that it simulated the experiment heat exchanger values. This was done by identifying the flow and geometrical variables influencing the SE heat exchanger theoretical results. It was found that in compact heat exchanger using woven wire mesh all geometrical variables influencing the theoretical results are captured in the porosity, while all flow variables are captured in the Reynolds number. Both the Reynolds number and porosity are captured in the thermal resistance. The experimentally calculated thermal resistance of the heater, cooler and regenerator was set as a reference to correct their respective porosities. The porosity is defined as the ratio of the wire mesh volume in the control volume to the total volume of the control volume, and its correction allows a volume of wire mesh correction and, by extension the number of laminating screens in the heat exchanger, and therefore the flow resistances. Hence, the porosity correction has led to the correction of the heat transfer coefficients and the pressure drop correlations used in the simulation of a SE heat exchanger using woven wire mesh, which now better predicts the experiments to meet the requirements of the sixth objective of this project.

The heat transfer rates between the air and the wire matrix in the heater, cooler and regenerator are function of the heat transfer area of the woven wire matrix. This was calculated by modelling the mesh as fins (see section 4.3.2). The fin model was developed according to an understanding on the heat distribution from the air to the woven wire matrix holes. However due to a lack of published information on how to do so, it is thus recommended that the calculation of heat transfer area in a porous medium such as woven wire mesh be further investigated in future studies.

In the second phase of experiment which concerned a fluctuating flow, a reciprocator driven by an electrical motor through a crankshaft mechanism was also designed and built to simulate the SE oscillating flow of the working fluid through the heat exchanger. The calculated pressure-volume diagram of the heat exchanger shows that the work developed in the heat exchanger is zero as the area representing the work developed in the compression space minus the area representing the work developed in the expansion space is almost zero (see figure 6.15(a)). The calculated heat transfer rate shows that the heat recovered will effectively be transferred to the SE through the heat exchanger (see figure 13(b)).

Vibration of the SE heat exchanger experimental assembly was a problem to deal with during the heat exchanger fluctuating flow tests. Hence a dynamic analysis of the SE heat exchanger was undertaken. The main sources of excitation in vibrations of the SE heat exchanger

experimental assembly were investigated and calculated based initially on the empirical correlations provided in the literature. Thereafter, a mathematical model of the SE heat exchanger experimental assembly was developed based on the energy equations for each moving part of the assembly. The kinetic and potential energy equations were formulated for each moving part of the heat exchanger experimental assembly. From the kinetic and potential equations the Lagrange operator was defined, and then the Lagrange formulations were used to derive the differential equations representing the dynamic behaviour of each moving part of the assembly. The differential equations were integrated to determine the system natural frequency. It was found that the smallest natural frequency $\omega_1=35000 \text{ rad/s}$ is by far much greater than all the system excitation in vibration frequencies. In conclusion, this means that vibrations in the system will not reach resonance, therefore the design was found to be safe.

9 References

- Adak AK, Rao IS, Srivastava VK & Tewari PK. 2006. Nuclear desalination by waste heat utilization in an advanced heavy water reactor. *International Journal of Nuclear Desalination*, 2(3), 234 – 243.
- Agrawal R, West DH & Balakotaiah V. 2007. Modeling and analysis of local hot spot formation in down-flow adiabatic packed-bed reactors. *Chemical Engineering Science* 62, 4926–4943.
- Andrews A. 2006. Radioactive waste streams: waste classification for disposal. *Congressional Research Service*, Order code RL32163, 13 December.
- Aritomi M, Nakahashi T & Chiang JH. 1992. Fundamental study on thermo-hydraulics during start-up in natural circulation boiling water reactors (I) thermo-hydraulic instabilities. *Journal of Nuclear Science and Technology*, 29, 631–641.
- Aritomi M, Sudi A, Miyata T & Horiguchi M. 1993. Thermo-hydraulics of boiling two-phase flow in high conversion light water reactors thermo-hydraulics at low velocities. *International Journal of Multiphase Flow*, 19, 51–63.
- Barron RF. 1999. *Cryogenic Heat Transfer*. Taylor and Francis: Philadelphia.
- Berchowitz DM and Urieli I. 1984. *Stirling cycle engine analysis*. Technology and engineering, Adam Hilgher Ltd: Bristol.
- Blanc H. 2004. *Dynamique des rotor en torsion-type d excitation permenante* [Online]. Available: <http://www.techniques-ingenieur.fr/base-documentaire/mecanique-th7/fonctions-et-composants-mecaniques-ti152/dynamique-des-rotors-en-torsion-bm5121>. [2011, January 16].
- Bork PV, Grote H, Notz D & Regler M. 1993. *Data Analysis Techniques in High Energy Physics Experiments*. Cambridge University Press: Cambridge.
- Borsukiewicz G and Nowak W. 2007. Comparative analysis of natural and synthetic refrigerants in application to low temperature Clausius–Rankine cycle. *Energy*, 32, 344–352.
- Briget R. 1980. *Les vibrations des machines tournantes et des structures*. Techniques et Documentation, ISBN 13: 9782852060623: London.
- Cengel YA. 2003. *Heat transfer a practical approach*. 2nd edn. McGraw Hill: New York.
- Cengel YA and Boles MA. 2002. *Thermodynamics an Engineering approach*. 4th edn. McGraw Hill: New York.

- Courrech J and Ronald L. 2002. Conditioning monitoring of machinery. *Harris' Shock and Vibration Handbook*, McGraw Hill: New York, 16.1-16.25.
- Darbour S, Nisan S & Charbit F. 2006. Utilization of waste heat from GT-MHR and PBMR reactors for nuclear desalination. *Desalination*, 205, 254-268.
- Del Pedro M and Pahud P. 1988. *Mechanique vibratoire, system discrets lineaires*. Presses polytechniques et universitaires romandes: Lausanne.
- Dobson RT. 1993. Transient response of a closed loop thermosyphon, *R&D Journal*, 9(1), 32-38.
- Dobson RT. 2006. *Fundamentals of thermodynamics, fluid mechanics and process Engineering*. Stellenbosch University: Stellenbosch.
- Dobson RT. 2007. Advanced heat transfer course, two-phase flow and heat transfer. Stellenbosch University, Stellenbosch.
- Dobson RT. 2008. PBMR technology development projects, Stellenbosch, South Africa. *Proceedings of the 4th international Tropical Meeting on High Temperature Reactor Technology*, HTR2008-58103, 28 September-October 1, Washington.
- DST. 2007. *South Africa's Climate Change Technology Needs Assessment* [Online]. Available: <http://unfccc.int/ttclear/pdf/TNA/South%20Africa/South%20Africa.pdf>. [2011, June 11].
- Dudley T, DeVilliers P, Wang Z, & Luh R. 2006. The thermal-hydraulic model for the PBMR plant training simulator. *3rd International Topical Meeting on High Temperature Reactor Technology*, 1-4 October, Johannesburg.
- Erickson DC, Papar R, Anand G & Tang J. 1998. Refinery waste heat powered absorption refrigeration-cycle specification and design. *Proceedings of ASME*, 38, 391-402.
- Eskom's Climate Change Commitment*. [S.a.]. [Online]. Available: http://www.eskom.co.za/content/GI0004_6_POINT_PLAN~2~1.pdf. [2011, September 11].
- Eskom Heritage*. [S.a.]. [Online]. Available: http://heritage.eskom.co.za/heritage/electricity_in_south_africa.htm. [2011, October 1].
- Faridi RA. 2011. *Waste heat recovery: new hope for energy conservation* [Online]. Available: <http://rashidfaridi.wordpress.com/2011/06/09/waste-heat-recoverynew-hope-for-energy-conservation/>. [2011, July 31].

Ferland K. 2007. *Industrial Waste Heat Recovery energy, round table Hudson, Technology Company* [Online]. Available: http://texasiof.ces.utexas.edu/PDF/Documents_Presentations/Roundtables/RoundTable_0807.pdf. [2010, September 20].

Fujima K, Kato Y & Nitawaki T. 2000. Zero heat release nuclear cogeneration system using carbon dioxide as working fluid. *Research Laboratory for Nuclear Reactors*, Tokyo Institute of Technology 2-12-1, Tokyo 152-8550.

Fuls WF and Mathews EH. 2006. Passive cooling of the PBMR spent and used fuel tanks. *Nuclear Engineering and design*, 237, 1354-1362.

Fuls WF, Viljoen C, Stoker C, Koch C & Kleingeld M. 2005. The interim fuel storage facility of the PBMR. *Annals of nuclear energy*, 32, 1854–1866.

Goswami DY, Xu L & Feng X. 1999. Analysis of a new thermodynamic cycle for combined power and cooling using low and mid temperature solar collectors. *Journal of solar energy Engineering ASME*. 121, 91-97.

Hettiarachchi MHD, Golubovic M, Worek WM & Ikegami Y. 2006. Optimum design criteria for an organic Rankine cycle using low-temperature geothermal heat sources. Institute of Ocean energy saga. University Honjomachi 1, Saga 840-8502, Japan.

Hoyt SL. 1954. *ASME hand book of metals properties*. 1st edn. McGraw Hill: New York.

Juchymenko V. 2007. *Waste heat recovery from gas compressor reciprocating engines* [Online]. Available: http://www.globalmethane.org/documents/events_oilgas_20070115_waste_heat_recovery_from_compressor.pdf. [2010, August 31].

Kakac S and Liu H. 2002. *Heat exchangers, selection, rating and thermal design*. 2nd edn. CCR press: Boca Raton.

Kakac S and Liu HT. 1991. *Two-phase flow dynamic instabilities in boiling, Multiphase Flow and Heat Transfer*. Hemisphere: Washington DC.

Kays WM and London AL. 1984. *Compact heat exchangers*. 3rd edn. McGraw-Hill: New York.

Kilundu B, Dehombreux P & Chimentin X. 2009. Early detection of bearing damage by means of decision trees. *Journal of Automation, Mobile Robotics & Intelligent Systems*, 3(3).

Kim JM and Lee SY. 1999. Experimental observation of flow instability in a semi-closed two-phase natural circulation loop. *Nuclear Engineering and Design*, 196, 359–367.

Kolin I. 1991. *Stirling, motor, history, theory and practice*. Zagreb University Publications: Zagreb.

- Kröger DG. 1998. *Air-cooled heat exchangers and cooling towers, thermal-flow performance evaluation and design*. Penwell Corporation: Tulsa.
- Lu S and Goswami DY. 2002. Theoretical analysis of ammonia-based combined power/refrigeration cycle at low refrigeration temperatures, *Solar Energy and Energy conversion laboratory University of Florida*, FL32611-6300, Gainesville.
- Mayson R. 2005. Latest Nuclear Reactor Technologies. In: *BEAwec Workshop*, 14 April.
- Meirovitch L. 2001. *Fundamentals of vibrations*. International Edn. McGraw-Hill: New York.
- Mills AF. 1999. *Heat Transfer*. 2nd edn. Prentice Hall: Upper Saddle River.
- Minassians AD. 2007. Stirling engines for low-temperature solar thermal electric power generation. PhD thesis, University of California: California.
- Morel J. 1979. Surveillance vibratoire et maintenance predictive. *Technique de l'Ingenieur*, doc R 6 100, 1-20.
- Mori M, Chiang JH & Aritomi M. 1993. Fundamental study on thermo-hydraulics during start up in natural circulation boiling water reactors (II) natural circulation oscillation induced by hydrostatic head fluctuation. *Journal of nuclear Science and technology*, 30, 203–211.
- Mulapi W. 2002. Cours d'équilibrage et vibration des machines. Université de Mbuji-Mayi: Mbuji-Mayi.
- Park JW, Dan R & Wirtz RA. 2002. *Thermal/fluid characteristics of isotropic plain Weave screen laminates as heat exchange surfaces*. University of Nevada: Reno.
- Pellegrino J, Brueske S, Carole T & Andres H. 2007. *Energy and Environmental Profiles of the U.S. Petroleum Refinery Industry*, the U.S Department of Energy [Online]. Available: http://www1.eere.energy.gov/industry/petroleum_refining/pdfs/profile.pdf. [2008, January 13].
- Reay DA. 1979. *Heat recovery systems, a directory of equipment and techniques*. Spon: London.
- Reiter S. 1983. *Industrial and Commercial Heat Recovery Systems*. Van Nostrand Reinhold Company Inc: New York.
- Ruppertsberg JC. 2008. Transient Modelling of a Loop Thermosyphon Transient Effects in Single and Two Phases natural circulation Thermosyphon loop suitable for the Reactor Cavity Cooling of a Pebble Bed Modular Reactor. Msc Thesis, University of Stellenbosch: Stellenbosch.

Schleicher R, Raffray AR, & Wong CP. 2001. An Assessment of the Brayton cycle for high performance power plants. *General Atomics*: University of California, and San Diego.

Senda FM. 2004. Analyse Dynamique du reducteur de vitesse Hassen Patent a la commande pour transporteur a bande, cas du transporteur n°3 de l usine central de la Miba. TFE, Universite de Mbuji-Mayi: Mbuji-Mayi.

Shah MM. 1979. A general correlation for heat transfer during film condensation inside pipes. *International journal of heat mass Transfer*, 22, 547-556.

Shigley JE, Mischke CR & Budynas RG. 2003. *Mechanical Engineering Design*. 7th edn. McGraw-Hill: Singapore.

Slabber J. 2006. Technical Description of the PBMR Demonstration Power Plant. PBMR Doc No. 016956, Rev 4.

Slabber J. 2008. Personal communication. 31 January, Stellenbosch.

Smith GR. 2006. Building, Testing and modelling of a Pulse Tube cryogenic cooler. Msc Thesis, University of Stellenbosch: Stellenbosch.

Snyman H, Harms TM & Strauss JM. 2008. Design analysis methods for Stirling engines. *Journal of energy in South Africa*, 19(3).

Soleimani AG. 2005. Simple functions for predicting the thermodynamic properties of ammonia-water mixture. *IJE Transactions A: Basics* 20(1).

South Africa.info. 2004. *Nuclear energy in South Africa* [Online]. Available: http://www.South-africa.info/doing_business/economy/infrastructure/nuclear-energy.htm [2011, September 3].

Taylor JR. 1982. *An Introduction to Error Analysis: The study of uncertainties in physical measurements*. 2nd edn. University Science Books: Colorado.

The PBMR. [S.a]. [Online]. Available: http://seagull.ukzn.ac.za/~moodley/ReactorTheory/PBMR_only.pdf.

Tlili S. 2002. Modelisation des moteurs Stirling. DEA, ecole national d' Ingenieurs de monastir: Tunisie.

Tlili S and Timoumi Y. 2006. Numerical simulation and losses analysis in a Stirling engine. *International journal of heat and technology*, 24, 97–103.

Thombare DG and Verma. 2006. Technological development in the Stirling cycle engines. *Renewable and sustainable energy review*, 12, 1-38.

Urieli I. 1977. A computer simulation of the Stirling cycle machine. PhD thesis, University of the Witwatersrand: Johannesburg.

US Department of Energy. 2005. Energy Tips-Process Heating (Process Heating Tip Sheet#8) [Online]. Available: http://www1.eere.energy.gov/industry/bestpractices/pdfs/install_waste_heat_process_htgts8.pdf. [2008, July 2].

Walker G. 1980. *Stirling engines*. Clarendon press: Oxford.

Walker G and Sent JR. 1985. *Free-piston Stirling engines*. Springer: Berlin.

Waste heat recovery systems. [S.a.]. [Online]. Available: <http://www.tesplcogen.com/Waste%20Heat%20Recovery%20Boiler.pdf>. [2008, June 30].

Webb RL. 1994. *Principles of enhanced heat transfer*. John Wiley and Sons: New York.

Wei D, Lu X, Lu Z, & Gu J. 2007. Performance analysis and optimization of organic Rankine cycle (ORC) for waste heat recovery. *Energy Conversion and Management*, 48, 1113–1119.

Welander PJ. 1967. On the oscillatory instability of a differentially heated fluid loop. *Journal of Fluid Mechanics*, 29(1), 17-30.

Yang R, Wang SB & Pan C. 2006. Experimental study on convective heat transfer of water flow in heated tube under natural circulation. *Nuclear Engineering and Design*, 236, 1902-1908.

Young W. 1975. *Roark's formulas for stress and strain*. 6th edn. McGraw-Hill: New York.

Yuan Z and Dybbs. 1992. Oscillating flow and heat transfer in a Stirling engine regenerator. *The 28th National Heat Transfer Conference and Exhibition*, 193, 73-85.

Zibi Z and Koronchinsky S. 2006. Dose rate analysis for the design process of the PBMR core conditioning system. *3rd international Topical Meeting on Temperature Reactor Technology*. 1-4 October, Johannesburg.

Appendix A Waste heat recovery systems thermal efficiencies computations algorithms

A.1 Dual-function absorption cycle thermal efficiency

Table A.1: Summary of calculation for different characteristic points of the DFAC

State	Temperature [K]	Pressure	Enthalpy	Quality
1	$T_1 = T_{abs}$ $T_{abs} = T_{amb} + 5$	$P_1 = P_{low}$ $P_{low} = P_{sat}(T_1)$ fluid:(NH ₂ +H ₂ O)	$h_1 = h(x_1, T_1)$	$x_1 = x(P_1, T_1)$
2	$T_2 = \frac{T_{2is} - T_1}{\eta_{is,p}} + T_1$ $T_{2is} = T_1 \left(\frac{P_2}{P_1} \right)^{\frac{1-n}{n}}$	$P_2 = P_{high}$ $P_{high} = P_{sat}(T_2)$ fluid:(NH ₂ +H ₂ O)	$h_2 = h(x_2, T_2)$	$x_1 = x_2$
3	$T_3 = T_2 - \frac{\epsilon_{reg}}{\dot{m}_3 c_p} [\min(\dot{Q}_{hot}, \dot{Q}_{cold})]$ $T_3 = T_{11} - 5$ See point 12	$P_{12} = P_{high}$	$h_3' = h(x_3, T_3)$ $h_3 = h(x_3, T_3)$	$x_3 = x_2$
4	$T_4 = T(x_4, h_4)$	$P_4 = P_{high}$	$h_4 = h_3 + h_{15}$	$x_4 = x_2$
5	$T_5 = T_{vg}$ $T_{vg} = T_{hot}$	$P_5 = P_{high}$	$h_5 = h(x_5, T_5)$	$x_5 = x(\bar{m}_{l,vg}, x_4, x_{11})$ See point 11
6	$T_6 = T_{rectifier}$	$P_6 = P_{high}$	$h_6 = h(x_6, T_6)$	$x_6 = x(\bar{m}_{l,rest}, x_5, x_7)$ See point 7
7	$T_7 = T_{rectifier}$	$P_7 = P_{high}$	$h_7 = h(x_7, T_7)$	$x_7 = \frac{x_5 - x_6}{\bar{m}_{v,rect}} + x_6$ $\bar{m}_{v,rect} + \bar{m}_{l,rect} = 1$ $\bar{m}_{v,rect} = \dot{m}_7 / \dot{m}_5$ $x_6 = \frac{x_5 - \bar{m}_{l,rect} x_7}{1 - \bar{m}_{l,rect}}$ $\bar{m}_{l,rect} = \dot{m}_7 / \dot{m}_5$
8	$T_8 = T_{sh}$	$P_8 = P_7$	$h_8 = h(x_8, T_8)$	$x_8 = x_7$
9	$T_9 = T_8 - \eta_{is,t} (T_{9is} - T_8)$	$P_9 = P_{low}$	$h_9 = h(x_9, T_9)$	$x_9 = x_8$
10	$T_{10} = T_{amb} - 5$	$P_{10} = P_9$	$h_{10} = h(x_{10}, T_{10})$	$x_{10} = x_9$
11	$T_{11} = T_5$	$P_{11} = P_5$	$h_{11} = h(x_{11}, T_{11})$	$x_{11} = \frac{x_4 - \bar{m}_{v,vg} x_5}{1 - \bar{m}_{v,vg}}$ $\bar{m}_{v,vg} + \bar{m}_{l,vg} = 1$ $\bar{m}_{v,vg} = \dot{m}_5 / \dot{m}_4$ $x_5 = \frac{x_{11} - \bar{m}_{l,vg} x_4}{1 - \bar{m}_{l,vg}}$ $\bar{m}_{l,vg} = \dot{m}_{11} / \dot{m}_4$

State	Temperature [K]	Pressure	Enthalpy	Quality
12	$T_{12} = T_{11} - \frac{\dot{Q}_{reg}}{\dot{m}_{11} c_p} [\min(\dot{Q}_{hot}, \dot{Q}_{cold})]$ $\dot{Q}_{hot} = \dot{m}_{11} (h_{11} - h'_{12})$ $\dot{Q}_{cold} = \dot{m}_3 (h'_3 - h_3)$ $T'_{12} = T_2 + 5$	$P_{12} = P_{high}$	$h'_{12} = h(x_{12}, T'_{12})$ $h_{12} = h(x_{12}, T_{12})$	$x_{12} = x_{11}$
13	$T_{13} = T(x_{13}, h_{13})$	$P_{13} = P_{high}$	$h_{13} = \frac{\dot{m}_6 h_6 - \dot{m}_{12} h_{12}}{\dot{m}_{13}}$	$x_{13} = \frac{\dot{m}_6 x_6 - \dot{m}_{12} x_{12}}{\dot{m}_{13}}$
14	$T_{14} = T(x_{14}, h_{14})$	$P_{14} = P_{low}$	$h_{14} = h_{13}$	$x_{14} = \frac{\dot{m}_1 x_1 - \dot{m}_{10} x_{10}}{\dot{m}_{14}}$
15	$T_{15} = T(x_{15}, h_{15})$	$P_{15} = P_{high}$	$h_{15} = h_4 - h_3$	$x_{15} = x_2$

Considering the DAFC energy flow schematic diagram as shown in figure 2.7, the thermal efficiency of the DAFC may be computed as proposed by Lu and Goswami (2002) in terms of their so-called first law efficiency given by the following equation

$$\eta_{DAFC} = \frac{W_{net} + \dot{Q}_{ref}}{\dot{m}_{hs} (h_{hs}^{in} - h_{hs}^{out})} \quad (A.1.1)$$

From figure 2.7, a summary of calculations for different characteristic points of the DAFC is presented in tables A.1.1a and A.1.1b. All the energy balanced equations characterising the DAFC are as follows:

The vapour generator heat input

$$\dot{Q}_{vg} = \dot{m}_{11} h_{11} - \dot{m}_5 h_5 - \dot{m}_4 h_4 \quad (A.1.2)$$

The super-heater heat input

$$\dot{Q}_{sh} = \eta_{is}^{-1} \dot{m}_6 (h_7 - h_8) \quad (A.1.3)$$

Rectifier heat transfer

$$\dot{Q}_{rect} = \dot{m}_7 h_7 + \dot{m}_6 h_6 - \dot{m}_5 h_5 = \dot{m}_{15} (h_{15} - h_2) \quad (A.1.4)$$

Heat regenerated

$$\dot{Q}_r = \dot{m}_3 h_3 - \dot{m}_{11} h_{11} - \dot{m}_{12} h_{12} - \dot{m}_2 h_2 \quad (A.1.5)$$

Absorber heat rejection

$$\dot{Q}_{abs} = \dot{m}_1 h_1 - \dot{m}_{14} h_{14} - \dot{m}_{10} h_{10} \quad (A.1.6)$$

Pump work input

$$W_p = \dot{m}_1 (h_2 - h_1) \quad (A.1.7)$$

Refrigeration output

$$\dot{Q}_{ref} = \dot{m}_9 (h_{10} - h_9) \quad (A.1.8)$$

Turbine work out put

$$W_t = \dot{m}_8 (h_9 - h_8) \quad (A.1.9)$$

Considering the basic cycle configuration shown in figure 3.7, eight independent variables are not sufficient to evaluate the characteristics points in the cycle. Two more variables are

required to determine the heat source conditions. Therefore, the following assumptions will be taken into consideration:

All losses in the system are neglected

The pressure losses in piping and equipment are neglected

An isentropic efficiency is assumed for the pump and the turbine

All processes are assumed to end in equilibrium thermodynamic states.

The absorber is set a little above the ambient temperature.

The DAFC thermal efficiency is computed from equation (A.1.1) with all cycle characteristic points found as presented in table (A.1.1a) and (A.1.1b). Therefore in equation (A.1.1) the cycle net work is found as:

$$W_{net} = W_t - W_p \quad (\text{A.1.10})$$

Thermodynamic properties such as enthalpy values are obtained from experimental correlations given in the literature by Soleimani, (2005)

A.2 Organic Rankine cycle

Cengel and Boles (2002) defined the thermal efficiency for an organic Rankine cycle as

$$\eta_{org} = \frac{\dot{Q}_{ev} - \dot{Q}_{co}}{\dot{Q}_{ev}} \quad (\text{A.2.1})$$

From figure 2.8 the heat supply to the generator is found as

$$\dot{Q}_{ev} = \dot{m}_{wf}(h_5 - h_3) \quad (\text{A.2.2})$$

The heat rejected to the condenser is found as

$$\dot{Q}_{co} = \dot{m}_{wf}(h_7 - h_1) \quad (\text{A.2.3})$$

Substituting equations (A2.2) and (A2.3) in (A2.1), and for the same working fluid mass flow rate \dot{m}_{wf} the ORC may be simplified as

$$\eta_{org} = 1 - \frac{T_7 - T_1}{T_5 - T_3} \quad (\text{A.2.4})$$

A.3 Stirling engine thermal efficiency

All losses encountering in a SE reduce the actual engine performances. This is well understood by defining the engine thermal efficiency as the ratio of the power output to the power input.

$$\eta_{FPSE} = P_{out}/\dot{Q} \quad (\text{A.3.1})$$

Walker, (1980) proposed Stirling engine efficiency as a function of the Carnot efficiency given by

$$\eta_{th} = \eta_c \frac{T_h - T_c}{T_h} \quad (\text{A.3.2})$$

With the Carnot efficiency selected in the range of 0.4 to 0.5

Appendix B Integration of conservation equations and heat transfer dimensionless parameters

B.1 Integration of conservation equations

Departing from equation (3.4.4) and considering the quasi-static and the incompressible flow assumptions in a homogenous flow

$$\frac{\Delta E}{\Delta t} = (\dot{m}h)_{in} - (\dot{m}h)_{out} \pm \dot{Q} \quad (\text{B.1.1})$$

$$\frac{\Delta}{\Delta t} [m(u + \frac{v^2}{2} + gz)] = (\dot{m}h)_{in} - (\dot{m}h)_{out} \pm \dot{Q} \quad (\text{B.1.2})$$

Considering equation (3.4.2) for the quasi-static and the incompressible flow

$$\frac{\Delta m}{\Delta t} = \dot{m}_{in} - \dot{m}_{out} \quad (\text{B.1.3})$$

$$0 = \dot{m}_{in} - \dot{m}_{out} \rightarrow \dot{m}_{in} = \dot{m}_{out} = \dot{m} = \rho v A_z \quad (\text{B.1.4})$$

So that equation (B.3) becomes

$$\frac{\Delta}{\Delta t} [m(u + \frac{v^2}{2} + gz)] = \dot{m}(h_{in} - h_{out}) \pm \dot{Q} \quad (\text{B.1.5})$$

Neglecting the kinetic and potential energy terms as explained in section 3.3.3.4 equation (B.1.5) becomes

$$\frac{\Delta}{\Delta t} [mu] = \dot{m}(h_{in} - h_{out}) \pm \dot{Q} \quad (\text{B.1.6})$$

The finite difference method may only be applied for small values of Δt , therefore when Δt converge to zero or simply if $\Delta t \rightarrow 0$ equation (B.1.6) takes the form

$$\frac{d}{dt} [mu] = \dot{m}(h_{in} - h_{out}) \pm \dot{Q} \quad (\text{B.1.7})$$

$$u \frac{dm}{dt} + m \frac{du}{dt} = \dot{m}(h_{in} - h_{out}) \pm \dot{Q} \quad (\text{B.1.8})$$

Substituting (B.1.3) in (B.1.8) it may be seen that

$$m \frac{du}{dt} = \dot{m}(h_{in} - h_{out}) \pm \dot{Q} \quad (\text{B.1.9})$$

Integrating equation (B.1.8) from t to $t+\Delta t$, it becomes

$$\int_t^{t+\Delta t} m du = \int_t^{t+\Delta t} (\dot{m}(h_{in} - h_{out}) \pm \dot{Q}) dt \quad (\text{B.1.10})$$

Solving the integral of equation (B.1.10)

$$u^{t+\Delta t} = u^t + \frac{\Delta t}{m} [\dot{m}(h_{in} - h_{out}) \pm \dot{Q}] \quad (\text{B.1.11})$$

For an incompressible liquid the internal energy and specific heat is a function of the temperature alone, therefore $du = c_v dT$. Thus (B.1.11) may be rewrite as

$$\int_t^{t+\Delta t} m c_v dT = \int_t^{t+\Delta t} (\dot{m}(h_{in} - h_{out}) \pm \dot{Q}) dt \quad (\text{B.1.12})$$

$$T^{t+\Delta t} = T^t + \frac{\Delta t}{m c_v} [\dot{m}(h_{in} - h_{out}) \pm \dot{Q}] \quad (\text{B.1.13})$$

Applying equation (B.1.13) to the cooling Jacket, the initial temperature assumed to be the temperature of the spent fuel in the fuel tank is known. Therefore on this particular section heat is added to the control volume as given in equation (3.3.1). The temperature of the working fluid in the thermosyphon heating section at the next time step may be computed given as

$$T_f^{t+\Delta t} = T_f^t + \frac{\Delta t}{mc_v} \left[\dot{m}(h_{in} - h_{out}) + \frac{T_{w,ft} - T_{cj}^t}{R_{ft,cj}} \right] \quad (B.1.14)$$

In the cooling jacket the term $\dot{m}(h_{in} - h_{out})|_{cj}$ is also equal to the evaporative heat transfer that leaves the cooling jacket, when heat is added from the fuel tank, therefore:

$$\dot{Q}_{ev} = \dot{m}(h_{in} - h_{out})|_{cj} = \dot{m}_{ev}h_{fg} \quad (B.1.15)$$

Substituting equation (B.1.15) in (B.1.14) the temperature of the working fluid at the next step in the thermosyphon heating section is found as

$$T_f^{t+\Delta t} = T_f^t + \frac{\Delta t}{mc_v} \left[\frac{T_{w,ft} - T_{cj}^t}{R_{ft,cj}} - \dot{m}_{ev}h_{fg} \right] \quad (B.1.16)$$

Applying equation (B.1.13) to an air cooled air condenser control volume as shown in figure B.1. Where the ambient temperature is know, it may be seen that the temperature of the working fluid at the next time step may be found as:

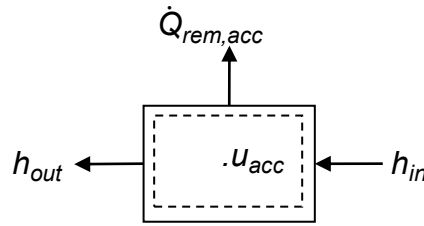


Figure B.1: Air-cooled condenser control volume

$$T_{acc}^{t+\Delta t} = T_{acc}^t + \frac{\Delta t}{mc_v} \left[\dot{m}c_p(T_{acc,in}^t - T_{acc,out}^t)_{ac} - \frac{T_{acc}^t - T_a}{R_{tot}} \right] \quad (B.1.17)$$

B.2 Heat transfer dimensionless parameter

B.2.1 Convection, boiling, evaporative and Froude number

The convection, boiling, evaporative and Froude numbers used in this project are given by the following equations

The convection number (Kakac and Liu, 2002)

$$Co = ((1-x)/x)^{0.8} (\rho_g / \rho_l)^{0.5} \quad (B.2.1)$$

The boiling number (Kakac and Liu, 2002):

$$Bo = \dot{Q}_{ev} / \dot{m}_{cw} h_{fg,cw} \quad (B.2.2)$$

The Froude number (Kakac and Liu, 2002):

$$Fr_l = G^2 / (\rho_l^2 g d_{ev,op}) \quad (B.2.3)$$

The cooling water mass flow rate may be computed as a function of the water velocity, the mean density and the shell side cross-sectional area as shown in figure 3.4b.

$$\dot{m}_{cw} = \bar{\rho} \dot{x}_{cw} A_{sh} = \bar{\rho} \dot{x}_{cw} ((d_{ev} - 2W_{ev})^2 - N_p d_{ev,op}^2) / 4 \quad (\text{B.2.4})$$

The values of the dimensionless parameter; in the bubble suppression regime ψ_{bs} , in the pure convective boiling regime ψ_{cb} and in the nucleate boiling regime ψ_{nb} are given in reference by Kakac and Liu (2002) as

$$\text{If } Co > 1 \text{ and } Bo > 0.3 \times 10^4 \text{ then } \psi_{cb} = 1.8Co^{-0.8} \text{ and } \psi_{nb} = 230Bo^{0.5} \quad (\text{B.2.5})$$

$$\text{If } Co > 1 \text{ and } Bo < 0.3 \times 10^4 \text{ then } \psi_{cb} = 1.8Co^{-0.8} \text{ and } \psi_{nb} = 1 + 46Bo^{0.5} \quad (\text{B.2.6})$$

$$\text{If } 0.1 < Co \leq 1 \text{ then } \psi_{bs} = Bo^{0.5} \exp(2.47Co^{-0.1}) \quad (\text{B.2.7})$$

$$\text{If } Co \leq 1 \text{ then } \psi_{bs} = FBo^{0.5} \exp(2.47Co^{-0.15}) \quad (\text{B.2.8})$$

The constant F in equations (B.2.7) and (B.2.8) is found as follows (Kakac and Liu, 2002)

$$F = 14.7 \text{ for } Bo \geq 11 \times 10^{-4} \text{ and } F = 15.43 \text{ for } Bo < 11 \times 10^{-4}$$

B.2.2 Friction factor

The laminar and turbulent friction factor correlations, as presented in Kakac and Liu (2002), are given by:

$$\text{If } Re_d \leq 1181 \text{ then } C_f = 1/Re_d \quad (\text{B.2.9})$$

$$\text{If } Re_d \leq 2 \times 10^3 \text{ then } C_f = 0.0791Re_d^{-0.25} \quad (\text{B.2.10})$$

$$\text{If } Re_d \geq 2 \times 10^3 \text{ then } C_f = 0.046Re_d^{-0.2} \quad (\text{B.2.11})$$

After extrapolating the smooth pipe curve until it intercepts the laminar flow curve in the Moody diagram, Dobson (2005) suggests that the transition point between laminar and turbulent flow is in the neighbourhood of the Reynolds number of 1181.

B.2.3 Nusselt Number

Heat transfer coefficients are approximated using the Nusselt model, as given in equation (3.2.26). The Nusselt number correlations are given first in terms of single-phase flow and then in terms of two-phase flow for a smooth surface condition in a single pipe and then in more than one pipe.

For laminar flow ($Re_d \leq 2300$), the Nusselt Number correlation is given as (Mills, 1999):

$$Nu_d = 3.66 + \frac{0.065(d/L)Re_d Pr}{1 + 0.04[(d/L)Re_d Pr]^{2/3}} \quad (\text{B.2.12})$$

For turbulent flow ($2300 \leq Re_d \leq 10^4$) the Gnielinski correlation is recommended and is given by (Kakac and Liu, 2002):

$$Nu_d = \frac{(f/2)(Re_d - 1000)Pr_d}{1 + 1.27(f/2)^{1/2}(Pr_d^{2/3} - 1)} \quad (\text{B.2.13})$$

In the case of a Reynolds numbers greater than 10^4 or ($10^4 \leq Re_d \leq 5 \times 10^6$), the Webb correlation is recommended, and is given by (Kakac and Liu, 2002):

$$Nu_d = \frac{(f/2)Re_d Pr_d}{1.07 + 9(f/2)^{1/2}(Pr_d - 1)Pr_d^{-1/4}} \quad (\text{B.2.14})$$

Appendix C Sample calculations

C.1 Properties of fluid

C.1.1 Properties of air

The following thermo-physical properties of air are adopted from Congel and Boles (2002)

$$\text{Density: } \rho = 8.52333344 \times 10^{-17} T^6 - 3.2630691 \times 10^{-13} T^5 + 5.0903405 \times 10^{-10} T^4 \\ - 0.00000041699 T^3 + 0.000192583462 T^2 - 0.049869465 T + 6.6708097$$

$$\text{Specific heat at constant pressure: } C_p = 6.4531274 \times 10^{-15} T^6 - 2.0858673 \times 10^{-11} T^5 \\ + 2.5725831 \times 10^{-8} T^4 - 0.000015461597 T^3 + 0.0051330888 T^2 - 0.94513242 T + \\ 1083.449$$

$$\text{Thermal conductivity: } k = -9.9188021 \times 10^{-20} T^6 + 3.6893529 \times 10^{-16} T^5 - 5.7660479 \times 10^{-13} T^4 \\ + 4.9974035 \times 10^{-10} T^3 - 2.6206987 \times 10^{-7} T^2 + 1.366277 \times 10^{-4} T - \\ 2.3880862 \times 10^{-4}$$

$$\text{Kinematic viscosity: } \mu/\rho = -2.1515612 \times 10^{-22} T^6 + 7.56314 \times 10^{-19} T^5 - 1.02857 \times 10^{-15} T^4 \\ + 6.6035816 \times 10^{-13} T^3 - 1.1432998 \times 10^{-10} T^2 + 6.2789679 \times 10^{-8} T - \\ 4.1066067 \times 10^{-6}$$

$$\text{Prandtl number: } Pr_a = \mu_a C_{p,a} / k_a$$

C.1.2 Properties of water

The following thermo-physical properties of saturated water from 273.15-380 K, are adopted from Kröger (1998)

Specific heat at constant pressure:

$$C_{p_v} = 1.3605 \times 10^3 + 2.331334 T - 2.46784 \times 10^{-10} T^5 + 5.91332 \times 10^{-13} T^6$$

$$C_{p_l} = 8.15599 \times 10^3 - 28.0627 T + 5.11283 \times 10^{-2} T^2 - 2.17582 \times 10^{-13} T^6$$

Dynamic viscosity:

$$\mu_v = 2.56243 \times 10^{-6} + 1.816683 \times 10^{-8} T + 2.579066 \times 10^{-11} T^2 - 1.06729831 \times 10^{-14} T^3$$

$$\mu_l = 2.4141 \times 10^{-5} \times 10^{247.8/(T-140)}$$

Thermal conductivity:

$$k_v = 1.3046 \times 10^{-2} - 3.75619 \times 10^{-5} T + 2.217964 \times 10^{-7} T^2 - 1.111562 \times 10^{-10} T^5$$

$$k_l = -6.14255 \times 10^{-3} + 6.9962 \times 10^{-3} T - 1.01075 \times 10^{-5} T^2 + 4.74737 \times 10^{-12} T^4$$

Density:

$$\rho_v = -4.062329056 + 0.10277044 T - 9.76300388 \times 10^{-4} T^2 + 4.475240795 \times 10^{-6} T^3 \\ - 1.004596894 \times 10^{-8} T^4 + 8.9154895 \times 10^{-12} T^5$$

$$\rho_l = (1.49343 \times 10^{-3} - 3.7164 \times 10^{-6} T + 7.09782 \times 10^{-9} T^2 - 1.90321 \times 10^{-20} T^6)^{-1}$$

Latent heat of evaporation:

$$h_{fg} = 3.483181 \times 10^6 - 5.8627703 \times 10^3 T + 12.139568 T^2 - 1.40290431 \times 10^{-2} T^3$$

Prandtl number:

$$Pr_l = \mu_l C_{p,l} / k_l$$

$$Pr_v = \mu_v C_{p,v} / k_v$$

The saturation temperature as a function of the saturation pressure:

$$T = 164.630366 + 1.832295 \times 10^{-3} P + 4.27215 \times 10^{-10} P^2 + 3.738954 \times 10^3 P^{-1} - 7.01204 \times 10^{-5} P^{-2} + 16.161488 \ln(P) - 1.437169 \times 10^{-4} P \ln(P)$$

C.2 Waste heat recovery

Calculations carried out on the waste heat recovery system are now described. First, theoretical sample calculations as developed in sections (3.3) and (3.4) are presented. Then calculations of the thermal resistance of the air-cooled condenser and the heat exchanger referring, on the experimental data measured relating to sections (3.4.3.2) and (3.4.3.3) are presented.

C.2.1 Theoretical calculations on the air-cooled condenser line

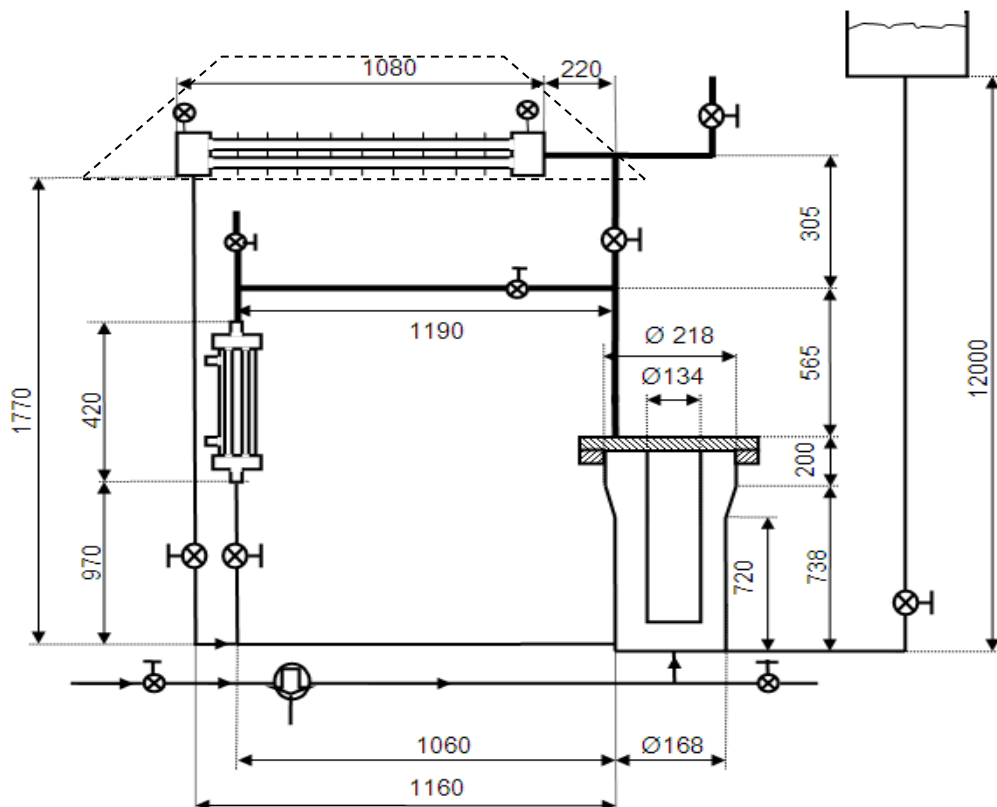


Figure C.1: Geometric dimensions of the WHR&US experimental set-up

Table C1 gives detailed layout geometrical dimensions and the thermo-physical properties of the material used for the air-cooled condenser. Referring to figure 3.6 and figure C.1, the dimensions used in the theoretical model are presented in table C.2. In this table L is the

length of the WHR&US experimental set-up sections as given in figure C.1. Sample calculation for one time step is shown for a section situated in the middle of the air-cooled condenser.

Table C.1: Air-cooled condenser layout geometrical dimensions and thermo-physical properties

Geometrical layout dimensions	Thermo-physical properties
Fin thickness: $t_{fin} = 0.0009 \text{ m}$ Length fin: $b = 0.12 \text{ m}$ Height fin: $a = 0.065 \text{ m}$ Longitudinal pitch: $S_L = 0.027 \text{ m}$ Transversal pitch: $S_T = 0.026 \text{ m}$ Fin space: $S_{fin} = 0.005 \text{ m}$ Pipe wall thickness: $t_p = 0.001 \text{ m}$ Number of pipes: $N_p = 7$	Fin density: $\rho_{fin} = 2600 \text{ kg/m}^3$ Fin specific heat: $c_{fin} = 900 \text{ J/kgK}$ Fin emissivity: $\varepsilon_f = 0.18$ Pipe emissivity: $\varepsilon_p = 0.7$ Form (view) factor: $F_{p,fin} = 1$ Air thermal expansion: $\beta_a = 1/\bar{T}_a = 3.1836 \times 10^{-3} \text{ K}^{-1}$ Stefan-Boltzmann constant: $\sigma = 5.67 \times 10^{-8} \text{ W/m}^2\text{K}^4$

Table C.2: WHR&US experimental setup grids dimensions

Number of grid N	ID		OD		Grid length $L_i = \frac{L}{N}$
	d_i	Number of pipes, N_i	d_o	Number of pipes, N_o	
N1 = 2	0	1	0.025	1	0.572
N2 = 4	0.134	1	0.168	1	0.2275
N3 = 1	0	1	0.022	1	0.565
N4 = 3	0	1	0.022	1	0.3966
N4a = 2	0	1	0.022	1	0.305
N5 = 1	0	1	0.022	1	0.113
N5a = 6	0	1	0.015	1	0.234
N6 = 4	0.015	4	0.054	1	0.105
N6a = 4	0	7	0.015	1	0.17
N7a=4	0	1	0.015	1	0.4425
N = 2	0	1	0.015	1	0.485
Na = 1	0	1	0.015	1	0.1

The time step interval, the initial values of the temperatures and mass flow rate used in the sample calculations are given in table C3.

Table C.3: The time step interval, the initial values of the temperatures and mass flow rate

Time step	Temperature	Mass flow rate
$\Delta t = 0.0015 \text{ s}$	$T_{acc,in,t} = 86.34567 \text{ }^\circ\text{C}$ $T_{acc,out,t} = 80.06748 \text{ }^\circ\text{C}$ $T_{acc,air,in,t} = 18.2342 \text{ }^\circ\text{C}$ $T_{acc,air,out,t} = 63.67827 \text{ }^\circ\text{C}$	$\dot{m} = 38.4524789 \times 10^{-3} \text{ kg/s}$

Pipe cross-section area control volume: $A_{o,unfin} = \pi N_p (d_o - 2t_p)^2 / 4 = 9.29126 \times 10^{-4} \text{ m}^2$

Pipe heat transfer area control volume: $A_{z,unfin} = \pi N_p (d_o - 2t_p) L_i = 49.076913 \times 10^{-3} \text{ m}^2$

Number of fins over the control volume length: $n_{fin} = (L_i / S_{fin}) + 1 = 34$

Total fin heat transfer area over the control volume:

$$A_{z,fin} = abn_{fin} \left[1 - (\pi d_i^2 / (2S_T S_L)) + (\pi d_i t_{fin} / (S_T S_L)) \right] = 147.64432 \times 10^{-3} \text{ m}^2$$

Fin volume void fraction: $\epsilon_{fin} = \pi d_i^2 / (4S_T S_L) = 0.25173$

Total fin cross-section: $A_{o,fin} = n_{fin} b t_{fin} (1 - \epsilon_{fin}) = 2.7476 \times 10^{-3} \text{ m}^2$

Volume of the fin control volume: $V_{fin} = A_{o,fin} L_i = 0.46699 \times 10^{-3} \text{ m}^3$

Fin wetted perimeter: $p_{fin} = A_{z,fin} / a = 2.27145 \text{ m}$

Mass of fin control volume: $m_{fin} = \rho_{fin} V_{fin} = 1.260873 \text{ kg}$

Volume of air control volume: $V_a = (n_{fin} - 1) S_{fin} ab = 1.287 \times 10^{-3} \text{ m}^3$

The ACC working fluid mean temperature: $\bar{T}_{acc,t} = (T_{acc,in,t} + T_{acc,out,t}) / 2 = 83.206575 \text{ }^\circ\text{C}$

The ACC air mean temperature: $\bar{T}_a = \bar{T}_{acc,air,t} = (T_{acc,air,in,t} + T_{acc,air,out,t}) / 2 = 40.956235 \text{ }^\circ\text{C}$

Mass of air control volume: $m_a = \rho(@\bar{T}_a) V_a = 1.423422 \times 10^{-3} \text{ kg}$

Mass of the working fluid: $m = \rho_l(@\bar{T}_{acc,t}) \pi (d_o - 2t_p)^2 L_i / 4 = 21.8875 \times 10^{-3} \text{ kg}$

C.2.1.1 Air-cooled condenser heat transfer resistance

Recalling equation 3.4.8, the control volume total resistance is $R_{tot,acc,t} = R_{co,ip} + R_{co,wp} + R_{th}$, where, $R_{co,ip}$ is the working fluid side resistance, $R_{co,wp}$ the pipe wall resistance, and R_{th} the air side thermal resistance.

The air side thermal resistance: $R_{th} = [R_{co,op}^{-1} + R_{co,fin}^{-1} + R_{rad}^{-1}]^{-1}$

The Rayleigh number: $Ra_L = [g\beta(\bar{T}_{acc,t} - \bar{T}_{acc,air,t}) / (\mu / \rho(@\bar{T}_{acc,air,t}))^2] L_i^3 Pr_a = 14706881.91$

The ambient Nusselt Number: $Nu_a = \max(Nu_{a,1}, Nu_{a,2}, Nu_{a,3})$

$$Nu_{a,1} = \left[0.6 + 0.387 Ra^{1/6} / (1 + (0.559 / Pr_a(@\bar{T}_{acc,air,t}))^{9/16})^{8/27} \right]^2 = 5.617$$

$$Nu_{a,2} = 0.0605 Ra_L^{1/3} = 14.82275$$

$$Nu_{a,3} = \left[1 + [0.104 Ra_L^{0.293} / (1 + (6310 / Ra_L)^{1.36})] \right]^{1/3} = 13.0969$$

The ambient air heat transfer coefficient: $h_a = Nu_{a,2} k_a(@\bar{T}_{acc,air,t}) / S_{fin} = 83.3034 \text{ W/m}^2\text{K}$

The fin parameter: $\beta = (h_a p_{fin} / (k_{fin} A_{o,fin}))^{1/2} = 16.6 \text{ m}^{-1}$

The fin efficiency: $\eta_{fin} = \tanh(a\beta) / (a\beta) = 0.735$

The fin heat transfer coefficient: $h_{fin} = n_{fin} \eta_{fin} h_a = 2081 \text{ W/m}^2\text{K}$

The fin thermal resistance: $R_{co,fin} = [\rho_{fin} b h_{fin}]^{-1} = 0.001763 \text{ K/W}$

The convective air heat transfer coefficient:

$$h_{co,op} = N_p Nu_{a,2} k_a(@\bar{T}_{acc,air,t}) / d_o = 192.3002 \text{ W/m}^2\text{K}$$

The convective air thermal resistance: $R_{co,op} = (A_{o,unfin} h_{co,op})^{-1} = 0.10596 \text{ K/W}$

The radiation thermal resistance:

$$R_{rad} = \sigma^{-1} \left[(1 - \epsilon_p) / \epsilon_p A_{z,unfin} + 1 / F_{p,fin} A_{z,unfin} + (1 - \epsilon_{fin}) / \epsilon_{fin} A_{z,fin} \right] = 715831264.4 \text{ K/W}$$

The working fluid thermal resistance

The mass fraction:

$$x = \dot{m} \left(C_{p,l} (@T_{acc,in,t}) T_{acc,in,t} - C_{p,l} (@T_{acc,out,t}) T_{acc,out,t} \right) / h_{fg} (@T_{acc,in,t}) = 0.0124$$

$$\text{The two-phase non dimensional parameter: } Z = ((1 - x)/x)^{0.8} Pr_l^{0.4} = 45.5605$$

$$\text{Velocity of the working fluid in the manifold: } \dot{x}_{mon} = \dot{m} / (\rho_l (@T_{acc,in,t}) ab) = 0.005098 \text{ m/s}$$

Maximum flow velocity:

$$\dot{x}_{max} = \dot{x}_{mon} \max \left\{ \frac{S_T}{S_T - d_i}, \frac{S_T/2}{[S_L^2 + (S_T/2)^2]^{1/2} - d_i} \right\} = 0.005098 \times \max\{2.4, 0.87\} = 0.0122 \text{ m/s}$$

$$\text{The mass velocity: } G_{max} = \rho_l (\bar{T}_{acc,t}) \dot{x}_{max} = 11.834 \text{ kg/m}^2\text{s}$$

$$\text{The liquid Reynolds number: } Re_l = G_{max} (1 - x) d_o / \mu_l (@\bar{T}_{acc,t}) = 532.366$$

$$\text{The liquid Nusselt number: } Nu_l = 0.023 Re_l^{0.8} Pr_l^{0.4} (@\bar{T}_{acc,t}) = 4.7122$$

The liquid only heat transfer coefficient:

$$h_l = N_p Nu_l k_l (@\bar{T}_{acc,t}) / (d_o - 2t_p) = 1715.24084 \text{ W/m}^2\text{K}$$

$$\text{The convective heat transfer coefficient: } h_{unfin,in} = h_l (1 + 3.8Z^{-0.95}) = 1888.401666 \text{ W/m}^2\text{K}$$

$$\text{The inner convective thermal resistance: } R_{co,ip} = (2\pi L d_o N_p h_{unfin,in})^{-1} = 0.000778 \text{ K/W}$$

$$\text{The conduction thermal resistance: } R_{co,wp} = \ln(d_o / (d_o - 2t_p)) / 2\pi N_p L k_{cu} = 0.000047727 \text{ K/W}$$

$$\text{The Air side thermal resistance: } R_{th} = [R_{co,op}^{-1} + R_{co,fin}^{-1} + R_{rad}^{-1}]^{-1} = 0.001734 \text{ K/W}$$

The total resistance:

$$R_{tot,acc,t} = R_{co,ip} \text{ K/W} + R_{co,wp} + R_{th} = 0.000778 + 0.000047727 + 0.001734 = 0.00256$$

C.2.1.2 Temperatures at the next time step

Table C.4 gives the air collector dimensions. The measured air velocity and the electrical voltage supplied to the heating elements as well as the value of their electrical resistance

Table C.4: The air collector dimensions, air velocity and heating element characteristics

Air collector length: $L_{ac} = 0.2 \text{ m}$	Air Velocity: $v_{air} = 1.4 \text{ m/s}$
Air collector wide: $t_{ac} = 0.15 \text{ m}$	Electrical resistance: $R_{elek} = 12 \Omega$
Air collector cross area: $A_{ac} = L_{ac} t_{ac} = 0.03 \text{ m}^2$	Voltage supplied: $V_{sup} = 190 \text{ V}$

$$\text{The air mass flow rate: } \dot{m}_a = \rho (@\bar{T}_a) A_{ac} v_{air} = 0.05082 \text{ kg/s}$$

The air temperature:

$$T_{acc,air,out,t}^{t+\Delta t} = T_{acc,air,out,t}^t + \Delta t \frac{\dot{m}_a C_{p,a} (@\bar{T}_a)}{\dot{m}_a C_{v,a} (@\bar{T}_a)} (T_{acc,air,out,t}^t - T_{acc,air,in,t}^t) = 63.67967 \text{ } ^\circ\text{C}$$

Recalling equation B.1.11, the working fluid temperature:

$$T_{acc,out,t}^{t+\Delta t} = T_{acc,out,t}^t + \frac{\Delta t}{mc_{v,i}(@\bar{T}_{acc,t})} \left[\dot{m}C_{p,i}(@\bar{T}_{acc,t})(T_{acc,in,t}^t - T_{acc,out,t}^t) - \frac{\bar{T}_{acc,t} - \bar{T}_{acc,air,t}}{R_{tot}} \right] = 86.351102 \text{ } ^\circ\text{C}$$

C.2.1.3 Mass flow rate

The Fanning friction factor: $C_{f,j} = 16/Re_l = 3.00545 \times 10^{-2}$

The gravity term: $\sum_{k=1}^N \rho_k A_{i,k} \Delta Z_k \text{g sin } \theta_k / \sum_{k=1}^N (m_k / \rho_k A_{i,k}) = 4.362505 \times 10^{-2} \text{ kg/s}^2$

The friction and minor loss term:

$$\left[\sum_{j=1}^N \frac{1}{2} \left(\frac{C_{f,j} + k_j}{\rho_j} \right) \frac{(\dot{m})^2}{A_{i,j}^3} A_{j,k} \right] / \left[\sum_{k=1}^N \frac{m_k}{\rho_k A_{i,k}} \right] = 4.351556 \times 10^{-2} \text{ kg/s}^2$$

The momentum term:

$$\left[\sum_{k=1}^N \frac{\dot{m}_k^2}{A_{i,k}} \left(\frac{1}{\rho_{k-1/2}} - \frac{1}{\rho_{k+1/2}} \right) \right] / \sum_{k=1}^N \frac{m_k}{\rho_k A_{i,k}} = 94 \times 10^{-9} \text{ kg/s}^2$$

The mass flow rate at the next time step

$$\dot{m}^{t+\Delta t} = \dot{m}^t + \Delta t \left[\frac{-\sum_{k=1}^N \frac{\dot{m}_k^2}{A_{i,k}} \left(\frac{1}{\rho_{k-1/2}} - \frac{1}{\rho_{k+1/2}} \right) - \sum_{k=1}^N \rho_k A_{i,k} \Delta Z_k \text{g sin } \theta_k - \sum_{k=1}^N \Delta p_{frict,loss,k} A_{j,k}}{\sum_{k=1}^N \frac{m_k}{\rho_k A_{i,k}}} \right] = 38.32176 \times 10^{-3} \text{ kg/s}$$

C.2.1.4 Pressures at each time step

Gravitational pressure change over the control volume:

$$\Delta P_g = -\sum_{k=1}^N \rho_k \Delta Z_k \text{g sin } \theta_k = -46.013137 \text{ N/m}^2$$

The friction pressure change over the control volume:

$$\sum_{j=1}^N \Delta p_{frict,loss,j} = \sum_{j=1}^N \frac{1}{2} \left(\frac{C_{f,j} + k_j}{\rho_j} \right) \frac{(\dot{m}^t)^2}{A_{i,j}^3} A_{j,k} = 7.47685 \times 10^{-2} \text{ N/m}^2$$

The momentum pressure change over the control volume:

$$\Delta P_m = \sum_{k=1}^N \frac{\dot{m}_k^2}{(A_{i,k})^2} \left(\frac{1}{\rho_{k-1/2}} - \frac{1}{\rho_{k+1/2}} \right) = 10.96 \times 10^{-5} \text{ N/m}^2$$

The total pressure drop: $\Delta P = \Delta p_{frict,loss,j} - \Delta P_g - \Delta P_m = 46.877959 \text{ N/m}^2$

The outlet pressure at the next time step: $P_{acc,out} = P_{acc,in} - \Delta P = 99953.122 \text{ N/m}^2$

C.2.2 Calculation referring to the use of experimental data measured

The electrical power: $\dot{Q}_{elek} = V_{sup}^2 / R_{elek} = 3008.333 \text{ kW}$

The heat removed by the air cooled condenser:

$$\dot{Q}_{acc} = \rho(\bar{T}_{acc,air}) v_{air} A_{ac} C_{p,air}(@\bar{T}_{acc,air})(T_{acc,air,out,t} - T_{acc,air,in,t}) = 2386.92 \text{ W}$$

The experimental working fluid mass flow rate:

$$\dot{m}_e = \dot{Q}_{acc} / (h_{fg}(T_{acc,in,e}) - C_{p,l}(@\bar{T}_{acc,air})(273.15 + T_{acc,out,t})) = 34.6754 \times 10^{-3} \text{ kg/s}$$

The heat lost by the system: $\dot{Q}_{loss} = \dot{Q}_{elek} - \dot{Q}_{acc} = 621.413 \text{ W}$

The logarithmic temperature difference:

$$\Delta T_{In,acc} = \left(\frac{((T_{acc,in,t} - T_{acc,out,t}) - (T_{acc,air,out,t} - T_{acc,air,in,t}))}{\ln\left(\frac{(T_{acc,in,t} - T_{acc,air,out,t})}{(T_{acc,air,out,t} - T_{acc,air,in,t})}\right)} \right) = 19.787 \text{ }^\circ\text{C}$$

The correction factor:

$$F = LMTD \left(\left(\frac{T_{acc,air,out,t} - T_{acc,air,in,t}}{T_{acc,in,t} - T_{acc,air,in,t}} \right), \left(\frac{T_{acc,in,t} - T_{acc,out,t}}{T_{acc,in,t} - T_{acc,air,in,t}} \right) \right) = LMTD(0.7, 0.14) \approx 1$$

The total experimental thermal resistance:

$$R_{tot,acc,e} = F \Delta T_{In,acc} / \dot{Q}_{acc} = 0.00830 \text{ K/W}$$

C.2.3 Theoretical sample calculations on the heat exchanger line

Table C.5: The time step interval, the initial values of the temperatures and mass flow rate

Time step	Temperature	Mass flow rate
$\Delta t = 0.0015 \text{ s}$	$T_{he,in,t} = 90.4423 \text{ }^\circ\text{C}$	$\dot{m} = 38.4524789 \times 10^{-3} \text{ kg/s}$
	$T_{he,out,t} = 62.5213 \text{ }^\circ\text{C}$	$\dot{m}_{cw} = 35.3526615 \times 10^{-3} \text{ kg/s}$
	$T_{cw,in,t} = 18.1323 \text{ }^\circ\text{C}$	Electrical resistance: $R_{elek} = 12 \Omega$
	$T_{cw,out,t} = 38.4911 \text{ }^\circ\text{C}$	Voltage supplied: $V_{sup} = 190 \text{ V}$

The heat exchanger mean temperature: $\bar{T}_{he,t} = (T_{he,in,t} + T_{he,out,t}) / 2 = 78.4818 \text{ }^\circ\text{C}$

The cooling water mean temperature: $\bar{T}_{cw} = (T_{cw,out,t} + T_{cw,in,t}) / 2 = 28.3117 \text{ }^\circ\text{C}$

Sample calculations for one time step are shown for the heat exchanger line section situated in the middle of the heat exchanger is shown in this section. Table C6 gives detailed layout geometrical dimensions and the thermo-physical properties of the material used for the heat exchanger.

Table C.6: Heat exchanger layout geometrical dimensions and thermo-physical properties

Geometrical given data	Thermo-physical properties
Longitudinal pitch: $S_L = 0.016 \text{ m}$	Pipe emissivity: $\epsilon_p = 0.7$
Transversal Pitch: $S_T = 0.016 \text{ m}$	Form factor: $F_{p,fin} = 1$

Recalling equation (3.3.45) the heat exchanger thermal resistance is:

$$R_{he,t} = (U_{he} A_{z,he})^{-1} = \pi L_{he} \left[(d_{he,ip} h_{he,ip})^{-1} + (\ln(d_{he,op}/d_{he,ip})/2k_{cu}) + (d_{he,op} h_{he,op})^{-1} \right]$$

Pipe wall thickness and the number of pipes: $t_p = 0.001 \text{ m}$ and $N_p = 4$ respectively

$$\text{The Rayleigh number: } Ra_{he} = \left[g \beta_{cw} (\bar{T}_{he,t} - \bar{T}_{cw,t}) / (\mu/\rho (@\bar{T}_{cw,t}))^2 \right] d_o^3 Pr_{cw} = 458213314.64$$

The heat exchanger Working fluid thermal resistance

The mass fraction:

$$x_{he} = \dot{m} \left(C_{p,l} (@T_{he,in,t}) T_{he,in,t} - C_{p,l} (@T_{he,out,t}) T_{acc,out,t} \right) / h_{fg} (@T_{he,in,t}) = 0.0549$$

$$\text{The two-phase non dimensional parameter: } Z_{he} = ((1-x)/x)^{0.8} Pr_l^{0.4} (@T_{he,in,t}) = 13.8129$$

Velocity of the working fluid in the manifold:

$$\dot{x}_{mon,he} = 4 \dot{m} / (\rho_l (@T_{he,in,t}) \pi (d_o - t_p)^2) = 0.01807 \text{ m/s}$$

Maximum flow velocity:

$$\dot{x}_{max,he} = \dot{x}_{mon,he} \max \left\{ \frac{S_T}{S_T - d_i}, \frac{S_T/2}{[S_L^2 + (S_T/2)^2]^{1/2} - d_i} \right\} = 0.005098 \times \max\{2.4, 0.87\} = 0.0964 \text{ m/s}$$

$$\text{The mass velocity: } G_{max,he} = \rho_l (@\bar{T}_{he,t}) \dot{x}_{max,he} = 93.8243 \text{ kg/m}^2\text{s}$$

$$\text{The liquid Reynolds number: } Re_{l,he} = G_{max,he} (1-x)(d_i t_p) / \mu_l (@T_{he,in,t}) = 3252.2$$

$$\text{The liquid Nusselt number: } Nu_{l,he} = 0.023 Re_{l,he}^{0.8} Pr_{l,he}^{0.4} (@T_{he,in,t}) = 21.0445$$

The liquid only heat transfer coefficient:

$$h_{l,he} = N_p Nu_{l,he} k_{l,he} (@T_{he,in,t}) / (d_o - 2t_p) = 4332.6 \text{ W/m}^2\text{K}$$

$$\text{The evaporative heat transfer coefficient: } h_{ev,ip} = h_{l,he} (1 + 3.8Z^{-0.95}) = 5691.7 \text{ W/m}^2\text{K}$$

$$\text{The evaporative heat transferred: } \dot{Q}_{he} = \dot{m}_{cw} C_{p,cw} (@\bar{T}_{cw}) (T_{cw,out,t} - T_{cw,in,t}) = 4357.6 \text{ W}$$

The cooling water mass fraction:

$$x_{cw} = \dot{m}_{cw} (C_{p,l} (@T_{cw,out,t}) T_{cw,in,t} - C_{p,l} (@T_{cw,in,t}) T_{cw,in,t}) / h_{fg} (@T_{cw,out,t}) = 0.0337$$

$$\text{The convection number: } C_o = ((1-x_{cw})/x_{cw})^{0.8} (\rho_g (@\bar{T}_{cw}) / \rho_l (@\bar{T}_{cw}))^{0.5} = 5.5371$$

$$\text{The boiling number: } Bo = \dot{Q}_{ev} / \dot{m}_{cw} h'_{fg,cw} (@T_{cw,out,t}) = 0.03491$$

$$\text{The Froude number: } Fr_l = (16(\dot{m}_{cw})^2 / \pi (d_o^2 - 4d_i^2)) / (\rho_l^2 @\bar{T}_{cw}) g d_o = 0.6 \times 10^{-5}$$

$$\text{The dimensionless parameter in the pure convective boiling regime: } \psi_{cb} = 1.8 Co^{-0.8} = 0.4578$$

$$\text{The dimensionless parameter in the nucleate boiling regime: } \psi_{nb} = 1 + 46 Bo^{0.5} = 9.5994$$

The dimensionless parameter; in the bubble suppression regime:

$$\psi_{bs} = F Bo^{0.5} \exp(2.47 Co^{-0.1}) = 18.572$$

The cooling water two-phase non dimensional parameter:

$$Z_{cw} = ((1-x_{cw})/x_{cw})^{0.8} Pr_{cw}^{0.4} (@\bar{T}_{cw}) = 29.3124$$

$$\text{The cooling water mass: } m_{cw} = \rho_{cw} (@\bar{T}_{cw}) \pi (d_o^2 - 4d_i^2) L_i / 4 = 1.52907 \text{ kg}$$

$$\text{The cooling water mass velocity: } G_{max,cw} = 4 \dot{m}_{cw} / \pi (d_o^2 - 4d_i^2) = 22.3276 \text{ kg/m}^2\text{s}$$

The shell liquid only Reynolds number:

$$Re_{cw} = G_{max,cw} (d_o - t_p - 2d_i) / \mu_l (@\bar{T}_{cw}) = 571.1483$$

The shell Nusselt number (Mills, 1999);

$$Nu_{cw} = 3.66 + \frac{0.065((d_o - 2d_i)/L_i)Re_{cw}(@\bar{T}_{cw})Pr_{cw}(@\bar{T}_{cw})}{1 + 0.04[(d_o - 2d_i)/L_i]Re_{cw}(@\bar{T}_{cw})Pr_{cw}(@\bar{T}_{cw})} = 8.8874$$

The shell liquid only heat transfer coefficient:

$$h_{cw} = N_p Nu_{cw} k_{cw} (@\bar{T}_{cw}) / ((d_o - 2t_p) - 2d_i) = 991.2624 \text{ W/m}^2\text{K}$$

The shell evaporative heat transfer coefficient:

$$h_{he,op} = \psi_{bs} h_{l,he} (1 + 3.8Z_{cw}^{0.95}) = 21235.001 \text{ W/m}^2\text{K}$$

The heat exchanger thermal resistance:

$$R_{he,t} = (\pi L_{he})^{-1} \left[(N_p d_{he,ip} h_{ev,ip})^{-1} + (\ln(d_{e,op}/d_{he,ip})/2k_{cu}) + (d_{he,op} h_{he,op})^{-1} \right] = 0.0042 \text{ K/W}$$

C.2.3.1 Temperatures at the next time step

The cooling water temperature:

$$T_{cw,out,t}^{t+\Delta t} = T_{cw,out,t}^t + \Delta t \frac{\dot{m}_{cw} C_{p,cw}(@\bar{T}_{cw,t})}{m_{cw} C_{v,cw}} (T_{cw,out,t}^t - T_{cw,in,t}^t) = 38.491312 \text{ }^\circ\text{C}$$

Recalling equation (B.1.11), the working fluid temperature:

$$T_{he,out,t}^{t+\Delta t} = T_{he,out,t}^t + \frac{\Delta t}{m C_{v,l}(@\bar{T}_{he,t})} \left[\dot{m} C_{p,l}(@\bar{T}_{he,t}) (T_{he,in,t}^t - T_{he,out,t}^t) - \frac{\bar{T}_{he,t} - \bar{T}_{cw}}{R_{he,t}} \right] = 62.5211096 \text{ }^\circ\text{C}$$

C.2.3.2 Mass flow rate

The Fanning friction factor: $C_{f,j} = 0.0791 Re_{i,he}^{-0.25} = 1.0474472 \times 10^{-2}$

The gravity term: $\sum_{k=1}^N \rho_k A_{i,k} \Delta Z_k \text{g sin } \theta_k / \sum_{k=1}^N (m_k / \rho_k A_{i,k}) = 5.350175 \times 10^{-2} \text{ kg/s}^2$

The friction and minor loss term:

$$\left[\sum_{j=1}^N \frac{1}{2} \left(\frac{C_{f,j} + k_j}{\rho_j} \right) \frac{(\dot{m}^t)^2}{A_{i,j}^3} A_{j,k} \right] / \left[\sum_{k=1}^N \frac{m_k}{\rho_k A_{i,k}} \right] = 6.128564556 \times 10^{-2} \text{ kg/s}^2$$

The momentum term:

$$\left[\sum_{k=1}^N \frac{\dot{m}_k^2}{A_{i,k}} \left(\frac{1}{\rho_{k-1/2}} - \frac{1}{\rho_{k+1/2}} \right) \right] / \left[\sum_{k=1}^N \frac{m_k}{\rho_k A_{i,k}} \right] = 96 \times 10^{-9} \text{ kg/s}^2$$

The mass flow rate at the next time step

$$\dot{m}^{t+\Delta t} = \dot{m}^t + \Delta t \left[\frac{-\sum_{k=1}^N \frac{\dot{m}_k^2}{A_{i,k}} \left(\frac{1}{\rho_{k-1/2}} - \frac{1}{\rho_{k+1/2}} \right) - \sum_{k=1}^N \rho_k A_{i,k} \Delta Z_k \text{g sin } \theta_k - \sum_{k=1}^N \Delta p_{frict,loss,k} A_{j,k}}{\sum_{k=1}^N \frac{m_k}{\rho_k A_{i,k}}} \right] = 38.45616 \times 10^{-3} \text{ kg/s}$$

C.2.3.3 Pressure at each time step

Gravitational pressure change over the control volume:

$$\Delta P_g = - \sum_{k=1}^N \rho_k \Delta Z_k g \sin \theta_k = 947.64637 \text{ N/m}^2$$

The friction pressure change over the control volume:

$$\sum_{j=1}^N \Delta p_{frict,loss,j} = \sum_{j=1}^N \frac{1}{2} \left(\frac{C_{f,j} + k_j}{\rho_j} \right) \frac{(\dot{m}^t)^2}{A_{i,j}^3} A_{j,k} = 8.43565 \times 10^{-2} \text{ N/m}^2$$

The momentum pressure change over the control volume:

$$\Delta P_m = \sum_{k=1}^N \frac{\dot{m}_k^2}{(A_{i,k})^2} \left(\frac{1}{\rho_{k-1/2}} - \frac{1}{\rho_{k+1/2}} \right) = 11.36 \times 10^{-5} \text{ N/m}^2$$

The total pressure drop: $\Delta P = \Delta p_{frict,loss,j} - \Delta P_g - \Delta P_m = 947.56212 \text{ N/m}^2$

The outlet pressure at the next time step: $P_{acc,out} = P_{acc,in} - \Delta P = 99052.43787 \text{ N/m}^2$

C.2.4 Calculation referring to the use of experimental data measured

The electrical power: $\dot{Q}_{elek} = V_{sup}^2 / R_{elek} = 3008.333 \text{ kW}$

The experimental working fluid mass flow rate:

$$\begin{aligned} \dot{m}_{he,e} &= \dot{Q}_{ev} / \left(C_{p,l}(@T_{he,in,t})(273.15 + T_{he,in,t}) - C_{p,l}(@T_{he,out,t})(273.15 + T_{he,out,t}) \right) \\ &= 34.004 \times 10^{-3} \text{ kg/s} \end{aligned}$$

The heat removed by the heat exchanger:

$$\dot{Q}_{he} = \dot{m}_{he,e} C_{p,l}(@\bar{T}_{he})(T_{he,in,t} - T_{he,out,t}) = 2812.71612 \text{ W}$$

The heat lost by the system: $\dot{Q}_{loss} = \dot{Q}_{elek} - \dot{Q}_{he} = 195.8838 \text{ W}$

The logarithmic temperature difference:

$$\Delta T_{ln,he} = \left(\frac{((T_{he,in,t} - T_{he,out,t}) - (T_{cw,out,t} - T_{cw,in,t}))}{\ln((T_{he,in,t} - T_{he,out,t}) / (T_{cw,out,t} - T_{cw,in,t}))} \right) = 23.9412 \text{ } ^\circ\text{C}$$

The correction factor:

$$F = LMTD \left(\left(\frac{T_{cw,out,t} - T_{cw,in,t}}{T_{he,in,t} - T_{cw,in,t}} \right), \left(\frac{T_{he,in,t} - T_{he,out,t}}{T_{he,in,t} - T_{cw,in,t}} \right) \right) = LMTD(0.3, 0.4) \approx 1$$

The total experimental thermal resistance:

$$R_{tot,he} = F \Delta T_{ln,he} / \dot{Q}_{he} = 0.0085 \text{ K/W}$$

C.3 Stirling engine heat exchanger

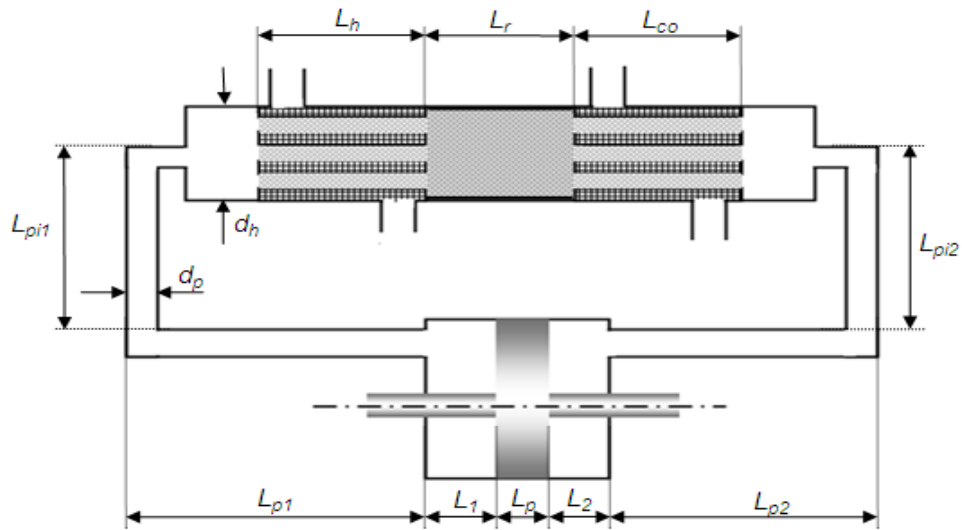


Figure C.2: Stirling engine heat exchanger geometrical dimensions

Referring to figure C.2, the dimensions used in the theoretical model of the Stirling engine heat exchanger are presented in table C.7. Sample calculations for one time step are shown for a section situated in the middle of the heat exchanger.

Table C.7: Geometrical data used in the Stirling engine heat exchanger theoretical model

Length piston: $L_p = 0.08 \text{ m}$	Heat ex pipe wall thickness: $\Delta w_p = 0.001 \text{ m}$
Length pipe1: $L_{p1} = 0.04 \text{ m}$	Heat ex transversal pitch: $S_T = 0.032 \text{ m}$
Length pipe2: $L_{p2} = 0.04 \text{ m}$	Heat ex longitudinal pitch: $S_L = 0.32 \text{ m}$
Length intermediate pipe1: $L_{pi1} = 0.04 \text{ m}$	The number of pipe: $N_p = 10$
Length intermediate pipe2: $L_{pi2} = 0.04 \text{ m}$	Mesh inner pipe: $Mesh_{ip} = 60$
Length working space: $L_{ws} = L_1 = L_2 = 0.1 \text{ m}$	Mesh regenerator: $Mesh_r = 60$
Length air pump: $L_{ap} = 0.15 \text{ m}$	Mesh outer pipe: $Mesh_{op} = 40$
Length pipe heat exchanger: $L_{p,he} = 0.1 \text{ m}$	Inner mesh thickness: $t_{scr,ip} = 0.00033 \text{ m}$
Length heat exchanger: $L_{he} = 0.135 \text{ m}$	Outer mesh thickness: $t_{scr,op} = 0.000525 \text{ m}$
Length regenerator: $L_r = 0.1 \text{ m}$	Diameter wire inner pipe: $d_{wi,ip} = 0.000165 \text{ m}$
Length dead space heat ex: $L_{ds,h} = 0.035 \text{ m}$	Diameter wire outer pipe: $d_{wi,op} = 2.6252 \times 10^{-4} \text{ m}$
Stoke: $X_{ap} = 0.06 \text{ m}$	Diameter wire regenerator: $d_{wi,r} = 0.000165 \text{ m}$
Diameter pipe: $d_p = 0.04 \text{ m}$	Length fins outer pipe: $L_{fin,op} = 0.005 \text{ m}$
Diameter air pump: $d_{ap} = 0.3 \text{ m}$	Outer diameter heat ex pipe: $d_{op} = 0.022 \text{ m}$
Diameter heat exchanger: $d_h = d_o = 0.133 \text{ m}$	Heat ex wall thickness: $\Delta w_h = 0.005 \text{ m}$

C.3.1 The theoretical model

C.3.1.1 Number of holes in the mesh

The inner mesh number: $M_i = M_r = (\text{Mesh}_{ip}/0.0254) = 2362.2$

The outer mesh number: $M_o = (\text{Mesh}_{op}/0.0254) = 1574.8$

The inner pipe number of screens: $N_{scr,i} = N_p(L_h/th_{60}) = 3030$

The outer pipe number of screens: $N_{scr,o} = (L_h/th_{40}) = 191$

The inner mesh number of holes per screen:

$$N_{holes,pers,ip} = \pi M_{in}^2 (d_{op} - \Delta w_p)^2 / 4 = 0.1753 \times 10^4$$

The inner mesh number of holes: $N_{holes,ip} = N_{scr,i} N_{holes,pers,ip} = 0.5312 \times 10^7$

The outer mesh number of holes per screen:

$$N_{holes,pers,op} = \pi M_o^2 ((d_h - 2\Delta w_p)^2 - N_p d_{op}^2) / 4 = 2.0041 \times 10^4$$

The outer mesh number of holes: $N_{holes,op} = N_{scr,o} N_{holes,pers,op} = 0.3817 \times 10^7$

The regenerator mesh number of holes per screen:

$$N_{holes,pers,r} = \pi M_{in}^2 d_r^2 / 4 = 6.63 \times 10^4$$

The regenerator mesh number of holes: $N_{holes,r} = N_{scr,r} N_{holes,pers,r} = 2.0089 \times 10^7$

C.3.1.2 Heat transfer area of the mesh

The heat transfer area per hole in the inner pipe mesh:

$$A_{z,perhole,ip} = 4\pi(S_{M,ip} - d_{wi,ip}) d_{wi,ip} / 2 = 0.2678 \times 10^{-6} \text{ m}^2$$

The heat transfer area per hole in the outer pipe mesh:

$$A_{z,perhole,op} = 4\pi(S_{M,op} - d_{wi,op}) d_{wi,op} / 2 = 0.6144 \times 10^{-6} \text{ m}^2$$

The heat transfer area per hole in the regenerator mesh:

$$A_{z,perhole,re} = 4\pi(S_{M,re} - d_{wi,r}) d_{wi,r} / 2 = 0.2678 \times 10^{-6} \text{ m}^2$$

The heat transfer area in the inner pipe mesh: $A_{z,ip} = N_{holes,ip} A_{z,perhole,ip} = 1.4227 \text{ m}^2$

The heat transfer area in the outer pipe mesh: $A_{z,op} = N_{holes,op} A_{z,perhole,op} = 2.3453 \text{ m}^2$

The heat transfer area in the regenerator mesh: $A_{z,r} = N_{holes,r} A_{z,perhole,r} = 5.380068 \text{ m}^2$

C.3.1.3 Cross-section area of the mesh holes

The inner mesh holes cross section per holes:

$$A_{perhole,ip} = (S_{M,ip} - d_{wi,ip})^2 = 0.0667 \times 10^{-6} \text{ m}^2$$

The outer mesh holes cross section per holes:

$$A_{perhole,op} = (S_{M,op} - d_{wi,op})^2 = 0.1388 \times 10^{-6} \text{ m}^2$$

The inner mesh holes cross-section: $A_{ip} = N_{holes,ip} A_{perholes,ip} = 0.3545 \text{ m}^2$

The inner mesh holes cross section: $A_{op} = N_{holes,op} A_{perholes,op} = 0.5297 \text{ m}^2$

C.3.1.4 Volume of the metal

The inner wire mesh volume: $V_{m,ip} = [\pi N_{scr,i} ((d_{op} - 2\Delta w_{op})^2 / 4) - A_{ip}] 2d_{wi,ip} = 0.1972 \times 10^{-3} \text{ m}^3$

The outer wire mesh volume:

$$V_{m,op} = [\pi N_{scr,o} ((d_h - 2\Delta w_h)^2 - N_p d_{op}^2) / 4 - A_{op}] 2d_{wi,op} = 0.53 \times 10^{-3} \text{ m}^3$$

C.3.1.5 Void volume of the exchanger

The inner pipes geometrical volume: $V_i = \pi L_p N_p (d_{op} - \Delta w_p)^2 / 4 = 0.3142 \times 10^{-3} \text{ m}^3$

The outer pipes geometrical volume: $V_o = \pi L_p ((d_o - \Delta w_h)^2 - N_p d_{op}^2) / 4 = 0.8081 \times 10^{-3} \text{ m}^3$

The working fluid volume in the heat exchanger inner pipe: $V_{wf,ip} = V_i - V_{m,ip} = 0.1170 \times 10^{-3} \text{ m}^3$

The working fluid volume in the heat exchanger outer pipe:

$$V_{wf,op} = V_o - V_{m,op} = 0.2781 \times 10^{-3} \text{ m}^3$$

C.3.1.6 Porosity

The inner pipes porosity: $\epsilon_{ip} = V_{wf,ip} / V_i = 0.3724$

The outer pipes porosity: $\epsilon_{op} = V_{wf,op} / V_o = 0.3441$

C.3.1.7 Number of fins

The inner pipe number of fins: $N_{fin,in} = (\pi L_p (d_{op} - \Delta w_p) / (S_{M,ip})) N_{scr,i} = 49020$

The outer pipe number of fins: $N_{fin,o} = (\pi (L_{fin,o} L_p) / S_{M,op}) N_{scr,o} = 4710$

The inner pipe heat transfer area per fin: $A_{fin,i} = \pi d_{wi,ip} L_{fin,i} = 0.0565 \times 10^{-4} \text{ m}^2$

The outer pipe heat transfer area per fin: $A_{fin,o} = \pi d_{wi,op} L_{fin,o} = 0.0259 \times 10^{-4} \text{ m}^2$

The total inner pipe fins heat transfer area: $A_{fin,tot,ip} = N_{fin,in} A_{fin,i} = 2.770 \text{ m}^2$

The total outer pipe fins heat transfer area: $A_{fin,tot,op} = N_{fin,o} A_{fin,o} = 0.122 \text{ m}^2$

C.3.1.8 Mesh correction and compression factor

The inner pipe mesh correction factor:

$$C_{ip} = 123(d_{wi,ip} M_{ip})^4 - 384(d_{wi,ip} M_{ip})^2 - 640 = -695.4970$$

The outer pipe mesh correction factor:

$$C_{op} = 123(d_{wi,op} M_{op})^4 - 384(d_{wi,op} M_{op})^2 - 640 = -702.0290$$

The inner pipe mesh compression factor:

$$C_{f,ip} = (-3.906 \times 10^{-4} C_{ip} \pi d_{wi,ip} M_{ip}) / (1 - \epsilon_{ip}) = 0.5300$$

The outer pipe mesh compression factor:

$$C_{f,op} = \left(-3.906 \times 10^{-4} C_{op} \pi d_{wi,op} M_{op} \right) / (1 - \varepsilon_{op}) = 0.5430$$

C.3.1.9 Laminating thickness

The inner pipe mesh laminating thickness: $L_{lam,ip} = 2C_{f,ip} N_{scr,ip} d_{wi,ip} = 0.5300 \text{ m}$

The outer pipe mesh laminating thickness: $L_{lam,op} = 2C_{f,op} N_{scr,op} d_{wi,op} = 0.0543 \text{ m}$

C.3.1.10 Hole hydraulic diameter

The inner mesh: $d_{h,ip} = \varepsilon_{ip} d_{wi,ip} / (1 - \varepsilon_{ip}) = 0.0979 \times 10^{-3} \text{ m}$

The outer mesh: $d_{h,op} = \varepsilon_{op} d_{wi,op} / (1 - \varepsilon_{op}) = 0.1377 \times 10^{-3} \text{ m}$

C.3.1.11 Specific surface area

The inner mesh: $B_{ip} = 4(1 - \varepsilon_{ip}) / d_{h,ip} = 256430$

The outer mesh: $B_{op} = 4(1 - \varepsilon_{op}) / d_{h,op} = 190490$

C.3.2 Calculation of the new values of volume, temperature and pressure

The calculations of the new values of volume, pressure, temperature and mass flow rate in the heater and the expansion space, control volume adjacent to the heater are shown in this section

The initial pressures in the expansion space and heater: $P_e = P_h = 100000 \text{ Pa}$

The initial volumes in the expansion space and the heater are calculated as:

The expansion side of reciprocator: $V_{hp,e} = \pi((d_{ap}^2 - d_{rod}^2)/4)L_1 = 0.0024 \text{ m}^3$

Volume of the working fluid in Pipe1: $V_{p1} = \pi(d_p^2/4)(L_{p1} + L_{pi1}) = 0.4072 \times 10^{-4} \text{ m}^3$

Volume of the working fluid in Pipe2: $V_{p2} = \pi(d_p^2/4)(L_{p2} + L_{pi2}) = 0.6005 \times 10^{-4} \text{ m}^3$

Volume of the heat exchanger expansion space:

$$V_{h,e} = \pi((d_h - 2\Delta w_h)^2/4)L_{ds,h} = 4.2951 \times 10^{-4} \text{ m}^3$$

Volume of the Working fluid in the heater: $V_h = V_{co} = V_{wf,ip} = 0.1390 \times 10^{-3} \text{ m}^3$

The total volume on the expansion side $V_e = V_{hp,e} + V_{p1} + V_{h,e} = 0.0029 \text{ m}^3$

The initial temperatures in the expansion space and heater are: $T_e = 27 \text{ }^\circ\text{C}$ and $T_h = 75 \text{ }^\circ\text{C}$

The initial masses in the expansion space and heater respectively are:

$$m_e = (P_e V_e) / (R(273.15 + T_e)) = 0.0034 \text{ kg}$$

$$m_h = (P_h V_h) / (R(273.15 + T_h)) = 0.0001 \text{ kg}$$

The initial densities in the expansion space and heater respectively are:

$$Rho_e = m_e / V_e = 1.1649 \text{ kg/m}^3$$

$$Rho_h = m_h / V_h = 1.0043 \text{ kg/m}^3$$

The cold water mass flow rate was calculated as:

The mass of the water between the low and high level of the return cold water reservoir weighted at 17 °C: $m_{cold}(17\text{ °C}) = 54.8\text{ kg}$.The average time the cold water takes to fill the return cold water reservoir from its low to high level mark: $t_{cold} = 2'55''35''' = 175.35\text{ s}$ Therefore, the mass of the cold water is : $m_{cold}(17\text{ °C}) = \rho(17\text{ °C})V_{cold} = 54.8\text{ kg}$.The volume of water in the return cold water reservoir from its low to high level marks is: $V_{cold} = m_{cold}(17\text{ °C})/\rho(17\text{ °C}) = 0.05485\text{ m}^3$. The mass of cold water at 33.06 °C: $m_{cold}(33.06\text{ °C}) = \rho(33.06\text{ °C})V_{cold} = 54.733\text{ kg}$. The mass flow rate of the cold water: $\dot{m}_{cold}(33.06\text{ °C}) = m_{cold}(33.06\text{ °C})/t_{cold} = 0.31214\text{ kg/s}$

The hot water mass flow rate was calculated as:

The mass of the water between the low and high level of the return hot water reservoir weighted at 17 °C: $m_{hot}(17\text{ °C}) = 53.47\text{ kg}$.The average time the hot water takes to fill the return hot water reservoir from its low to high level mark: $t_{hot} = 2'2''30''' = 122.3\text{ s}$. Therefore, the mass of the cold water is: $m_{hot}(17\text{ °C}) = \rho(17\text{ °C})V_{cold} = 53.47\text{ kg}$.The volume of water in the return hot water reservoir from its low to high level marks is: $V_{hot} = m_{hot}(17\text{ °C})/\rho(17\text{ °C}) = 0.05368\text{ m}^3$. The mass of cold water at 73.57°C is: $m_{hot}(73.57\text{ °C}) = \rho(73.57\text{ °C})V_{hot} = 52.354\text{ kg}$. The mass flow rate of the cold water is: $\dot{m}_{hot}(73.57\text{ °C}) = m_{cold}(73.57\text{ °C})/t_{hot} = 0.4281\text{ kg/s}$

The cross-sectional area of the piston in the reciprocator: $A_{ap} = \mu(d_{ap}^2 - d_{rod}^2)/4 = 0.07\text{ m}^2$

The new volume for the first time step when steady state is reached

$$V_e^{new}(t) = V_e - A_{ap}x_e = 0.5 \times 10^{-2}\text{ m}^3$$

$$V_h^{new}(t) = V_h = 0.1390 \times 10^{-3}\text{ m}^3$$

The instantaneous pressure for the first time step when steady state is reached

$$P^{new} = \frac{RM}{\frac{V_e^{new}}{(273.15 + T_e^{new})} + \frac{V_h^{new}}{(273.15 + T_h^{new})} + \frac{V_r^{new}}{(273.15 + T_r^{new})} + \frac{V_c^{new}}{(273.15 + T_c^{new})} + \frac{V_{co}^{new}}{(273.15 + T_{co}^{new})}}$$

$$P^{new}(t) = 112\text{ kPa}$$

The new masses in the expansion space and heater are:

$$m_e^{new}(t) = (P^{new}V_e^{new})/(R(273.15 + T_e^{new})) = 0.0057\text{ kg}$$

$$m_h^{new}(t) = (P^{new}V_h^{new})/(R(273.15 + T_h^{new})) = 0.0002\text{ kg}$$

The new densities in the expansion space and heater are:

$$Rho_e^{new}(t=3500.001) = m_e^{new}/T_e^{new} = 1.0221\text{ kg/m}^3$$

$$Rho_h^{new}(t) = m_h^{new}/T_h^{new} = 1.0331\text{ kg/m}^3$$

The new masse flow rate in the expansion space and heater are:

$$\dot{m}_{eh}^{new}(t) = Rho_e^{new}A_{ip}\dot{x}_e^{new}/\epsilon_{ip} = 0.6502 \times 10^{-3}\text{ kg/m}^3$$

$$\dot{m}_{hr1}^{new}(t) = Rho_e^{new}A_{ip}\dot{x}_e^{new}/(\epsilon_{re}\epsilon_{ip}) = 0.5617 \times 10^{-3}\text{ kg/m}^3$$

C.3.3 The energy balance

The energy brought to the system is found as:

$$\text{With, } T_{h,i} = 80.045\text{ °C}, T_{h,o} = 72.359\text{ °C} \text{ and } \bar{T}_h = (T_{h,i} + T_{h,o})/2 = 76.202\text{ °C}$$

$$\bar{Q}_{hot} = \dot{m}_{hot}C_p(@\bar{T}_h)(T_{h,i} - T_{h,o}) = 13786.677\text{ W}$$

The energy taking out of the system

With, $T_{c,i} = 26.276 \text{ }^\circ\text{C}$, $T_{c,o} = 34.359 \text{ }^\circ\text{C}$ and $\bar{T}_c = (T_{c,i} + T_{c,o})/2 = 30.3175 \text{ }^\circ\text{C}$

$$\dot{Q}_{cold} = \dot{m}_{cold} C_p (@\bar{T}_c) (T_{c,o} - T_{c,i}) = 10536.2 \text{ W}$$

The heat transferred to the regenerator matrix:

The pressure drop through the regenerator wire matrix: $\Delta P_r(t) = 797.408 \text{ N/m}^2$

From the experimental regenerator pressure drop the regenerator air velocity is:

$$V_{a,r} = \sqrt{2\Delta P_r(t) / C_{f,r} \rho_{a,r} (@\bar{T}_r)} = 68.772 \text{ m/s}$$

with, $T_{r,h} = 68.634 \text{ }^\circ\text{C}$ and $T_{r,c} = 35.124 \text{ }^\circ\text{C}$ the heat transferred to the regenerative matrix is:

$$Q_{a,r} = \rho_{a,r} (@\bar{T}_r) V_{a,r} \pi d_p^2 c_{p,a,r} (T_{r,h} - T_{r,c}) / 4 = 3063.0796 \text{ W}$$

The heat loss to the by the heat exchanger

$$\dot{Q}_{loss} = \dot{Q}_{hot} - (\dot{Q}_{cold} + \dot{Q}_{a,r}) = 187.3974 \text{ W}$$

C.3.4 Pressure drop

The pressure drop through the heater: $\Delta P_h = 1445.65 \text{ N/m}^2$

C.3.5 Mass flow density

The friction factor experimentally calculated is: $C_{f,h} = [\bar{\rho} (\pi d_p)^2 \Delta P_h] / (8 \dot{m}_{a,h}) = 0.35$

The heater velocity: $\dot{x}_h = \sqrt{2\Delta P_h / C_{f,h} \bar{\rho}} = 89.95 \text{ m/s}$

The heater pipe velocity:

$$\dot{x}_{p,h} = \max \left[\frac{S_T}{S_T - (d_{op} - \Delta W_p)}, \frac{S_T/2}{\sqrt{((S_T/2)^2 + S_L^2) - (d_{op} - \Delta W_p)}} \right] = 239.8653 \text{ m/s}$$

The heater screens mesh velocity:

$$\dot{x}_{mean,h} = \max \left[\frac{S_{M,ip}}{S_{M,ip} - 4(S_{M,ip} - d_{wi,p})}, \frac{S_{M,ip}/2}{\sqrt{((S_{M,ip}/2)^2 + S_{M,ip}^2) - 4(S_{M,ip} - d_{wi,p})}} \right] = 307.706 \text{ m/s}$$

C.3.6 Finned heat transfer coefficient

The heater mass velocity: $G_h(t) = \rho_h (@\bar{T}_h) \dot{x}_{mean} / \varepsilon_{ip} = 918 \text{ kg/m}^2\text{s}$

The Reynolds number: $Re_h(t) = G_h d_{h,ip} / \mu_g = 4494.2$

The friction factor: $f_h = (1.078 + 64/Re_h) ((\varepsilon_{ip} / (1 - \varepsilon_{ip}))^{0.4}) = 0.8864$

the Colburn factor:

$$J_h = 5.86 Re_h^{-0.68} ((1 - \varepsilon_{ip}) / \varepsilon_{ip})^{0.2} (d_{wi,ip} / L_{fin,ip}) = 0.0008$$

The fins heat transfer coefficients:

$$h_{h,fin} = G_h C_p (@\bar{T}_h) J_h (Pr_g (@\bar{T}_h))^{-2/3} = 985.32 \text{ W/m}^2 \text{ K}$$

C.3.7 Unfinned heat transfer coefficient

The Nusselt number: $Nu_h = 0.023 Re_h^{0.8} (Pr_h (@\bar{T}_h))^{0.4} = 16.5725$

The heat transfer coefficient: $h_h = Nu_h k_g (@\bar{T}_h) / (d_{h,ip}) = 5080 \text{ W/m}^2 \text{ K}$

C.3.8 Theoretical thermal resistance

The heater thermal resistance

$$R_{h,t} = \frac{1}{A_{z,ip} h_h + \eta_{fin,ip} A_{fin,tot,ip} h_{h,fin}} + \frac{\text{Ln}(d_{op}/(d_{op} - 2\Delta W_p))}{2\pi k_{cu} N_p L_p} + \frac{1}{A_{z,op} h_{hot} + \eta_{fin,op} A_{fin,tot,op} h_{hot,fin}}$$

$$R_{h,t} = 0.00001045 + 0.0000378 + 0.0000036 = 0.0001459 \text{ K/W}$$

C.3.9 Experimental thermal resistance

The heat transferred to the heater:

$$\dot{Q}_{a,h} = \dot{m}_a C_{p,a} (T_e - T_{r,h}) = \dot{m}_{hot} C_{p,hot} (T_{h,i} - T_{h,o}) = UA_{z,h} (\bar{T}_{hot} - \bar{T}_{hot,g}) = 13786.677 \text{ W}$$

where, the mean gas temperature in the heater is :

$$\bar{T}_{hot,g} = (T_e + T_{r,h})/2 = (76.501 + 67.634)/2 = 72.0675 \text{ }^\circ\text{C}$$
 and the mean hot temperature is

$$\bar{T}_{hot} = (T_{h,i} + T_{h,o})/2 = (80.045 + 72.359)/2 = 76.202 \text{ }^\circ\text{C}$$

The heater experimental thermal resistance is:

$$R_{h,exp} = \frac{1}{UA_{z,h}} = \frac{(\bar{T}_{hot} - \bar{T}_{hot,g})}{\dot{Q}_{a,h}} = 0.0003 \text{ K/W}$$

C.3.10 Correction of the thermal resistance

$$R_{h,t} = \frac{1}{A_{z,ip} h_h + \eta_{fin,ip} A_{fin,tot,ip} h_{h,fin}} + \frac{\text{Ln}(d_{op}/(d_{op} - 2\Delta W_p))}{2\pi k_{cu} N_p L_p} + \frac{1}{A_{z,op} h_{hot} + \eta_{fin,op} A_{fin,tot,op} h_{hot,fin}}$$

The outer pipe thermal resistance is comparatively too good as water is used as a cooling medium of the heat exchanger, therefore for a very good approximation, it is essentially zero,

$$\frac{1}{A_{z,op} h_{hot} + \eta_{fin,op} A_{fin,tot,op} h_{hot,fin}} = 0$$

$$R_{h,t} = \frac{1}{A_{z,ip} h_h + \eta_{fin,ip} A_{fin,tot,ip} h_{h,fin}} + \frac{\text{Ln}(d_{op}/(d_{op} - 2\Delta W_p))}{2\pi k_{cu} N_p L_p} + 0$$

or

$$R_{h,t} - \frac{\text{Ln}(d_{op}/(d_{op} - 2\Delta W_p))}{2\pi k_{cu} N_p L_p} = \frac{1}{A_{z,ip} h_h + \eta_{fin,ip} A_{fin,tot,ip} h_{h,fin}}$$

Assuming $A_{fin} = A_{fin,tot,ip}$

$$A_{z,ip}h_h + \eta_{fin,ip}A_{fin}h_{h,fin} = \frac{1}{R_{h,t} - \frac{\ln(d_{op}/(d_{op} - 2\Delta W_p))}{2\pi k_{cu}N_p L_p}}$$

$$A_{z,ip}0.023Re_h^{0.8}(Pr_h)^{0.4}k_g/(d_{h,ip}) + \eta_{fin,ip}A_{fin}G_h C_p J_h (Pr_g)^{-2/3} = \frac{1}{R_{h,t} - \frac{\ln(d_{op}/(d_{op} - 2\Delta W_p))}{2\pi k_{cu}N_p L_p}}$$

Assuming that the right hand side can be represented by a single factor R^{-1}

$$A_z \frac{0.023(\rho\bar{x})^{0.8}(1-\varepsilon)^{0.2}(Pr)^{0.4}k}{\varepsilon(d_w)^{0.2}(\mu)^{0.8}} + \eta_{fin}A_{fin}C_p \frac{5.86(\rho\bar{x})^{0.32}(1-\varepsilon)^{0.88}(\mu_g)^{0.68}(d_{wi})^{0.32}}{(\varepsilon)^{1.2}(Pr)^{-2/3}L_{fin}} = R^{-1}$$

where the variable $R = R_{h,exp} = 0.0003 \text{ K/W}$ may be experimentally determined as shown in section C.3.9. Equating the left hand side for $R^{-1} = R_{h,exp}^{-1}$ the heater corrected porosity is $\varepsilon_h = 0.596$. Similarly the cooler and regenerator porosity is $\varepsilon_c = 0.576$ and $\varepsilon_r = 0.507$ respectively. The corrected volume of the wire matrix in the heater, cooler and regenerator are:

$$V_{m,h} = (1 - \varepsilon_h)V_h = 0.0001269 \text{ m}^3$$

The corrected number of screens in the heater and cooler are given as:

$$N_{scr,h} = \frac{4V_{m,h}}{2d_w \left[\pi(d_p - 2\Delta W_p)^2 - 4N_{holes,pers,ip}A_{perholes,ip} \right]} = 1900.3$$

Appendix D Reciprocator dynamic and design calculations

A reciprocator was designed to circulate the air through the heat exchanger. The design calculations of the reciprocator are now briefly described. The reciprocator is driven back and forth by a crankshaft mechanism. Important relevant design calculations are also summarised here.

D.1 Parameters of stroke and diameter of the piston

In this design, it was expected that the SE will operate at a frequency up to 40 Hz. According to the present design, the reciprocator piston will displace 4 litres of air as it oscillates. As given in table D.1, this volume of air ($V=0.004 \text{ m}^3$) defines the parameter of the stroke and diameter of the piston, and hence the overall design. The designed internal pressure of air in the reciprocator is assumed to be $P=300 \text{ kPa}$.

Table D.1: The parameter of stroke and diameter of the piston

Standard tube ID [mm]	Standard tube OD [mm]	Standard tube wall [mm]	Nominal bore & schedule	Cylinder ID, d [mm]	Stroke, $l \geq \frac{4V}{\pi d^2}$ [mm]
247.65	273.05	12.7	250/80S	250	81
298.45	323.85	12.7	300/80S	300	57

The most convenient reciprocator cylinder inner diameter is 300 mm, with a stroke of at least 57 mm, which may be rounded off to 60 mm.

D.2 The reciprocator cylinder strength

For ease of calculation, the reciprocator cylinder was assumed to be a continuous, closed-ended tube, having no holes cut into its side. The cylinder wall thickness to radius is 12.7/150 hence thin cylinder theory will be applied. For AISI 316 Stainless steel the yield stress at 20 °C is $\sigma = 195 \text{ Mpa}$. Assuming a safety factor of 20, the design stress is 9.75 MPa. The maximum axial stress and the maximum hoop stress are given in table D.2

Table D.2: Maximum axial and hoop stress

Maximum axial stress (Young, 1975)	Maximum hoop stress (Young, 1975)
$\sigma_a \geq \frac{Pd}{4t}$ so $t \geq \frac{Pd}{4\sigma_a} = 0.00225 \text{ m}$	$\sigma_h \geq \frac{Pd}{2t}$ so $t \geq \frac{Pd}{2\sigma_h} = 0.0045 \text{ m}$

From Table D.2, a minimum wall thickness of 4.5 mm is required for the reciprocator cylinder. The deflection of the wall when the Young's Modulus, $E = 200 \text{ GPa}$, and the Poisson's ratio $\nu=0.29$ is given as (Young, 1975):

$$\Delta R = \frac{Pd^2}{4Et} \left(1 - \frac{\nu}{2}\right) = 6.42 \mu\text{m} \quad (\text{D.2.1})$$

The strength is well within the requirements and the deflection of the bore, under the conditions assumed is negligible.

D.3 The reciprocator closure strength

For ease calculation, the closures were assumed to have, an outer edge fixed at $2a=300 \text{ mm}$ diameter, an inner edge fixed at $2b=40 \text{ mm}$, a wall thickness of $t=16 \text{ mm}$, a uniform pressure load of 300 kPa and no holes cut into their sides. The deflection, moment and closure stress will be presented in table D.3 (Young, 1975):

Table D.3: The closure deflection, moment, stress and safety factor

Deflection	Moment
$y_{b=0.016} = \frac{12(1-\nu^2)Pa^4}{Et^3} \left[\frac{C_1 L_{14}}{C_4} - L_{11} \right] = 24 \mu\text{m}$	$M_r = Pa^2 \left[L_{17} - \frac{C_7}{C_4} L_{14} \right] = 580.1 \text{ Nm}$
With, $C_1 = \frac{(1+\nu)b}{2} \frac{1}{a} \ln\left(\frac{a}{b}\right) + \frac{(1-\nu)}{4} \left[\frac{a}{b} - \frac{b}{a} \right] = 1.481$ $C_4 = \frac{1}{2} \left[(1+\nu) \frac{a}{b} + (1-\nu) \frac{b}{a} \right] = 2.749$ $C_7 = \frac{1}{2} (1-\nu^2) \left[\frac{a}{b} - \frac{b}{a} \right] = 3.374$ $L_{11} = \frac{1}{16} \left[1 + 4 \left(\frac{b}{a}\right)^2 - 5 \left(\frac{b}{a}\right)^4 - 4 \left(\frac{b}{a}\right)^2 \left[2 + \left(\frac{b}{a}\right)^2 \right] \ln\left(\frac{a}{b}\right) \right] = 0.016$ $L_{14} = \frac{1}{16} \left[1 - \left(\frac{b}{a}\right)^4 - 4 \left(\frac{b}{a}\right)^2 \ln\left(\frac{a}{b}\right) \right] = 0.062$ $L_{17} = \frac{1}{4} \left[1 - \left(\frac{1-\nu}{4}\right) \left[1 - \left(\frac{b}{a}\right)^4 \right] - \left(\frac{b}{a}\right)^2 \left[1 + (1+\nu) \ln\left(\frac{a}{b}\right) \right] \right] = 0.205$	
Stress	Calculated safety factor
$\sigma_{cl} = \frac{6M_r}{t^2} = 13.6 \text{ MPa}$	$s = \frac{\sigma_{cl}}{\sigma} = 14.3$

The most satisfactory material at elevated temperatures is AISI 316, but it is difficult to machine. AISI 304, though easier to machine is marginally satisfactory. Only AISI marginally exceeds the safety factor $s=20$ set for the analysis based on yield.

A stress analysis was conducted on the reciprocator closures to inspect the dynamic behaviour of the working fluid at the closure holes. The reason of the stress analysis is, especially because of the maximum high operating pressure developed in the reciprocator. A finite element analysis, conducted with Inventor professional version 9, from which a summary of results is presented in figure D.1, was use to analyse stresses on the closure holes. Results indicate that that the highest absolute stresses occur on the inside of the bolt holes at the

perimeter. As expected, the greatest deflection is at the centre. In general, the stresses in the closure are minimal. The excessive stresses in the bolts are unexpected, and could be caused by the boundary conditions imposed of being held fixed when in fact they can move and deflect.

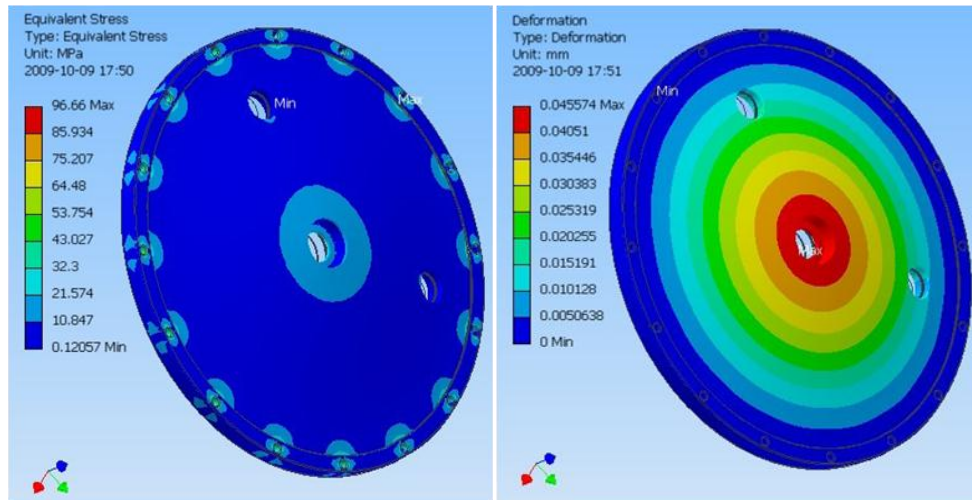


Figure D.1: Closure stress analysis

D.4 Piston Strength

During each cycle, the piston is subjected to high accelerations. The maximum calculated acceleration was $\gamma = 384 \text{ m/s}^2$. The piston has a mass $M = 3 \text{ kg}$ including the mass of the seals. Therefore, the force on the piston at the highest acceleration is $F = M\gamma = 1152 \text{ N}$. The shear stress area is $A_s = dt = 0.24t$, and the shear stress is $\sigma_{sh} = 1152/0.024t = 48 \times 10^3/t$. The yield shear stress of aluminium is 69 MPa. Therefore, the minimum thickness of the piston web is

$$t = 1152/0.024\sigma_{sh} = 0.0007 \text{ m} \quad (\text{D.4.1})$$

The present design has a thickness of 12.5 mm , hence the safety factor is $69 \times 10^6 \times 0.0125 / 48 \times 10^3 = 18$.

D.4.1 Crank mechanism

When a linear motor is not used, then a rotating motor with a flywheel, crankshaft and slider mechanism is used.

D.4.2 Inertia

The motion of the reciprocator is governed by the inertia of the moving parts as shown below in table D.4. The acceleration, forces and power requirements of the piston are calculated as shown in table D.5

Table D.4: Matrix mass constant summary

Component	Diameter, d_j [m]	Length , L_j [m]	Density, ρ_i [kg/m ³]	Mass, m_j [kg]	Mass inertia, $J_j = \frac{1}{8} m_j d_j^2$ [kgm ²]
Motor	0.25			120	0.94
Motor shaft	0.042	0.11	7850	1.2	0.00025
Shaft					
Section1	0.04	0.1925	7850	1.9	0.00038
Section 2	0.045	0.0075	7850	0.094	0.000024
Section3	0.065	0.0015	7850	0.04	0.00002
Section4	0.11	0.0485	7850	3.62	0.0055
Total				5.654	0.005924
Flywheel			7850		
Section1	OD=0.396	0.003		3	0.06
Section2	ID=0.350 OD=0.396	0.012		2.54	0.011
Holes (x8) total	0.008	0.003		-0.0095 5.5305	0.071
Piston shaft (x2)	0.0024	0.18	7850	1.3	
Piston	0.3	0.0125	2600	2.22	
Connector	0.06	0.055	7850	1.22	
Holes (x2)	0.01	0.017	7850	-0.021	
Cut off	H=0.06 W=0.026	0.025	7850	-0.31	
Total				4.409	
Crank shaft			7850		$J_j = \frac{1}{8} m_j L_j^2$ [kgm ²]
Section1 (x2)	H=0.025 W=0.015	0.04		0.2355	0.000047
Section 2	H=0.015 W=0.015	0.105		0.185	0.000255
Total				0.4205	0.000302

Table D.5: Reciprocator dynamic characteristics

Frequency, f [Hz]	Maximum piston displacement, x_p [m]	Acceleration, $a = \frac{2x_p}{t^2} = 2x_p f^2$ [ms ⁻²]	Force , $F=ma$ [N]	Power, $P=Fx_p f$ [kW]
10	0.12	24	105.816	0.127
20	0.12	96	423.264	1.0156
30	0.12	216	952.344	3.4284
40	0.12	384	1693.056	8.1266

D.4.3 The components stiffness

The stiffness of the heat exchanger experimental set-up components, presented in table D.6 were calculated using the modulus of elasticity $E = 210 \text{ GPa}$, and the shear modulus of elasticity $G = 75 \text{ GPa}$.

Table D.6: Heat exchanger experimental setup components stiffness

Component	Torsion $k_{t,j} = \frac{Gl_{p,j}}{L_j} = \frac{\pi G d_j^4}{32 L_j}$	Compression, or extension $k_{c,j} = \frac{EA}{L_j} = \frac{\pi E d_j^2}{4 L_j}$	Bending $k_{b,j} = \frac{48 E I_{o,j}}{L_j^3} = \frac{3 \pi E d_j^4}{4 L_j^3}$
Motor shaft	66300.34	—	—
Coupling	—	2.0526×10^{10}	—
Shaft	97176.7	—	—
Flywheel	—	1.465×10^{12}	—
Piston shaft	—	—	56297340.35
Crank Shaft			$k_{b,j} = \frac{48 E I_{o,j}}{L_j^3} = \frac{6 E W H_j^3}{L_j^3}$ 44478960.75

The gas stiffness is $k_g = (c_p/c_v) A_{o,unfin}^2 P/V_a = 93.907 \text{ N/m}$

D.4.4 The flywheel

The flywheel will absorb excess energy of the rotating system. The change in energy is found as:

$$\Delta E = J \omega^2 C_{fl} = \frac{1}{2} \pi^2 f^2 m d^2 C_{fl} \quad (D.4.1)$$

Therefore, the mass of the flywheel

$$m = \rho V = 2 \Delta E / \pi^2 f^2 m C_{fl} = 0.02375 / d^2 \quad (D.4.2)$$

The volume of the flywheel is

$$V = \pi \left(\left(\frac{OD}{2} - t \right)^2 - \frac{OD^2}{4} \right) \quad (D.4.3)$$

D.4.5 Matrix characteristic of the dynamic behaviour of the SE heat exchanger experimental set-up

Recalling the Lagrange formulation of section 7.3

$$\frac{d}{dt} \left(\frac{\partial L}{\partial \dot{\varphi}_m} \right) - \frac{\partial L}{\partial \varphi_m} = (J_m + J_{co}) \ddot{\varphi}_m + (k_{t,m} + k_{c,co}) \varphi_m - k_{c,co} \varphi_a = \theta_{max} \sin(\omega t) \quad (7.3.7)$$

$$\frac{d}{dt} \left(\frac{\partial L}{\partial \dot{\varphi}_a} \right) - \frac{\partial L}{\partial \varphi_a} = (J_{fw} + J_a - J_{co}) \ddot{\varphi}_a - k_{c,co} \varphi_m + (k_{t,a} + k_{e,fw} + k_{c,co}) \varphi_a - k_{e,fw} \frac{L}{2} \theta_{cr} = 0 \quad (7.3.8)$$

$$\frac{d}{dt} \left(\frac{\partial L}{\partial \dot{\theta}_{cr}} \right) - \frac{\partial L}{\partial \theta_{cr}} = \left(\frac{L^2}{4} m_{cr} - J_{fw} \right) \ddot{\theta}_{cr} - \frac{L}{2} k_{e, fw} \varphi_a + (k_{b, cr} + k_{e, fw}) \theta_{cr} + \frac{L}{2} k_{b, cr} y_{cr} = 0 \quad (7.3.9)$$

$$\frac{d}{dt} \left(\frac{\partial L}{\partial \dot{y}_{cr}} \right) - \frac{\partial L}{\partial y_{cr}} = m_{cr} \ddot{y}_{cr} + k_{b, cr} y_{cr} + k_{b, cr} \frac{L}{2} \theta_{cr} = 0 \quad (7.3.10)$$

$$\frac{d}{dt} \left(\frac{\partial L}{\partial \dot{x}_p} \right) - \frac{\partial L}{\partial x_p} = \left(m_{ps} + m_p + \frac{1}{3} m_g \right) \ddot{x}_p + \frac{1}{6} m_g \ddot{x}_g + \frac{k_{c, c} k_{b, ps}}{k_{c, c} + k_{b, ps}} x_p = 0 \quad (7.3.11)$$

$$\frac{d}{dt} \left(\frac{\partial L}{\partial \dot{x}_g} \right) - \frac{\partial L}{\partial x_g} = \frac{1}{3} m_g \ddot{x}_g + \frac{1}{6} m_g \ddot{x}_p + k_g x_g = 0 \quad (7.3.12)$$

For the simplicity of notation of equations (7.3.7) to (7.3.12) it was assumed that, $(J_m + J_{co}) = J_M$, $(k_{t, m} + k_{c, co}) = k_M$, $(J_{fw} + J_a - J_{co}) = J_A$, $(k_{t, a} + k_{e, fw} + k_{c, co}) = k_A$, $\left(\frac{L^2}{4} m_{cr} - J_{fw} \right) = J_{FW}$, $(k_{b, cr} + k_{e, fw}) = k_{FW}$, and $\left(m_{ps} + m_c + m_p + \frac{1}{3} m_g \right) = M$, therefore a simplified matrix representing the heat exchanger experimental set-up dynamic behaviour is given as

$$\begin{bmatrix} k_M - \omega^2 J_M & -k_{c, co} & 0 & 0 & 0 & 0 \\ -k_{c, co} & k_A - \omega^2 J_A & -k_{e, fw} \frac{L}{2} & 0 & 0 & 0 \\ 0 & -k_{e, fw} \frac{L}{2} & k_{FW} - \omega^2 J_{FW} & \frac{L}{2} k_{b, cr} & 0 & 0 \\ 0 & 0 & \frac{L}{2} k_{b, cr} & k_{b, cr} - \omega^2 m_{cr} & 0 & 0 \\ 0 & 0 & 0 & 0 & \frac{k_{c, c} k_{b, ps}}{k_{c, c} + k_{b, ps}} - \omega^2 M & -\omega^2 \frac{m_g}{6} \\ 0 & 0 & 0 & 0 & -\omega^2 \frac{m_g}{6} & k_g - \omega^2 \frac{m_g}{3} \end{bmatrix} \quad (7.3.13)$$

Substituting the mass, the mass inertia and the stiffness with their values the dynamic behaviour matrix of equation (6.3.13) becomes:

$$\begin{bmatrix} 21 \times 10^9 - 0.9 \omega^2 & -21 \times 10^9 & 0 & 0 & 0 & 0 \\ -21 \times 10^9 & 15 \times 10^{11} - 0.07 \omega^2 & -7325 \times 10^6 & 0 & 0 & 0 \\ 0 & -7325 \times 10^6 & 107 \times 10^5 - 0.071 \omega^2 & 4.1 \times 10^6 & 0 & 0 \\ 0 & 0 & 4.1 \times 10^6 & 4.4 \times 10^7 - 0.43 \omega^2 & 0 & 0 \\ 0 & 0 & 0 & 0 & 5.62 \times 10^7 - 4.5 \omega^2 & -0.00026 \omega^2 \\ 0 & 0 & 0 & 0 & -0.00026 \omega^2 & 94 - 0.00052 \omega^2 \end{bmatrix}$$

The no-trivial equation obtained from the determinant of the above matrix gives the system frequency natural equation as

$$1.38 \omega^{12} + 20.8 \omega^{10} - 76.38 \omega^8 + 104.1 \omega^6 - 903 \times 10^{30} \omega^4 + 153.15 \times 10^{49} \omega^2 - 1.87418 \times 10^{60} = 0$$

Appendix E Error Analysis

No measurement of a physical quantity can be entirely accurate. It is convenient to know how the measured value is likely to deviate from the unknown, true value of a quantity. This Appendix presents brief discussions on how errors are reported and the types of errors that may occur.

E.1 Systematic errors

Systematic errors arise from a flaw in the measurement scheme which is repeated each time a measurement is made. Some sources of systematic errors are the following (Bork et al., 1993):

- errors in the calibration of the measuring instruments.
- incorrect measuring technique
- bias of the experimenter.

E.2 Random errors

Random errors arise from the fluctuations that are most easily observed by carrying out multiple trials of a given measurement. Since the measured values are not the same each time that a measurement is taken, the result is uncertain. There are several common sources of such random uncertainties in the types of experiments that are likely to be performed (Taylor, 1982), for example:

- uncontrollable fluctuations in initial conditions in the measurements
- limitations imposed by the precision of the measuring apparatus, and the uncertainty in interpolating between the smallest divisions.
- lack of precise definition of the quantity being measured.
- sometimes the quantity measured is well defined but is subject to inherent random fluctuations.

E.3 Absolute and relative errors

The absolute error in a measured quantity is the uncertainty in the quantity and it has the same units as the quantity itself. The relative error (also called the fractional error) is obtained by dividing the absolute error in the quantity by the quantity itself. The relative error is usually more significant than the absolute error. This section presents an evaluation of the relative errors on the measured values in the heat exchanger, the air cooled condenser, the heater, the cooler and the regenerator (Bork et al., 1993).

Once some experimental results were obtained, they were compared to theoretical results in order to obtain the desired quantity. In order to determine the estimated error, the theoretical results must be combined with the experimental results in relative error formulae to evaluate errors in the input quantities. The simplest procedure would be to add the errors. This would

be a conservative assumption, but it overestimates the uncertainty in the result. Clearly, if the errors in the inputs are random, they will cancel each other out at least some of the time. If the errors in the measured quantities are random, and if they are independent, then error theory shows that the uncertainty in a calculated result can be obtained from a few simple rules, some of which were developed referring to Bork et al. (1993) and Taylor (1982) and used in this section to evaluate the relative error in the results.

The air-cooled condenser thermal resistance relative error is

$$\frac{\Delta R_{tot,acc,e}}{R_{tot,acc,e}} = \frac{\Delta(\Delta T_{In,acc})}{\Delta T_{In,acc}} - \frac{\Delta \dot{Q}_{acc}}{\dot{Q}_{acc}} \quad (E.3.1)$$

The air-cooled condenser log mean temperature difference relative error is:

$$\frac{\Delta(\Delta T_{In,acc})}{\Delta T_{In,acc}} = \sqrt{\left[\frac{\partial(\Delta T_{acc})}{(\Delta T_{acc})} \right]^2 + \left[\frac{\partial \ln \left(\frac{(T_{acc,in} - T_{acc,out})}{(T_{acc,air,out} - T_{acc,air,in})} \right)}{\ln \left(\frac{(T_{acc,in} - T_{acc,out})}{(T_{acc,air,out} - T_{acc,air,in})} \right)} \right]^2} \quad (E.3.2)$$

The air-cooled condenser temperature difference $\Delta T_{acc} = (T_{acc,in} - T_{acc,out}) - (T_{acc,air,out} - T_{acc,air,in})$

The air-cooled condenser temperature difference absolute error is

$$\partial(\Delta T_{acc}) = \left| \left[(T_{acc,in} - T_{acc,out}) - (T_{acc,air,out} - T_{acc,air,in}) \right] - \left[(T_{acc,in,t} - T_{acc,out,t}) - (T_{acc,air,out,t} - T_{acc,air,in,t}) \right] \right| \quad (E.3.3)$$

The air-cooled condenser logarithmic ratio absolute error is

$$\partial \ln \left[\frac{T_{acc,in} - T_{acc,out}}{T_{acc,air,out} - T_{acc,air,in}} \right] = \left| \ln \left[\frac{T_{acc,in} - T_{acc,out}}{T_{acc,air,out} - T_{acc,air,in}} \right] - \ln \left[\frac{T_{acc,in,t} - T_{acc,out,t}}{T_{acc,air,out,t} - T_{acc,air,in,t}} \right] \right| \quad (E.3.4)$$

The air-cooled condenser heat transfer rate relative error

$$\frac{\Delta \dot{Q}_{acc}}{\dot{Q}_{acc}} = \sqrt{\left(\frac{\partial \rho_{acc,air}}{\rho_{acc,air}} \right)^2 + \left(\frac{\partial v_{air}}{v_{air}} \right)^2 + \left(\frac{\partial c_{p,air}}{c_{p,air}} \right)^2 + \left[\frac{\partial (T_{acc,air,out} - T_{acc,air,in})}{(T_{acc,air,out} - T_{acc,air,in})} \right]^2} \quad (E.3.5)$$

Using equations (E.3.1)-(E.3.5), air-cooled condenser thermal resistance is given in table E.1.

Table E.1: Air-cooled condenser line relative errors

Designation	Relative error	
	Single to two phase mode	Heat pipe mode
log mean temperature difference	8.6%	7.7%
The heat transfer rate	7.1%	6.5%
The thermal resistance	8.8%	6.8%

The heat exchanger condenser thermal resistance relative error is

$$\frac{\Delta R_{tot,he}}{R_{tot,he}} = \frac{\Delta(\Delta T_{In,he})}{\Delta T_{In,he}} - \frac{\Delta \dot{Q}_{he}}{\dot{Q}_{he}} \quad (E.3.6)$$

The heat exchanger log mean temperature difference relative error is

$$\frac{\Delta(\Delta T_{In,he})}{\Delta T_{In,he}} = \sqrt{\left[\frac{\partial(\Delta T_{he})}{(\Delta T_{he})} \right]^2 + \left[\frac{\partial \ln \left(\frac{(T_{he,int} - T_{he,out})}{(T_{cw,out} - T_{cw,in})} \right)}{\ln \left(\frac{(T_{he,in} - T_{he,out})}{(T_{cw,out} - T_{cw,in})} \right)} \right]^2} \quad (E.3.7)$$

The heat exchanger temperature difference $\Delta T_{he} = ((T_{he,in,t} - T_{he,out,t}) - (T_{cw,out,t} - T_{cw,in,t}))$

The heat exchanger temperature difference absolute error is

$$\partial(\Delta T_{he}) = \left| \left[(T_{he,int} - T_{he,out}) - (T_{cw,out} - T_{cw,in}) \right] - \left[(T_{he,int,t} - T_{he,out,t}) - (T_{cw,out,t} - T_{cw,in,t}) \right] \right| \quad (E.3.8)$$

The heat exchanger logarithmic ratio absolute error is

$$\partial \ln \left[\frac{T_{he,int} - T_{he,out}}{T_{cw,out} - T_{cw,in}} \right] = \left| \ln \left[\frac{T_{he,int} - T_{he,out}}{T_{cw,out} - T_{cw,in}} \right] - \ln \left[\frac{T_{he,int,t} - T_{he,out,t}}{T_{cw,out,t} - T_{cw,in,t}} \right] \right| \quad (E.3.9)$$

The heat exchanger heat transfer rate relative error

$$\frac{\Delta \dot{Q}_{he}}{\dot{Q}_{he}} = \sqrt{\left(\frac{\partial \dot{m}_{he}}{\dot{m}_{he}} \right)^2 + \left(\frac{\partial c_{p,he}}{c_{p,he}} \right)^2 + \left[\frac{\partial (T_{he,in} - T_{he,out})}{(T_{he,in} - T_{he,out})} \right]^2} \quad (E.3.10)$$

Using equations (E.3.6)-(E.3.10), air-cooled condenser thermal resistance is given in table E.2.

Table E.2: Heat exchanger line relative errors

Designation	Relative error	
	Single to two phase mode	Heat pipe mode
log mean temperature difference	7.0%	6.3%
The heat transfer rate	6.6%	5.4%
The thermal resistance	8.0%	6.1%

The heater thermal resistance relative error is:

$$\frac{\partial R_{h,exp}}{R_{h,exp}} = \sqrt{\left[\frac{\partial (\bar{T}_{hot} - \bar{T}_{hot,g})}{(\bar{T}_{hot} - \bar{T}_{hot,g})} \right]^2 - \left(\frac{\partial \dot{Q}_{a,h}}{\dot{Q}_{a,h}} \right)^2} \quad (E.3.11)$$

The hot temperatures absolute error is

$$\partial(\bar{T}_{hot} - \bar{T}_{hot,g}) = |(\bar{T}_{hot} - \bar{T}_{hot,g}) - (\bar{T}_{hot,t} - \bar{T}_{hot,g,t})| \quad (E.3.12)$$

The heater heat transfer rate relative error is:

$$\frac{\Delta \dot{Q}_{he}}{\dot{Q}_{he}} = \sqrt{\left(\frac{\partial \dot{m}_{hot}}{\dot{m}_{hot}} \right)^2 + \left(\frac{\partial c_{p,hot}}{c_{p,hot}} \right)^2 + \left[\frac{\partial (T_{h,i} - T_{h,o})}{(T_{h,i} - T_{h,o})} \right]^2} \quad (E.3.13)$$

Using equation (E.3.11)-(E.3.13) and, similarly, with respect to the flow direction for the cooler and regenerator, the heater, cooler and the regenerator respectively thermal resistance relative errors are summarised in table E.3.

Table E.3: Stirling heat exchanger relative errors

Designation	Heater	Cooler	Regenerator
Heat transfer rate	8.0%	9.0%	11.0%
Thermal resistance	7.1%	7.3%	10.0%

Appendix F Calibration of experimental measuring instruments

F.1 Calibration of thermocouples

The calibrated sub-standard thermometer made of platinum (manufactured by ISOTECH South Africa, model number 935-14-72, serial number 191069), and an oil bath was used to calibrate the thermocouples. Table F.1 shows the calibration of the 3 K-type thermocouples used to measure the temperature of the fuel tank wall. The thermocouples T1, T2 and T3 have a minimum and maximum relative error of 0.29 and 2.399% respectively.

Table F.1: K-type thermocouples calibration

Reference	K-type thermocouples, T [°C]			Relative error [%]		
	T1	T2	T3	T1	T2	T3
Temp						
20.215	20.7	20.7	20.7	2.399	2.399	2.399
35.132	34.9	35	35	0.660	0.375	0.375
40.326	40.1	40.1	40.1	0.560	0.560	0.560
51.265	51.1	51.1	51.1	0.32	0.321	0.321
60.576	60.4	60.4	60.4	0.290	0.290	0.290
70.837	70	70	70	1.181	1.181	1.181
77.448	78.9	78.9	78.9	1.874	1.874	1.874
78.981	80.6	80.6	80.6	2.049	2.049	2.049
80.955	82.4	82.4	82.4	1.784	1.784	1.784
83.045	84.4	84.4	84.4	1.631	1.631	1.631
88.833	88	88	88	0.937	0.937	0.937
91.483	90.7	90.7	90.7	0.855	0.855	0.855
101.144	100.2	100.4	100.3	0.933	0.735	0.834

Table F.2(a) completed by Table F.2(b) show the calibration of T-type thermocouples used to measure the temperature in the WHR&U system thermosyphon loop and in the SE heat exchanger. The thermocouples T4, T5, T6, and T7 have minimum and maximum relative errors of 0.29% and 2.399%, respectively, while the thermocouple T8 has minimum and maximum relative errors of 0.29% and 2.682%, respectively.

Table F.2 (a): T-type thermocouple calibration

Ref	T-Type thermocouples, T [°C]					Relative error [%]				
	T4	T5	T6	T7	T8	T4	T5	T6	T7	T8
Temp										
20.215	20.7	20.7	20.7	20.7	20.7	2.399	2.399	2.399	2.399	2.399
35.132	35	35	35	35	35.4	0.375	0.375	0.375	0.3757	0.762
40.326	40.1	40.1	40.1	40.1	40.6	0.560	0.560	0.560	0.5604	0.679
51.265	51.1	51.1	51.1	51.1	51.7	0.321	0.321	0.321	0.321	0.848
60.576	60.4	60.4	60.4	60.4	60.9	0.290	0.290	0.290	0.290	0.534

Table F.2 (b): T-type thermocouple calibration

70.837	70	70	70	70	71.1	1.181	1.181	1.181	1.181	0.371
77.448	78.9	78.9	78.9	78.9	79.2	1.874	1.874	1.874	1.874	2.262
78.981	80.6	80.6	80.6	80.6	81.1	2.049	2.049	2.049	2.049	2.682
80.955	82.4	82.4	82.4	82.4	82.6	1.784	1.784	1.784	1.784	2.031
83.045	84.4	84.4	84.4	84.4	85	1.631	1.631	1.631	1.631	2.354
88.833	88.1	88	88	87.9	88.8	0.825	0.937	0.937	1.050	0.037
91.483	90.7	90.7	90.7	89.7	91.4	0.855	0.855	0.855	1.948	0.090
91.483	100.4	100.1	100	99.1	101.2	0.735	1.032	1.131	2.020	0.055
101.144	100.4	100.1	100	99.1	101.2	2.399	2.399	2.399	2.399	2.399

Table F.3 shows the other T-type thermocouples used to measure the temperature in the waste heat recovery and utilisation thermosyphon loop and the SE heat exchanger. T9 and T10 have maximum relative error of 3.388%, while their minimum relative errors are 0.369% and 0.204% respectively. T11 and T12 have minimum and maximum relative error of 0.66% and 2.515% respectively.

Table F.3: T-type thermocouple calibration

Reference Temp	T-Type thermocouples, T [°C]				Relative error [%]			
	T9	T10	T11	T12	T9	T10	T11	T12
20.215	20.9	20.9	20.6	20.6	3.388	3.388	1.904	1.904
35.132	35.4	35.5	34.9	34.9	0.762	1.047	0.660	0.660
40.326	40.6	40.7	40	40	0.679	0.927	0.808	0.808
51.265	51.5	51.8	50.6	50.6	0.458	1.043	1.297	1.297
60.576	60.8	60.7	60.1	60.1	0.369	0.204	0.785	0.785
70.837	71.8	71.4	69.8	69.8	1.359	0.794	1.463	1.463
77.448	79.1	79.2	78.6	78.6	2.133	2.262	1.487	1.487
78.981	81	81.3	80.4	80.4	2.556	2.936	1.796	1.796
80.955	82.9	82.7	82.3	82.3	2.402	2.155	1.661	1.661
83.045	85	85.1	84.1	84.1	2.354	2.474	1.270	1.270
88.833	89.4	89.6	86.9	86.9	0.638	0.863	2.175	2.175
91.483	91.9	92.4	89.4	89.4	0.455	1.002	2.276	2.276
101.144	101.6	102.3	98.6	98.6	0.450	1.142	2.515	2.515

F.2 Calibration of Endress and Hauser pressure sensor

An Endress and Hauser PDM230-CU1B2ED1A pressure transducer was used to measure the pressure drop across the heat exchangers. The pressure transducer was calibrated using a Van Essen Betz micromanometer, Type 5000 model. The Betz micromanometer has a range of -10 to 5000 Pa and an accuracy of ± 0.2 Pa. The Betz micromanometer is calibrated to the Netherlands Calibration Organization (Nederlandse Kalibratie Organisatie, 1991) standard and

is therefore the laboratory standard which the PDM230-CU1B2ED1A pressure transducer must adhere to. Figure F.1 shows the pressure transducer calibration.

The calibration was done by connecting both the micromanometer and the PDM230-CU1B2ED1A pressure transducer in parallel to a single tube. Air was then blown into this tube and the measured values of the PMD75 were compared to the Betz micromanometer reading. A linear calibration curve was obtained from the data in Figure F.1, with $R^2=0.954$. The calibration equation is given as

$$P_{corrected}=2595.9875P_r-2485.8765 \tag{F.2.1}$$

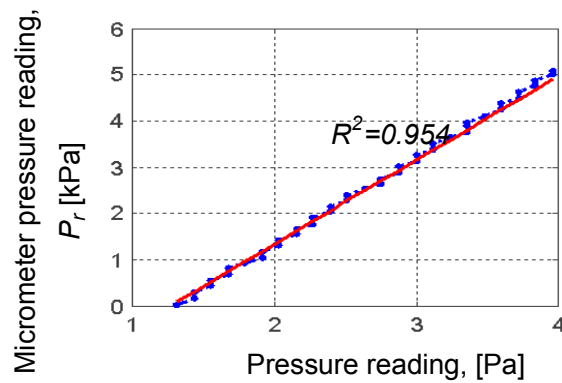


Figure F.1: Pressure transducer calibration

F.3 Festo MS6-SFE flow sensor calibration

The Festo (MS6-SFE series) flow sensor was calibrated using the Type 55D41/42 calibration unit. Figure F.2 shows the flow sensor calibration.

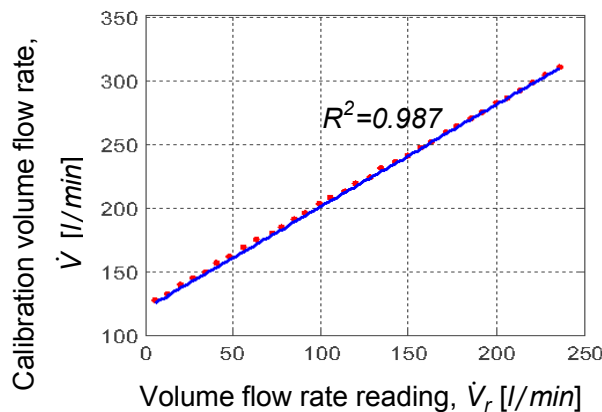


Figure F.2: Flow sensor calibration

From figure F.2 the calibration equation was determined by plotting a linear trendline through the data points, with $R^2=0.987$ the calibration equation is given as

$$\dot{V}_{corrected}=1.47598\dot{V}_r-47.13 \tag{F.2.2}$$